Hydrogen storage on nanoporous carbons

Odunsi, Oluwatoni Yewande

Award date:
2007

Awarding institution:
University of Bath

HYDROGEN STORAGE ON NANOPOROUS CARBONS

Oluwatoni Yewande Odunsi

A thesis submitted for the degree of Doctor of Philosophy

University of Bath

Department of Chemical Engineering

April 2007

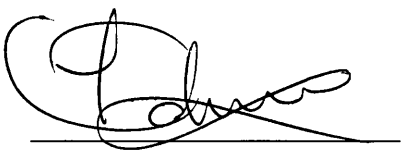

ProQuest LLC
789 East Eisenhower Parkway
P.O. Box 1346
Ann Arbor, MI 48106-1346

DEDICATION

Dedicated to the memory of my loving mother, Modupe Adeyosola Odunsi and to my father, Joseph Odunsi.

ABSTRACT

The pressure to reshape our energy future by developing or finding environmentally benign energy alternatives is mounting. This has created a great interest in hydrogen as the next energy carrier to fuel the proposed transition to the 'Hydrogen Economy'. The advancement towards this new energy era is not without its milestones both technological and social. The efficient storage of hydrogen is a key step that needs to be taken for the efficient and safe storage of hydrogen in vehicular (mobile) and stationary applications. Investigation of the potential of nanoporous carbon materials to store H_2 has been carried out to bridge this technological gap. Gravimetric and volumetric sorption measurements along with the structural characterisation of these materials have been carried out to this effect. These reveal that gas purity affects the hydrogen storage capacity of nanoporous carbons to varying extents depending on the temperature used. Nanoporous carbons with high surface area and pore volume such as the Norit CNR 115 activated carbons do have the potential to be suitable stores for hydrogen at liquid nitrogen temperatures. At room temperature, storage of large amounts of hydrogen appears unlikely for the activated carbons. The calculated average isosteric heats of adsorption for the activated carbons are 4.04, 5.49, 2.70 kJ mol^{-1} for BPL, Norit CNR 115 and SRD/667/1 respectively. These values although similar to values obtained in the literature are relatively low for hydrogen-carbon interactions, which is detrimental to hydrogen storage capacity of these materials.

ACKNOWLEDGMENTS

Firstly, I would like to acknowledge Dr. Tim Mays for his supervision, enthusiasm and guidance throughout this PhD. I also acknowledge the funding support provided by the Engineering and Physical Sciences Research Council (EPSRC). The United Kingdom – Sustainable Hydrogen Energy Consortium (UK-SHEC) and the University of Bath are also acknowledged. I would also like to thank the technical and administrative staff in the Department of Chemical Engineering for their assistance. Thanks are also due to Dr. Yufeng He for his scholarly chats and advice, all the friends I have made while at Bath, especially to Julien for his numerous words of encouragement, support and for being there throughout. To my family, thank you so much for your prayers, your love and constant reminder of how proud you are of me.

CONTENTS

INDEX OF FIGURES

INDEX OF TABLES

NOMENCLATURE

w	Pore Width
T_c	Critical Temperature
n^a	Amount of Gas Adsorbed at p/p^0
m_s	Mass of Solid Material
p	Equilibrium Pressure
T	Temperature
p^0	Saturation Pressure of the Gas at T
p/p^0	Relative Pressure
$n(t)$	Uptake of Gas at time, t
k	Adsorption Rate Constant
Δn	Total Change in Gas Uptake
t	Time
V_s	Chamber of Unknown Volume
V_x	Sample of Unknown Volume
V_r	Reference Chamber of known Volume
P_s	Sample Chamber Pressure
P_r	Reference Chamber Pressure
P_{sys}	System Pressure
W_e	Excess Adsorbed Weight
W	Detected Weight of the Adsorbent
W_s	Sample Weight
W_t	Total Adsorption
V_a	Adsorbate Pore Volume

W_a	Weight of the Adsorbed Phase
V	Volume
Z	Gas Compressibility Factor
R	Gas Molar Constant
a, b	Peng-Robinson Equation of State Constants
C	Brunauer Emmett Teller Energy Constant
n^a_m	Monolayer Capacity
A_s	Brunauer Emmett Teller Surface Area
L	Avogadro's Constant
a_m	Adsorptive Molecular Cross Sectional Area
V	Volume of gas adsorbed at p/p^0
V_0	Volume needed to fill micropores
A	Adsorption Affinity/Differential Free Energy of Adsorption
E_0	Dubinin Radushkevich Characteristic Energy
D	Dubinin Radushkevich Empirical Constant
$V_{\alpha s}$	Micropore Volume (α_s Method)
S_{ext}	External Surface Area
$V(P)$	Experimentally determined Excess Volume of Gas
$F(H)$	Pore Size Distribution
H_{max}	Maximum Pore Size
H_{min}	Minimum Pore Size
IP	Horvath Kawazoe Interaction Parameter
d_0	Average Molecular Diameter
u	Order of Diffraction
d	Sample Characteristic Interplanar Spacing
c_0	Lattice Constant
n_0	Maximum Adsorption Capacity of Adsorbent
b	Adsorption Affinity Constant
K	Freundlich Model Constant
c	Freundlich Model Heterogeneity Parameter
t	Toth Model Heterogeneity Parameter
s	Unilan Model Heterogeneity Parameter
r	Molecular Radius

D	Fractal Dimension of the Adsorbent Surface
y	Experimental Observation
y_i	Model Prediction
N_d	Number of Data Points
N_p	Number of Parameters
ΔH	Heat of Adsorption
b_0	Affinity Constant at Reference Temperature
E	Adsorption Energy
ΔG	Change in Free Energy
ΔS	Change in Entropy
k_1	Fast Adsorption Rate Constant
k_2	Slow Adsorption Rate Constant
R_p	Adsorbent Particle Radius

Greek Symbols

ρ_b	Gas Bulk Density
ρ_s	Sample Density
ρ_a	Adsorbed Phase Density
α, κ	Peng-Robinson Constants
ω	Accentric Factor
β	Dubinin Radushkevich Scaling Factor
$v(H, P)$	Excess Volume of Gas at P
σ	Gas Solid Nuclear Separation
λ	X-Ray Wavelength for Copper K_α Radiation
θ	Diffraction Angle

Abbreviations

WEO	World Energy Outlook
IEA	International Energy Agency
US DOE	United States Department of Energy
UK-SHEC	United Kingdom – Sustainable Hydrogen Energy Consortium
ICE	Internal Combustion Engine
PSA	Pressure Swing Adsorption
SMR	Steam Methane Reforming
IGCC	Integrated Gasification Combined-Cycle
PV	Photovoltaic
CHP	Combined Heat and Power
PEM	Polymer Electrolyte Membrane
AFC	Alkaline Fuel Cell
PAFC	Phosphoric Acid Fuel Cell
MCFC	Molten Carbonate Fuel Cell
SOFC	Solid Oxide Fuel Cell
NASA	National Aeronautics and Space Administration
H_2 – ICE	Hydrogen Internal Combustion Engine
UTC	United Technologies Company
NHA	National Hydrogen Association
LEL	Lower Explosion Limit
UEL	Upper Explosion Limit
ISO	International Standards Organisation
IUPAC	International Union of Pure and Applied Chemistry
TGA	Thermogravimetric Analyser
IGA	Intelligent Gravimetric Analyser
TEM	Transmission Electron Microscopy
STM	Scanning Tunnelling Microscopy
SWNT	Single-Walled Nanotube
GNF	Graphitic Nanofibres
MWNT	Multi-Walled Nanotube
TPD	Temperature Programmed Desorption

CVD	Catalytic Vapour Deposition
LDF	Linear Driving Force
ASAP	Accelerated Surface Area and Porosimetry
XRD	X-Ray Diffraction
LG-H_2	Low Grade Hydrogen
HG-H_2	High Grade Hydrogen
UHP-H_2	Ultra High Purity Hydrogen
BDDT	Brunauer Deming Deming and Teller
GCMC	Grand Canonical Monte Carlo
db	Dry Basis
BET	Brunauer Emmett Teller
DR	Dubinin Radushkevich
PSD	Pore Size Distribution
DFT	Density Functional Theory
HK	Horvath-Kawazoe
BJH	Barrett, Joyner and Halenda
HRTEM	High Resolution Transmission Electron Microscopy
RMSE	Root Mean Square Error
MLDF	Modified Linear Driving Force

Chapter One

Introduction and Scope

1.1 Thesis Context

There is an increased awareness today that the worldwide dependence on fossil fuels is faced with a number of issues including the forecasted depletion of these resources, climate change, and energy security as the major suppliers of these resources are either economically or politically unstable. According to estimates, the production of fossil fuels (i.e. oil, coal and natural gas) will peak around the year 2010 and then will start to decline. If we produce synthetic fossil fuels (i.e. synthetic gasoline and synthetic natural gas) from coal, then their production will continue to rise until the year 2025, and will start to decline thereafter. (Veziroglu and Babir, 1992). Energy demand is another factor that is driving research on alternative sources of energy. According to the World Energy Outlook (WEO) 2005, supplied by the International Energy Agency (IEA) world energy demand is expected to expand by more than 50% between now and 2030, to 16.3 billion tonnes of oil equivalent. Global carbon dioxide emissions are expected to increase by 1.6% per year over 2003-2030. By 2010, energy related CO_2 emissions will be 38% higher than at 1990.

This knowledge has led to the search for more sustainable, secure and environmentally friendly energy alternatives to the current fossil fuel economy.

Hydrogen is at present one of the prime candidates as a future energy vector to provide an alternative to the current fossil fuel era. It has a variety of social, economic and environmental benefits, such as its capability to reduce pollution and greenhouse gas emissions, when produced from sustainable sources or coupled with CO_2 sequestration techniques.

Until recently, the use of hydrogen has been centred on other technologies such as in the production of methanol, hydrocracking and desulphurisation of oil. In spite of the many advantages of adopting an energy economy with hydrogen as an energy carrier, there still remain a number of technological milestones to be overcome. These include the sustainable production of hydrogen, its delivery, storage and end applications.

Being the lightest element, with the lowest density (0.09 kg m^{-3}) under normal conditions (20 °C, 101.325 kPa) (Tzimas *et al.*, 2003) hydrogen gas is difficult to store in small volumes making mobile applications difficult. The development of suitable technologies for hydrogen storage is at present the subject of a great deal of research worldwide. According to several authors, hydrogen can currently be stored as a compressed gas to increase its density in compact gas tanks where hydrogen is stored at high pressures of up to 800 bar. Although the most mature technology, hydrogen storage by compression has the drawback of size, weight cost and safety especially on board vehicles. Hydrogen can also be stored as a liquid at 20 K (its most energy dense form), which requires the use of cryogenic vessels but requires less volume than gas storage. The major setback of this technology is the liquefaction of hydrogen, which is an energy intensive process that consumes a large amount of energy equivalent to about a third of the energy content of hydrogen (Zhou *et al.*, 2003, de la Casa-Lillo *et al.*, 2002, Cheng *et al.*, 2000, Levesque *et al.*, 2002; Zhao *et al.*, 2005, Hirscher and Becher, 2003). Hydrogen can be stored in chemical compounds, such as methanol and ammonia using a variety of technologies, and also on solid-state materials by physisorption or chemisorption (Texier-Mandoki *et al.*, 2004, Poirier *et al.*, 2004) but these technologies are still in the research stages.

To meet the energy storage requirements of a future hydrogen economy requires that the problem of storage be solved. This store would be essential for the provision of hydrogen in periods of low energy supply. For example, where hydrogen is produced

from wind energy, part of the energy produced will be diverted for hydrogen production, which can then be subsequently stored for periods of low wind supply. Presently, a compact, lightweight hydrogen storage system for transportation is not available. Hydrogen storage is therefore the key enabling technology that must be significantly advanced in terms of performance and effectiveness if hydrogen is to become an important part of the world's energy economy (Dillon and Heben, 2001, Cheng *et al.*, 2000, Kajiura *et al.*, 2003, de la Casa-Lillo *et al.*, 2002).

A storage medium is required that can hold a useful amount of hydrogen in a small volume without compromising cost and safety. It is required that the store be easily charged and discharged. The target set by the US Department of Energy (DOE) is 9 wt % by 2015 for systems (US DOE, 2006), which is adopted internationally.

1.2 Research Scope

This research is concerned with the assessment of the potential of nanoporous carbon materials as hydrogen storage media. Carbon materials for hydrogen storage have been the subject of much research in the past and reported by several authors. In an early publication by Dillon *et al.*, (1997) it was stated that single-walled carbon nanotubes can store 5-10 wt % hydrogen at ambient temperature. Values as large as 60 wt % for graphitic nanofibres have been also quoted by Chambers *et al.*, (1998). These values have not been verified or reproduced via experiments and theoretical calculations, leading to a great deal of controversy in this field of study.

In this work, a number of commercially available nanoporous carbon materials have been acquired and analysed for their ability to store hydrogen at temperatures ranging from cryogenic (77 K) to high temperature (303 K). The structural properties of these materials have also been assessed to correlate the results and make reasonable judgements on the suitability of these materials for hydrogen storage.

A detailed analysis of the experimental results is carried out by applying thermodynamic calculations and fitting semi-empirical adsorption models to the data.

1.3 Thesis Structure

This thesis consists of seven chapters. Chapter one is an introduction to the thesis, it briefly brings the research into context and highlights the surrounding issues. It also describes the scope of the research as well as the structure of this thesis. Chapter two gives a detailed insight to, and attempts to provide a critical review of, the vast literature available on the hydrogen economy, the current state of the art on hydrogen production, storage, delivery and its end use. It also assesses the issues that may affect the acceptance of hydrogen as a future energy vector. The chapter continues with a description of adsorption theory; it gives an overview of the preparation, treatment, nature and a literature review of existing data available on hydrogen storage in nanoporous carbon materials, which is within the scope of this research. This chapter concludes with a statement of the overall aim of this research. In Chapter three, a detailed description of the experimental methods adopted for the characterisation of the nanoporous materials studied is reported. It provides information on the materials selected and the experimental methods used in their analysis. Chapters four and five present the characterisation and hydrogen storage results for the nanoporous carbons obtained by methods described in chapter three. In Chapter six, analysis of the gravimetric hydrogen storage results are presented along with a discussion of the results. The thesis summary, conclusions and suggestions for future work are finally detailed in Chapter seven.

1.4 Dissemination

The work detailed in this thesis has been presented on a number of occasions to a varying audience with different research interests. These include six monthly United Kingdom – Sustainable Hydrogen Energy (UK-SHEC) Consortium meetings, where the details of this work were challenged and scrutinised. It also includes a number of poster presentations at the 7th World Chemical Engineering Conference in Glasgow, 2005 (Odunsi *et al.*, 2005); 7th International Conference on the Characterisation of Porous Solids in Aix-en-Provence, France, 2005 (Odunsi *et al.*, 2006) and at the Britain's Young Engineers competition held at the House of Commons, London, 2005. A paper is also being prepared for publication in the Journal of Materials Chemistry.

Chapter Two

Background to Thesis

2.1 Introduction

This chapter summarises the vast literature surrounding the hydrogen economy, its potential adoption and hence the importance of finding a suitable storage medium to support its implementation. The current and future situation and issues affecting the adoption of the proposed hydrogen economy are discussed. This chapter also presents nanoporous carbon materials as a means of solving the storage problem. Finally, the chapter concludes with a statement on the aims of the thesis.

2.2 The Hydrogen Economy

Carbon dioxide emissions, the main greenhouse gas from human activities, the continuing rise in energy demand, the depletion of fossil fuel reserves, poor air quality and the security of energy supply are the subject of a worldwide debate about energy sustainability and the stability of the global climate (Goltsov and Veziroglu, 2001; Conte *et al.*, 2001; Cherry, 2004; Gosselink, 2002; Uhrig, 2004). To this effect driving the global energy system into a sustainable path is progressively becoming a

major concern. The emergence of a sustainable global energy system, however, is a gradual long-term process that will require a profound transformation of its current structure (Barreto *et al.*, 2003). Alternative solutions are the subject of current research interest. The hydrogen economy has received particular attention. A hydrogen-based energy system is regarded as an advantageous option for delivering high-quality energy solutions (Ogden, 1999). Hydrogen (when produced from renewable energy sources), used as an energy vector in the stationary power, transportation, industrial, residential and commercial sectors has been proposed as a suitable path to solving the world's energy issues.

The transition to a hydrogen-based energy economy, where the main chemical energy carrier is hydrogen and the main non-chemical energy form is electricity, is being made gradually, and is likely to continue to the middle or end of the 21st century. Current world hydrogen production is approximately 45 Mt year^{-1}, which is equivalent to 2 % of world energy demand (Raman, 2003). However, current total annual worldwide hydrogen consumption is in the range of 36 - 45 Mt year^{-1}. Of this quantity, approximately 97 % is captive, that is, the hydrogen is produced at the site of consumption or internal production and only about 3 % is provided from merchant sources (Manitoba Energy Development Initiative, 2003).

To expand the role of hydrogen in the near term (present – 2010), several approaches are being proposed. One is to use hydrogen for transportation by mixing it with natural gas (hythane) as a fuel for internal combustion engines (ICE); this would increase engine performance and decrease pollution. Another approach involves producing hydrogen at central locations and distributing it to refuelling stations. The hydrogen will then be pumped into vehicles for use in fuel cells and power plants (Midilli *et al.*, 2005). Hydrogen-powered fuel cell vehicles produce no emissions other than water vapour.

According to Midilli *et al.*, (2005), a hydrogen economy will likely be introduced over a long time period and involve near, intermediate and long term phases:

In the near term (present – 2010) it is proposed that hydrogen will be produced primarily by advanced steam reforming of natural gas, either at central or distributed

facilities. This process presents an opportunity to decrease the amount of carbon dioxide released to the atmosphere, since a by product of steam reforming is a high purity carbon dioxide that can be collected and used, or sequestered in many ways, such as in coal seams, depleted oil and natural gas fields, or saline aquifers.

In the intermediate term (2010 – 2025), restructuring of the electric utility industry will present opportunities for distributed generation, where hydrogen-powered fuel cells will provide on-site generation of electricity. In addition to electricity, these fuel cells will also produce thermal energy for hot water, space heating and industrial processes. During this phase, hydrogen will be increasingly produced from coal and from the pyrolysis or gasification of biomass. Biomass for hydrogen production will come from dedicated crops, agricultural residues, or municipal solid wastes. Dedicated crops will be particularly valuable for offsetting carbon dioxide emissions because biomass crops re-grown specifically for energy will recycle carbon dioxide from the atmosphere, resulting in no net carbon dioxide emissions. In the intermediate term, an increasing number of hydrogen-fuelled zero-emission vehicles will also be on the road, due to improvements in onboard storage and other technologies. This occurrence will provide a need for building a hydrogen infrastructure.

In the long term (post 2025), strong hydrogen markets and a growing hydrogen infrastructure will create opportunities for renewable hydrogen systems. Intermittent energy technologies such as wind turbines or photovolatiacs, for example, will power electrolysers to produce hydrogen for fuel cells. The fuel cells will use the hydrogen to provide electricity during higher demand periods or to supplement the intermittent energy sources. This era will likely also witness the emergence and growth of advanced technologies that produce hydrogen from water and sunlight and that store hydrogen in high energy density systems. Market penetration of advanced technologies to produce, store and use hydrogen will mark the establishment of the hydrogen energy economy.

Midilli *et al.*, (2005) presents the work of Jones, which cites the uncertainties of a hydrogen economy:

- The hydrogen economy is an end state based on hydrogen produced from renewable energy such as solar or wind. But it is not yet economical to produce hydrogen in this way.
- Hydrogen-powered fuel cells promise to provide clean and efficient energy for future vehicles and stationary power generation, but that is only achievable if the hydrogen is produced cleanly.
- A long transition to hydrogen from hydrocarbons is likely.
- Cost and technical hurdles must be overcome to allow mass adoption of fuel cells and other hydrogen technologies.

Despite these issues, there is an increased momentum for a hydrogen economy due to global environmental problems, energy security and supply issues, and technological innovations. Figure 2.2-1 is a diagrammatic representation of the technological pathway for hydrogen economy development.

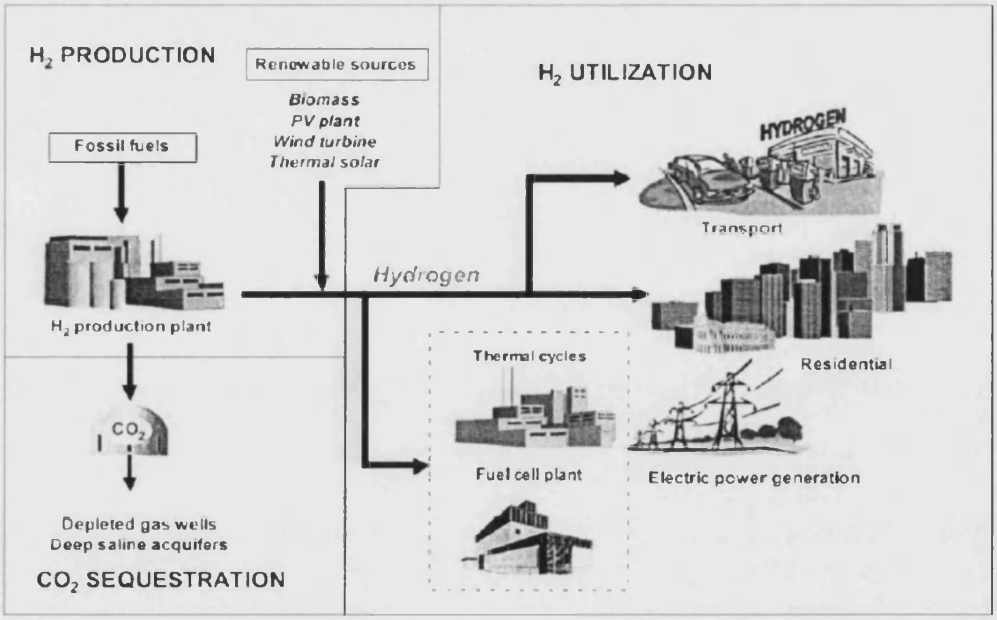

Figure 2.2-1: Technological Pathway for Hydrogen Economy Development (Conte *et al.*, (2001))

2.2.1 Why Hydrogen?

Hydrogen is the lightest, simplest and one of the most abundant elements in nature (Momirlan and Veziroglu, 2005; Uhrig, 2004). It is a non-toxic clean energy carrier with a high specific energy density on a mass basis in comparison to other fuels, as shown in Figure 2.2-3 and Table 2.2-1. As an example, the energy content of 9.5 kg of hydrogen is equivalent to that of 25 kg of gasoline (Midilli *et al.*, 2005). On a volumetric basis the energy density is reduced (Figure 2.2-4). The specific energy is reported in terms of higher heating values (HHV). These values refer to the amount of heat released by these materials on combustion with any water produced present in liquid form. This differs from the lower heating value (LHV) where the water produced is present as vapour.

Many production processes for hydrogen exist (Rosen and Scott, 1998) from fossil fuel and renewable based technologies. When combusted, hydrogen produces non-toxic exhaust emissions and its use can play a significant role in all parts of the global energy economy. Hydrogen can be produced from and converted into electricity at a relatively high efficiency. System efficiencies of commercial water electrolysers range from 60-73 % (Turner, 2004). The raw material for hydrogen production is water. According to Turner (2004), the amount of water needed for hydrogen production required for transportation is not great. Conversion of the U.S. light duty fleet (some 230 million vehicles) to fuel cell vehicles would require about 100 billion gallons (U. S.) of water per year to supply the needed hydrogen. Hydrogen is a completely renewable fuel, since the product of hydrogen utilisation (either through combustion or through electrochemical conversion) is pure water in liquid or vapour form. It can be stored as a liquid or gas and can be transported over large distances using pipelines, tankers or rail trucks (Johnston *et al.*, 2004). It can be converted into other forms of energy in more ways and more efficiently than any other fuel, that is, in addition to flame combustion hydrogen may be converted through catalytic combustion, electrochemical conversion, and hydriding. Hydrogen as an energy carrier is environmentally compatible but results in the production of small amounts of NO_x if it is burned with air at high temperatures (Sherif *et al.*, 2005).

Despite these compelling benefits, the realisation of a hydrogen economy faces multiple challenges. Unlike gasoline and natural gas, hydrogen has no existing large-scale infrastructure – and building one will require major investment. Although hydrogen is currently playing a back role in our energy industry (chemical and refining), the cost of exploiting hydrogen as a big player in supplying the world's energy demands is still too great. In attaining a hydrogen economy, there are several technological factors, which need to be considered such as hydrogen production, its delivery, storage and conversion. These factors are also affected by cost and safety. They are the key milestones that will be encountered on the path to a hydrogen economy as illustrated in Figure 2.2-2.

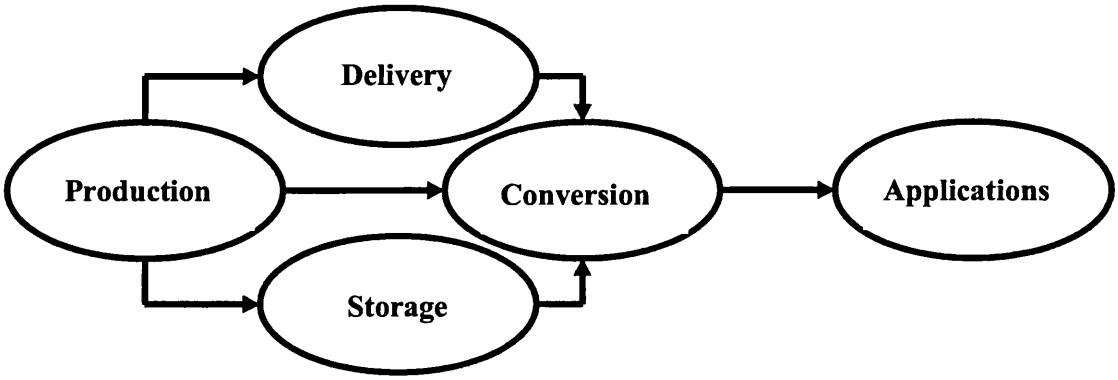

Figure 2.2-2: Factors affecting the development of the hydrogen economy (Adapted from US DOE National Hydrogen Energy Roadmap, 2002).

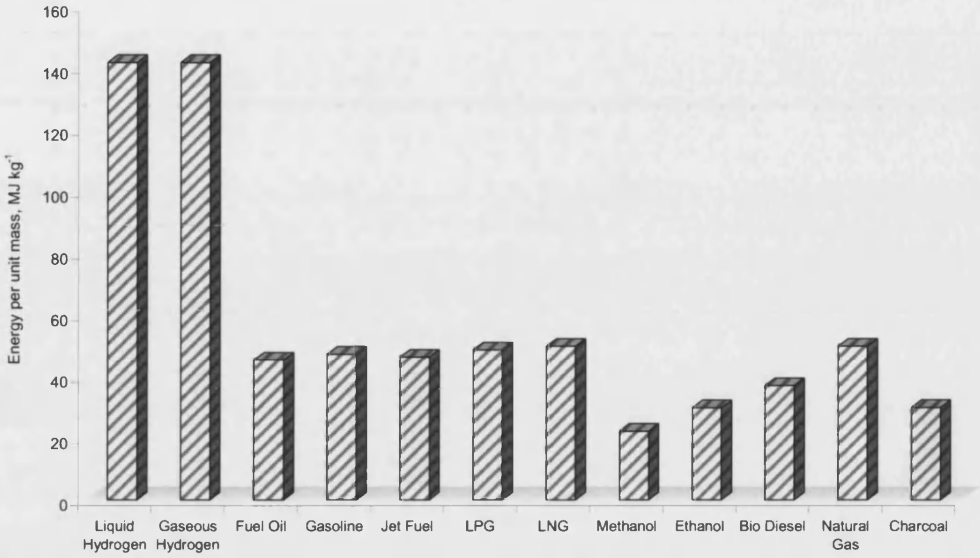

Figure 2.2-3: Energy per unit mass (Higher Heating Value) generated for various fuels (at 25 °C and 1 atm).

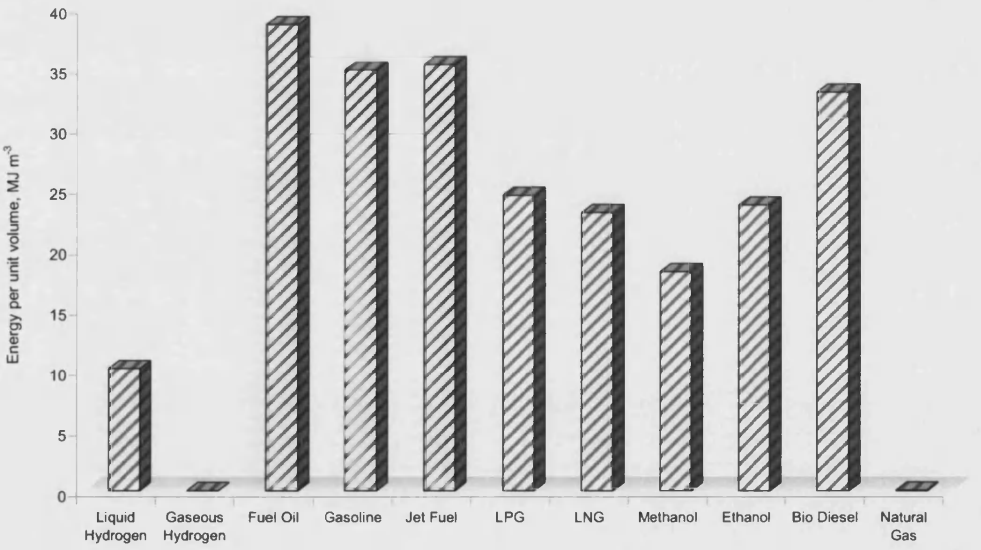

Figure 2.2-4: Energy per unit volume (Higher Heating Value) generated for various fuels (at 25 °C and 1 atm).

Data collected from Veziroglu and Babir, 1992; Midilli *et al.*, 2005; Conte *et al.*, 2001.

Table 2.2-1: Comparison of the key properties of hydrogen and other fuels (Adapted from Veziroglu and Babir, 1992; Midilli *et al.*, 2005; Conte *et al.*, 2001).

Fuel Type	Energy per unit mass ($MJ\ kg^{-1}$)	[1]Energy per unit volume ($MJ\ m^{-3}$)	Specific carbon emission ($kg_C\ kg^{-1}$ fuel)
Liquid Hydrogen	141.90	10.10	0.00
Gaseous Hydrogen	141.90	0.013	0.00
Fuel Oil	45.50	38.65	0.84
Gasoline	47.40	34.85	0.86
Jet Fuel	46.50	35.30	-
LPG	48.80	24.40	-
LNG	50.00	23.00	-
Methanol	22.30	18.10	0.50
Ethanol	29.90	23.60	0.50
Bio diesel	37.00	33.00	0.50
Natural gas	50.00	0.04	0.46
Charcoal	30.00	-	0.50

[1]Values relevant at ambient temperature (25 °C) and atmospheric pressure (1 atm)

2.2.2 The Current and Future Hydrogen Industry

2.2.2.1 Hydrogen Production

Hydrogen, like electricity is an energy carrier or vector, not an energy resource. It does not occur naturally in nature and must be extracted from other sources (Uhrig, 2004; Stiegel and Ramezan, 2006). According to Sherif *et al.*, (2005) most of the technologies required for hydrogen production, storage and utilisation have already being developed, while only a few of them are at a level where they can compete with the existing energy technologies.

Hydrogen is already being produced from fossil fuels (natural gas, oil and coal) in huge volumes, about 45 Mt $year^{-1}$ and is used in a variety of industries (Conte *et al.*, 2001). These include its use in refineries to upgrade crude oil by hydrotreating or hydrocracking, in the chemical industry to synthesise various chemical compounds such as ammonia and methanol, and in metallurgical processes as a reduction or protection gas. Technologies for the production of hydrogen from fossil fuels have been developed and are used to produce industrial hydrogen. On the other hand, there is a great deal of research into environmentally benign methods for producing hydrogen, this is necessary if the ultimate goals of cleaner and better air quality and climate change is to be addressed. Some of the methods for producing hydrogen are described below and summarised in Figure 2.2-6.

2.2.2.2 Hydrogen Production from Fossil Fuels

Two methods for producing hydrogen that are proven technology today are steam methane reforming (SMR) using natural gas (typically more than 95 % methane) and water as the sources of hydrogen (Turner, 2004), and partial oxidation of fossil fuels (Conte *et al.*, 2001; Uhrig, 2004; Stiegel and Ramezan, 2006; Simbeck, 2004; Utgikar and Thiesen, 2005).

Steam methane reforming of natural gas

This involves a catalytic, endothermic reaction where natural gas is reacted with steam over a nickel catalyst bed at about 850 °C and high pressure to produce a mixture of carbon monoxide and hydrogen (syngas). The gas mixture is cooled to about 400 °C and reacted further with more steam over a water gas shift catalyst where additional hydrogen is produced, and carbon monoxide is converted into carbon dioxide. The carbon dioxide and other impurities are removed by pressure swing adsorption (PSA) leaving pure hydrogen (Moore and Raman, 1998). One factor noted by the US National Renewable Energy Laboratory is that hydrogen production plants using the SMR technology contribute significantly to the emission of greenhouse gases into the atmosphere, since carbon dioxide is the dominant gas released (NREL, 2006). The current industrial production methods using SMR technology are very expensive (Johnston *et al.*, 2004). The typical overall efficiency of steam methane reforming is about 80 %, that is, the energy content of the hydrogen produced is about 80 % of the energy of the methane used to produce it, while about 20 % of its energy is consumed in supplying energy for the endothermic reaction (Uhrig, 2004).

Partial oxidation of heavy oil

This method of producing hydrogen is occasionally practised on a large scale using low value refinery by-products such as heavy residual oils. Heavy oil is reacted with pure oxygen in less than stoichiometric ratio to yield a mixture of carbon monoxide and hydrogen at 1200-1350 °C. The gas mixture is cooled and subjected to the shift reaction followed by separation via pressure swing adsorption (PSA) to obtain pure hydrogen. The process also produces a low pressure waste hydrogen stream and excess steam. Without a location which can utilise these by-products the economics are unattractive (Moore and Raman, 1998).

Partial oxidation of coal

This is one of the methods proposed by the US DOE to produce electricity and hydrogen via the integrated gasification combined-cycle technology (IGCC). Partial oxidation or gasification combines coal, oxygen and steam to produce synthesis gas

(hydrogen and carbon monoxide) that is cleaned of impurities such as sulphur and mercury. To produce hydrogen, this synthesis gas is further processed using mature water-gas shift reactor technology to increase hydrogen and convert carbon monoxide to carbon dioxide. Hydrogen is then separated using PSA technology. This process is about 60 % efficient (DeLuchi, 1989). To reduce costs, novel and advanced technologies must still be developed in all phases of the gasification process through to hydrogen separation phases. This process also has a by-product, carbon dioxide which is detrimental to the overall purpose of a hydrogen economy.

Methanol reformation

Methanol can easily be reformed with water over a catalyst at low temperatures (250 – 350 °C) to produce a mixture of hydrogen and carbon dioxide. This is separated via PSA to yield pure hydrogen. Since methanol is easy to ship and store, this is a convenient way of producing hydrogen in areas where natural gas is not readily available. The major cost component of hydrogen produced by this method is the cost of the methanol feedstock. Inexpensive methanol is necessary to make this process attractive. In recent years, however, the world price of methanol has shown wide fluctuations (Moore and Raman, 1998).

The production of hydrogen via these methods cannot be viewed as a long term solution as a result of the consequent release of carbon dioxide. To enhance the environmental prospects of hydrogen generated from fossil fuel sources, the idea of carbon sequestration is being developed. Carbon sequestration is an integrated process that includes the capture of CO_2 from emission sources and the atmosphere, the transportation of CO_2 and the permanent storage and possible reuse of CO_2. It is most applicable to large combustion plants and specifically to thermal power stations where it could contribute to preventing the release into the atmosphere of about 90 % of the CO_2 generated. It is plausible that carbon sequestration technologies may play a catalytic role in the deployment of a hydrogen economy by enabling sustainable hydrogen production from fossil fuels (Tzimas and Peteves, 2005; Simbeck, 2004).

2.2.2.3 Hydrogen Production from Sustainable Sources and Nuclear Energy

To achieve the key goals of climate change and poor air quality, the main feature of an alternative energy carrier such as hydrogen is that it should ultimately be produced from renewable and sustainable energy sources that minimise environmental impact. Hydrogen can be produced renewably from wind, solar, geothermal, hydropower power sources (Yalcin, 1989). The energy obtained from these sources can be used to electrolyse water to produce hydrogen. The production of hydrogen from biomass offers another option for its sustainable production. Sustainable hydrogen production processes include: water electrolysis; thermochemical cycles; photochemical and photoelectrochemical processes; photobiological processes.

Electrochemical Processes

Water electrolysis is one of the most important industrial processes for hydrogen production today, and is expected to become more important in the future. This technology uses an electrolyser powered by electricity. The required electricity may come from conventional power plants, such as coal or nuclear, but can also use renewable energy sources such as wind, solar thermal, PV and hydropower (Adamson, 2004). The three major technologies currently under consideration for electrolytic hydrogen production are classified as alkaline, polymer membrane and ceramic oxide electrolyte (Momirlan and Veziroglu, 1999). A principal focus of modern research in hydrogen production by electrolysis is to discover electrode materials that exhibit good electrochemical reactions. It is desirable that these materials are inexpensive, abundantly available, easy to manipulate and non-polluting.

Thermochemical Processes

Water can be decomposed in a series of cyclical chemical reactions in which H_2 and O_2 are produced (DeLuchi, 1989). Thermochemical cycles will require a primary energy source capable of supplying thermal energy. Thermal sources, both of fossil and non-fossil origin and including solar and nuclear energy have been proposed in

the work of Dang and Steinberg (1980) reported in the subsequent paper by Steinberg and Cheng (1989), and also by Utgikar and Thiesen, 2005. Several different thermochemical processes are under investigation; the more promising ones utilise iodine, bromine and sulphur. Unfortunately, these and some of the other chemicals involved are toxic and/or corrosive (DeLuchi, 1989).

The thermochemical cycles are Carnot cycle limited, which means that higher temperatures can improve efficiencies of conversion. Higher temperatures cause severe damage of construction materials, especially when corrosive chemical reagents are usually involved. Any loss of these costly reagents becomes a severe economic burden on the process. Hydrogen is a very low cost commodity compared to the chemicals used in thermochemical water splitting (Steinberg and Cheng, 1989; Utgikar and Thiesen, 2005). Several thermochemical cycles have been reported, but the technical status of many of them is at the experimental or bench-scale stage. The main reasons for this are the technical problems to be solved before commercialisation, such as the separation of products and the development of infrastructure for industrialisation. In addition to this, thermochemical reactions may cause pollution problems if the process is not completely closed (Mormirlan and Veziroglu, 1999). As a result, many researchers do not think thermochemical production is very promising.

Plasma, solar and radiation processes

Several high temperature and high-energy processes have been suggested in the past and are as follows (Steinberg *et al.*, 1974):

(a) Plasma-arc process: The plasma-arc essentially heats water to high temperature by means of an electric field to an extreme temperature reading up to 5000 °C. The process is equilibrium limited in that the water is cracked to seven radical and molecular components H, H_2, O, O_2, OH, HO_2 and H_2O. Up to about 50 % concentration by volume of H and H_2 components is possible. In order to stabilise the hydrogen components, so that no recombination with the oxygen constituents takes place a very rapid quench of the plasma gases must take place. This can be accomplished with direct water injection. Because of this highly irreversible quench

process, the process is very wasteful of energy. The requirement of electrical energy for the arc taken together with a wasteful energy system makes the process extremely expensive.

(b) Photolytic laser process: The photolytic process which uses light absorption in a mercury catalysed water vapour system at a wavelength of 306 nm is a low efficiency system in that energy must be converted from thermal to electrical to photolytic radiant energy which is then transmitted to mercury which then transmits it to water. The overall efficiency is usually less than 10 %. Lasers in recent years which can emit more intense photon radiation in specific wavelengths, improves efficiencies somewhat but even these devices cannot yield an overall efficiency greater than 10 %.

(c) High-energy radiation process: With the advent of nuclear energy there was much effort over several decades in developing high-energy radiation processes for the synthesis and production of chemicals. One system investigated was the radiation decomposition of waste. Gamma, beta and fission fragment radiation were used. The highest yield obtained was with fission fragment radiation directly in a nuclear reactor. However, the energy efficiency obtained for the process never exceeded about 18 %. Furthermore, the separation of highly radioactive particulates and gases as well as the separation of hydrogen from oxygen are severe process problems.

Solar photovoltaic water electrolysis process

There appears to be a growing interest in directly generating electrical energy using solar energy by means of photovoltaic (PV) devices. New solar cell materials such as amorphous silicon have reached solar to electrical energy conversion efficiencies of 12 % for large area laboratory modules. Manufacturing plants are presently expected to produce cells for a cost of $1 per peak watt. By directing this PV cell output to water electrolysis at 84 % efficiency, it is projected according to the work of Ogden and Williams (reported by Steinberg and Cheng, 1989) that, in the time frame of the next 15 or 20 years, it will be possible to produce PV cells for as low as $0.20 to $0.40 per peak watt and to generate hydrogen in solar intensive areas such as in the Southwest U.S. for $3-5 $(10^3\ ft^3)^{-1}$ at capacities of 0.5 million cubic feet per day.

Biological Methods of Hydrogen Production

Currently, the two fundamental ways of biologically producing hydrogen are biophotolysis and bacteria fermentation (Goswami *et al.*, 2003). The fermentation of bacteria is an anaerobic process that converts organic substances to hydrogen and oxygen without the need of sunlight and oxygen. Most biologically produced hydrogen in the biosphere is evolved in microbial fermentation processes (Vijayaraghavan and Amin Mohd Soom, 2004). Fermentation materials such as starch, cellulose, sucrose and xylose can produce hydrogen and other metabolites. Biophotolysis on the other hand is a process that uses micro-algae-cyanobacteria and green algae to produce hydrogen in the presence of sunlight and water. The microorganisms contain enzymes, known as hydrogenases that either oxidise hydrogen to protons and electrons or reduce protons and thus release molecular hydrogen (Vijayaraghavan and Amin Mohd Soom, 2004).

Biological systems have the potential for low capital costs due to the extended periods of viable cells. The biological species involved in hydrogen production, include green algae, cyanobacteria heterocystous, cyanobacteria non- heterocystous, photosynthetic bacteria and fermentative bacteria, with green algae being one of the most promising groups for hydrogen production through photosynthesis (Vijayaraghavan and Amin Mohd Soom, 2004).

Hydrogen Production from Biomass

Goswami *et al.*, (2003) reports that biomass resources are the most versatile non-fossil energy resources and have been used around the world for a long time. It has relatively low sulphur content in comparison to fossil fuels. Biomass resources include agricultural residues such as corn stover, wheat straw and rice straw; forest residues such as tree stumps and leaves; industrial wastes such as sugarcane, bagasse, citrus peel and milling residues; and energy crops such as tall grasses and fast growing trees (Goswami *et al.*, 2003). There are a number of ways to convert biomass to hydrogen, including all the methods of conversion of fossil fuels as shown in Figure 2.2-5 adapted from the work of Milne *et al.*, (2001). Biomass may also be converted to hydrogen through the electrolysis path by using electricity from biomass power plants. Adamson (2004), reports that two important factors in assessing the

future potential of biomass for hydrogen production are the yield per hectare and the energy content of the crop under consideration. These are said to vary widely from corn which has an energy content of 18.5 MJ kg^{-1} and yield per hectare of 7.1 t ha^{-1}, to Sorghum, which has a similar energy content of 18.3 MJ kg^{-1} but a per hectare yield of 80 t ha^{-1}, some factor of 11 greater. From the work of Katofsky (1993), Adamson (2004) reported that an average of 19 European crops, gives a yield of 8 t ha^{-1} with an energy yield of 18 MJ kg^{-1}. Before the gasification process, the biomass needs to be processed, this mainly involves drying. The average moisture content of biomass is 45 %, and typically processing and drying leads to a 10 % loss of the energy content. The average observed efficiency of the biomass gasifiers is 63 % in the work of DeLuchi *et al.*, (1991) also reported by Adamson (2004).

Majority of these renewable based processes for hydrogen production have not been developed to commercial status presently (Kreith and West, 2004). The available information is not sufficient to reach conclusions about their costs and efficiencies. A review of the U.S. department of Energy's Renewable Energy Programs published in 2000, recognised that these renewable energy pathways are challenges for longer term Research (U.S. DOE, 2000).

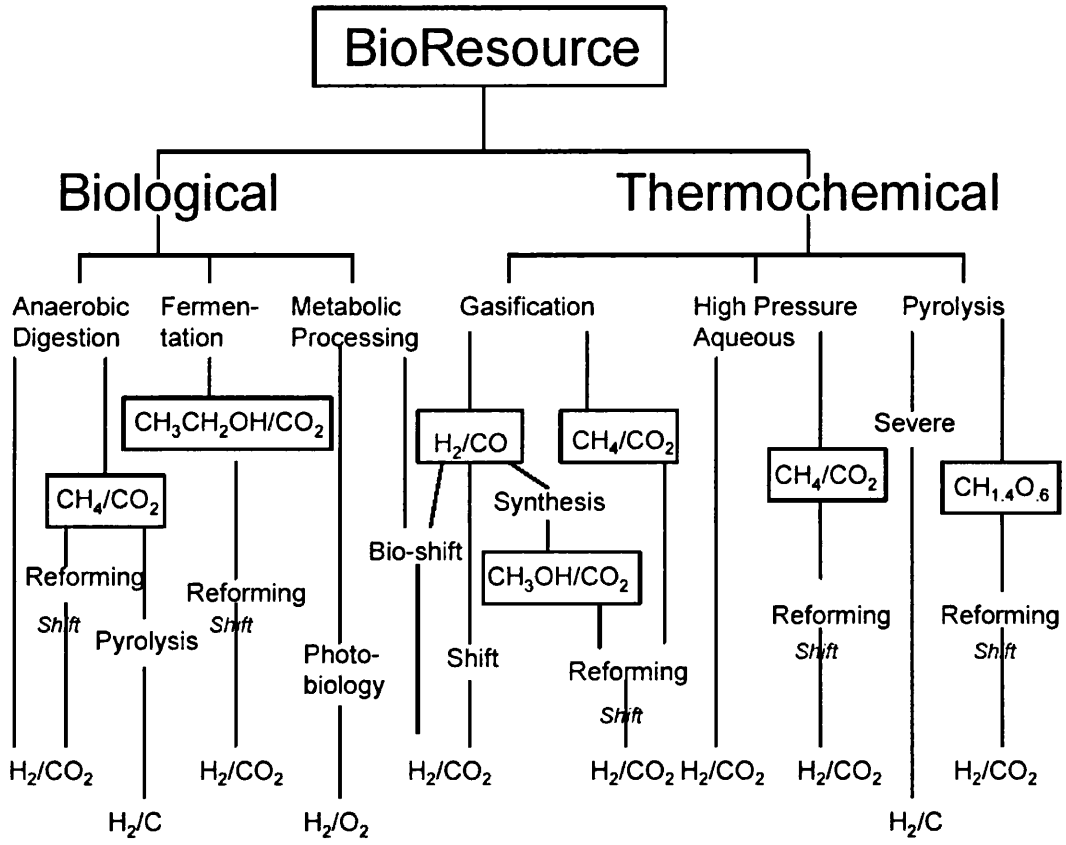

Figure 2.2-5: Pathways from biomass to hydrogen. Storable intermediates are shown in boxes Adapted from Milne *et al.*, (2001).

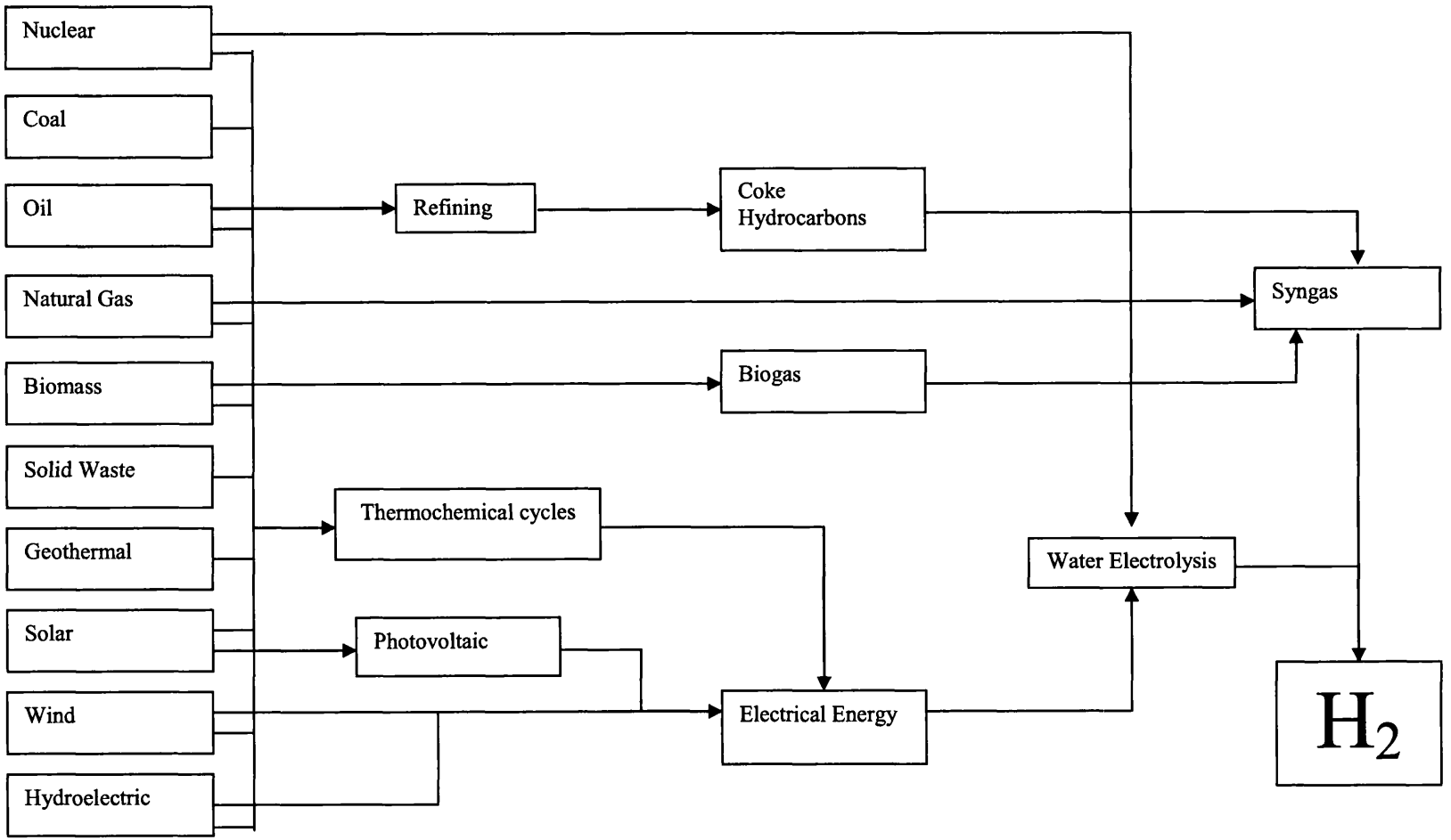

Figure 2.2-6: Summary of different hydrogen production techniques (adapted from Conte *et al.*, 2001)

2.2.3 Hydrogen Storage

The storage of hydrogen is one of the technological challenges that need to be overcome in the progression towards a hydrogen economy. As mentioned previously, to store useful amounts of hydrogen requires a large space as a result of its low volumetric energy density (see Table 2.2-1). For example, for a hydrogen vehicle to achieve a practical driving distance, 4 kg of hydrogen is needed, which occupies a volume of about 49 m^3 at ambient temperature and atmospheric pressure. This corresponds to a balloon of about 5m in diameter (Zhou, 2005; Schlapbach and Zuttel, 2001). The storage of hydrogen basically implies the reduction of the enormous volume of the hydrogen gas. In order to increase the hydrogen density in a storage system work must either be applied to compress hydrogen, or the temperature has to be decreased below the critical temperature (33 K) or finally, by the interaction of hydrogen with another material. One other important criterion of a hydrogen storage system is the reversibility of the hydrogen uptake. This criterion excludes all covalent hydrogen-carbon compounds as hydrogen storage materials because the hydrogen is only released from these materials if they are heated to temperatures above 800 °C or if the carbon is oxidised.

In the current state of the art in hydrogen storage, no single technology satisfies all of the criteria required. These include high hydrogen content per unit mass and unit volume, reversible storage and release of hydrogen on demand, high cycling stability, safety and minimal costs (Conte *et al.,* 2004), for which the U. S. Department of Energy (DOE) has set targets as shown in Table 2.2-2. Current hydrogen storage technologies include compression, liquefaction, storage on carbon based materials and porous structures, metallic hydrides and complex hydrides. The following section focuses on these methods and illustrates their advantages and disadvantages (Zuttel, 2003; Momirlan and Veziroglu, 2005; DeLuchi, 1989; Tzimas *et al.*, 2003; Texier-Mandoki *et al.*, 2004).

Compression

When hydrogen is used in its gaseous form, it may be compressed to an elevated pressure, a process which requires that work be done on the gas. The compressed hydrogen is stored in high-pressure gas cylinders with a maximum pressure of 20 MPa (Zhou, 2005). New lightweight composite cylinders have been developed which are able to withstand pressures of up to 80 MPa and so the hydrogen can reach a volumetric density of 36 kg m^{-3} approximately half as much as in its liquid form at the normal boiling point (Zuttel, 2003). The storage of hydrogen under high pressure is a well-established technology. The current technology for natural gas storage can also be used for hydrogen with the exception of materials subject to embrittlement such as alloy or high strength steels (ferritic, martensitic and bainitic), titanium and its alloys and some nickel based alloys. Most pressure cylinders today have used austenitic stainless steel, copper, or aluminium alloys, which are largely unaffected by hydrogen at ambient temperatures (Tzimas *et al.*, 2003).

In spite of the satisfactory and widespread use of compressed gas storage systems in the industrial sectors and laboratories, they are not suitable for vehicular applications. The main reasons for such a limitation centre on the difficulties of high volume, pressure and weight, potential safety hazards and the overall costs associated with the method of hydrogen storage (Das, 1996; US DOE, 2006). The possibility of a sudden release of compressed gas on-board vehicles is a particular problem associated with high pressure hydrogen storage.

Liquefaction

Hydrogen can be stored as a liquid at –253 °C (20 K) in super insulated vacuum tanks at ambient pressure (Zuttel, 2001; Tzimas *et al.*, 2003). In its liquid form, hydrogen has a considerably higher volumetric density than in its gaseous form (see Table 2.2-1). The mass density of liquid hydrogen is 0.070 kg L^{-1}, compared to 0.030 kg L^{-1} for 10,000 psi (690 bar) (US DOE, 2006) gas tanks making it an attractive storage medium. It takes up less storage volume than gas but requires cryogenic containers. The use of liquid hydrogen for long distance transportation and in airplanes is attractive, and the use, handling and knowledge of liquid hydrogen is very advanced (US DOE, 2002). Liquid hydrogen and the enabling technology have already been

used in space (Space shuttle, Ariane) but also in military aircrafts (Tzimas *et al.*, 2003; Momirlan and Veziroglu, 2005). This hydrogen storage technology is rather effective but has disadvantages, mainly the liquefaction of hydrogen, which is an energy intensive process and results in large evaporative losses, about a third of the energy content of hydrogen is lost in the process. Also the strict control needed on the container temperature stability to avoid the risk of overpressure. It also requires cryogenic vessels and suffers from hydrogen losses through evaporation from the containers, particularly the smaller ones (they have a larger surface to volume ratio than larger containers, hence larger losses of hydrogen) (DeLuchi, 1989; Das, 1996). The hydrogen molecule consists of two atoms and is present in two forms; ortho-hydrogen and para-hydrogen; with their differences being in the orientation of their nuclear spins. In ortho-hydrogen, both atoms have the same spin (parallel), while in para-hydrogen the atoms have opposite spins (anti-parallel). Normal hydrogen molecules at room temperature conditions contain 25 % of the para form and 75 % of the ortho form (Tzmias *et al.*, 2003). However the proportion of these forms is dependent on temperature. When hydrogen is cooled, ortho-hydrogen transforms into para-hydrogen. This is accompanied by a release of heat reported to be 703 J g^{-1}. According to Tzmias *et al.*, (2003) this state conversion has significant consequences on the liquefaction and storage of hydrogen, since it leads to a release of energy that is greater than the heat of evaporation (445.6 J g^{-1}), leading to hydrogen losses due to boil-off (Tzmias *et al.*, 2003).

Cryogenic storage because of its low working pressure compared to high pressure storage systems has a great potential to reduce weight by using new composite materials with enhanced performance. With such systems, specific energy storage mass similar to conventional fuel tanks can be achieved. In spite of the caution taken on the design part of these storage tanks to ensure protection from unwanted heat entry, cryogenic liquids and therefore liquid hydrogen do evaporate (boil-off) due to the impact of heat in the tank system (Kreith and West, 2004). This phenomenon cannot be avoided, but only minimised. If a vehicle equipped with such a system is left unused for a rather short time (about 3 days), the tank pressure rises as a result of the heat ingress. A critical pressure value is finally reached that triggers unacceptable hydrogen evaporation losses. Linde AG claim to have developed a re-cooling system

that can minimise these evaporative losses leading to an extension of the critical time before boil-off occurs to more than 12 days (Tzimas *et al.*, 2003).

2.2.3.1 Materials Based Hydrogen Storage

Storage in Porous Systems

According to several authors, the storage of hydrogen in porous systems when compared to gaseous and liquid media offers the advantage of lower pressure hydrogen storage, increased safety, design flexibility and reasonable volumetric storage efficiency (Dakrim and Levesque, 2000; Texier-Mandoki *et al.*, 2004; Tzimas *et al.*, 2004). However this technology is still at the research stages. Solutions are yet to be found for issues surrounding weight and space constraints on board vehicles, cost and thermal management issues associated with this option. The materials included in this category are:

- Carbon based materials, nanotubes, nanofibres, activated carbons, templated carbons, powders, doped carbon and cubic boron nitride alloys
- Organics, polymers, zeolites, silicas (aerogels), porous silicon, metal hydrides, metal organic frameworks (MOFs).

Storage in carbon-based materials

Materials with large specific area like nanostructured carbon and carbon nanotubes are possible substrates for physisorption. These materials are very attractive because of their porous structure. Finding the highest hydrogen storage capacity is as important as achieving a high reversibility of the sorption/desorption process and chemical stability. From a practical point of view, a process that occurs under ambient conditions of temperature and pressure is desired. It has been known that different carbons have the ability to adsorb hydrogen. Research on adsorbing materials with high surface area is still emerging, but the design of practical systems awaits better understanding of the fundamental adsorption/desorption processes and development of high-volume manufacturing processes for the materials. The storage of hydrogen in these materials is reviewed in more detail in Section 2.5 and is the main subject of this thesis.

Storage in non-carbon materials

(a) Metal Hydrides. Certain metals and alloys have the ability to absorb hydrogen at moderate temperature and pressure to create hydrides. A hydride is a compound that contains hydrogen and one or more other elements. The elements most used in hydrides are iron (Fe), magnesium (Mg), nickel (Ni), manganese (Mn) and titanium (Ti) (DeLuchi, 1989). At the metal surface, hydrogen molecules separate into hydrogen atoms, which get absorbed into the metal crystals at interstitials. Such an absorption reaction produces heat, which needs to be removed during the charging operation.

Similarly, the desorption reaction consumes heat, which must be supplied during discharging (Das, 1996). The main criteria used to evaluate hydrides are low cost, high energy density, low desorption or hydrogen release temperature, high rate of hydrogen absorption, low susceptibility to fouling by impurities in the gas and low volumetric expansion. Researchers have not yet identified a hydride that meets all these requirements (DeLuchi, 1989). According to Conte *et al.*, (2004), the principal disadvantages of metal hydrides, apart from cost, are the low hydrogen content (< 2 %) at low temperature (La or Ti based alloys) and the difficulty of reducing the desorption temperature and pressure of hydrides with high hydrogen storage capacity.

(b) Liquid Chemical Hydrides. The use of these materials as potential hydrogen stores is the subject of current research by several authors (Kojima *et al.*, 2004; Aiello *et al.*, 1999; Amendola *et al.*, 2000a; Amendola *et al.*, 2000b; Kong *et al.*, 1999). Classical chemical hydrides such as $NaBH_4$ and $LiBH_4$ are considered a safe and practical means of storing hydrogen for applications were a small amount of hydrogen is required, but these materials are also unstable and sensitive to moisture in the air. This makes them difficult to handle and the solid by-products of their hydrolysis reactions pose problems by inhibiting heat transfer from the reaction medium and suppressing further reaction. Hydrogen can be generated from these materials as the product of hydrolysis with water or via a thermally initiated reaction with NH_4Cl (Aiello *et al.*, 1998). Both these reaction mechanisms are irreversible. In the work of Libowitz (1965), he reported that the hydrolysis and thermally initiated reactions of these classical hydrides are often violent and release large amounts of heat, which makes them impractical for use in portable applications.

Glass Microspheres

Hydrogen can be stored at high pressures in hollow glass spheres. They are called microspheres since they are less than 100 μm in diameter (Sherif *et al.*, 2005). According to some authors, storage in these materials is a promising technology for small-scale storage of hydrogen for vehicular applications. Microspheres, among several other advantages, offer the potential for low material cost, as far as automotive application is concerned (DeLuchi, 1989). However, there are some problems, which must be addressed before any large-scale implementation is carried out. The microspheres require extremely high levels of pressure compressors and charging vessels. Being essentially a high-pressure gaseous storage system, it also suffers from the intrinsic problem of poor volumetric storage density of gaseous hydrogen. On a comparative scale, it has been found that the glass microspheres could at best store only a fraction of the hydrogen in a given volume that can be stored either in liquid hydrogen storage system or in hydrides. It has been observed that sometimes the glass microspheres leak slowly even at room temperature. It has also been found that most advanced microspheres can exhibit a burst pressure of about 1000 MPa (Das, 1996).

Zeolites

These are crystalline aluminosilicates with molecular-scale channels and cavities of definite size and geometry. Traditionally these materials are used for the sieving of gases. Broadly speaking, zeolites are conceptually equivalent to a molecular-sized version of the glass microsphere storage system. Therefore, this method does not offer any specific well-pronounced advantage over the microsphere option (Das, 1996).

Table 2.2-2: US DOE Hydrogen Storage Targets (US DOE, 2006)

Storage Parameter	Units	2007	2010	2015
Usable, specific energy from H_2 (Net useful energy/max system mass) (Gravimetric capacity)	kWh kg^{-1} (wt% H_2)	1.5 (4.5 %)	2 (6 %)	3 (9 %)
Usable energy density from H_2 (Net useful energy/max system volume) (volumetric capacity)	kWh L^{-1} (kg H_2 L^{-1})	1.2 (0.036)	1.5 (0.045)	2.7 (0.081)
Storage system cost	\$ $kW^{-1}h^{-1}$ net (\$ kg^{-1} H_2)	6 (200)	4 (133)	2 (67)
Fuel cost	\$ per gallon gasoline equivalent at pump	3	1.5	1.5
Operating ambient temperature	°C	-20/50	-30/50	-40/60
Cycle life (1/4 tank to full)	Cycles	500	1000	1500
Cycle life variation	% of mean (min) @ % confidence	N.A.	90/90	99/90
Minimum and maximum delivery temperature of H_2 from tank	°C	-20/85	-30/85	-40/85
Minimum full flow rate	(g s^{-1}) kW^{-1}	0.02	0.02	0.02
Minimum delivery pressure of H_2 from tank; FC = Fuel Cell, ICE = Internal Combustion Engine	Atm (abs)	8 FC 10 ICE	4 FC 35 ICE	3 FC 35 ICE
Maximum delivery pressure of H_2 from tank	Atm (abs)	100	100	100
Start time to full flow at 20 °C	s	4	4	0.5
Start time to full flow at minimum ambient	s	8	8	2
System fill time for 5 kg of H_2	min	10	3	2.5
Loss of useable H_2	(g h^{-1}) kg^{-1} H_2 stored	1	0.1	0.05
Permeation and Leakage	scc h^{-1}	Federal enclosed area safety standards		
Toxicity		Meets or exceeds applicable standards		
Safety		Meets or exceeds applicable standards		
Purity (H_2 from storage system)		98 % (dry basis)		

2.2.4 Hydrogen Distribution and Delivery

An important element of the overall hydrogen energy infrastructure is the delivery system that moves the hydrogen from its point of production to an end-use device. Delivery system requirements vary with the production method and end-use application. If there is a widespread use of hydrogen as an energy carrier, then adequate infrastructure will be required to transport and distribute the hydrogen. The hydrogen could be produced on-site at the fuelling station (Johnston *et al.*, 2004). The transport of hydrogen also presents difficulties in terms of infrastructure. It is important to note that pure hydrogen reacts at the surface of certain pipeline steels, embrittling them and accelerating the growth of fatigue cracks. Materials that can withstand these properties will have to be developed (Conte *et al.*, 2001).

Typically hydrogen would be transported from the site of production to end-users as a gas, via pipeline or in containers by road and rail transportation. There is an argument that gaseous hydrogen could be distributed in pipelines currently used for natural gas (Kreith and West, 2004). DeLuchi, 1989 states that this would be ideal for the initial stages of a transition to hydrogen (DeLuchi, 1989). Sherif *et al.*, 2005 reports that the transmission of hydrogen through pipelines requires larger diameter piping and more compression power than natural gas for the same energy throughput. The author adds that in economic terms, most studies found that the cost of large-scale transmission of hydrogen is about 1.5-1.8 times larger than that of natural gas transmission (Sherif *et al.*, 2005). However, according to Oney *et al.*, 1994, the transportation of hydrogen over distances greater than 1000 km is more economical than transmission of electricity (Oney *et al.*, 1994). Hydrogen could also be shipped in liquid form, for short distances in vacuum-jacketed pipelines. Transporting liquid hydrogen would incur large amounts of heat losses and require insulating the pipelines to hold a cryogenic temperature. Furthermore, a nationwide cryogenically insulated piping system would have to be constructed at enormous financial costs (Kreith and West, 2004).

2.2.5 Hydrogen Conversion

Currently, the main use of hydrogen is in the chemical and oil industry. As the hydrogen economy advances, hydrogen will be used as fuel both for power generation and or combined heat and power (CHP) production. A range of technologies for the conversion and use of hydrogen have already been developed and demonstrated as shown in Table 2.2-3. In almost all cases hydrogen is converted more efficiently than any other fuel (Sherif *et al.*, 2005).

Hydrogen can be used in both heat engines and fuel cells. Engines can combust hydrogen in the same manner as gasoline or natural gas, while fuel cells use the chemical energy of hydrogen to produce electricity and thermal energy. Since electrochemical reactions are more efficient than combustion at generating energy, fuel cells are more efficient than internal combustion engines (U. S. DOE, 2002).

Hydrogen can be combusted in the same manner as gasoline or natural gas. The benefit of using hydrogen combustion over fossil fuel combustion is that it releases fewer emissions, with water being the only major by-product. No carbon dioxide is released, and nitrogen oxides, produced by a reaction with the nitrogen in the air, can be significantly lower than with the combustion of fossil fuels. The use of hydrogen in engines is a fairly well developed technology – The National Aeronautics and Space Administration (NASA) use it for applications such as the space shuttle's main engines and unmanned rocket engines. Other combustion applications such as new designs of combustion equipment specifically for hydrogen in turbines and engines are still being researched. Hydrogen internal combustion engines are being demonstrated. Ford and BMW have made significant progress in the advanced Hydrogen Internal Combustion Engine (H2-ICE) vehicles in 2001. Also, the combustion of hydrogen blends (methane/hydrogen, heptane/hydrogen) is being tested.

Table 2.2-3: Hydrogen Energy Conversion Technologies and Applications (Adapted from U. S. DOE, 2002)

Technology	Application
	Combustion
Gas Turbines	-Distributed Power -Combined Heat and Power -Central Station Power
Reciprocating Engines	-Vehicles -Distributed Power -Combined Heat and Power
	Fuel Cells
Polymer Electrolyte Membrane (PEM)	-Vehicles -Distributed Power -Combined Heat and Power Portable Power
Alkaline (AFC)	-Vehicles -Distributed Power
Phosphoric Acid (PAFC)	-Distributed Power -Combined Heat and Power
Molten Carbonate (MCFC)	-Distributed Power -Combined Heat and Power
Solid Oxide (SOFC)	-Truck APVs -Distributed Power -Combined Heat and Power

2.2.5.1 Fuel Cells

Fuel cells are one of the most attractive and most promising hydrogen technologies and have been the subject of much interest. Fuel cells utilise the chemical energy of hydrogen and oxygen to produce electricity and thermal energy. A fuel cell is a quiet, clean source of energy. These systems are zero emission when fuelled with pure hydrogen, giving just water vapour as the exhaust gas (Conte *et al.*, 2001).

Fuel cells can achieve higher efficiencies than internal combustion engines because they convert fuel directly into energy through an electrochemical reaction, while combustion requires the conversion of the fuel into heat and then into mechanical energy (Fuel Cell Store™, 2006). Current fuel cell efficiencies are in the 40 – 50 % range, with up to 80 % efficiency reported (Conte *et al.*, 2001; Ahmed and Krumpelt, 2001) when used in combined heat and power applications. Fuel cells are similar to batteries in that they are composed of positive and negative electrodes with an electrolyte or membrane. The difference between them lies in the fact that energy is not recharged and stored in fuel cells. Fuel cells receive their energy from the hydrogen or similar fuels applied to them, hence recharging is not necessary. Fuel cells are characterised by their electrolyte, operating temperature and level of hydrogen purity required. Phosphoric acid fuel cells are the most developed fuel cells for commercial use. Many stationary units have been installed to provide grid support and reliable back-up power, and mobile units are powering buses and other large vehicles.

Polymer electrolyte membrane (PEM) fuel cells are being developed and tested for use in transportation, stationary, and portable applications. Interest in polymer-electrolyte membrane fuel cells has experienced a tremendous upsurge over the past few years, and most major automotive manufacturers are developing fuel cell concept cars. Alkaline fuel cells have been used in military applications and space missions (to provide drinking water and electricity for astronauts). Currently these fuel cells are being tested for transport applications. Solid oxide and molten carbonate fuel cells are best for use in generating electricity in stationary combined cycle applications and cogeneration applications in which waste heat is used for cogeneration. They also fit

well for portable power and transportation applications, especially large trucks (U. S. DOE, 2002; Conte *et al.*, 2001; Divisek *et al.*, 1998).

Fuel cells have operating advantages for both stationary and mobile applications in that they are quiet and typically have high efficiencies at partial loads. They also have environmental advantages when hydrogen is used as the fuel as there are no emissions of sulphur or nitrogen oxides, or particulates. If the hydrogen comes from a net-carbon-free renewable or nuclear energy source, the system will also be free of carbon dioxide emissions. Fuel cells are classified based on the type of electrolyte used. A summary of the characteristics of the different fuel cell types is shown in Table 2.2-4.

Table 2.2-4: Summary of Fuel Cell Types (U. S. DOE, 2002)

Fuel Cell	**Electrolyte**	**Operating Temperature (°C)**	**Sensitivity to H_2 Purity**
Proton Exchange Membrane	Solid organic polyperfluorosulphonic acid	60-100	High sensitivity to impurities, must have less than 10 ppm CO
Alkaline	Aqueous solution of potassium hydroxide soaked in a matrix	90-100	High sensitivity to carbon dioxide
Phosphoric Acid	Liquid phosphoric acid soaked in a matrix	175-200	Sensitive to CO
Molten Carbonate	Liquid solution of lithium, sodium and/or potassium carbonates, soaked in a matrix	600-1000	Low sensitivity to CO, Hydrogen/carbon monoxide mixtures can be used. CO_2 is required.
Solid Oxide	Solid zirconium oxide to which a small amount of ytrria is added	600-1000	Low sensitivity to CO, Hydrogen/carbon dioxide/ methane mixtures can be used

2.2.6 End Use Energy Markets

The end-use applications of hydrogen energy include stationary, transportation, and portable devices. Currently, the most common use for hydrogen is in industrial processes such as those for oil refineries. It is also used as a fuel at NASA, where the combustion of hydrogen has fuelled its space shuttle main engines and propulsion systems for years. Other hydrogen energy uses are generally limited to research and demonstrations.

One application of hydrogen fuel cells is for distributed generation. A number of United Technologies Company (UTC) Fuel Cell's phosphoric acid fuel cells are operating in locations around the world, providing heat and power for buildings and industrial applications. These units include a reformer component to generate a hydrogen-rich gas from natural gas.

In the transportation sector, a number of fuel cell vehicles are being tested and developed. Vehicular use of hydrogen energy requires a compact power system and refuelling stations. Given the current state of hydrogen technologies, city-owned buses are a promising application because they are capable of carrying large tanks of hydrogen and typically refuel at a single location. In November 2003, for example London became the first city in the United Kingdom to use hydrogen fuel cells to power buses for use in its public transit system. Several car manufacturers, including Hyundai, Ford, General Motors, Toyota, Honda, and Daimler Chrysler are developing fuel cell vehicles for personal use.

Portable fuel cells can also be used to power small devices such as mobile telephones or personal computers. Large power generators for recreation and other off-grid applications are under development. For example, Ballard Power Systems has developed the Nexa^{TM} power module, a PEM fuel cell system that generates up to 12000 watts of unregulated direct current electrical power that can be used for industrial and consumer end-product applications. This portable power application is still under development.

Today's emerging hydrogen energy industry is eager to develop hydrogen fuel infrastructure technology that can be used to generate power for stationary, transportation and portable power applications. Much work still needs to be done to reach this goal.

2.2.6.1 Hydrogen in aircrafts

Hydrogen can also be used in combustion engines and turbines. In air travel, hydrogen has many advantages over conventional jet fuel. In addition to a cleaner environment, hydrogen as an energy vector offers greater performance, increased safety, and lower noise levels.

Liquid hydrogen's high specific energy reduces fuel mass by a factor of 2.8, which means it is possible to use smaller engines with less noise. Even better utilization is achieved by using liquid hydrogen to cool the engines instead of conventional air cooling. It has been determined that the life of jet turbines will be increased by 25 %, and the need for maintenance and repairs will be reduced respectively. This is in part due to the purity of the fuel (Brewer 1991).

The only disadvantage compared with kerosene jet fuel is that hydrogen has a lower density and therefore requires larger fuel tanks. Building a hydrogen infrastructure for airplanes is not difficult, and NASA's many years of experience with LH_2 for space travel can be drawn upon.

2.2.7 Other Factors Affecting the Development of a H_2 Economy

As mentioned earlier the adoption of hydrogen as a future energy carrier is somewhat slow in spite of its numerous advantages. Some of the technical factors responsible for this, such as, the production, storage and distribution of hydrogen have been discussed earlier. Important factors such as public perception and safety need to be given due consideration as they are significant in the drive towards the hydrogen economy.

2.2.7.1 Perception of the Hydrogen Economy

The negative history surrounding hydrogen and its use centres on the Hindenburg disaster in 1937. According to Johnston *et al.*, (2004), there is a cause-effect relationship for many people between hydrogen and the Hindenburg disaster. Popular belief led to the conclusion that the explosion was caused by the ignition of the hydrogen gas, which was used to lift the airship. In 1997, Bain Addison a retired NASA scientist published results of a study indicating that the explosion was the result of the ignition of iron oxides and aluminium that had been painted on the ship's outer skin. The airship did not explode as most believed; it caught on fire (Dunn, 2002). Memories of the hydrogen bomb, first detonated in the pacific in 1952 (BBC, 2006) also add to the negative history surrounding hydrogen.

As hydrogen usage starts to spill over into the public arena, inaccurate perceptions need to be addressed. The government, hydrogen producers and the auto industry will all have a key role to play in communication and education. In the US, the California Fuel Cell Partnership has as one of their key objectives, to increase public awareness. The auto industry has also taken a lead role in educating the public as well as targeting the education system. General Motors, Toyota and Ford have educational kits to assist teachers in explaining the technology. Appropriate field tests and demonstrations will be needed to increase public confidence and acceptance of hydrogen technologies (U.S. DOE, 2002, Dunn, 2002).

2.2.7.2 Safety Issues

Hydrogen, like all fuels has combustible properties, which when handled properly is as safe as the others (Johnston *et al.*, 2005). Hydrogen's high buoyancy and diffusivity and small molecular size make it difficult to contain and can create combustible situations (National Hydrogen Association, NHA, 2003). The risk of hydrogen must be considered relative to common fuels such as gasoline or natural gas (Sherif *et al.*, 2004). In a paper by Abdel-Aal *et al.*, (2005), the fuel characteristics of gasoline, methane and hydrogen are compared. Hydrogen is ranked as the safest fuel (Adel-Aal *et al.*, 2005). Shinnar, 2003 disputes this in a paper, where it is stated that hydrogen is the least safe. A 1997 Ford study sponsored by the U. S. Department of Energy (DOE), concluded that hydrogen is not more dangerous than fuels like gasoline, propane and natural gas. It was stated that hydrogen may be safer than the hydrocarbon fuels used for nearly a century (Hydrogen 2000 and Plug Power Inc, 2006).

Hydrogen also has some unique characteristics. It is non-toxic, unlike gasoline at higher concentrations. Compared to gasoline or natural gas, hydrogen is flammable over a wide range of concentrations, between 4% lower explosion limit (LEL) and 75 % upper explosion limit (UEL) but due to its buoyancy, it dissipates much quicker than either in a spill (Johnston *et al.*, 2004). For a hydrogen fire to occur, an adequate concentration of hydrogen, the presence of ignition source and the right amount of oxidiser (e.g. oxygen) must be present at the same time. Hydrogen does not puddle like gasoline, thereby eliminating the potential of fire. Hydrogen flames have low radiant heat with pure hydrogen/oxygen flames being nearly invisible to the naked eye making it difficult to visually detect if a hydrogen leak is burning. Since it escapes from leaks rapidly, storage areas should be well ventilated and monitored continuously to detect and manage leaks. A comparison of the physical properties of hydrogen with natural gas and petrol is shown in Table 2.2-5.

Hydrogen is simply different from other fuels and so will require new safety standards and handling procedures. There are standards for the safe storage of hydrogen on-

board vehicles currently being developed internationally within the International standards Organisation (ISO).

Industrial production of hydrogen has been in existence for over four decades and the safety record is a good one. As with any type of fuel, understanding the chemical properties and following safe handling and storage procedures is the key to an accident free environment. Many organisations such as the Compressed Gas Association and the American Society for Mechanical Engineers publish safety standards. Guidelines for distribution are issued by the Department of Transportation and the National Fire Association publishes storage requirements (Johnston *et al.*, 2004).

Table 2.2-5: Comparison of the Physical Properties of Hydrogen and other Fuels

Physical Property	Hydrogen Gas	Natural Gas	Petrol
Auto-ignition temperature, °C	585	540	228-501
Flame Temperature, °C	2045	1875	2200
Limits of flammability in the air, vol %	4 - 75	5.3 - 15	1.0 - 7.6
Minimum ignition energy, mJ	0.02	0.29	0.24
Theoretical explosive energy, TNT m^{-3} gas	2.02	7.03	44.22

2.2.7.3 Cost

The use of hydrogen as a future energy carrier to supply the energy needs of the economy requires that consideration be given to what the cost of building such an infrastructure would pose to the government. It is necessary that along with research, cost analysis of proposed 'hydrogen economy' technology be analysed. The cost of hydrogen will depend on how it is produced, stored and delivered.

The production costs for gaseous hydrogen made from natural gas is about \$1 kg^{-1}, with the natural gas priced at \$0.18 m^{-3}, about 45 % of the cost is due to natural gas. Hydrogen produced by electrolysis costs about three times this much, around \$3 kg^{-1}, with electricity at \$0.05 kW^{-1} h^{-1}, and about 85 % of the price is due to the electricity (Kreith and West, 2004).

2.3 Adsorption

The focus of this thesis is the storage of hydrogen on nanoporous carbons, hence the theory of adsorption is presented here. Adsorption is the principle means by which hydrogen is stored in nanoporous carbon and other materials. This section, therefore, is a discussion on the theoretical aspects. It consists of a description of the types of adsorption forces, the methods by which adsorption isotherms are measured along with a description of the types of isotherms observed in gas adsorption.

2.3.1 Adsorption Theory

Adsorption occurs whenever a solid surface is exposed to a gas or liquid: it is defined as the enrichment of a material or increase in the density of the fluid in the vicinity of an interface (Rouquerol and Sing, 1999). Adsorption is brought about by the interactions between the solid and the molecules in the fluid phase. There are two kinds of forces involved, which give rise to either physical adsorption (physisorption) or chemisorption. The nature of the physisorption forces are the same as van der Waals forces responsible for the condensation of vapours to the liquid state and deviations from the ideal gas behaviour (Gregg and Sing, 1982). In addition to the attractive dispersion forces and the short-range repulsive forces, specific molecular interactions (e.g. polarisation, field-dipole, field gradient-quadrupole) usually occur as a result of particular geometric and electronic properties of the adsorbent and adsorptive. In chemisorption interactions are essentially those responsible for the formation of chemical compounds (Sing *et al.*, 1985). The important distinguishing features between physisorption and chemisorption are summarised in Table 2.3-1.

The interfacial layer between the adsorbent and the adsorptive can be regarded as comprising two regions: the surface layer of the adsorbent and the adsorption space in which enrichment can occur. The material in the adsorbed state is known as the adsorbate and is separate from the adsorptive, which is the substance in the bulk fluid phase capable of being adsorbed. When the molecules of the adsorptive penetrate the

surface layer and enter the structure of the bulk solid, the term absorption is used. Desorption refers to the opposite of adsorption, this occurs when the amount adsorbed decreases. The relation at constant temperature, between the amount adsorbed and the equilibrium pressure of the gas is known as the adsorption isotherm (Gregg and Sing, 1982).

Many adsorbents of high surface area are porous and with such materials it is often useful to distinguish between the external and internal surface. The external surface is usually regarded as the envelope surrounding the discrete particles or agglomerates, while the internal surface comprises of the walls, all cracks, pores and cavities which are deeper than they are wide and which are accessible to the adsorptive (Sing *et al.*, 1985). In the context of physisorption, it is necessary to classify pores according to their width. The classification of pores according to their width was originally proposed by Dubinin (1947) and is now adopted by the International Union of Pure and Applied Chemistry (IUPAC) as shown in Table 2.3-2.

These limits are to some extent arbitrary since the pore filling mechanisms are dependent on the pore shape and are influenced by the properties of the adsorptive and by the adsorbent-adsorbate interactions. The whole of the accessible volume present in micropores may be regarded as adsorption space and the process, which then occurs, is micropore filling. Micropore filling may be regarded as a primary physisorption process, whereas physisorption in mesopores takes place in two more or less distinct stages (monolayer-multilayer adsorption and capillary condensation).

In monolayer adsorption all the adsorbed molecules are in contact with the surface layer of the adsorbent. In multilayer adsorption the adsorption space accommodates more than one layer of molecules so that not all adsorbed molecules are in direct contact with the surface layer of the adsorbent (Sing *et al.*, 1985). When the adsorption conditions are sub-critical, that is, the temperature of adsorption is less than the critical temperature (T_c), of the gas capillary condensation may occur, which implies that the residual pore space remaining after multilayer adsorption becomes filled with condensate separated from the gas phase by menisci. For super-critical adsorption conditions where the temperature of adsorption is greater or equal to the critical temperature of the gas, such as is the case in this investigation, capillary

condensation does not occur. For the case of hydrogen with a critical temperature (T_c) of 33 K, condensation will not occur when adsorption is carried out at temperatures higher than this value, as pressure is increased, the density of hydrogen in the pores will also increase.

Table 2.3-1: Distinguishing Features between Physisorption and Chemisorption (Rouquerol and Sing, 1999)

Physisorption	Chemisorption
It is a general phenomenon with a relatively low degree of specificity.	It is dependent on the reactivity of the adsorbent and adsorptive.
At high pressures, physisorption generally occurs as a multilayer.	Chemisorbed molecules are linked to reactive parts of the surface and the adsorption in necessarily confined to a monolayer.
A physisorbed molecule keeps its identity and on desorption returns to the fluid phase in its original form.	If a chemisorbed molecule undergoes reaction or dissociation, it loses its identity and cannot be recovered by desorption.
Physisorption is always exothermic, but the energy involved is generally not much larger than the energy of condensation of the adsorptive. However it is enhanced when physisorption takes place in narrow pores.	The energy of chemisorption is the same order of magnitude as the energy change in a comparable chemical reaction.
Physisorption systems generally attain equilibrium fairly rapidly, but equilibration may be slow if the transport process is rate – determining.	Activation energy is often involved in chemisorption and at low temperature the system may not have sufficient thermal energy to attain thermodynamic equilibrium.

Table 2.3-2: Classification of Pores according to their width
(Adapted from Gregg and Sing, 1982)

Classification	**Pore Width (w)**
Micropores	Less than 2 nm
Mesopores	Between 2 and 50 nm
Macropores	More than 50 nm

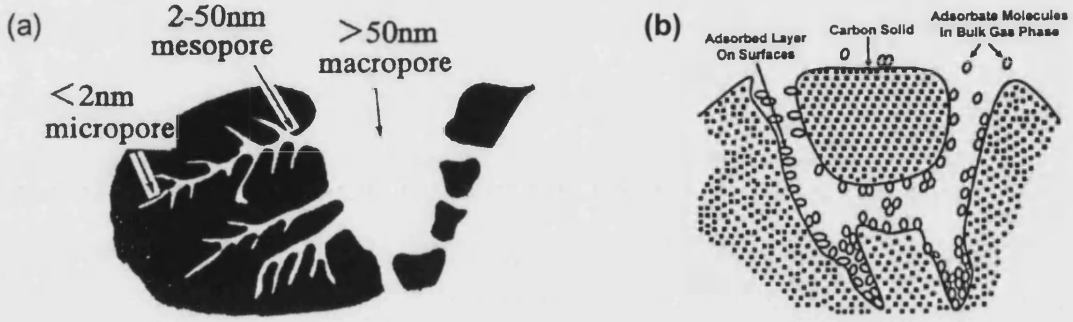

Figure 2.3-1: (a) Pore structure of granular activated carbon; (b) Adsorption process in activated carbon: transfer of adsorbate to adsorbent, (Manocha, 2003).

2.3.2 Physisorption of Gases

The amount of gas adsorbed, n^a, by the mass, m^s, of solid is dependent on the equilibrium pressure, p, the temperature, T, and the nature of the gas-solid system.

Thus $\frac{n^a}{m^s} = f(p,T,system)$ **Equation 2.3-1**

For a given gas adsorbed on a solid at constant temperature we have

$$\frac{n^a}{m^s} = f(p)_T \qquad \textbf{Equation 2.3-2}$$

If the gas is below its critical temperature, it is possible to write

$$\frac{n^a}{m^s} = f(p/p^\circ)_T \qquad \textbf{Equation 2.3-3}$$

Where here, the standard pressure p° is equal to the saturation pressure of the adsorptive at T. Equations 2.3-2 and 2.3-3 represent the relationship between the amount adsorbed by unit mass of solid and the equilibrium pressure (or relative pressure), at a known temperature. The experimental adsorption isotherm is usually represented in graphical form (Rouquerol and Sing, 1999).

2.3.3 Types of Adsorption Isotherms

Experimental adsorption isotherms measured on a wide variety of gas-solid systems have a variety of forms. The majority of these isotherms, which result from physical adsorption, can be grouped into six types in the IUPAC classification as shown in the diagram below. The reversible Type I isotherm is concave to the p/p^o axis and the amount of gas adsorbed by a unit mass of solid, (n^a/m^s) approaches a limiting value as $p/p^o \rightarrow 1$. Type I isotherms are generally observed in microporous solids having relatively small external surfaces such as activated carbons, molecular sieve zeolites and certain porous oxides. The limiting uptake is governed by the accessible pore volume rather than by the internal surface area (Sing *et al.*, 1985). These are the types

of isotherms of significance in this report. It is important to note that Type I isotherm shapes occur for both sub-critical and super-critical adsorption, but for different reasons. Type I behaviour in sub-critical systems is due to physisorption in either purely microporous solids, or sub-monolayer chemisorption on non-porous solids. In contrast, Type I behaviour in super-critical systems simply reflects the gradual densification of fluids near solid surfaces as pressure is increased.

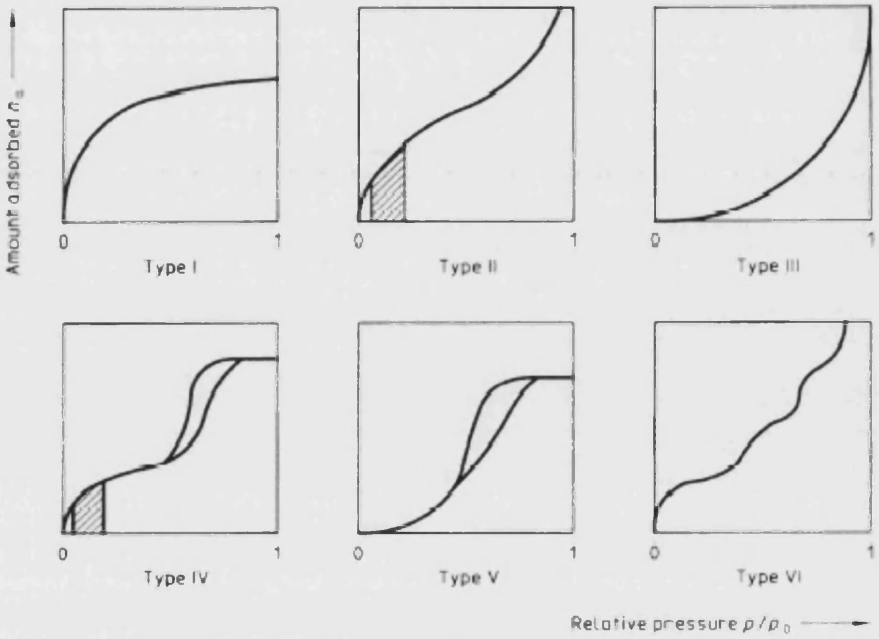

Figure 2.3-2: The six main types of gas physisorption isotherms, according to the IUPAC classification (BS 4359-1: 1996; ISO 9277:1995(E); Rouquerol and Sing, 1999).

2.3.4 Methods for measuring gas uptake

The many different procedures, which have been, devised for measuring the amount of gas adsorbed can be divided into two groups:

(a) Those that depend on the amount of gas removed from the gas phase that is volumetric methods.

(b) Those, which involve the measurement of the uptake of the gas by the adsorbent for example, the direct determination of increase in mass by gravimetric methods.

In practice, static or dynamic techniques may be used to determine the amount of gas adsorbed. In the static volumetric technique a known quantity of pure gas is usually admitted to a confined volume containing the adsorbent, maintained at constant temperature. As adsorption takes place, the pressure in the confined volume falls until equilibrium is established.

The amount of gas adsorbed at the equilibrium pressure is given as the difference between the amount of gas admitted and the amount of gas required to fill the space around the adsorbent, that is, the dead space at the equilibrium pressure. The adsorption isotherm is usually constructed point-by-point by the admission to the adsorbent of successive charges of gas with the aid of a volumetric dosing technique and application of the gas laws. The volume of dead space must be known accurately: it is obtained either by pre-calibration of the confined volume and subtracting the volume of the adsorbent (calculating from its density), or by the admission of a gas which is adsorbed to a negligible extent (Sing *et al.*, 1985).

Nitrogen adsorption isotherms at cryogenic conditions and ambient pressure are generally determined by the volumetric method; they provide a basis for the various standard procedures, which have been proposed for the determination of surface area.

Recent developments in vacuum microbalance techniques have revived the interest in gravimetric methods for the determination of adsorption isotherms. With the aid of an adsorption balance the change in weight of the adsorbent can be followed directly during the outgassing and adsorption stages. A gravimetric procedure is especially convenient for measurements with vapours at temperatures not too far removed from ambient. At both high and low temperatures, however it becomes difficult to control and measure the exact temperature of the adsorbent, which is particularly important in the determination of mesopore size distribution.

In principle, a continuous procedure can be used to construct the isotherm under quasi-equilibrium conditions: the pure adsorptive is admitted or removed at a slow or constant rate and a volumetric or gravimetric technique is used to follow the variation in the amount adsorbed with an increase or decrease in pressure.

A carrier gas technique, making use of conventional gas chromatographic equipment, may be employed to measure the amount adsorbed provided that the adsorption of the carrier gas is negligible. In all types of measurement involving gas flow it is essential to confirm that the results are not affected by change in flow rate and to check the agreement with representative isotherms determined by a static method (Sing *et al.*, 1985).

2.4 Nanoporous Carbon Materials

Carbon is widely known as a good adsorbent for gases. This is because some carbon materials can have very large internal surface areas (Darkrim *et al.*, 2002).

The discovery at the beginning of the last decade of new forms of carbon aggregation with the basic particle size in the nanoscale range has created a variety of scientific and technological speculations and investigations about their potential applications. Fullerenes, carbon nanotubes and nanofibres along with activated carbon, have been developed and proposed for the storage of hydrogen, through the low-pressure adsorption of compressed hydrogen (Conte *et al.*, 2001).

Most porous carbons are manufactured by the controlled pyrolysis of carbonaceous materials, naturally occurring woods or synthetic polymeric materials. They are unique and versatile because of their extended surface area, microporous structure and high adsorption capacity (Manocha, 2003). In 1991 Iijima discovered graphitic tubules, these nanotubes can be conceptualised as rolled graphene sheets with an inner diameter of about one to several nanometers and a length of 10 to 100 micrometers (Iijima, 1991).

There are a variety of tubes that consist of one layer called single-walled nanotubes (SWNT) or of more than one layer, called multi-walled nanotubes (MWNTs) or sometimes called tubular formed graphitic nanofibres (Hirscher and Becher 2003). Despite the large interest in nanotubes, the advantages may be as many as the disadvantages and carbon nanotubes could not be confirmed to be a promising carrier of hydrogen. On the other hand, hydrogen adsorption on activated carbons still seems interesting because activated carbons are cheap, readily available and are capable of storing higher quantities of hydrogen compared to nanotubes (Zhou *et al.*, 2003). The works carried out by several authors on these adsorbents are reviewed below.

2.4.1 Material Preparation and Treatment

With the varying number of nanoporous carbons available and the relative importance of their use as adsorbents in many applications such as water treatment, air pollution control, solvent recovery, catalyst support (Arriagada *et al.*, 1997), a number of techniques have been developed for their synthesis. These techniques vary according to the intended application of the materials.

2.4.1.1 Activated Carbons

Activated carbons can be prepared from a variety of precursors, but the ones most commonly used ones are peat, coal, wood and coconut shells (Wigmans, 1989). Among these raw materials, coal is the most commonly used due to its low cost and large supply. It is considered that activated carbon materials produced using coal are superior to those derived from lignocellulosic materials in terms of mechanical properties (Ahmadpour and Do, 1996). According to Cagnon *et al.*, (2003) and Rodriuez-Reinoso *et al.*, (1995) the microporous properties of resulting activated carbons depend on the precursor and the conditions of carbonisation and activation (Cagnon *et al.*, 2003; Rodriuez-Reinoso *et al.*, (1995)).

There are two different processes for the preparation of active carbon: physical and chemical activation. In physical activation the carbonaceous precursor is carbonised followed by the activation of the resulting char in the presence of some activating agents such as carbon dioxide or steam (Ahmadpour and Do, 1996; Hu and Srinivasan, 1999; Rodriuez-Reinoso *et al.*, 1995; Tam and Antal, 1999). On the other hand, chemical activation is a single step method. It involves the carbonisation of the precursor in the prescence of chemical agents (Ahmadpour and Do, 1996; Lua and Guo; 2001; Lillo-Rodenas *et al.*, 2003). According to the work of Kandiyoti *et al.*, (1984) reported by Ahmadpour and Do (1996), in physical activation, elimination of a large amount of internal carbon mass is necessary to obtain a well developed carbon structure, whereas in the chemical activation process all the chemical agents used are dehydrating agents that influence the pyrolytic decomposition and inhibit formation of

tar, thus enhancing the yield of carbon. The chemical agents used in the chemical process are normally alkali and alkaline earth metals containing substances and acids such as KOH, NaOH, $ZnCl_2$, $MgCl_2$, and H_3PO_4 (Ahmadpour and Do, 1996; Hu and Srinivasan; 1999; Lillo-Rodenas *et al.*, 2003). In the work of Arriagada *et al.*, (1997) where a comparative analysis of the carbons produced by physical activation using CO_2 and H_2O was carried out. The results obtained showed important differences between the two activating agents: while water vapour was said to develop both micro- and mesoporosity from the beginning of the reaction, carbon dioxide mainly developed the microporosity (Arriagada *et al.*, 1997).

2.4.1.2 Carbon Nanotubes

The discovery of nanotubes is linked to the discovery of fullerenes by Kroto and Smalley (1985). However, the real breakthrough on carbon nanotube research came with Iijima's report on the experimental observation of carbon nanotubes using transmission electron microscopy (Iijima, 1991).

A single wall carbon nanotube can be described as a graphene sheet rolled into a cylindrical shape so that the structure is one dimensional with axial symmetry. If the two ends of a carbon nanotube are neglected, these nanotubes can be considered as one-dimensional nanostructures (Saito *et al.*, 1998). The existence of single-wall carbon nanotube has been confirmed experimentally through high resolution transmission electron microscopy (TEM) and scanning tunnelling microscopy (STM). These techniques are especially useful for the characterisation of carbon nanotubes (Saito *et al.*, 1998; Harris, 1999; Reich *et al.*, 2004).

Single-wall Nanotube (SWNT) and Multiwalled Nanotubes (MWNT) Synthesis Methods

(a) Laser Vaporisation Synthesis Method. This is an efficient route for the synthesis of bundles of single wall carbon nanotubes with a narrow diameter distribution that employs the laser vaporisation of graphite (Saito *et al.*, 1998). In the

earlier reports of this technology, high yields of > 70 % of SWNT were observed (Thess *et al.*, 1996). The single-wall nanotubes are held together by weak van der Waals inter-nanotube bonds to form a two-dimensional triangular lattice with a lattice constant of 1.7 nm, and an intertube separation of 0.315 nm. By varying the growth temperature, the catalyst composition and other growth parameters, the average nanotube diameter distribution can be varied (Saito *et al.*, 1998; Thess *et al.*, 1996).

(b) Arc Method of Synthesising Carbon Nanotubes. The carbon arc provides a simple and traditional tool for generating the high temperatures needed for the vaporisation of carbon atoms into a plasma (> 3000 °C) (Ebbesen and Ajayan, 1992; Ebbesen *et al.*, 1993; Seraphin *et al.*, 1993). This technique has been used for the synthesis of single and multi-walled nanotubes. (Saito *et al.*, 1998; Journet *et al.*, 1997). Catalysts used to prepare isolated single-wall carbon nanotubes include transition metals such as Co, Ni, Fe and rare earth metals such as Y and Gd. During arc synthesis fullerenes are predominantly found in the soot produced by the arc and removed by the helium gas flow, while the nanotube are contained in a deposit on the cathode (Saito *et al.*, 1998). According to Harris (1999), nanotube production is sensitive to the helium pressure used in synthesis. It is believed that there is a striking increase in the number of tubes evident as the pressure is increased. At pressures above 500 Torr (0.7 bar) there is no obvious change in sample quality, but a fall in total yield. Thus 500 Torr appears to be the optimum helium pressure for nanotubes production (Harris, 1999).

(c) Vapour Growth Method. The synthesis of carbon nanotubes using this method requires equipment similar to that used for the preparation of vapour-grown carbon fibres. In this method, the furnace temperature is held at 1100 °C with Fe catalyst particles but low benzene gas pressure (Endo *et al.*, 1993; Endo *et al.*, 1995). A range of other hydrocarbons, catalyst and catalyst supports have been used successfully by various groups worldwide to synthesise carbon nanotubes. A big advantage of the vapour growth approach is that carbon nanotubes can be made continuously. Thus, if the optimum growing conditions are found, this method will be useful for large scale production of nanotubes under controlled conditions (Saito *et al.*, 1998).

(d) Other production routes: The condensation of carbon vapour in the absence of an electric field has also been described by a group at the Russian Academy of Sciences led by Leonid Chernozatonskii, in 1992 and also described by Maohui Ge and Klaus Sattler of the University of Hawaii, pyrolytic methods (Studies by Morinobu Endo and colleagues form Shinshu university together with workers from Sussex, have shown that multiwalled nanotubes can be produced by the pyrolysis of benzene in the presence of hydrogen); electrochemical synthesis of nanotubes (described by the Sussex group, it involved the electrolysis of molten lithium chloride using a graphite cell in which the anode was a graphite crucible and the cathode a graphite rod immersed in a melt (Endo *et al.*, 1993; Sarkar *et al.*, 1995; Endo *et al.*, 1995).

Purification of Synthesised Carbon Nanotubes

In many of the synthesis methods that have been reported, carbon nanotubes are found along with other materials, such as amorphous carbon and carbon nanoparticles (Saito *et al.*, 1998). Purification generally refers to the isolation of carbon nanotubes from other entities. Three basic methods have been used with limited success for the purification of the nanotubes: gas phase, liquid phase, and intercalation methods (Ebbesen, 1997). The classical methods for purification such as filtering, chromatography, and centrifugation have been tried and found not to be effective in removing the carbon nanoparticles, amorphous carbon and other unwanted species. (Saito *et al.*, 1998). Heating preferentially decreases the amount of disordered carbon relative to carbon nanotubes. Heating could thus be useful for purification, except that it results in an increase in nanotube diameter due to the accretion of epitaxial carbon layers from the carbon in the vapour phase resulting from heating (Saito *et al.*, 1998).

The gas phase method removes nanoparticles and amorphous carbon in the presence of nanotubes by oxidation or oxygen burning process (Ebbesen, 1994; Tsang *et al.*, 1993; Ajayan *et al.*, 1993). Much slower layer by layer removal of the cylindrical layers of multi-wall nanotubes occurs because of the greater stability of a perfect graphene layer to oxygen than disordered or amorphous carbon or material with pentagonal defects (Tsang *et al.*, 1993; Ajayan *et al.*, 1993). The oxidation reaction for carbon nanotubes is thermally activated with an energy barrier of 225 kJ mol^{-1} in

air (Ajayan *et al.*, 1993). The gas phase purification process also tends to burn off many of the nanotubes, so to remove all the nanoparticles, it is necessary to oxidise more than 99 % of the raw sample. When 95 % of the original material is oxidised, about 10-20 % of the remaining sample consists of nanoparticles, while an oxidation of 85 % results in no enrichment at all. According to Harris (1999) and Saito *et al.*, (1998), these results suggest that the reactivity of nanotubes and nanoparticles towards oxidation are very similar, so that only a narrow window exists between the selective removal of nanoparticles and complete oxidation of the sample (Harris, 1999; Saito *et al.*, 1998). The carbon nanotubes obtained by gas phase purification are generally multi-walled nanotubes with diameters in the range of 0.2 - 20 nm and 10 nm – 1 μm in length, since the smaller diameter tubes tend to be oxidised with the nanoparticles.

Liquid phase removal of nanoparticles and other unwanted carbons has been carried out with some success using potassium permanganate $KMnO_4$ treatment method which tends to give higher yields than the gas phase method, but results in nanotubes of shorter length (Ebbesen, 1997; Hiura *et al.*, 1995).

2.5 Hydrogen Storage on Nanoporous Carbons

As mentioned earlier, the interest in hydrogen as an energy vector is growing dramatically and there has been advances made in hydrogen production and utilisation technologies. However, hydrogen storage technologies must be significantly advanced if a hydrogen based energy system is to be established.

Possible current approaches to vehicular hydrogen storage include physical storage via compression or liquefaction, chemical storage in irreversible hydrogen carriers (e.g. methanol, ammonia), reversible metal and chemical hydrides and gas-on-solid adsorption. Although each method has its desirable attributes, no approach presently satisfies all of the efficiency, size, weight, cost and safety requirements for personal transportation vehicles.

2.5.1 Past

Lightweight carbon adsorbent materials have become interesting for possible use in a hydrogen storage system. Work in this area has been ongoing since the 1960s; one of the first investigations of the adsorption of hydrogen on high-surface area carbon was reported by Kidnay and Hiza, (1967). That work was focused on the behaviour of adsorbents from a cryogenic engineering perspective. Adsorption isotherms for hydrogen on coconut-shell charcoal were reported at 76 K and pressures up to 90 atm.

Carpetis and Peschka, (1980) were among the first to suggest that hydrogen could be inexpensively stored on activated carbon materials by adsorption at cryogenic temperatures. Adsorption isotherms were reported for a variety of different types of high surface area carbon materials at 78 and 65 K at pressures up to 41.5 atm. Unfortunately, the total mass of the adsorbent used in each experiment was not reported so it is impossible to determine from the paper if the cryogenically cooled

container could have stored more hydrogen if the carbon was not present. A maximum amount of ~ 5.2 wt-% for a 'F12/350' carbon material exposed to 41.5 atm of hydrogen at 65 K was achieved. The more open, porous carbon materials that were tested adsorbed more hydrogen than the denser carbons studied. A detailed analysis concluded that a cryo-adsorption storage system would have ~ ¼ the volumetric energy density of a liquid hydrogen storage system.

Dillon and Heben, (2001) reported the work of the J. A. Schwarz research group at Syracuse University. The group was active in studying the storage of hydrogen on activated carbons in the late 1980s and early 1990s. Their efforts were focused on developing a detailed understanding of the fundamental aspects of hydrogen adsorption on activated carbon materials. They investigated how the operating temperature of the adsorbent could be increased, the effect of surface acidity and metal modification. Despite their efforts, the best activated carbon identified adsorbed ~ 4.8 wt-% H_2 at a temperature of 87 K and a pressure of 59 atm. As with previous investigations, this storage system did not significantly benefit from the incorporation of carbon under the chosen operating conditions. It is important to note that the inclusion of activated carbon material in a storage tank can enhance the overall hydrogen energy storage density under certain pressure and temperature conditions.

2.5.2 Present

2.5.2.1 Hydrogen storage in carbon nanofibres

Graphite nanofibres are an example of engineering material that has recently been investigated for hydrogen storage applications. These materials are produced by decomposition of mixtures of ethylene, hydrogen and carbon monoxide on selected metal and alloy catalysts (Rodriguez *et al.*, 1995). Three distinct structures may be produced: 'tubular' (90°), 'platelet' (~ 0°) and 'herringbone' (45°), the angle in parentheses indicates the direction of the nanofibres axis relative to the vector normal to the graphene sheets (Atkinson and Roth, 2003). The nanofibres typically range in

diameter from 5 to 500 nm (Rodriguez *et al.*, 1995) and have lengths of between 10 and 100 μm (Chambers *et al.*, 1998). Very high hydrogen storage densities exceeding 50 and 60 wt-% have been reported for the platelet and herringbone structures respectively, while the tubular structure exhibited storage densities exceeding 10 wt-% (Chambers et al. 1998). The hydrogen uptake was recorded as a drop in pressure from an initial value of 112 atm over a period of ~ 24 h at a temperature of 298 K.

Ahn *et al.*, (1998) carried out hydrogen adsorption studies on similarly fabricated carbon fibres for temperatures between 77 and 300 K. Hydrogen gas was admitted into an evacuated chamber to achieve a typical pressure of 4.5 or 80 atm for the 77 K runs or 180 atm for the 300 K runs. The absolute level of hydrogen desorption measured for the graphitic nanofibres (GNFs) was typically less than 0.01 H/C or ~ 0.08 wt-%, (Ahn *et al.*, 1998). Fan *et al.*, (1999) also reported hydrogen storage capacities of 10–13 wt-% on vapour grown fibres, which were not graphitic. Based on their initial studies the group projects that higher storage values will be obtained upon graphitisation, (Fan *et al.*, 1999).

2.5.2.2 Hydrogen Storage in Multi-wall Carbon Nanotubes

Multi-wall carbon nanotubes consist of layers of nested concentric cylinders of graphite with a hollow centre. The spacing between each cylinder is similar to the inter-planar spacing in graphite (3.4 Å) (Rzepka *et al.*, 1998), and the number of shells varies from 2 to about 50 (Iijima, 1991). Chen *et al.*, (1999) reported remarkable hydrogen storage capacities for alkali-metal doped MWNTs formed by the catalytic decomposition of CH_4. The walls of the nanotubes formed via this process are conical in shape and for this reason these nanotubes are sometimes classified as graphitic nanofibres. Lithium and potassium were incorporated into the carbon the carbon nanotubes through solid-state reactions with the metal carbonates or nitrates. Hydrogen adsorption and desorption were measured by the thermo gravimetric analysis (TGA) and temperature-programmed desorption (TPD). The hydrogen uptake was shown to be 20 wt-% for Li-doped nanotubes at 653 K and 14 wt-% for K-doped nanotubes at room temperature. The K-doped nanotubes were reported to combust upon exposure to air. The hydrogen adsorption was believed to

proceed by a dissociative mechanism, and an infrared spectrum of the hydrogen charged Li-doped material was interpreted to indicate the presence of both Li-H and C-H species, (Chen *et al.*, 1999).

In a subsequent TGA study, Li-doped MWNTs formed under identical conditions were shown to exhibit a weight increase of 12 wt-% when exposed to 'wet H_2' and only 2.5 wt-% in the presence of 'dry H_2' (Yang 2000). In another report on the hydrogen storage properties of Li-doped MWNTs, large cycling mass changes similar to those observed by Chen *et al.*, (1999) were again attributed to the presence of water impurities in the TGA atmosphere. No evidence of hydrogen adsorption by the sample was detected (Pinkerton *et al.*, 2000).

A report on the hydrogen adsorption properties of multiwalled nanotubes synthesised by the catalytic decomposition of CO and CH_4 on powdered La_2O_3 catalysts was shown by Wu *et al.*, (2000). The nanotubes were purified and annealed in vacuum to increase their crystallinity. TGA analysis in hydrogen revealed that the nanotubes were capable of adsorbing a small quantity of hydrogen (0.25 wt-%) when the sample was cooled between 200 °C and room temperature (Wu *et al.*, 2000). Hou *et al.*, (2001) compared the gravimetric hydrogen storage capacities of as-prepared and purified MWNTs. The purified nanotubes showed higher hydrogen storage capacity (6.3 wt-%) than the as-prepared MWNT. They concluded that pore structure and surface modifications were important for the improvement of hydrogen storage capacity (Hou *et al.*, 2001).

2.5.2.3 Hydrogen Storage in Single-wall Carbon Nanotubes

In physisorption, the gas adsorption performance of a porous solid is maximised when the pores are not larger than a few molecular diameters (Gregg and Sing 1982). Under these conditions the potential fields of the so-called micropores overlap to produce a stronger interaction than would be possible for adsorption on a semi-finite plane. If the escaping tendency of a gas is much less than the adsorption potential, the entire micropore may be filled with a condensed adsorbate phase. For the case of hydrogen with a kinetic diameter of ~ 2.9 Å, pores would have to be significantly smaller than

40 Å to begin to condense hydrogen by a nanocapillary filling mechanism (Dillon and Heben 2001).

The ideal hydrogen adsorbent should have uniform and small micropores in as high a density as possible, minimal macroporosity and high thermal conductivity. The first characteristic is required for an enhanced heat of adsorption, which may aid ambient temperature adsorption, while the first two characteristics together ensure the internal volume of the adsorbent is not wasted. The third characteristic provides for managing heat fluxes that will hopefully be relatively large by virtue of an enhanced heat of adsorption. A model, which provides all of these features, is an array of bundled carbon single-wall nanotubes. An individual SWNT is essentially a sheet of graphite that is wrapped to meet itself forming a single elongated and seamless tube (Dillon and Heben 2001).

Dillon *et al.*, (1997) investigated the hydrogen adsorption properties of the early SWNT materials. Although these materials contained only ~ 0.1-0.2 wt-% SWNTs, hydrogen adsorption on the carbon nanotubes fraction was estimated for ambient conditions to be between ~ 5-10 wt-% and a heat of adsorption of 19.6 kJ mol^{-1} was measured. This demonstrated enhanced interaction between hydrogen and SWNTs relative to planar graphite, where the heat of adsorption is only ~ 4 kJ mol^{-1} (Pace and Sieberts 1959).

Ye *et al.*, (1999) were the first to report hydrogen adsorption investigations on purified SWNTs. Hydrogen adsorption on purified crystalline ropes of SWNTs was 8 wt-% at 40 atm and 80 K. High hydrogen storage capacities on a total sample weight basis were subsequently demonstrated on SWNTs with a large mean diameter of about 1.85 nm produced at high yield by a semi-continuous arc discharge method. The purity of the nanotubes was estimated to be ~ 50-60 %. A sample first soaked in HCl and then heat treated in vacuum was shown to adsorb 4.2 wt-% hydrogen at room temperature and 10 MPa. Approximately 80 % of the adsorbed hydrogen could be released at room temperature (Liu *et al.*, 1999).

Electrochemical hydrogen storage has also been demonstrated for carbon single-wall nanotubes. Arc-generated SWNT soot containing 0.7-1.2 nm diameter SWNTs was

mixed with either copper or gold as a compacting powder in a ratio of 1:4 to form electrodes. The kinetics of the electrode were relatively poor, however, the capacity at low discharge currents was high corresponding to an uptake of ~ 0.39 wt-% (Nutzenadel *et al.*, 1999). Assuming that all of the stored hydrogen was contained in the SWNT fraction of the sample, the results indicate that electrochemical hydrogen storage should be further investigated.

2.5.3 Future

2.5.3.1 Optimising and Understanding the Interaction between Hydrogen and Carbon Materials

From the analysis made above it is evident that if carbon adsorbents are to be eventually applied in a hydrogen storage system, several advances remain to be made. It is obviously important to maximise the hydrogen adsorption capacity for a given carbon system at room temperature and moderate pressures and that the system charges and discharges rapidly and completely at near ambient conditions. In order to optimise a carbon based hydrogen storage system it will be necessary to obtain a better understanding of the adsorption mechanism and to determine the precise adsorption sites in the carbon network that are responsible for the more promising adsorption properties. When optimisation is complete, it will be necessary to scale up the techniques that generate the ideal adsorption materials. The development of industrial scale, cost-effective procedures will be necessary (Dillon and Heben, 2001).

To date the hydrogen adsorption process that has been most thoroughly analysed is that which occurs on nanotubes. In a recent report by Zhou *et al.*, (2003) comparing hydrogen adsorption on super activated carbon and carbon nanotubes, it was discovered that although the adsorption isotherms on both activated carbon and MWNT show the same type of adsorption mechanism, the amount adsorbed on MWNT is 3.6-5.1 times less than that on activated carbon. The conclusion drawn was that carbon nanotubes are not promising carriers of hydrogen for practical applications based on the less quantity adsorbed, the much less heat of adsorption and the much

smaller surface area in comparison to activated carbon. The results of this finding are yet to be confirmed by other authors.

2.6 Thesis Aims

The need for a sustainable energy system in the long term has been discussed with a Hydrogen Economy being recognised as one of the ways this can be achieved. This is coupled with a requirement to develop infrastructure to cope with the foreseeable demand of hydrogen use in the future.

The challenge of hydrogen storage, the focus of this project has also been discussed along with a review of the current available technology. This review has shown that there is the lack of a suitable hydrogen storage method that can meet transportation and stationary application requirements without comprising factors such as safety, cost, and space requirements. It is the aim of this investigation to study the potential of storing hydrogen in nanoporous carbon materials. To achieve this aim, a number of objectives have been highlighted:

i. Measure hydrogen sorption isotherms at different temperatures (77, 195 and 303 K) with a maximum pressure of 20 bar. Focus on the effects of adsorption temperature, gas purity, and sample cycling on the amount of hydrogen adsorbed.

ii. The use of semi-empirical adsorption models to analyse isotherms and to assess the mechanism of adsorption taking place in these materials using kinetic data obtained experimentally.

iii. Correlation of structural characterisation data of the nanoporous carbons with their hydrogen adsorption properties.

Chapter Three

Experimental Details

3.1 Introduction

This chapter describes the different experimental techniques and equipment used to investigate the hydrogen storage properties/potential and to characterise a selection of nanoporous carbon materials. It refers to the instrumentation, methodology and the assumptions made for each characterisation method.

The chapter opens, in Section 3.2 with a description of the carbon materials selected for study. This is followed by a description of the gravimetric apparatus used for the hydrogen sorption measurements, the major source of the experimental data in this investigation with methodology applied in carrying out the measurements in Section 3.3. The chapter then continues with a description of the equipment and methods used to obtain other characterisation data in Sections 3.4 and 3.5. These include the sample skeletal density for buoyancy correction, the ash content of each carbon material, surface area, pore size distribution, pore structure data and microscopic information obtained using transmission electron microscopy (TEM). The X-ray diffraction equipment and methodology is also described.

3.2 Material Selection

A series of commercially available activated carbons, single and multi-walled nanotubes have been selected for analysis. These materials have been selected because they represent a wide range of precursors, particle sizes, preparation and activation methods in the case of the activated carbons. The nanotubes have been selected because they cover a broad range of preparation routes, purity, diameters, lengths and structure (end-capped or open-ended). Each material is described in more detail in Section 3.2.1 and 3.2.2 and also summarised in Table 3.2-1 and Table 3.2-2.

3.2.1 Activated Carbons

The activated carbons include BPL, a bituminous coal based granular material activated at high temperature in steam supplied by Calgon Carbon Corporation UK. Norit CNR 115, a pelletised chemically activated carbon, produced from a renewable raw material source via a version of the phosphoric acid process. It is a high activity, medium density grade carbon supplied by Norit Activated Carbon UK. SRD/667/1, a coconut shell based steam activated granular active carbon supplied by Sutcliffe Speakman (now acquired by Calgon Carbon Corporation) UK. Table 3.2-1 shows the manufacturers properties for these materials.

3.2.2 Carbon Nanotubes

Two single-walled and multi-walled carbon nanotubes samples were selected for analysis. SWNT-1 is an 85 % pure single-walled carbon nanotube supplied by Carbon Nanotechnologies Incorporated (CNI), Houston, Texas, USA. SWNT-2 is also a single-walled carbon nanotube with about 70-90 % purity supplied by Thomas Swan and Co. Ltd. County Durham, U.K. MWNT-1 is a high purity (95 %) multi-walled

carbon nanotube supplied by Nanoledge, France, while MWNT-2 is an end opened multi-walled carbon nanotube with a purity > 90 %, supplied by BuckyUSA, Houston, Texas, USA. Table 3.2-2 show the material properties supplied by the respective manufacturers.

Table 3.2-1: Manufacturer Properties for the Selected Commercial Activated Carbons

Material	Carbon Precursor	Activation Method	Particle Size Range	
			Mesh Size	mm
BPL	Bituminous Coal	Steam / physical activation	6 by 16	2.8 by 1.0
Norit CNR 115	Renewable material	Phosphoric acid / chemical activation	-	2 mm extrudate
SRD/667/1	Coconut shells	Steam / physical activation	14 by 25	1.40 by 0.71

Table 3.2-2: Manufacturer Properties for the Selected Carbon Nanotubes

Material	Preparation Method	Purity	Diameter, nm	Length	End-capped / Open ended
SWNT-1	High Pressure Carbon monoxide	85 %	0.8-1.3	100-1000 nm	End-capped
SWNT-2	Catalytic CVD	70-90 %	< 2	microns	End-capped
MWNT-1	CVD	95 %	I.D.:8; O.D.:17	120-180 nm	End-capped
MWNT-2	Arc produced Cathode Deposit	>90 %	1.2	Several microns	Open ended

3.3 Equipment

The hydrogen gas adsorption isotherms and kinetic measurements were carried out using an Intelligent Gravimetric Analyser (IGA) supplied by Hiden Analytical Ltd., Warrington, U.K. This instrument combines computer-control and measurement of weight change, pressure and temperature to enable the determination of adsorption and desorption isotherms including the kinetics of each pressure increment in diverse operating conditions. The mass uptake is measured as a function of time and the approach to equilibrium monitored by a computer-controlled algorithm. When equilibrium is established at the set pressure point, the pressure is increased to the next set pressure value and the subsequent uptake measured until equilibrium is again established. Table 3.3-1 shows the operating limits of the IGA. All the gravimetric sorption results reported in Chapter 5 have been carried out within these limits. Figure 3.3-1 and Figure 3.3-2 are snapshots of the equipment setup in the laboratory while Figure 3.3-3 is a schematic representation of the IGA.

Table 3.3-1: IGA Operating Limits and Description

Parameter	Limits
Pressure	
Ultimate Vacuum	10^{-6} mbar
Leak Rate	$<10^{-9}$ mbar s^{-1}
Operating Pressure Range	0 – 20 bar
Pressure Transducer Ranges	0 –1 bar, 0 – 10 bar and 0 – 20 bar
Pressure Resolution	1/16000 of range
Pressure Controller	Set-point regulation/ramp control
Accuracy (set-point regulation)	+/-0.02 % of range
Maximum rate of Change of Pressure (admittance)	~1 % of range/s
Temperature	
Temperature Sensors	Type K thermocouple (with Cold Junction compensation)
Maximum Measurement Range	-270 to 1000 °C
Typical Resolution/Accuracy	+/-1 °C
Response Time	0.05 s
Linearisation	Software Algorithm
Temperature Controller	Set-point regulation/ramp control of resistive load
Weight	
Balance Capacity	5 g
Sample Capacity	Balance capacity less the weight of hang-down and container (typically < 0.25 g)
Weight Range	0 – 200 mg
Tare	Mechanical
Hang-down	Tungsten wire (0.15 mm dia.)
Settling Time	User adjustable 1 – 30 s
Weighing Resolution	0.2 μg
Stability in an inert atmosphere at room Temperature*	Long term: +/-1 μg Short term: +/-0.1 μg

*Depends on sample environment at alternative temperatures and pressures.

3.3.1 Design

Figure 3.3-1: Layout of the Gravimetric Hydrogen Storage Equipment: (a) Intelligent Gravimetric Analyser (IGA) main unit; (b) Thermostat; (c) Standard 500 °C furnace; (d) Computer; (e) N4.5 and N6.0 H_2 Gas Cylinders; (f) Liquid N_2 Dewar and Flask.

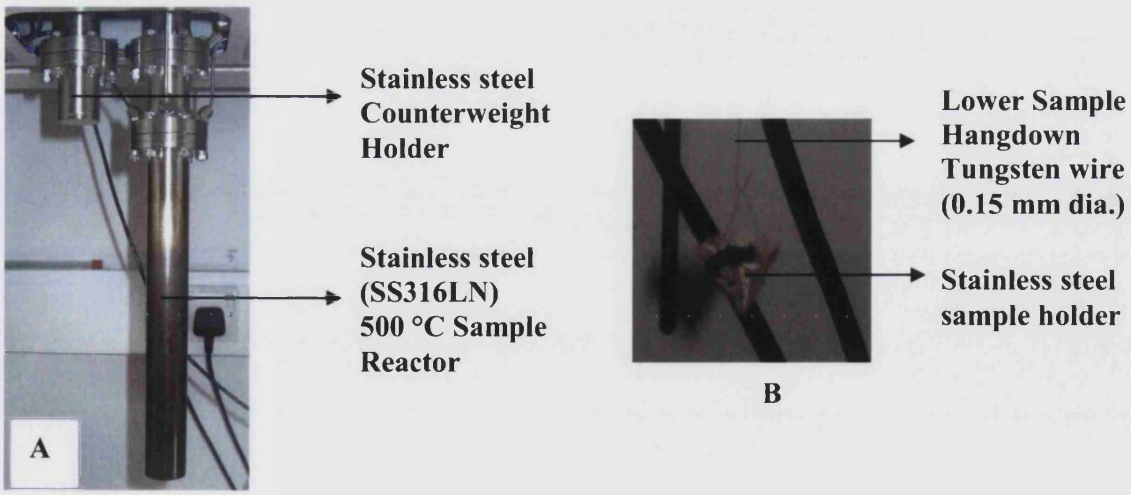

Figure 3.3-2: Picture showing (A) The Intelligent Gravimetric Analyser Counterweight and Sample sections; (B) The Sample Holder and Hangdown for the Intelligent Gravimetric Analyser System.

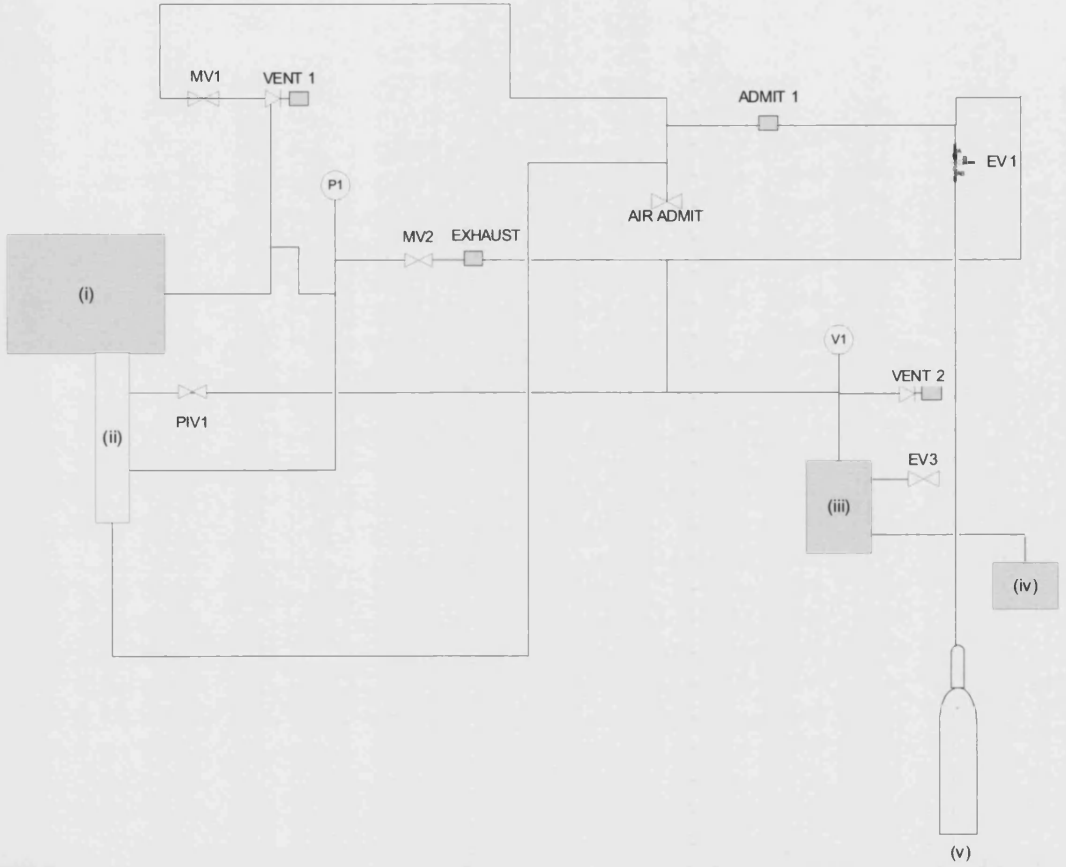

Figure 3.3-3: Schematic of the Intelligent Gravimetric Analyser (IGA) Set-up; (i) IGA Unit; (ii) Sample Reactor; (iii) Two-Stage Rotary Pump (10^{-2} mbar); (iv) High Vacuum Turbomolecular Pump (10^{-6} mbar); (v) Hydrogen Gas Cylinder.

3.3.2 Operation

The main operation of the gravimetric analyser for measuring sorption isotherms can be categorised into three main parts namely: sample loading, sample preparation and isotherm determination. The operation procedure is standardised to ensure reproducibility in the data and avoid uncertainties and is described below.

3.3.2.1 Sample Loading

Prior to sample loading, the system is decontaminated by evacuating the system under high vacuum (10^{-6} mbar) to remove traces of other gases/vapour that may be present. The sample pan is then cleaned by blowing it with air, weighed and loaded onto the balance hangdown shown in Figure 3.3-2. At this stage, the balance is tared and approximately 150 mg of the carbon sample is loaded onto the balance hangdown. When the balance is stable, as observed on the stability meter (Figure 3.3-7), the sample reactor shown in Figure 3.3-2 is then sealed tightly and the thermostat replaced. Figure 3.3-6 shows a snapshot of the buoyancy table set-up for sorption analysis. Here, the empty sample pan (container) weight is entered along with its density. The weights and density of the balance hangdown for the sample and counterweight sides are also entered during the sample loading stage. Figure 3.3-7 shows a snapshot of the IGA electronic balance. This informs the user of the stability of the balance and also the weight of the loaded sample.

3.3.2.2 Sample Preparation and Isotherm Determination

At this stage, the sample is set to degas at a ramp rate of 100 mbar min^{-1} to high vacuum (10^{-6} mbar) and elevated temperature, which was chosen to be 250 °C for a dwell time of 4 hours. This temperature and duration was found to be reasonable based on thermogravimetic analysis (TGA) carried out on the activated carbons as

described. Approximately 40 mg of the sample is loaded into the thermogravimetric analyser and ramped from room temperature to the set temperature (150 or 250 °C) at a rate of 2 °C min^{-1} in a nitrogen atmosphere. The change in weight of the sample is monitored until it reaches a stable value. The thermogravimetric profile obtained for Norit CNR 115 at 150 °C and 250 °C is shown in Figure 3.3-4 and Figure 3.3-5. It is evident that at 250 °C, the sample weight reaches stability much quicker than at 150 °C. It is worth noting that since this analysis is carried out in a nitrogen atmosphere, under vacuum, the approach to stability will be much quicker. Figure 3.3-8 shows a snapshot of the IGA system in sample preparation mode.

After sample preparation, the 'dry/clean' sample mass is recorded and the reactor is allowed to cool to room temperature. The application temperature and analysis gas is then selected. Then the isotherm pressure points and the equilibration parameters are entered. Isothermal analysis is started once the system has reached the required temperature.

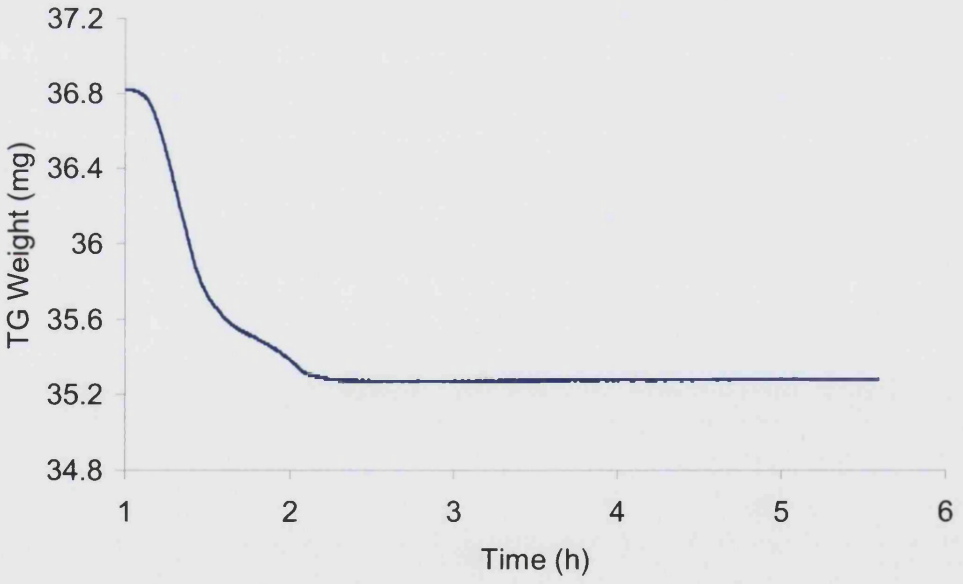

Figure 3.3-4: Graph showing the thermogravimetric profile of Norit CNR 115 with a ramp of 2 °C min^{-1} from 25 °C to 150 °C.

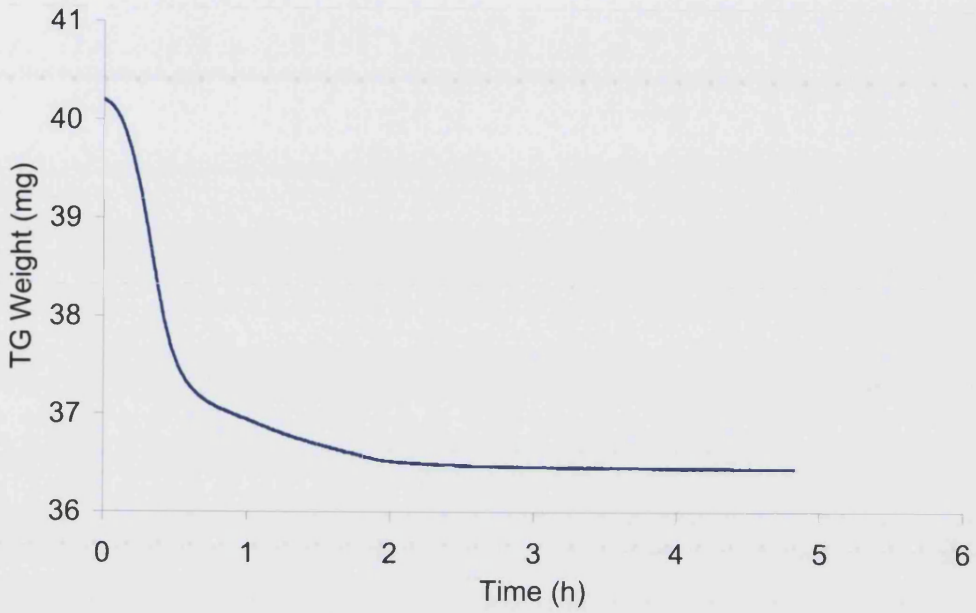

Figure 3.3-5: Graph showing the thermogravimetric profile of Norit CNR 115 with a ramp of 2 °C min^{-1} from 25 °C to 250 °C.

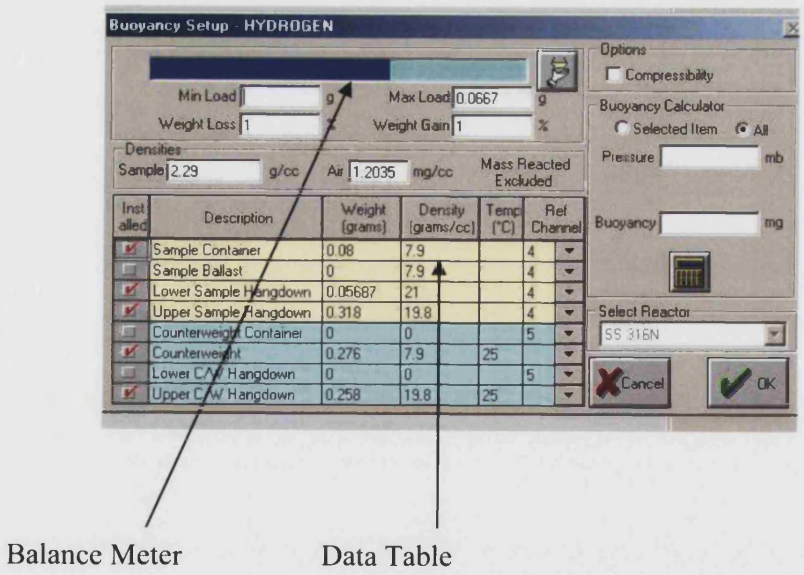

Figure 3.3-6: Snapshot of Buoyancy Table set up for Hydrogen Sorption Analysis

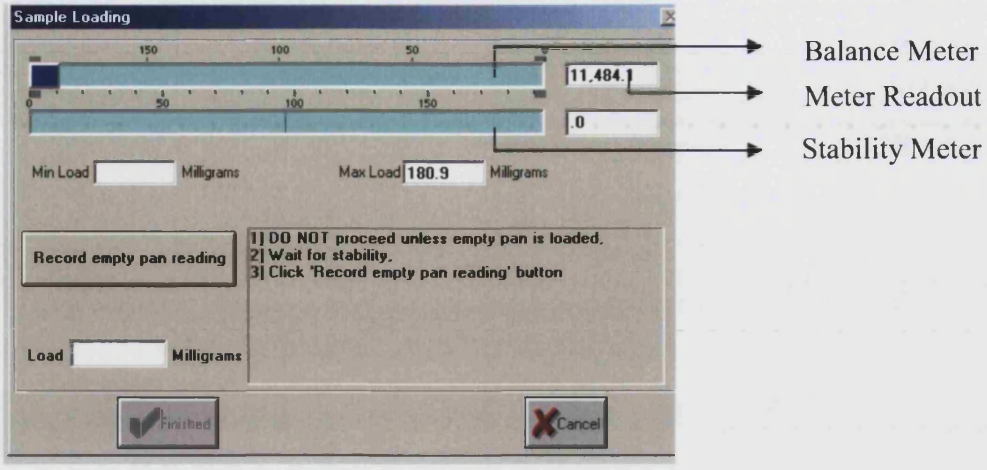

Figure 3.3-7: Snapshot of IGA Electronic Balance and Sample Loading Screen

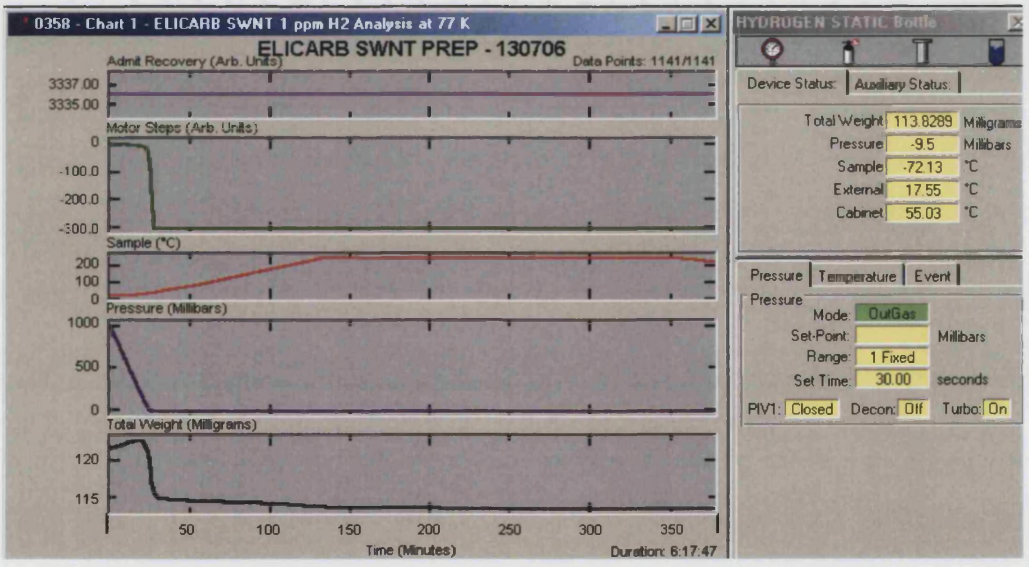

Figure 3.3-8: Sample Snapshot of IGA system in Sample Preparation Mode

3.3.2.3 Computer-Controlled Algorithm

In the determination of adsorption isotherms, the main aim is to measure the equilibrium uptake of the adsorptive (hydrogen) on the adsorbent (carbon) following changes in chemical potential (such as gas pressure). The time-scale of equilibration is quite variable and it varies depending on the pressure, temperature and nature of the sample.

The IGA is incorporated with a real-time processor to continuously analyse the actual time-scale of equilibration during isotherm determination from the measured sorption-time curve. The real-time processor records data for sufficient time following each change in chemical potential so that equilibrium uptake is measured accurately for each isotherm point. The equilibrium uptake cannot be directly measured but can be extrapolated so that the best approximation for its value can be determined (IGA Systems manual, 2003).

The IGA real-time processor uses least-square regression of a diffusion model to extrapolate a value of the asymptote. This method is not only used to actively adjust the total time for which data is collected for each isotherm point, but can also provide kinetic parameters which describe how interaction kinetics vary on different parts of the isotherm. The method requires the software to wait at a set pressure until the change of uptake has reduced below some threshold. The threshold is set based on uptake rather than the rate of uptake. A sensible threshold is to measure the value of uptake until it has settled by a fixed percentage of the asymptotic change. This follows from the simplest mathematical model for equilibration, which is the linear driving force (LDF) model. This equation is discussed in further detail in Section 6.4. The LDF model is applied in the IGA in the form shown in Equation 3.3-1 (IGA Systems manual, 2003) to determine the point at which equilibration is achieved.

$$n(t) = \Delta n(1 - e^{-t/k}) \qquad \textbf{Equation 3.3-1}$$

Where $n(t)$ is the uptake at time t with a time-scale governed by time constant k and Δn is the total change in uptake. The rate at time t is then given by Equation 3.3-2.

$$\frac{\delta n}{\delta t} = \Delta n e^{-t/k}$$ **Equation 3.3-2**

Which is a function of both Δn and k. Trend analysis using least square fitting is used by the IGA software to extrapolate Δn and find the kinetic parameters, k. The uptake is measured until it is stable or has reduced by a fixed percentage of the asymptotic change. The LDF model as used by the IGA software is,

$$n(t) = n_o + \Delta n(1 - e^{-(t - t_0)/k})$$ **Equation 3.3-3**

Where n_0 is the uptake at the time origin t_0, k is the exponential time constant and Δn is the change in uptake and $n_0 + \Delta n$ is the asymptotic uptake.

3.3.2.4 The Minimum and Maximum Data Collection Time

These are timing parameters that set a minimum and maximum for the total data collection time during measurements. They determine the length of time in which the software continues to collect data at a particular pressure point. Therefore, no isothermal point can be completed until the minimum time ('Min Time') has at least elapsed, which has been set to 5 minutes during hydrogen sorption measurements. In the case of the maximum data collection time ('Timeout'), this value has to be determined practically to ensure good use of machine time. The problem if timeout expires is that the isotherm point may not be in equilibrium. This can be pinpointed by looking at the kinetic data for the particular point. This has normally been set to 60 minutes for the isotherms presented in Chapter 5.

3.3.2.5 The Equilibration Criterion

In real-time analysis, a criterion for equilibration is required, which decides when to advance from one isotherm point to another when sufficient data is acquired. Sufficient data are acquired when the uptake has changed by a defined fraction of the difference between the initial reading n_{00} and the predicted asymptote $n_0 + \Delta n$. This

fraction is expressed as a percentage and is set by the IGA parameter labelled 'Wait Until'. This means that any given isotherm point will have a variable total time between the 'Min time' and 'Timeout'. As the value of 'Wait Until' is increased so does the data collection time. The actual data collection time $\Delta t(W)$ for an isotherm point is measured with respect to the original time origin t_0, and is given by Equation 3.3-4.

$$\Delta t(W) = t_0' - t_0 - \left(k \log[(n_0 + \Delta n - n_{00})(1 - W/100)/\Delta n]\right)^{1/x} \qquad \textbf{Equation 3.3-4}$$

where $x = 1$ for the LDF model. The total collection time during data acquisition is then be set by the criterion;

'Min Time' < $\Delta t(W)$ < Δt > 'Timeout'

3.3.2.6 Kinetic Data

As mentioned in Section 3.3, the IGA system software obtains the kinetic data from one equilibrium point on the sorption isotherm to another. This data give a picture of what might be happening during the measurement of isotherms as a result of changes in chemical potential from one pressure increment to another. It invariably shows the transition through which an equilibrium isotherm is generated. A step increase in pressure at constant temperature is accompanied by an uptake of gas and at equilibrium the corresponding mass uptake is recorded, this process continues until all the pressure steps within the specified range are completed as shown in Figure 3.3-9.

Figure 3.3-10 represents actual kinetic data obtained on Norit CNR 115 at 77 K. It is evident that the change in pressure is more of a ramp to the set point rather than a step rise. The temperature curve shows the exotherm associated with adsorption and the equivalent increase in weight due to adsorption is shown by the weight curve. The slight drop in weight noticeable on the initial part of the weight curve can be attributed to the disturbance of the sample pan as a result of the input of gas at a new pressure.

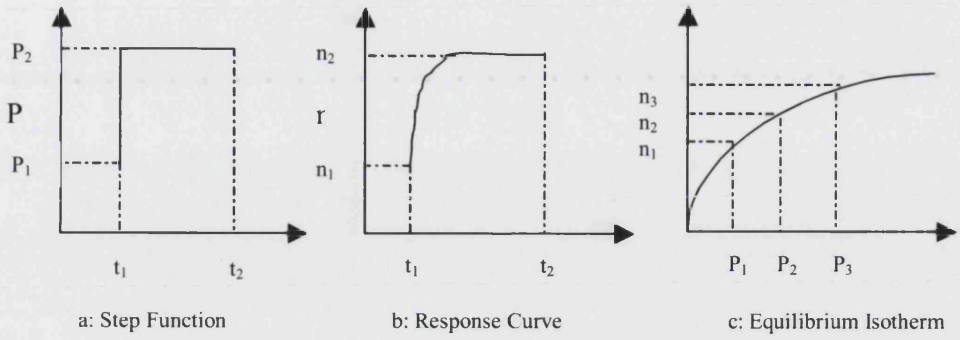

a: Step Function b: Response Curve c: Equilibrium Isotherm

Figure 3.3-9: Process of generating adsorption isotherm data

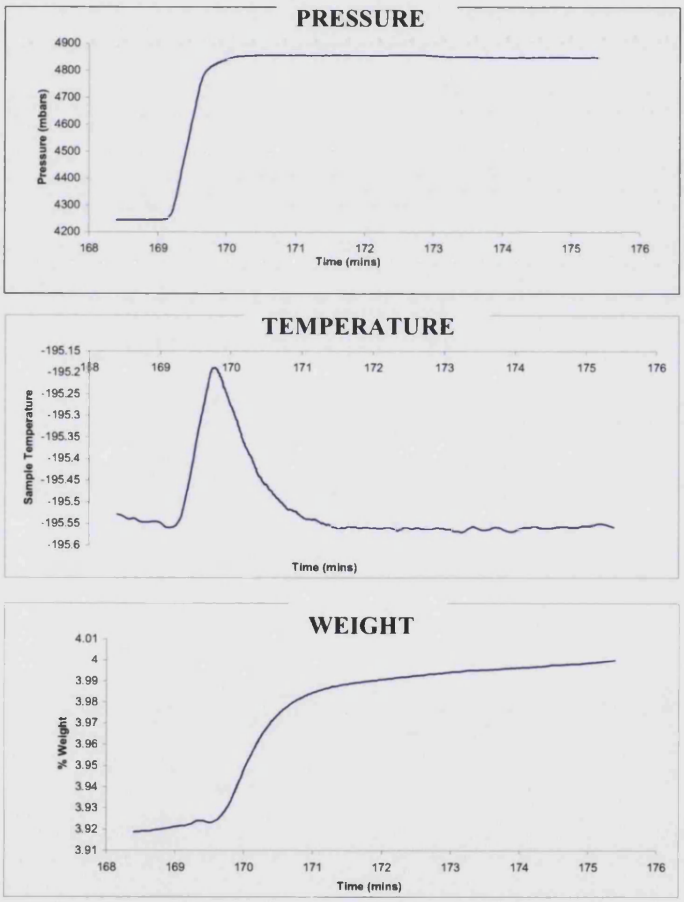

Figure 3.3-10: Example of kinetic data obtained from the IGA System. Pressure in mbar; Temperature in °C and Weight in wt-%.

3.3.3 Experimental Variables

Work has been done to study hydrogen uptake on nanoporous carbon materials. The effect of temperature and hydrogen gas purity on the amount adsorbed by the samples has been investigated. The sample behaviour on cycling has been explored and the degree of sample-to-sample variability also measured. Table 3.3-2 shows the purity specification for the gases used for the hydrogen adsorption isotherms and Table 3.3-3 shows the range of experiments carried out and the results are presented in Chapter 5.

Table 3.3-2: Hydrogen Gas Purity Specification (Supplied by BOC Special Gases, U.K. and Air Products, U.K.)

Grade	Purity (% min)	O_2 ppm	N_2 ppm	[1]THC ppm	CO_2 ppm	H_2O ppm	CO ppm
N 4.5	99.995	Total impurities 50 ppm maximum					
N 5.5	99.9995	1	2	0.5	0.5	1	-
N 6.0	99.9999	0.1	0.2	0.05	0.025	0.5	0.025

[1]Total Hydrocarbon Content

Table 3.3-3: Matrix of Experimental Design for Assessing the Effect of Temperature and Hydrogen Gas Purity on Uptake Results

Sample	Temperature (K)	[1]LG -H_2	[2]HG - H_2	[3]UHP-H_2
BPL	77 - 303	✓	✓	✓
Norit CNR 115	77 - 303	✓	✓	✓
SRD/667/1	77 - 303	✓	✓	✓
SWNT-1	77	✓	-	✓
SWNT-2	77	✓	-	✓
MWNT-1	77	✓	-	✓
MWNT-2	77	✓	-	✓
BLANK RUNS	77, 303	✓	✓	-

[1]N4.5 (99.995% pure H_2); [2]N5.5 (99.9995% pure H_2); [3]N6.0 (99.9999 % pure H_2).

3.3.3.1 Sample Cycling Effects

The effect of reusing the nanoporous carbon materials for storing hydrogen without intermediate regeneration of the materials by heating to high temperatures (250 °C) and exposure to high vacuum was investigated. These were carried out at 77 K within the pressure range of 0 – 20 bar on samples with the highest hydrogen uptake measured prior to this stage.

3.3.3.2 Sample Variability and Repeatability

The extent of sample variability and reproducibility has been explored by carrying out repeat isotherms on 'fresh' samples at different temperatures. A minimum of two experiments were carried out for all samples for the different grades of hydrogen as shown in Table 3.3-3. The results of this analysis are reported in Section 6.3.

3.4 Determination of Skeletal Density

The skeletal density (also known as the true, real, apparent or absolute density) has been obtained for the nanoporous carbons studied. This type of density is obtained when the volume measured excludes the pores as well as the void spaces between particles within the bulk sample, hence removing their volume from the measurement. The density data obtained is essential in buoyancy correction calculations for the original weight data obtained from the IGA. This is discussed further in Section 4.2. The values were obtained using helium pycnometry via an AccuPyc 1330 supplied by Micromeritics, U.S. The technique is described below along with equipment specifications.

3.4.1 Helium Pycnometry

The Micromeritics AccuPyc 1330 is a gas displacement pycnometer. It operates by detecting the pressure change resulting from gas displacement by a solid object. Helium is the displacement gas of choice because it will penetrate readily into very fine pores at room temperature and near ambient pressure. It is assumed that the helium will not adsorb under these conditions, though there is dispute among researchers whether this is a reasonable assumption. The nanoporous carbons are pre-dried in an oven at 120 °C overnight and then left to cool in a dessicator. The sample to be analysed (with an unknown volume) is then weighed on a balance and placed immediately in the sample chamber of the pycnometer for analysis.

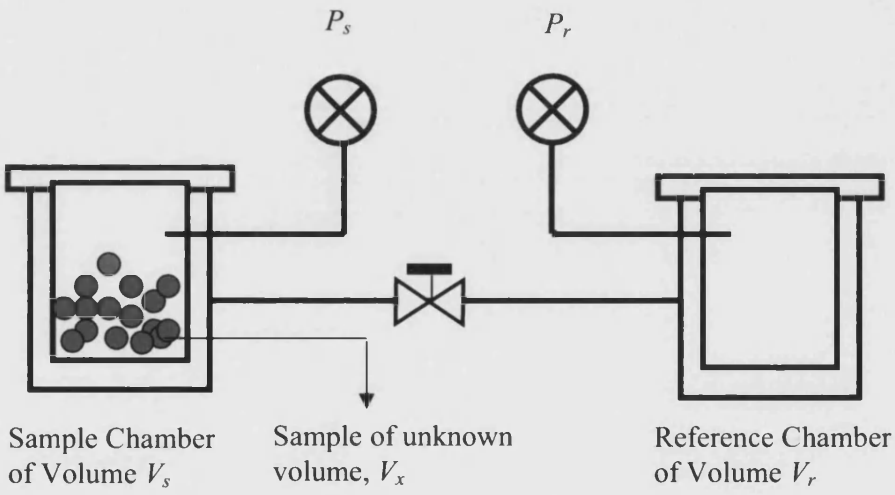

Figure 3.4-1: Schematic showing the operation of a pre-calibrated pycnometer (Adapted from Webb, 2001).

An object of unknown volume, V_x is placed into a sealed sample chamber of known volume, V_s. After sealing, the pressure in the sample chamber is measured, P_s. Then, an isolated reference chamber of known volume V_r is charged to a pressure, P_r, which is greater than that of the sample chamber. A valve isolating the two chambers is opened and the pressure P_{sys} of the system is allowed to equilibrate. The ideal gas law, $PV = nRT$ is applied to determine the unknown volume as follows:

Assume the system is maintained at a constant temperature T and there is no net loss or gain of gas, the number of gas molecules n is constant throughout the experiment. When the valve linking the reference and sample chamber is opened, the pressure in the reference volume falls and the pressure in the sample chamber rises. The larger the volume of the unknown, the higher the final system pressure. This is expressed mathematically as shown in Equation 3.4-4, which is the working equation of the pycnometer. Helium is assumed to behave as ideal gas under the conditions of the experiment (298 K and 1.31 bar) (Micromeritics Accupyc 1330 systems manual, 2000).

Initially,

$$P_s(V_s - V_x) + P_rV_r = nRT \qquad \textbf{Equation 3.4-1}$$

where R is the molar gas constant.

After the valve is opened, the condition changes to

$$P_{sys}(V_s + V_r - V_x) = nRT \qquad \textbf{Equation 3.4-2}$$

Leading to the expression

$$P_s(V_s - V_x) + P_rV_r = P_{sys}(V_s + V_r - V_x) \qquad \textbf{Equation 3.4-3}$$

Solving in terms of the unknown quantity V_x, we have

$$V_x = \frac{(P_{sys}V_s + P_{sys}V_r - P_sV_s - P_rV_r)}{(P_{sys} - P_s)} \qquad \textbf{Equation 3.4-4}$$

3.5 Material Structure Characterisation

3.5.1 Determination of the Ash Content

The measurement of the ash content in the nanoporous carbon materials studied was carried out using a SETARAM TG 92 thermogravimetric analyser. This comprises of a balance, furnace, gas circuit and computer for data output. It measures sample weight change as a function of time and temperature in a flowing gas stream. The system is initially purged for about 1 hour to remove traces of other residual gases. A 170 μl alumina crucible is then cleaned and loaded onto the balance. The balance meter is tared at this point and approximately 50 mg of sample is loaded into the crucible for analysis. At this stage, the temperature programme is then set up with a furnace heating rate of 10 °C min^{-1} from 25 °C to 1000 °C. When the analysis is started, air (20 v % O_2 and 80 v % N_2) is injected into the system at a flow rate of about 25 ml (STP) min^{-1} and the sample weight change is measured till the maximum temperature is reached. The ash content measurements on these nanoporous carbon materials give a quantitative value of the amount of sample that is not made up of carbon, therefore providing an indication of the impurity content of the material. The results of these measurements are shown in Section 4.2.

3.5.2 Surface Area and Pore Size Distribution (PSD)

The surface areas and pore size distributions of the nanoporous carbon materials have been studied using N_2 and CO_2 adsorption isotherms at 77 K and 273 K measured on a Micromeritics Accelerated Surface Area and Porosimetry (ASAP) 2010 analyser (Figure 3.5-1). Such structural information is useful in interpreting hydrogen adsorption data. Although a N_2 adsorption isotherm at 77 K allows the collection of information on the whole range of porosity of the carbon materials, it can be influenced by diffusional limitations in the narrowest micropores (Cazorla-Amoros *et al.*, 1996). CO_2 can be used as an adsorptive to complement N_2 adsorption due to its smaller molecular size of 0.33 nm in comparison to N_2 at 0.36 nm, CO_2 is able to

diffuse into the smaller micropores in these materials. Results published by Cazorla-Amoros *et al.*, 1996, showed that (i) CO_2 adsorption at subatmospheric pressures can be used to determine the volume of narrow microporosity, (ii) it is an adequate technique to complement the characterisation of porosity by N_2 adsorption at 77 K, which is of special relevance for the characterisation of activated carbons with narrow porosity not accessible to N_2 at 77 K, (iii) It is more convenient to use CO_2 adsorption at 273 K than at 298 K because of the higher uncertainty of the density of the adsorbed CO_2 at higher temperature (Cazorla-Amoros *et al.*, 1996; Cazorla-Amoros *et al.*, 1998).

A minimum of 100 mg of sample is weighed and loaded into the glass sample holder sealed with a TranSeal™ stopper of known weight and connected to the sample preparation port of the analyser for preliminary preparation. The sample is degassed at 250 °C for 4 hours till vacuum of 0.04 mbar is reached. The gases evolved from the sample surface are directed to a liquid N_2 cold trap. At this point, the sample is then allowed to cool, unloaded and then reweighed to obtain its dry mass needed for subsequent data analysis. The sample is then transferred to the analysis port where it is dosed with volumes of gas (N_2 or CO_2), the pressure is allowed to stabilise and the uptake of gas is recorded when equilibrium is established. The TranSeal™ for sample tubes allows for the preparation of the sample on the ASAP analyser degas rack followed by sealing under vacuum or pure nitrogen without breaking the seal prior to the beginning of sample analysis. Helium is used to measure the cold and warm freespace in the sample tubes needed for data correction. The matrix showing the nitrogen and carbon dioxide gas adsorption experiments carried out on the ASAP 2010 are summarised in Table 3.5-1, the results of which are presented in Section 4.3.1.

Table 3.5-1: Matrix of Sample Characterisation Experiments on ASAP 2010

Sample	N_2 at 77 K	CO_2 at 273 K
BPL	✓	✓
Norit CNR 115	✓	✓
SRD/667/1	✓	✓
SWNT-1	✓	✓
SWNT-2	✓	✓
MWNT-1	✓	✓
MWNT-2	✓	✓

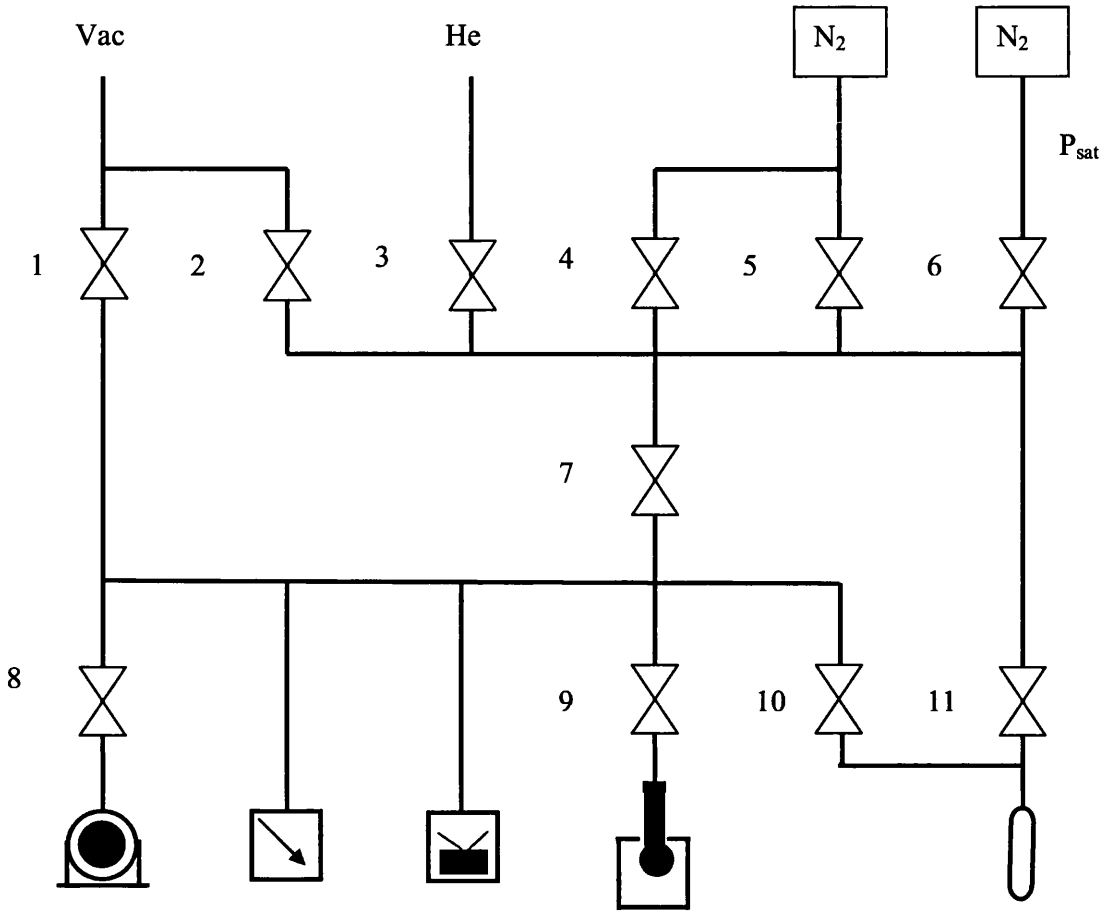

Figure 3.5-1: Schematic of the ASAP 2010 System. (1) Unrestricted vacuum valve; (2) Restricted vacuum valve; (3) Helium inlet valve; (4) Restricted analysis gas inlet valve; (5) Unrestricted analysis gas inlet valve; (6) P_{sat} gas; (7) Lower manifold isolation valve; (8) Calibration chamber valve; (9) Sample port inlet valve; (10) Restricted P_{sat} tube port; (11) Unresticted P_{sat} tube port valve.

3.5.3 Transmission Electron Microscopy (TEM)

A JEOL JEM1200 transmission electron microscope with an operating voltage of 40 to 120 keV was used to study the structure of the carbon nanotubes. It has been applied in this work to reveal the alignment of the carbon nanotubes, surface defects and impurities, which may be present in the materials. The activated carbons were not studied using this technique because there was insufficient time to collect the high number of images required for statistical significance in these disordered materials. This technique was applied because of its higher resolution in comparison with other microscopic techniques. The nanotubes were prepared for analysis by dispersing them in isopropyl alcohol. SWNT-1 was placed in a sonicator for 5 minutes to improve its dispersion in isopropanol. A small quantity of the dispersed mixture was then pipetted and a droplet placed onto a support grid for TEM studies. The TEM images can be observed on a computer screen via a Gatan Dualvision digital camera. The images obtained using this technique are shown in Section 4.6.

3.5.4 X-ray Diffraction (XRD)

X-ray diffraction is an effective technique to study the average structural properties of carbon nanotube or nanoporous carbon samples (Reznik *et al.,* 1995). It provides an indication of the extent of crystallinity of the materials and the extent of their disordering from that of perfect graphite. X-ray diffraction patterns for each nanoporous carbon material have been obtained using a Philips PW1730/00 4 kW x-ray powder diffractometer with a long fine focus copper target x-ray tube operated at 40 kV and 25 mA with a wavelength (λ) of 1.5418 Å. Samples were scanned in a step-scan mode (0.01° / step) over the angular range (2θ) of 5° to 90°. See Figure 3.5-2 for a simplified diagram of an X-ray diffractometer. The analysis yields important information about the structural properties of these materials and the results are presented in Section 4.7.

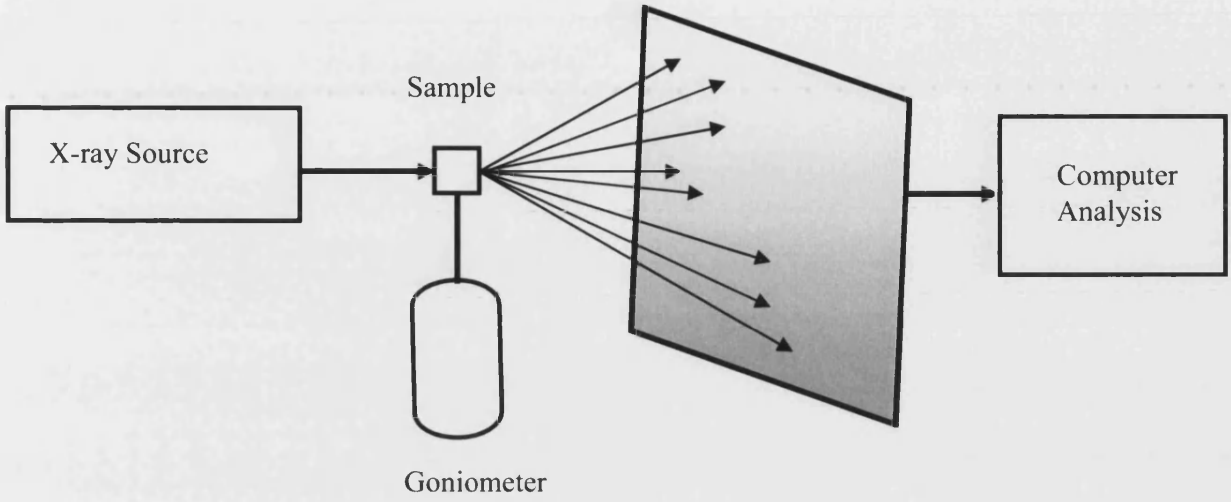

Figure 3.5-2: Simplified Diagram of an X-ray Diffractometer, (Adapted from Bucky Balls, Diamond and Graphite, 2006).

Chapter Four

Sample Characterisation: Results and Analysis

4.1 Introduction

This chapter presents the results of the sample characterisation experiments carried out using methods discussed in Chapter 3. The results are organised into four main sections and illustrated using graphs and tables along with discussions on the assumptions and equations used. In the first section, the results obtained from thermogravimetry and helium pycnometry are outlined to show their relative importance in interpreting hydrogen sorption data for nanoporous carbon materials. Secondly, the results of sample characterisation using gas adsorption techniques and analysis methods are presented with a view to resolving the porosity of the carbon materials. Finally, in the third and fourth sections, transmission electron microscopy (TEM) images of the carbon nanotubes and x-ray diffraction results are presented. An additional discussion of these results is presented in Chapter 5 and 6 to highlight the main findings.

4.2 Thermogravimetry, Skeletal Density and Moisture Content Results

Thermogravimetry, helium pycnometry and the IGA have been used to measure basic properties of the nanoporous carbon materials. The methods are described in Chapter 3. The values of the ash content of these materials obtained from thermogravimetry provide a quantitative description of the amount of non-carbon material present in each sample. The skeletal density provides useful information needed for the buoyancy correction of the gravimetric isotherm data. The values measured here include the ash present in a particular material, which may be denser than the actual carbon. The moisture content on the other hand provides an initial direction for the necessary pre-treatment of the materials prior to isotherm analysis.

A summary of the obtained results is presented in Table 4.2-1 below. It is observed from the data that Norit CNR 115 has the highest ash content (10.02 % db) of the nanoporous carbons, with MWNT-1 having none. A detailed study of the ash composition of all the nanoporous carbon materials in relation to their chemical heterogeneity has not been considered in this work. Lueking and Yang (2002) and (2003) reported that residual metal in nanoporous carbons can play a role in the hydrogen adsorption properties of these materials. This is reported to take place via hydrogen spillover from the metal to the carbon surface thus enhancing hydrogen uptake in some carbons (Lueking and Yang, 2004). According to Argawal *et al.*, (1987), the presence of oxygen functional groups is also important in the physisorption of hydrogen onto activated carbons since it increases the oxidation of an activated carbon leading to increased physisorption. X-ray microanalysis was carried out on only on BPL and Norit CNR 115. This revealed the presence of aluminium (Al), sodium (Na), oxygen (O) in both carbons in addition to the phosphorus (P) present in Norit CNR 115. This provides an insight into understanding the adsorption properties of these materials as subsequently discussed in Chapter 5 and 6.

In terms of the skeletal density of each material, the activated carbons having disordered structures all have values lower than the density of pure crystalline graphite (2.26 g cm^{-3}) as expected, even accounting for the presence of metallic ash. This is also observed with the carbon nanotubes.

Table 4.2-1: Summary of sample structural data

Sample	Ash Content[1], % mass, db	Ash* Composition	Skeletal Density[2], g cm^{-3}	Moisture Content of as received samples[3], % mass
BPL	7.40	Al, Na, O	1.69	6.20
Norit CNR 115	10.02	Al, Na, O, P	1.93	10.10
SRD/667/1	1.69	-	2.08	13.70
SWNT-1	9.78	-	2.22	8.70
SWNT-2	4.23	-	1.96	4.90
MWNT-1	0.00	-	2.01	0.77
MWNT-2	2.43	-	1.99	1.60

[1]Obtained using thermogravimetry and values shown are calculated on dry sample basis (db).

[2]Obtained from Helium pycnometry at room temperature (293 K). [3]Obtained by weighing dried samples under vacuum, *Obtained from sample x-ray microanalysis.

4.3 Structural Characterisation using Gas Adsorption

Characterising the porous texture of carbonaceous materials is relevant in their study since many of their properties are strongly influenced by porosity (Cazorla-Amoros *et al.*, 1998). According to Sing *et al.*, (1985), gas adsorption appears to be the most suitable characterisation method, as it provides information both about the pore size distribution and the surface characteristics of the materials. The adsorption of nitrogen at 77 K is therefore routinely applied for this purpose. It provides information about the whole range of porosity of the materials, although it can be influenced by the diffusional limitations in the narrowest micropores. Hence, carbon dioxide adsorption at 273 K has also been applied, since it has been shown to be a good alternative to complement nitrogen adsorption data. This is because it can be used to determine the volume of narrow microporosity not accessible to nitrogen at 77 K (Cazorla-Amoros *et al.*, 1996, Stoeckli *et al.*, 2001, Guillot and Stoeckli, 2001) although their molecular diameters are quite similar, 0.36 nm and 0.33 nm for nitrogen and carbon dioxide respectively. N_2 and CO_2 gas adsorption experiments have therefore being carried out on the nanoporous carbon materials at 77 K and 273 K respectively.

When gas adsorption isotherms have been measured, suitable calculation methods from the wide range available must be selected for interpreting the data. Each method is subject to limitations as reviewed by several authors (Kruk *et al.*, 1998; Jaroneic *et al.*, 1995). The methods chosen and results of data analysis for this work are discussed in Sections 4.4 and 4.5 below.

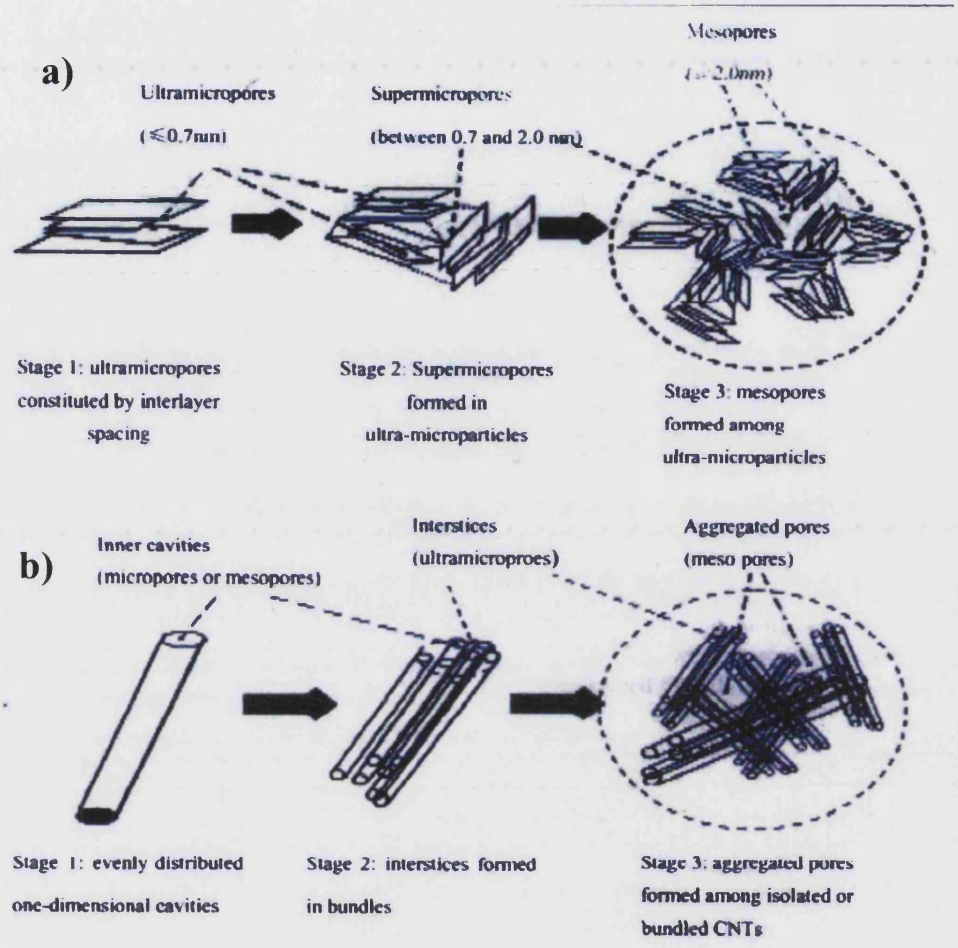

Figure 4.3-1: Pore formation model of (a) Conventional porous carbon (top) and (b) Single walled carbon nanotubes (bottom). Adapted from Liu and Cheng (2005).

4.3.1 Nitrogen and Carbon dioxide Adsorption Measurements

Figure 4.3-2 to Figure 4.3-4 show the sorption curves for nitrogen on the nanoporous carbon materials. The activated carbons BPL, Norit CNR 115 and SRD/667/1 exhibit Type 1 behaviour according to the Brunauer, Deming, Deming and Teller (BDDT) classification of isotherm types (Sing *et al.*, 1985), implying that the materials are microporous. The isotherms of these materials are characterised by a plateau in the amount adsorbed, which is nearly (BPL and Norit) or quite (SRD/667/1) horizontal showing a tail as the saturation pressure is approached. This is said to exist as a result of the complete filling of micropores such that the nitrogen molecules are adsorbed in the adsorption space within the micropores (Gregg and Sing, 1982). The BPL activated carbon isotherm shows a slight upward turn at relative pressures close to 1, representing the filling of larger micropores or the presence of a small amount of mesoporosity in the material.

The N_2 sorption isotherms of SWNTs can be divided into three parts as studied by Yang *et al.*, (2002). This indicates a multistage adsorption process as shown in Figure 4.3-3. In Part 1, the ultra low pressure range, the isotherm exhibits a Type 1 characteristic, which occurs in pores of molecular size indicating the presence of micropores (less than 2 nm in diameter). Part 2 of the isotherm, corresponds to the mid pressure region indicating the onset of multilayer adsorption occurring in the larger pores analogous with the condensation of the gas phase adsorptive (N_2). At higher values of relative pressure (Part 3), there is a hysteresis loop (Type H4) caused by the changed state of the adsorbate where the desorption curve follows a different path to the adsorption curve until the condensate becomes unstable at a critical relative pressure. The Type H4 hysteresis is often associated with narrow slit like pores, as opposed to cylindrical pore structure in carbon nanotubes. The interstitial pores between the in-bundle SWNTs are not detected. This might be due inaccessibility of nitrogen.

In contrast, the nitrogen adsorption isotherms of MWNTs have been divided into four parts (Liu and Chang, 2005) as shown in Figure 4.3-4. In Part 1, the isotherm is of

Type 1 behaviour indicated by the sharp rise in the amount adsorbed at very low relative pressures. This corresponds to the initial filling of the micropores suggesting that there may be micropores present in the open inner cavities of the MWNT with very small diameters. Part 2 of the isotherm shows a slower rise in the amount adsorbed related to the formation of a monolayer. Parts 3 and 4 are characterised by the presence of a hysteresis loop (H4) associated with capillary condensation in the mesopores. All the single and multiwalled nanotubes show Type 4 isotherm behaviour with capillary condensation occurring within relative pressures of 0.5 – 0.9. The instability (following a parallel path to the adsorption branch) of the desorption branch of the isotherms for the SWNTs is observed to continue well into the very low regions of relative pressure. For the MWNTs, the instability subsides at high relative pressures of ~0.85.

It is observed that the single walled nanotubes (SWNT-1 and SWNT-2) have a higher uptake of nitrogen than the multiwalled nanotubes (MWNT-1 and MWNT-2), this might be as a result of better porous structure related to their production route, and purification method. At this stage it is important to assess more closely the structural parameters of these materials that may influence their adsorbent characteristics by using the nitrogen and carbon dioxide adsorption isotherm results. The empirical methods used and the results are presented in Section 4.4 and 4.5.

Figure 4.3-5 shows the CO_2 adsorption isotherms at 273 K for the activated carbons, CO_2 employed as a probe molecule in the activated carbons provides the advantage of access to the microporous pore size range in these materials. The experiments are carried out at subatmospheric pressures with a maximum relative pressure of ~ 0.03. It is observed that SRD/667/1 has the highest uptake of carbon dioxide followed by Norit CNR 115 and then BPL. This is an indication that SRD/667/1 contains a higher amount of very small pores (ultramicropores; pores less than 0.7 nm) compared to BPL and Norit CNR 115. A diagram showing the pore formation model of conventional porous carbon and single walled nanotubes is shown in Figure 4.3-1. According to Liu and Cheng (2005), it shows that in porous carbons, the ultramicropores are constituted by interlayer spacing followed by the supermicropores, which are formed in ultra-microparticles and then mesopores formed among ultra-microparticles. In the case of the single-walled nanotubes, the

micropores or mesopores can be found in the hollow cavities of open nanotubes, the ultramicropores are said to be found in the interstices of the nanotube bundles, while other mesopore can be formed among isolated carbon nanotube bundles (Liu and Cheng, 2005).

In Figure 4.3-6, the subatmospheric CO_2 adsorption isotherms for the carbon nanotubes are shown. It is observed that SWNT-1 and SWNT-2 show higher uptakes of CO_2 than MWNT-1 and MWNT-2. This is not surprising based on their low uptake of N_2 also. Preliminary interpretation of these graphs suggests that SWNT-1 and SWNT-2 have a higher volume of narrow micropores in comparison to the multi-walled nanotubes. The CO_2 adsorption isotherms are further analysed to yield micropore volumes and pore size distributions in Section 4.4 and 4.5.

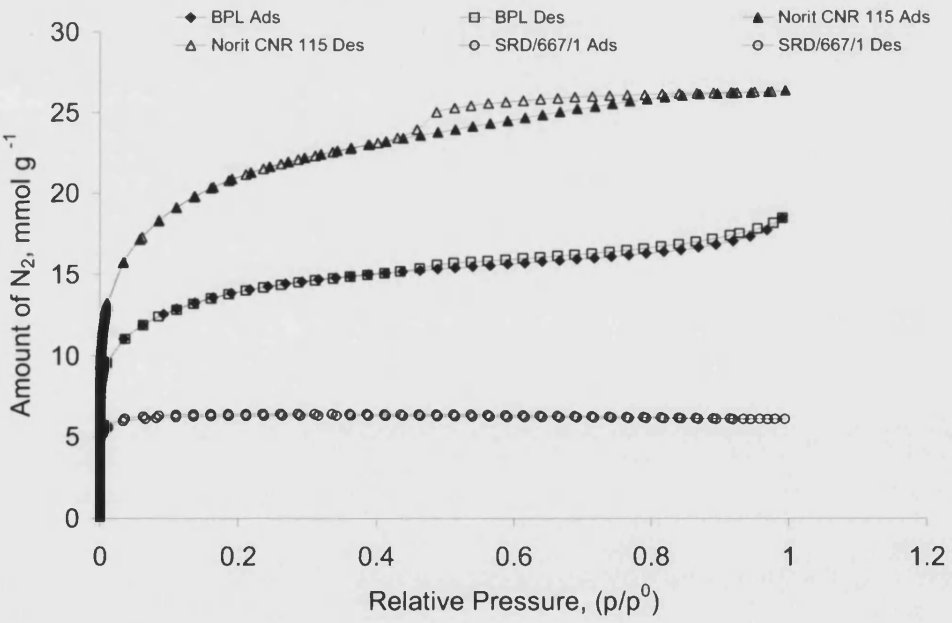

Figure 4.3-2: N_2 sorption isotherms for the activated carbons at 77K.

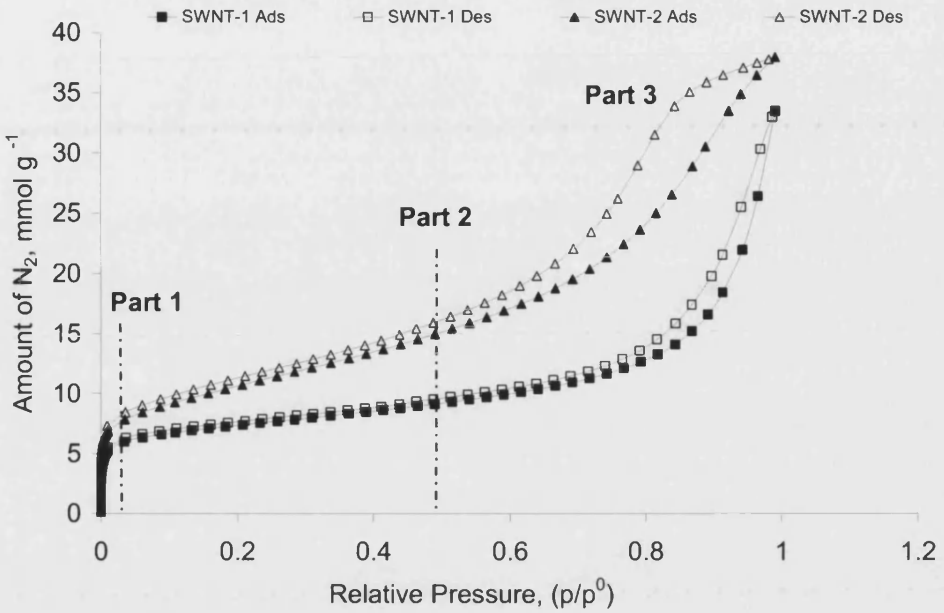

Figure 4.3-3: N_2 sorption isotherms for the single walled carbon nanotubes (SWNT). Part 1: Micropore region; Part 2: Multilayer adsorption in larger pores (meso/macropores) and Part 3: Hysteresis loop region.

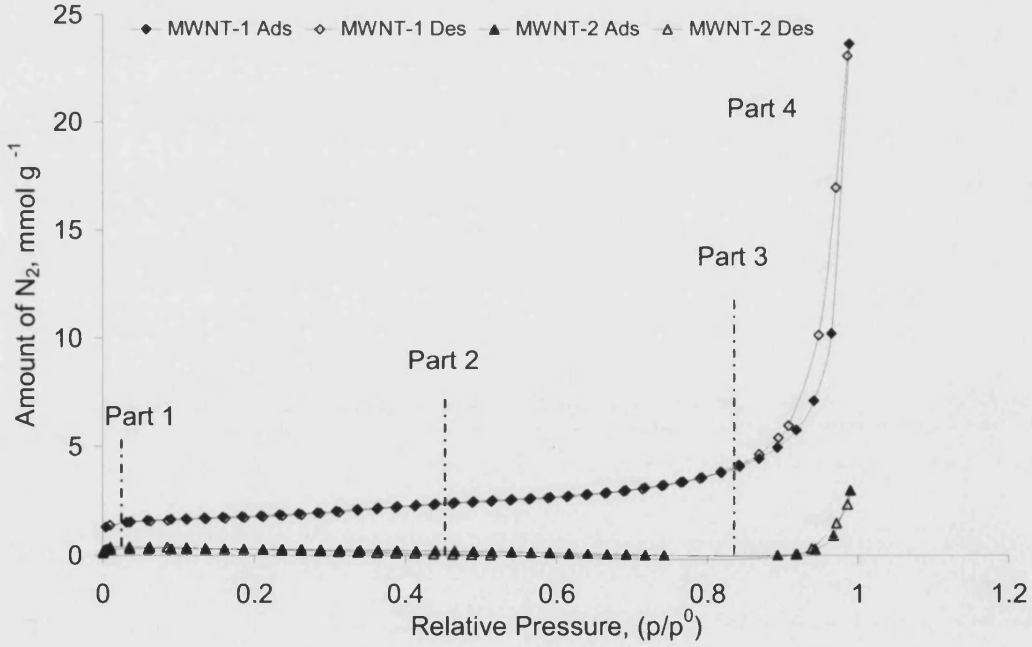

Figure 4.3-4: N_2 sorption isotherms for the multi-walled carbon nanotube (MWNT). Part 1: Micropore region; Part 2: Formation of a complete monolayer; Part 3 and 4: Hysteresis loop and Capillary condensation region.

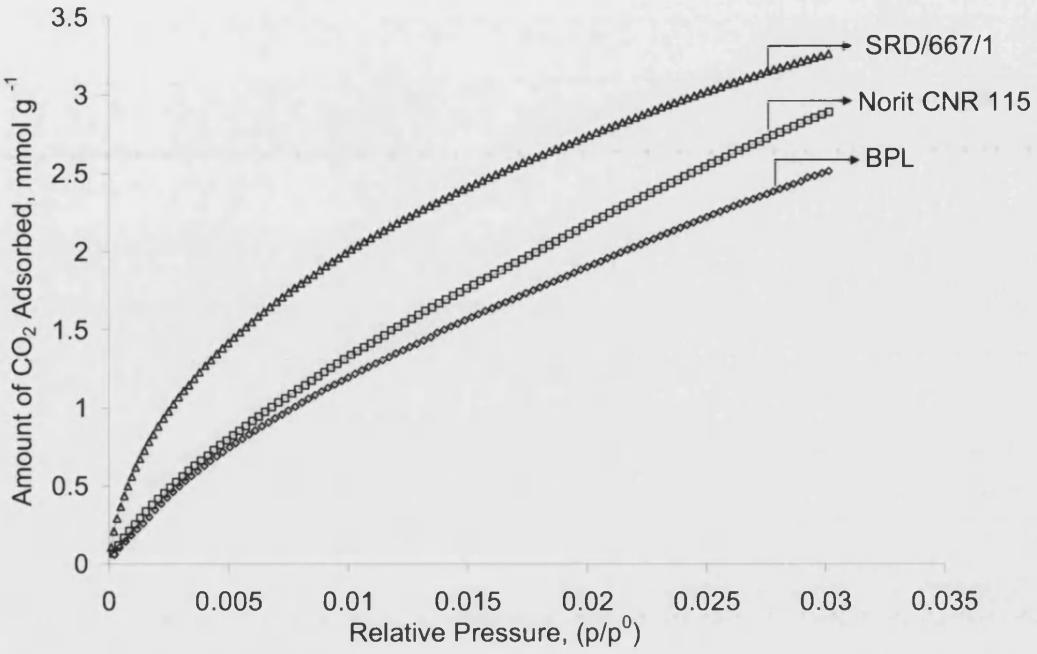

Figure 4.3-5: CO_2 adsorption isotherms for the activated carbons at subatmospheric pressures and 273 K.

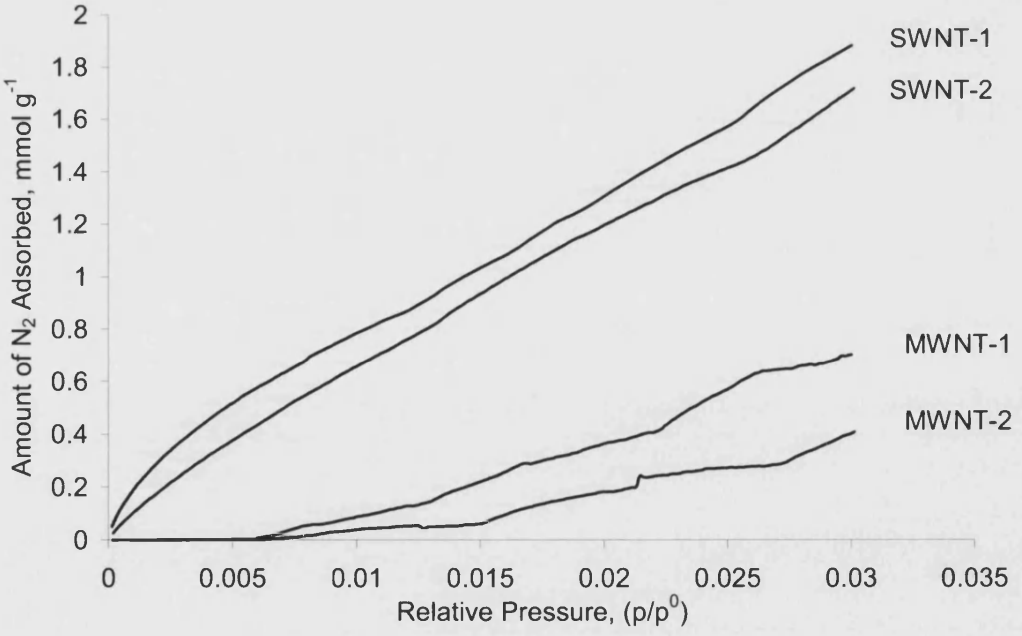

Figure 4.3-6: CO_2 adsorption isotherms for the carbon nanotubes at subatmospheric pressure and 273 K.

4.4 Determination of the Surface Area and Pore Volume

4.4.1 The Brunauer-Emmett-Teller (BET) Method

It is now standard practise to apply the Brunauer-Emmett-Teller (BET) method to determine the surface area of porous materials from physisorption isotherm data. This is in spite of the oversimplification of the model on which the theory is based (Sing *et al.*, 1985). Nitrogen at 77 K is the recommended adsorptive for determining the surface area and pores size distribution, but it is necessary to employ a range of probe molecules to obtain a reliable assessment of the micropore size distribution (Rouquerol *et al.*, 1994). The BET equation is applied in the form shown in Equation 4.4-1 below.

$$\frac{p}{n^a(p^0-p)} = \frac{1}{n_m^a C} + \frac{(C-1)p}{n_m^a C p^0} \qquad \textbf{Equation 4.4-1}$$

Where n^a is the amount adsorbed at the relative pressure p/p^0, n_m^a is the monolayer capacity and C is a constant dependent on the shape of the isotherm. The BET equation requires a linear relationship between $p/n^a(p^0-p)$ and p/p^0 in the BET plot. The range of linearity is restricted to a limited part of the isotherm within the p/p^0 range of 0.05 – 0.30. The second stage in the application of the BET method is the determination of the surface area $A_s(BET)$ from the monolayer capacity. This is calculated using Equation 4.4-2.

$$A_s(BET) = n_m^a . L . a_m \qquad \textbf{Equation 4.4-2}$$

Here, L is the Avogadro constant, a_m is the average area (i.e. molecular cross-sectional area) occupied by each adsorbate molecule in the complete monolayer. It is usually assumed that the BET nitrogen monolayer is close-packed giving $a_m(N_2) = 0.162$ nm^2 at 77 K bearing in mind that it is unlikely that this value is constant over a wide range of adsorbents (Rouquerol *et al.*, 1994; Sing *et al.*, 1985).

Although the BET method provides a means for determining the surface area of a porous solid/adsorbent; it is worth noting that adsorption systems such as with ultramicroporous solids are not amenable to a simple BET analysis. According to Rouquerol *et al.*, (1994), the BET theory has been recognised as being unsound since it is an oversimplified extension of the Langmuir mechanism for multilayer adsorption. To obtain reliable values of n_m^a it is necessary that the BET constant, C is not less than 100, values lower than 20 create doubt on the validity of the BET method (Rouquerol *et al.*, 1994; Sing *et al.*, 1985).

From the results of the BET analysis shown in Table 4.4-1, it is observed that the value of the BET constant, C is negative in all cases implying that the application of the BET equation does not correlate with the geometrical surface area of these nanoporous carbons and can only be considered as the equivalent BET surface area. This is to be expected for samples with an extended range of microporosity as are the materials studied in this work. The BET equation in this case serves only as a means of quantifying the surface areas and comparing these materials. It has been shown by several authors that the BET surface area of many porous adsorbents can be linked to their hydrogen storage capacity (Texier-Mandoki *et al.*, 2004; Nijkamp *et al.*, 2001). Therefore, within this context the surface area results obtained are applied with an understanding of the limitations in its meaning. The activated carbon Norit CNR 115 has been observed to have the highest BET surface area (1624.3 $m^2 g^{-1}$) with MWNT-2 appearing to have the least (16.3 $m^2 g^{-1}$). The surface area of BPL has been measured by several authors (Ehrhurger-Dolle *et al.*, 1999; Sima-Ella *et al.*, 2005) quoting values similar to those reported in this work.

The BET surface area of the carbon materials can be compared to their respective hydrogen uptakes (Zuttel *et al.*, 2004), Norit CNR 115 has an experimentally observed ultra high purity hydrogen storage capacity of 13.74 % while MWNT-2 can only store 0.85 % at 77 K. It is thus meaningful to say that the higher the surface area of a porous adsorbent, the higher its hydrogen storage capacity. This relationship is discussed further in Section 6.5. Figure 4.4-1 shows the BET linear plots for the carbon materials applied within the valid range of linearity of the BET equation.

Table 4.4-1: Summary of BET parameters from N_2 adsorption at 77 K on the nanoporous carbons

Sample	Relative Pressure Range	A_s(BET) N_2, $m^2 g^{-1}$	n_m^a, mmol g^{-1}	C
BPL	0.08-0.19	1069.6	10.97	-135.7
Norit CNR 115	0.11-0.22	1624.3	16.65	-134.0
SRD/667/1	0.08-0.19	468.1	4.80	-93.0
SWNT-1	0.11-0.26	543.5	5.57	-89.0
SWNT-2	0.16-0.30	807.6	8.28	-539.0
MWNT-1	0.11-0.28	133.9	1.37	-81.3
MWNT-2	0.19-0.24	16.3	0.17	-14.6

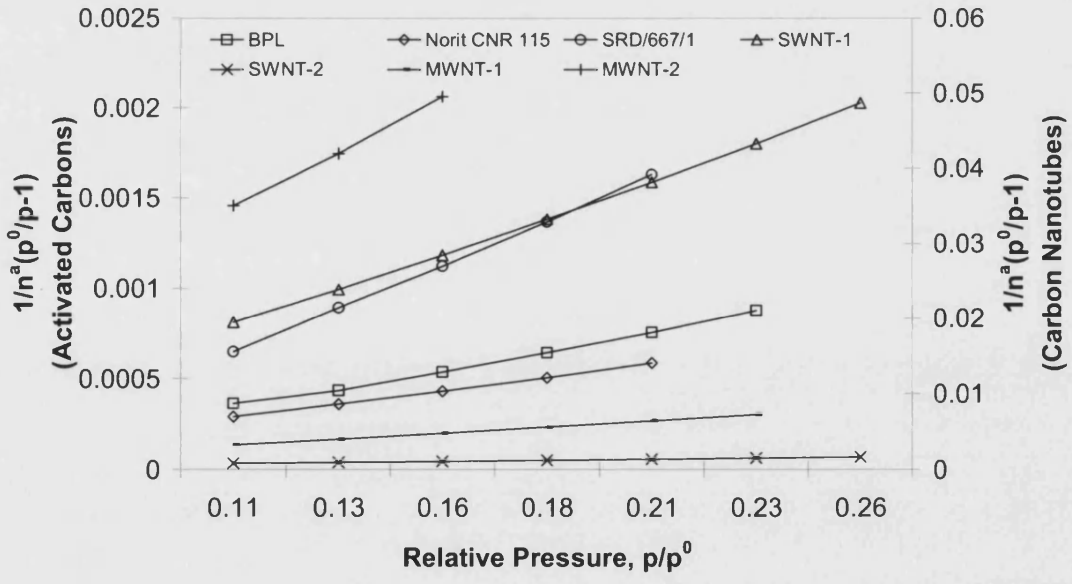

Figure 4.4-1: Brunauer, Emmett, Teller (BET) N_2 plots for the nanoporous carbon materials.

4.4.2 The Dubinin-Radushkevich (DR) Method

In the work of Dubinin, the potential theory of Polanyi was adapted to express the physisorption data for a given microporous adsorbent in the form of a 'characteristic curve' (Schuth *et al.*, (ed.), 2002; Rouquerol *et al.*, 1999). The corresponding DR equation for the characteristic curve, which was proposed in 1947 by Dubinin and Radushkevich (1947), can be expressed as follows

$$V/V_0 = \exp[-(A/\beta E_0)^2] \qquad \textbf{Equation 4.4-3}$$

Where V is the volume of gas adsorbed at p/p^0; V_0 is the volume needed to fill the micropores, A is the adsorption affinity or differential free energy of adsorption, β is a scaling factor and E_0 is the characteristic free energy of adsorption

$$A = RT\ln(p/p^0) \qquad \textbf{Equation 4.4-4}$$

By combining Equation 4.4-3 and 4.4-4, the (DR) equation can be obtained.

$$V/V_0 = \exp[-B(T/\beta)^2 \log_{10}^2(p^0/p)] \qquad \textbf{Equation 4.4-5}$$

Where B is the 'structural constant'.

In its simplest form, the DR equation becomes

$$\log_{10} V = \log V_0 - D\log_{10}^2(p^0/p) \qquad \textbf{Equation 4.4-6}$$

Where D is an empirical constant directly related to the structural constant and characteristic energy. That is,

$$D = B(T/\beta)^2 \qquad \textbf{Equation 4.4-7}$$

β is chosen to be 0.33 for N_2 and 0.35 for CO_2 (Carzola-Amoros *et al.*, 1996). The DR method has been applied for the assessment of the microporosity of the nanoporous carbons, bearing in mind that it is purely empirical.

According to Equation 4.4-6, a DR plot of log V against $\log_{10}^2$ (p^0/p) should be linear with a slope D and intercept log V_0, where V_0 is the micropore capacity. Generally, the DR plot derived from a reversible isotherm on an ultramicroporous (<0.7 nm) carbon has a long linear range of low slope, which corresponds to a high E_0. If the adsorbent is supermicroporous (between 0.7 and 2.0 nm), the linear range of the DR plot is shortened and confined to the initial part of the isotherm (Schuth *et al.*, (ed.), 2002).

Figure 4.4-2 to Figure 4.4-7 show the respective DR plots for the nanoporous carbons for nitrogen and carbon dioxide. The range of linearity of the DR (N_2) plots for the activated carbons extends over a wide range of relative pressure with the DR (CO_2) linearity extending over the entire range of relative pressures as shown in Table 4.4-2. The persistence of linearity at relative pressure 0.99 for SRD/667/1 is observed. This might be due to a highly microporous structure present in this sample in comparison to BPL and Norit CNR 115. There are slight deviations from linearity observed in BPL and Norit CNR 115 at high relative pressures (Figure 4.4-2), which are concave to the x-axis. This corresponds to the filling of the few larger pores (mesopores) present.

Figure 4.4-3 and Figure 4.4-4 show the DR (N_2) plots for the single and multiwalled carbon nanotubes respectively. These materials exhibit a much shorter range of linearity than the activated carbons and deviate quicker from linearity characterised by the concave plots to the x-axis. This is as expected because the range of microporosity of these materials is smaller than the activated carbons and this deviation is analogous to the filling of the larger mesopores present in the sample.

In Figure 4.4-5 to Figure 4.4-7, the DR (CO_2) plots of the carbon materials are presented. As expected, the linear range of these plots for the activated carbons is over

the entire measured range (Table 4.4-2) because the CO_2 measurements are carried out at low relative pressures to help reveal the narrow microporosity of the materials otherwise not accessible to N_2 (Cazorla-Amoros *et al.*, 1996, Stoeckli *et al.*, 2001, Guillot and Stoeckli, 2001). The carbon nanotubes on the other hand deviate from linearity but to a lesser extent than obtained with N_2.

A summary of the DR parameters, microporous pore volume (V_p) and characteristic energy E_0, calculated for each material is shown in Table 4.4-2. The linear regression of the linear region of the plots were converted into the micropore volume by assuming the pores are filled with liquid adsorptive 0.808 g cm^{-3} for N_2, while the characteristic energy was calculated using the slope. The multi-walled nanotubes appear to have the lowest pore volumes while the high BET surface area activated carbons have the highest values. The observed DR (CO_2) values are smaller than the DR(N_2), for all the samples with the exception of SRD/667/1 showing similar values for both adsorptives. The difference in pore volumes observed for the different probe molecules is not surprising as both molecules at the temperature applied define different portions of the characteristic curve. Similar results have been observed by Rodriguez-Reinoso (1989) and reported by Gregg and Sing, (1982).

Also noticeable from Table 4.4-2 is the different values obtained for the respective characteristic energies (E_0) of the samples. The values for N_2 appear to be within the same order of magnitude with the exception of SRD/667/1, which has a characteristic energy of 23.73 kJ mol^{-1} as a result of its range of microporosity observed from the N_2 sorption isotherms. In the case of the characteristic energies obtained for CO_2, the values are also within the same order of magnitude but comparatively larger than the values observed for N_2. Bearing in mind that the characteristic energy is dependent on the adsorbate used (Do and Do, 1995), the disparity in the magnitude of these values can be linked to the enhanced interaction of CO_2 with itself and the walls of the each adsorbent since it is applied here in the subcritical pressure range to probe the narrow microporosity of the nanoporous carbons. N_2 on the other hand probes the entire porosity of the materials with limitations in the microporous range hence it implies that there is a lower interaction between N_2 molecules and the walls of the adsorbent in the pores of wider dimensions (mesopores).

To further verify the results observed using the DR equation, the application of another approach to characterise the nitrogen adsorption isotherms may be required using the α_s method described in Section 4.4.3.

Table 4.4-2: Summary of DR parameters obtained from N_2 (77 K) and CO_2 (273 K) isotherms

Sample	N_2 77 K			CO_2 273 K		
	Range of Linearity, p/p^0	DR , V_p $cm^3\ g^{-1}$	E_0, kJ mol^{-1}	Range of Linearity, p/p^0	DR, V_p $cm^3\ g^{-1}$	E_0, kJ mol^{-1}
BPL	$1.4 \times 10^{-6} - 0.09$	0.46	15.65	$2.26 \times 10^{-4} - 0.03$	0.22	22.15
Norit CNR 115	$3.7 \times 10^{-6} - 0.03$	0.62	14.30	$1.90 \times 10^{-4} - 0.03$	0.25	22.32
SRD/667/1	$7.2 \times 10^{-6} - 0.99$	0.22	23.73	$8.40 \times 10^{-5} - 0.03$	0.23	26.80
SWNT-1	$5.4 \times 10^{-8} - 2.4 \times 10^{-4}$	0.17	17.42	$1.44 \times 10^{-4} - 0.0039$	0.10	27.26
SWNT-2	$8.8 \times 10^{-7} - 6.9 \times 10^{-5}$	0.22	14.92	$5.32 \times 10^{-4} - 0.0124$	0.12	21.92
MWNT-1	$3.10 \times 10^{-2} - 0.134$	0.06	13.98	$2.30 \times 10^{-2} - 0.027$	0.05	14.67
MWNT-2	$1.10 \times 10^{-3} - 0.010$	0.01	15.28	$9.38 \times 10^{-3} - 0.019$	0.61	11.84

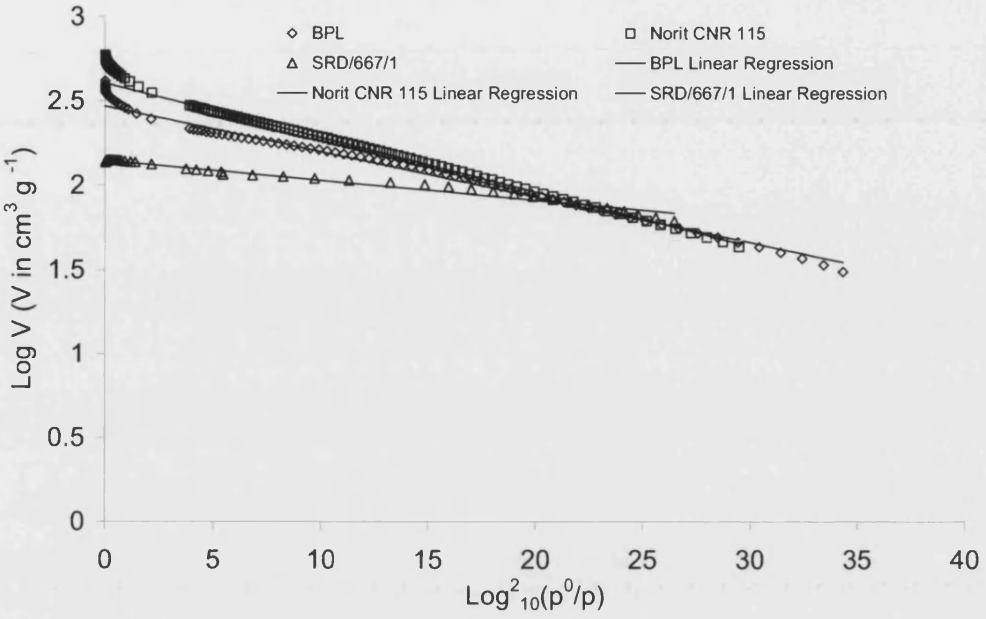

Figure 4.4-2: DR (N_2) plots for the activated carbons

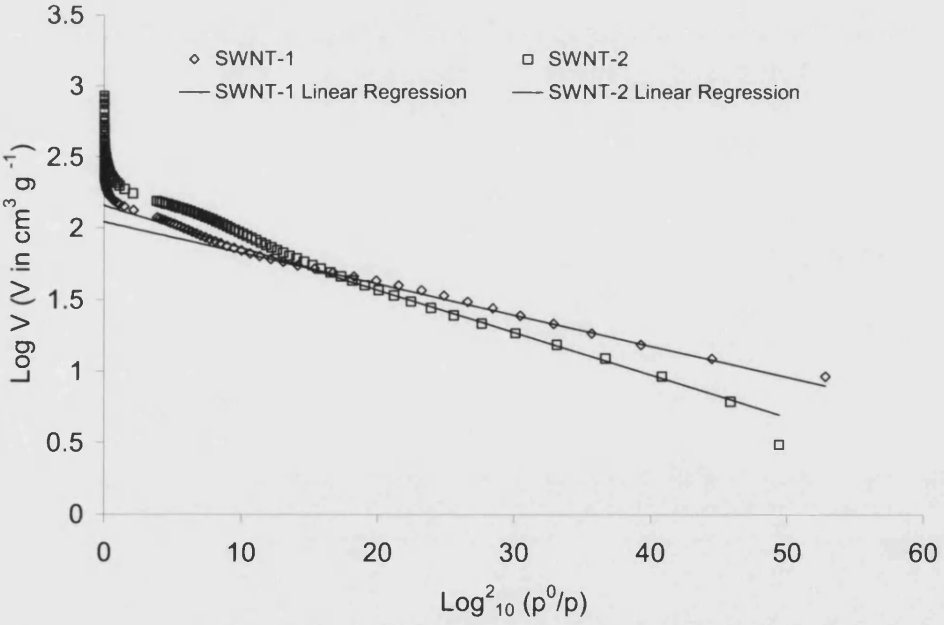

Figure 4.4-3: DR (N_2) plots for SWNT-1 and SWNT-2

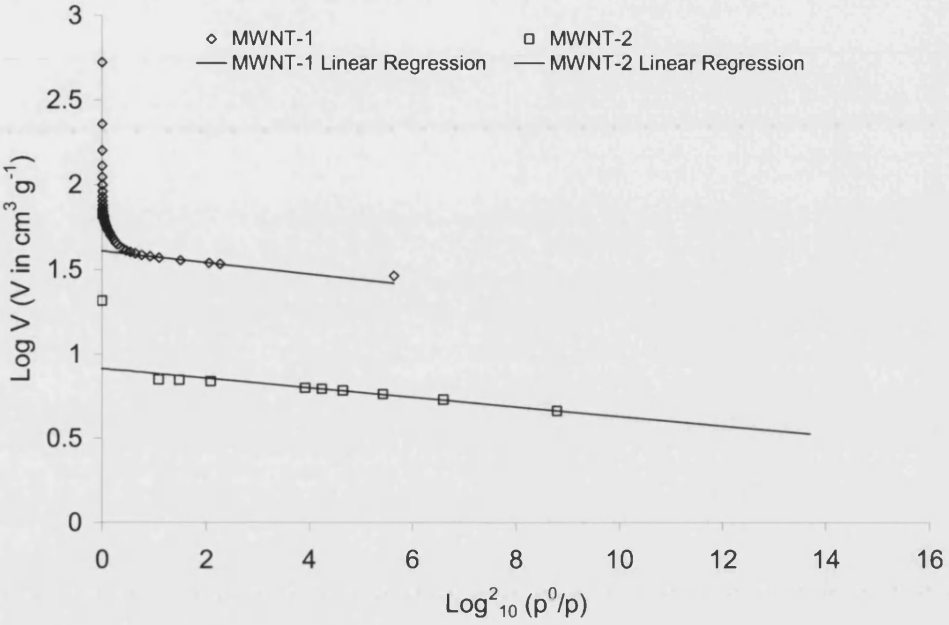

Figure 4.4-4: DR (N_2) plots for MWNT-1 and MWNT-2

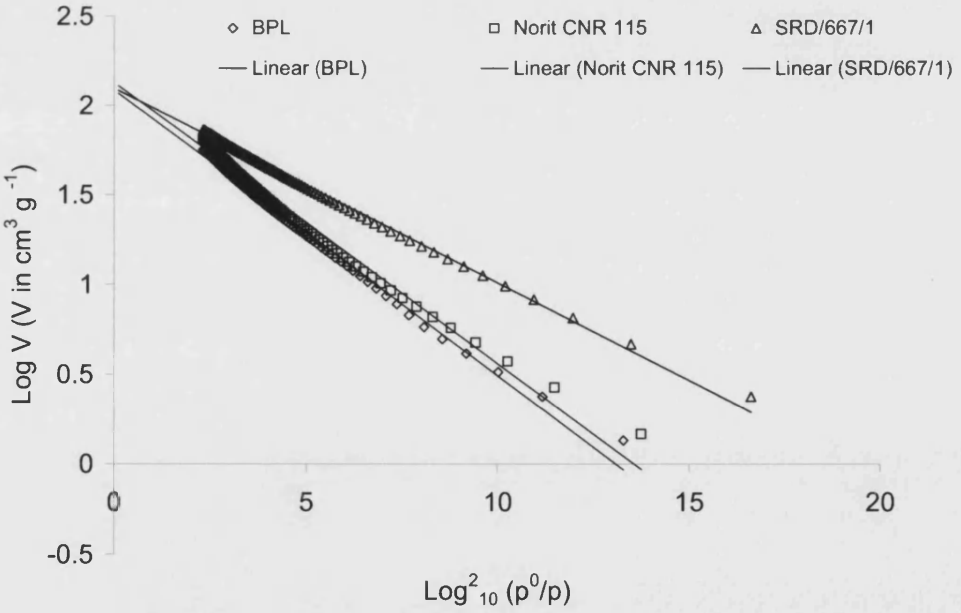

Figure 4.4-5: DR (CO_2) plots for activated carbons

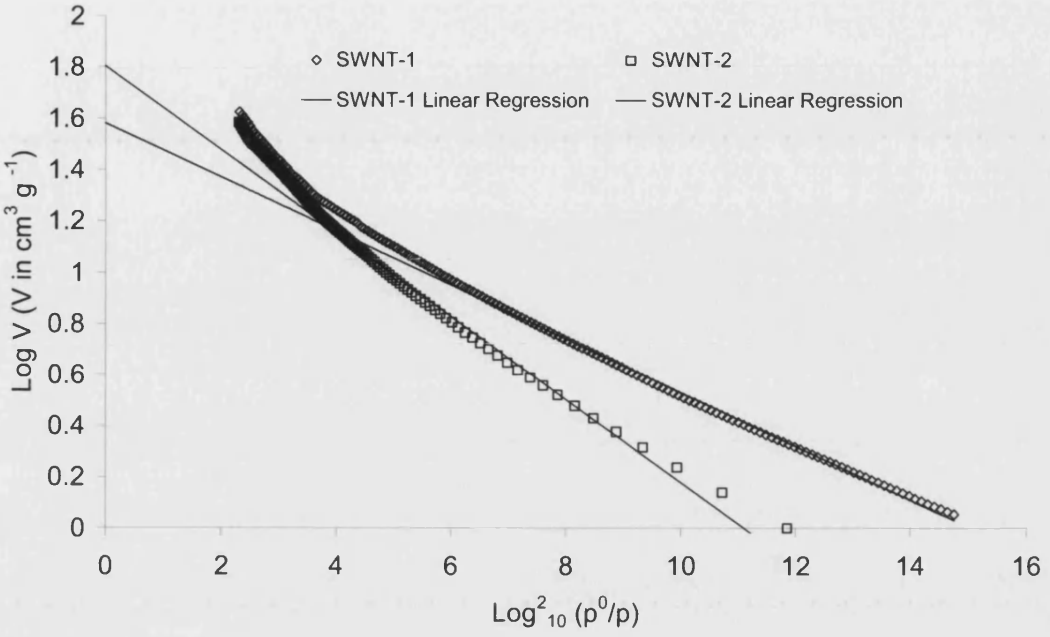

Figure 4.4-6: DR (CO_2) plots for SWNT-1 and SWNT-2

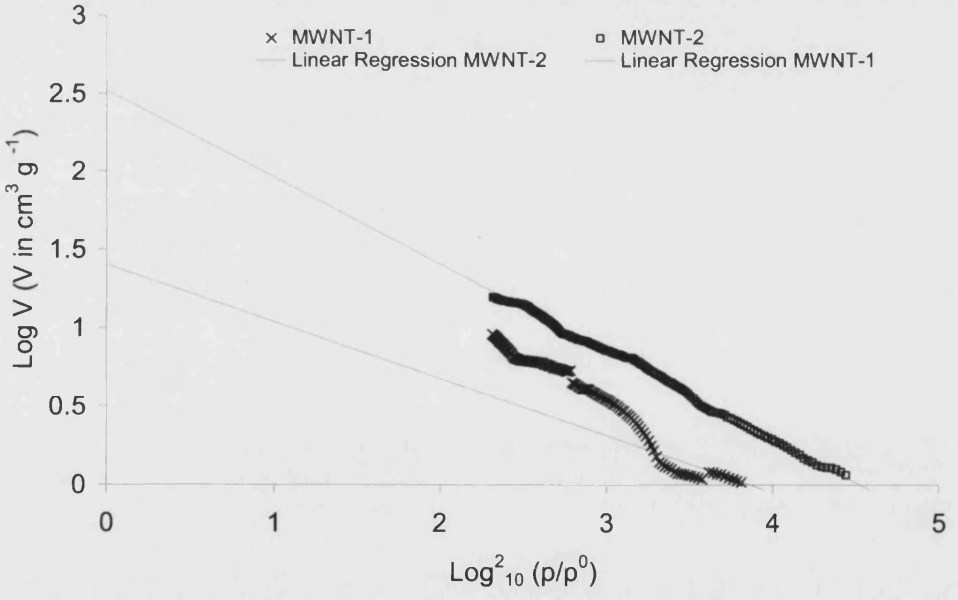

Figure 4.4-7: DR (CO_2) plots for the MWNTs

4.4.3 The α_s Method

The α_s method is another empirical procedure for the determination of useful information about the internal and external surface areas and micropore volumes (Rodriguez-Reinoso *et al.*, 1986; Schuth *et al.*, (ed.), 2002; Rodriguez-Reinoso, 1989; Sing and Williams, 2005) of nanoporous carbon materials. The application of this method requires the comparison of the shape of a given isotherm on a porous solid with that of a standard isotherm on a nonporous solid, with preferably similar surface structure to the material under investigation. This allows the micropore volume and the non-microporous surface area to be estimated (Rodriguez-Reinoso *et al.*, 1986).

In the past, it has been suggested that the reference isotherm chosen should have a similar BET constant, C to the material to be tested. IUPAC since recommended that the standard isotherm should be obtained for the particular adsorption system. Hence, for the purpose of this study, the reference material chosen was an activated carbon prepared by the carbonisation of olive stones at 1123 K in N_2 and activated using CO_2 at 1073 K. To make this material nonporous it was heat treated to 2073 K to close the open micropores (Rodriguez-Reinoso *et al.*, 1986). The reported reduced isotherms and α values (Rodriguez-Reinoso *et al.*, 1986) were used to construct α_s plots for the nanoporous carbons.

The comparative α_s method has been used to calculate the external surface area (S_{ext}) from the slope of the linear segment of the comparative plot in the high relative pressure regions and the micropore volume ($V_{\alpha s}$) from the Y-intercept of the comparative plot linear regression line as shown in Figure 4.4-8 and Figure 4.4-9. Comparing the results obtained from the DR method (Table 4.4-2) with the α_s method (Table 4.4-3), there is a good agreement in the micropore volumes $V_{\alpha s}$ obtained, with the exception of SWNT-2 where a value of the micropore volume could not be deduced (zero intercept) due to the linearity of the comparison plot. This is a result of the very similar shape of the nitrogen adsorption isotherms from the reference material and SWNT-2 isotherm.

Figure 4.4-8 and Figure 4.4-9 show the standard adsorption, α_s (N_2) plots for the activated carbons and carbon nanotubes. The initial linear part of the plots observed for the activated carbons, which can be back extrapolated to the origin reveals that undistorted monolayer adsorption is the first stage of physisorption. The pronounced downward deviation observed at relatively low p/p^0 for these materials indicates the filling of some wide micropores (supermicropores). It should be noted that for the activated carbon SRD/667/1, the initial portion of its α_s (N_2) plot could be back extrapolated to origin if more values of volume adsorbed at lower p/p^0 are available. The shortened linear region of the plots for SRD/667/1 and the carbon nanotubes could also be as a result of the distortion of the isotherm due to ultramicopore filling at very low p/p^0. On inspection of the α_s (N_2) plots for the nanotubes, there is a distortion of the plots from linearity at very high relative pressures that is concave to the x-axis. It has been reported by Schuth *et al.*, (ed.), (2002) and Sing and Williams (2005) that this is analogous to adsorbents exhibiting Type 4 isotherms. This coincides with the findings in this study.

For all materials, the upper long linear part of the plots correspond to multilayer adsorption on the external surface. It would be expected that the ultramicroporous adsorbents, SRD/667/1, SWNT-1, SWNT-2, MWNT-1 and MWNT-2 would have low external surface areas (Schuth *et al.*, (ed.), 2002), whereas the supermicroporous materials would have appreciable external areas. From the results obtained (Table 4.4-3) low external surface areas are obtained for BPL, SRD/667/1 and MWNT-2 with much higher values obtained for the other materials. An interesting analysis at this point would have been to carry out standard α_s plots using the carbon dioxide isotherms. This is not possible due to the lack of standard data for this probe molecule on a suitable nonporous adsorbent.

Table 4.4-3: Summary of α_s results for the nanoporous carbons

Sample	N_2 (77 K)	
	$V_{\alpha s}$, $cm^3\ g^{-1}$	S_{ext}, $m^2\ g^{-1}$
BPL	0.46	39.55
Norit CNR 115	0.63	110.62
SRD/667/1	0.20	13.75
SWNT-1	0.10	127.58
SWNT-2	-	311.16
MWNT-1	0.02	39.74
MWNT-2	0.01	1.73

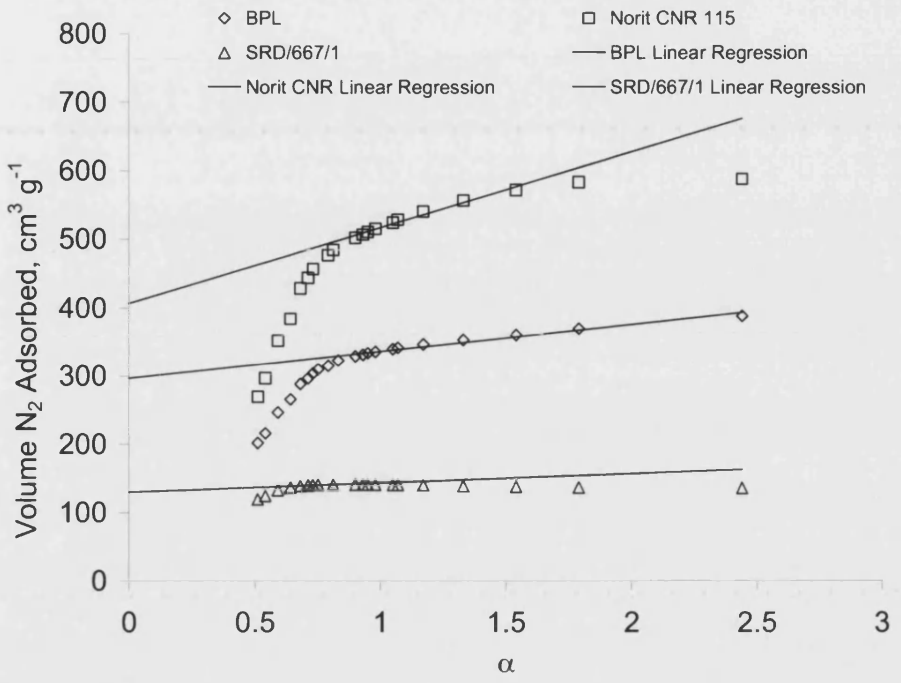

Figure 4.4-8: Standard adsorption α_s (N_2) plots for the activated carbons.

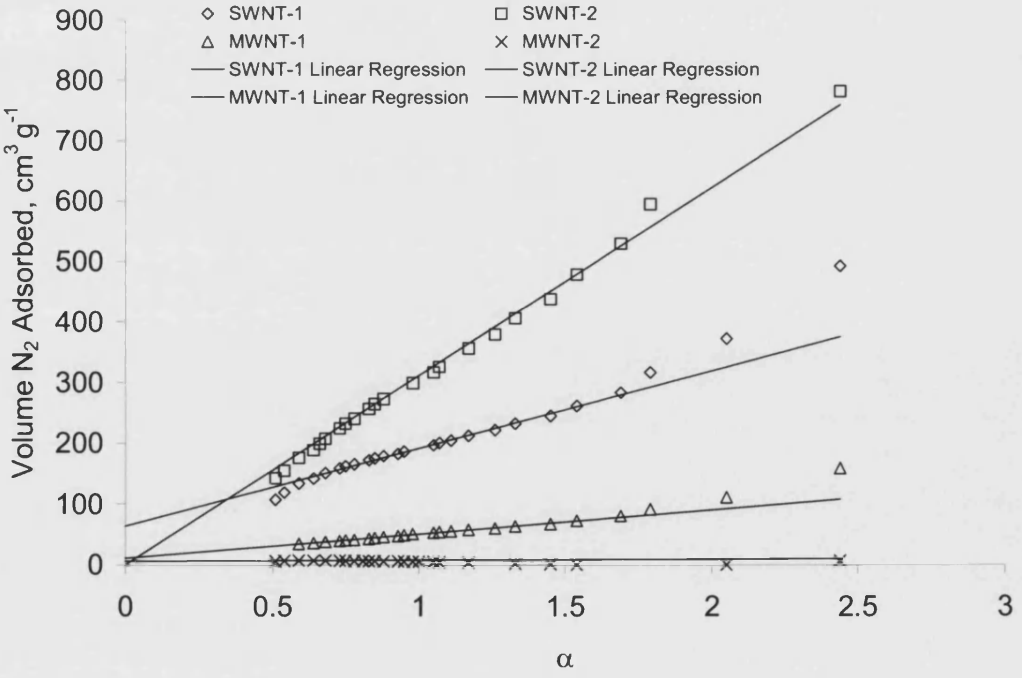

Figure 4.4-9: Standard adsorption α_s (N_2) plots for the carbon nanotubes.

4.5 Sample Pore Size Distribution

4.5.1 N_2 and CO_2 Pores Size Distribution (PSD) Results for the activated carbons using Density Functional Theory (DFT)

In order to correlate and therefore understand the mechanism of gas adsorption and the properties of the nanoporous carbon materials, it is important to establish their pore size distribution. The IUPAC classification of pore sizes is shown in Table 2.3-2. Performing calculations based on computational, statistical and empirical models, such as the Dubinin-Astakhov (Dubinin, 1989), Horvath-Kawazoe (Horvath and Kawazoe, 1983), Kelvin equation (reviewed by Schuth *et al.*, (ed.), 2002, Choma *et al.*, 2001), and more recently Grand Canonical Monte Carlo (GCMC) simulations (Do and Do, 2003) and DFT (Olivier, 1995) can be used to obtain the PSD. Methods based on empirical models are subject to limitations as reviewed by several authors (Kruk *et al.*, 1998; Gregg and Sing, 1985; Valladares *et al.*, 1998) while the GCMC requires a great deal of computation time.

Density functional theory (DFT), a method developed by Olivier (1995) has been chosen as the method of use because it is quite effective in the study of micropore filling in regular micropores (Tanaka *et al.*, 2001) and it has an improved capability of predicting the range of pore sizes present in nanoporous materials. This method has become popular and is incorporated into the computational software (DFT Plus) supplied with the ASAP 2010. It is based on the idea that the free energy of an inhomogeneous fluid can be expressed as a functional of its average density making it suited to the study of physical adsorption, where the density of the adsorptive species is said to be capable of changing by orders of magnitude over small distances near the surface of the adsorbent (Olivier, 1995). Obtaining PSD via this method requires solving the integral

$$V(P) = \int_{H_{min}}^{H_{max}} F(H)v(H,P)dH \qquad \textbf{Equation 4.5-1}$$

where *V(P)* is the experimentally determined excess volume of gas adsorbed at STP/g of material, *F(H)* is the required PSD and *v (H, P)* is the excess volume of gas at pressure in a pore of size *H*. The integral is solved over all pore sizes, *H*. Solutions are then required for the 'kernel' functions *v (H, P)*. In order to find a solution, a model of the pore structure geometry is required. The microstructure of the activated carbon materials studied were assumed to be a polydisperse assembly of infinite slit pores with walls formed by seminfinite graphite layers (Scaife *et al.*, 2000; Do and Do, 2003).

It is a desired property of a carbon material to have a large volume of pores in the microporous range for the enhancement of its hydrogen adsorption capacity. This is because McEnaney *et al.*, (1987) state that the adsorption energy decreases rapidly with increases in the pore size of a microporous carbon (McEnaney *et al.*, 1987). Figure 4.5-1 to Figure 4.5-4 show the PSD obtained for the activated carbon materials using N_2 and CO_2 as probe molecules. The PSD (N_2) for Norit CNR 115 appears to peak at 1.18 nm in the supermicroporous range while the PSD (N_2) for BPL and SRD/667/1 peak at 0.54 and 0.59 nm respectively in the ultramicroporous range. This value supports earlier statements on the ultramicroporosity of SRD/667/1 from the α_s results. It is observed from Figure 4.5-1 that the PSD (N_2) for these materials lie mostly in the supermicroporous region for Norit CNR 115 and in the ultramicroporous region for BPL and SRD/667/1.

Figure 4.5-2 to Figure 4.5-4 show the PSD (CO_2) for the activated carbon materials. It is evident from the plots that carbon dioxide is able to reveal or probe the microporosity of the carbon materials to a greater extent than nitrogen. The distribution of pores in the ultramicroporous range of each material can therefore be determined. The ultramicroporosity of BPL peaks at 0.58 nm, while for Norit CNR 115 and SRD/667/1 peaks at 0.84 and 0.87 nm respectively in the supermicroporous range are observed. The distribution of pores obtained with carbon dioxide are in the

range of values less than 1 nm compared to that observed for nitrogen providing supporting evidence that the use of carbon dioxide as an alternative probe molecule to nitrogen is beneficial in the assessment of the entire range of the PSD of carbon materials.

According to Bhatia and Myers (2006), the optimum pore size for a carbon adsorbent wide enough to accommodate exactly two layers of hydrogen (one layer near each wall of the graphene sheets) is 0.92 nm (Bhatia and Myers, 2006). This value is close to that obtained for the Norit CNR 115 and SRD/667/1 as previously mentioned.

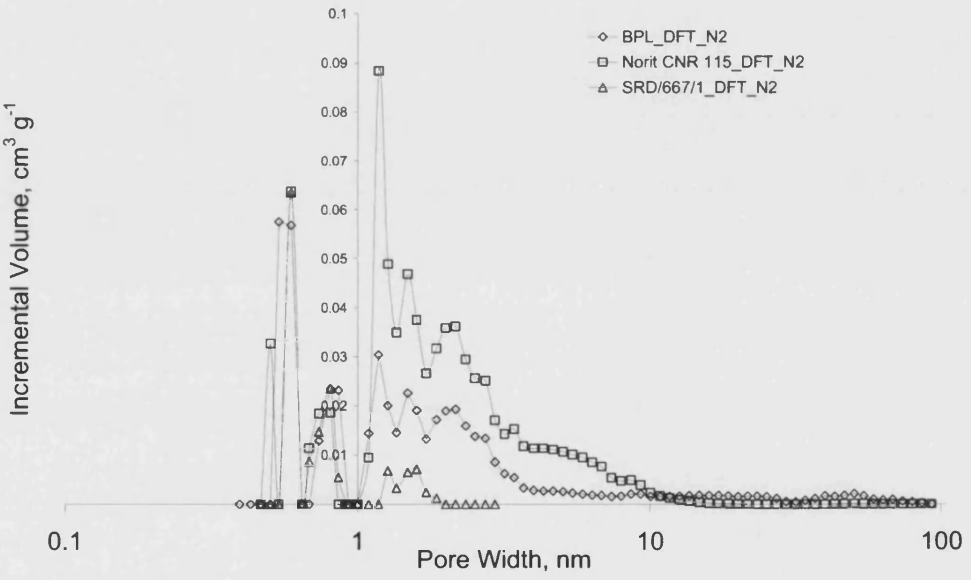

Figure 4.5-1: Nitrogen pore size distribution for the activated carbons using Density functional theory.

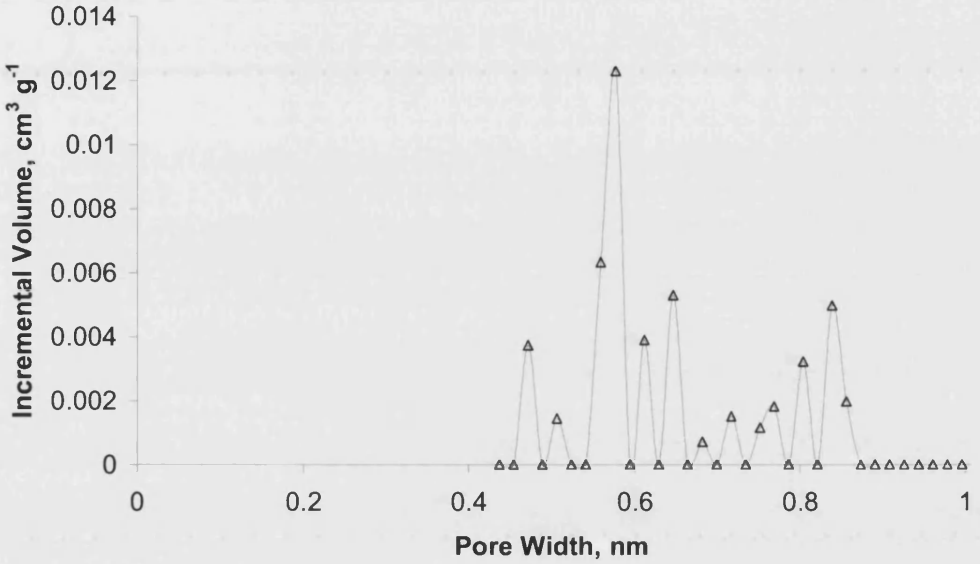

Figure 4.5-2: Carbon dioxide pore size distribution for BPL activated carbon using density functional theory.

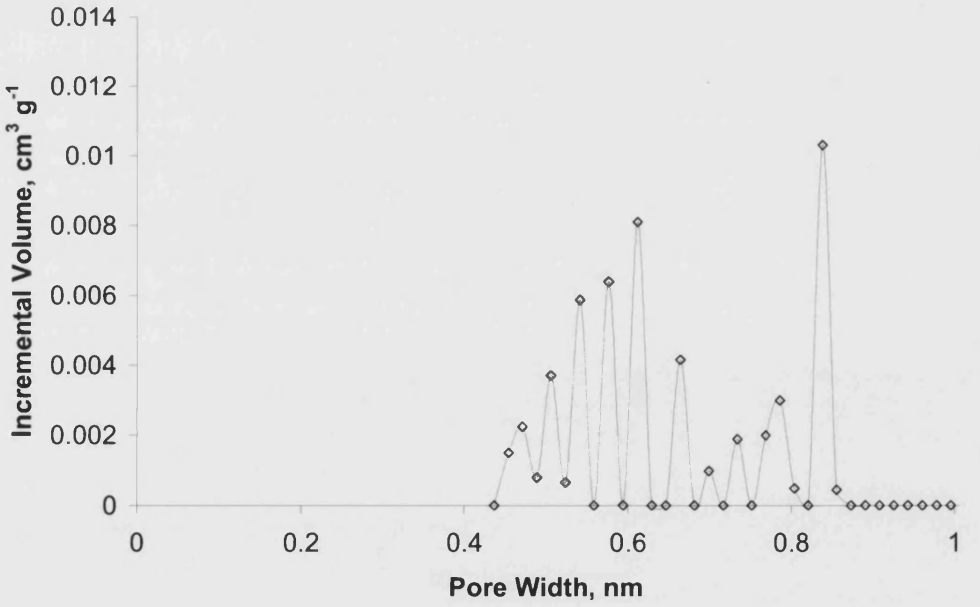

Figure 4.5-3: Carbon dioxide pore size distribution for Norit CNR 115 activated carbon using density functional theory.

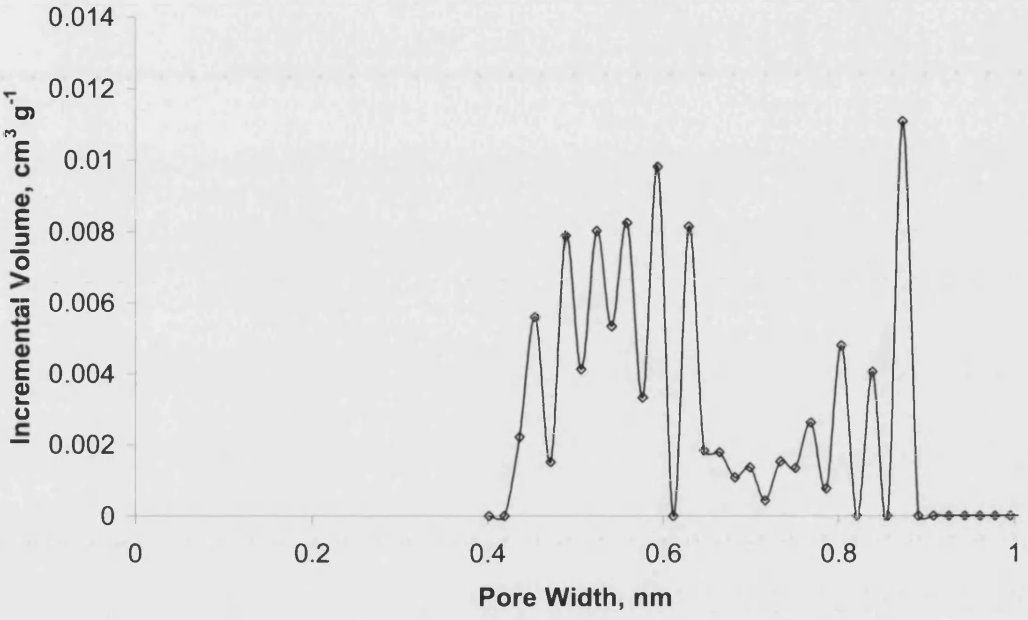

Figure 4.5-4: Carbon dioxide pore size distribution for SRD/667/1 using density functional theory.

4.5.2 N_2 Pores Size Distribution (PSD) Results for the Carbon Nanotubes using the Horvath- Kawazoe (HK) and the Barrett, Joyner and Halenda (BJH) Method

The PSD for the carbon nanotubes have been obtained using a combination of the semi-empirical Horvath-Kawazoe (HK) method (Horvath and Kawazoe, 1983) and the Barrett, Joyner and Halenda (BJH) computational method (Barrett *et al.*, 1951) based on the Kelvin equation (reviewed by Schuth *et al.*, (ed.), 2002). The HK method is used for the assessment of the microporous (< 2 nm) region of the PSD, while the BJH method is used to assess the mesoporous (2 – 50 nm) region. Li *et al.*, (2004) and Chen *et al.*, (2006) have applied these two methods in a similar way.

The method proposed by Horvath and Kawazoe is to calculate an average potential function inside the micropore, relating the average fluid-fluid and solid-fluid interaction energy of an adsorbed molecule to its free energy change on adsorption (Horvath and Kawazoe, 1983; Lastoskie *et al.*, 1994). The resulting relationship between the filling pressure and the slit width is Equation 4.5-2.

$$\ln\left(\frac{p}{p^0}\right) = \frac{L}{RT}\left[\frac{IP\times 10^{32} JA^4/Jcm^4}{\sigma^4(w-2d_0)}\right]\left[\frac{\sigma^4}{3(w-d_0)^3} - \frac{\sigma^{10}}{9(w-d_0)^9} - \frac{\sigma^4}{3d_0^{\,3}} + \frac{\sigma^{10}}{9d_0^{\,9}}\right]$$

Equation 4.5-2

where L is the Avogadro's number (6.023×10^{23} mol^{-1}), R is the molar gas constant, T is the analysis bath temperature (K), σ is the gas solid nuclear separation at zero interaction energy, w is the pore width (nucleus to nucleus), p is the equilibrium pressure, p^0 is the saturation pressure, IP is the interaction parameter and d_0 is the average molecular diameter.

Although the HK method acknowledges the strong solid-fluid attractive forces in micropores, it gives poor results for mesopore PSD and must be combined with a

Kelvin type equation such as the BJH method for the assessment of the entire PSD of the carbon nanotubes.

In the application of this method, the nanotubes are treated as a single graphene sheet (SWNT) or coaxial carbon layers (MWNT) that are cylindrical, hence the Saito-Foley (Saito and Foley, 1995) corrections of the original HK equations (Equation 4.5-2) accounting for the effects of curvature on the forces of adsorption have been used. The BJH method is applied for the analysis of the mesoporous PSD of the carbon nanotubes. This method is based on a model of the adsorbent as a collection of cylindrical pores. It accounts for capillary condensation in the pores using the classical Kelvin equation, which in turn assumes a hemispherical liquid-vapour meniscus and a well-defined surface tension (Barrett *et al.*, 1951).

The results obtained by applying the above mentioned methods are shown in Figure 4.5-5 and Figure 4.5-6. As expected the results obtained from the BJH method shows the distribution of pores for the carbon nanotubes in the mesoporous range with SWNT-2 exhibiting the highest peak at 9.2 nm. It also exhibits a series of other peaks ranging from 2 – 7.7 nm. SWNT-1 and MWNT-1 show their highest peak at 27 nm while the volume of mesopores for MWNT-2 is distinctively smaller exhibiting a broad peak at 37.2 nm. The results of the PSD defined by the HK method show two peaks for SWNT-2 at 0.7 (secondary) and 1.3 (primary) nm within the supermicroporous range, SWNT-1 also shows 2 peaks at 0.9 (primary) and 1.4 nm (secondary) exhibiting a degree of supermicroporosity, it is worth noting that these peaks coincide with the manufacturer specified nanotube diameter range of (0.8 – 1.3 nm). MWNT-1 and 2 show very low peaks in comparison to SWNT-1 and 2 exhibiting supermicroporous peaks at 1.6 and 1.4 nm respectively.

It is clear from the results that all the carbon nanotubes exhibit micro and mesoporosity but to varying extents as described above. A comparison of the BJH and HK pore size distributions emphasises the limitations of both methods. The HK is limited to defining the microporous region of the pore size, the BJH method is limited to the mesoporous range.

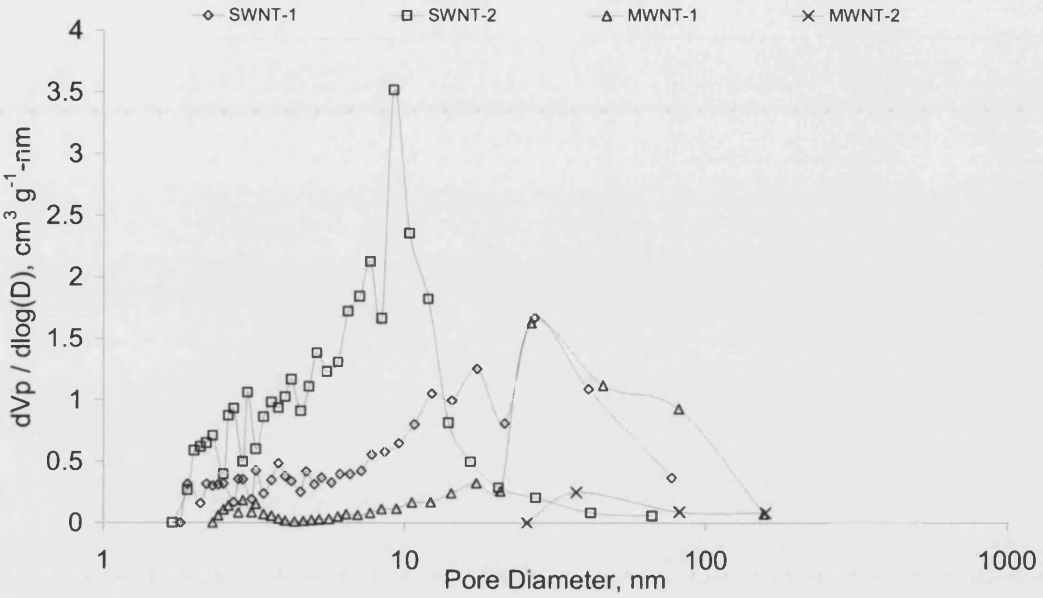

Figure 4.5-5: Barett Joyner and Halenda pore size distribution for the carbon nanotubes.

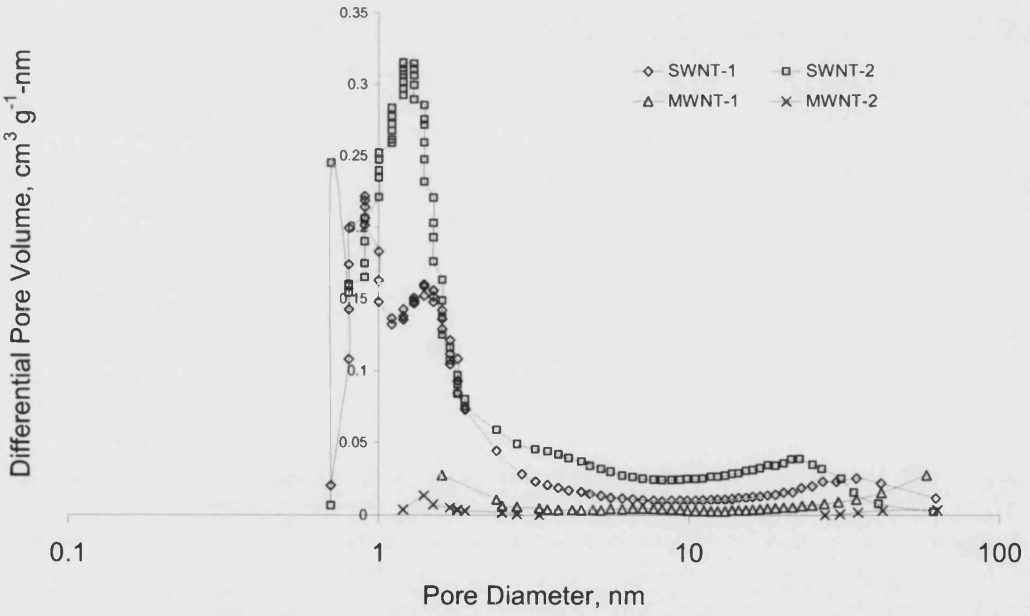

Figure 4.5-6: Horvath Kawazoe pore size distribution for the carbon nanotubes.

4.6 Transmission Electron Microscopy (TEM) Images of the Carbon Nanotubes

Transmission electron microscopy has been used as a qualitative characterisation tool for the carbon nanotubes studied. Figure 4.6-1 (A) and (B) show the images obtained for the SWNTs. The underlying structure of these materials is made apparent. Narrow, intertwined and long tubules are observed, which are characteristic of these materials. The black spots present on Figure 4.6-1 (A) are representative of the residual catalyst particles present as impurities in SWNT-1. SWNT-1 and SWNT-2 were observed to consist of SWNT bundles.

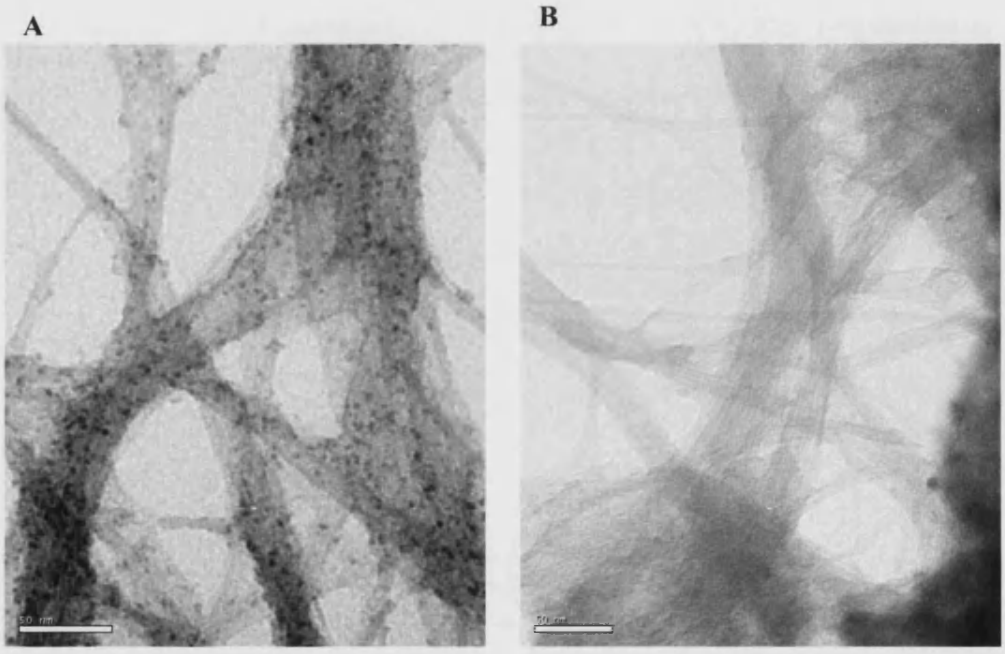

In Figure 4.6-1 (C) and (D), images of the multiwalled nanotubes are shown. These materials are also long and narrow tubules with a hollow centre. The image of MWNT-1 shows how entangled the nanotubes can become forming an entangled fleece. In Figure 4.6-1 (D), it is observed that MWNT-2 has surface defects that can be attributed to the purification methods applied to open its ends.

A higher resolution TEM (HRTEM) would have produced images at higher magnification for closer observation of the material structure.

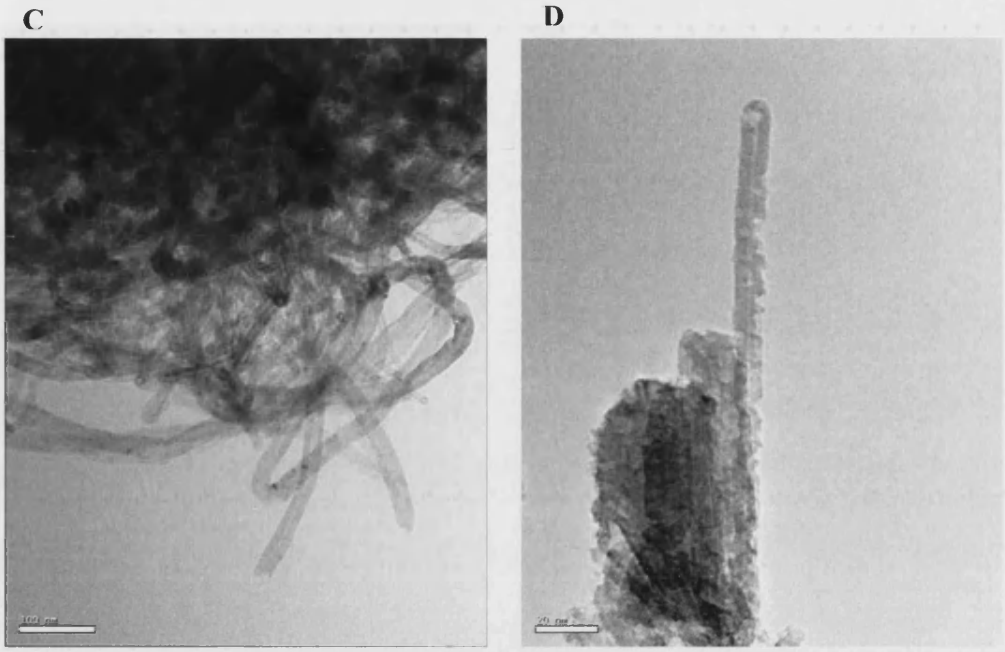

Figure 4.6-1: TEM images of the carbon nanotubes; (A) SWNT-1; (B) SWNT-2; (C) MWNT-1; (D) MWNT-2.

4.7 X-ray Powder Diffraction (XRD) Results

X-ray diffraction is an effective technique to study the average structural properties of nanoporous carbon samples (Reznik *et al.*, 1994). It enables the probing of the crystal structure of materials at the atomic level. The patterns obtained from powder diffraction are used here to identify the nanoporous carbons, and changes in peak width or position can be used to determine their purity and texture. In this section, the results of analysis carried out using the XRD method described in Section 3.5.4 are presented.

For diffraction to occur, Braggs Law must be satisfied (Equation 4.7-1) below. The diffracted beam from a crystal is built up of rays scattered by all the atoms of the crystal which lie in the path of the incident beam with the diffraction of monochromatic x-rays taking place only at the particular angles of incidence that satisfy Braggs Law (Cullity and Stock, 2001).

$$u\lambda = 2d\sin\theta \qquad \textbf{Equation 4.7-1}$$

where u is the order of diffraction (u = 1, 2, 3, ...); λ is the x-ray wavelength = 1.51418 Å for copper K_α radiation; d is the characteristic interplanar spacing of the sample and θ is the diffraction angle. The angle between the diffracted and transmitted beam is always 2θ, which is measured experimentally.

Figure 4.7-1 to Figure 4.7-3 show the x-ray powder diffraction patterns of the nanoporous carbons. The patterns can be indexed on the basis of hexagonal close–packed graphite (Zhou *et al.*, 1994). In all patterns, most noticeably the patterns for MWNT-1 and MWNT-2 in Figure 4.7-3, there is a significant peak observed at the 2θ value close to that of ordered graphite (26°), which corresponds to an interlayer spacing (d_{002}) of 3.354 Å (Zhou *et al.*, 1994). The intensity of the peak indicates the high purity of the materials (> 95 % for MWNT-1 and >90 % for MWNT-2) and the resolving of the multilayer structure of these materials by x-ray radiation. For SWNT-

1 and SWNT-2 broad low intensity peaks are observed in the *002* peak region. This is most likely due to the presence of impurities such as soot in these materials or the close packing or bundling of the nanotubes such that the spaces (interstices) between tubes behave like carbon layers as a result of the van der Waals interactions between them. An important feature of the diffraction pattern for the SWNTs shown in Figure 4.7-2 is a peak at $2\theta = 6°$ corresponding to an interlayer spacing of about 14 Å (1.4 nm). According to Schuth (Ed.) *et al.*, (2002) this peak is assigned to cylindrical lattice of nanotubes that are well ordered in the bundle and the intensity an indication of the sample quality (Schuth (Ed.) *et al.*, 2002).

The Miller Bravais (*hkl*) (Cullity and Stock, 2001) indices for these patterns are evident and are labelled on Figures 4.7-1 to 4.7-3. The interplanar spacing for the relevant graphite peaks have been calculated using the Bragg's equation (Equation 4.7-1) i.e. d_{002}, d_{004} and d_{110}. According to Iwashita *et al.*, (2004), the *hkl* indices of carbon and their corresponding diffraction angles can be found in the 2θ ranges shown in Table 4.7-1 below.

Table 4.7-1: *hkl* indices and diffraction angles for carbon (Adapted from Iwashita *et al.*, 2004)

hkl	2θ (°)
002	25.9 – 26.6
004	53.2 – 54.7
110	Near 77.6
112 and *006*	83.6 and near 87

Table 4.7-2 shows the diffraction peak angles and interlayer spacing calculated for the nanoporous carbons in the 002 graphite diffraction range. The diffracted angles at the respective peaks have been calculated by separating the peaks and fitting them to a Pearson VII function while the lattice constants, c_0 have been calculated using the simple relationship $c_0 = 2d_{002}$ (Iwashita *et al.*, 2004). Results of the other diffraction peaks (004, and 110), 2θ angles and lattice constants obtained are available in Appendix B.

From the results of Table 4.7-2, it can be seen that the interlayer spacing for BPL (3.82 Å), Norit CNR 115(3.78 Å) and SRD/667/1(3.77 Å) are larger than that of a

perfect graphite crystal and is also the case for the carbon nanotubes. Zhou *et al.*, (1994) and Saito *et al.*, (1993) have obtained similar results. While Zhou *et al.*, (1994) attribute this to the lack of positional correlation between carbon atoms in different shells of the same nanostructure (Zhou *et al.*, 1994), Saito *et al.*, (1993) believe it to be due to the turbostratic stacking of graphitic sheets (neighbouring graphitic sheets are parallel to each other, but translational and rotational correlations within a sheet plane are random) (Saito *et al.*, 1993). The effects described can be attributed to the materials under investigation in this work.

Although the basic configuration of the graphitic layer in activated carbons is similar to that of pure graphite, there are some deviations, for example, the interlayer spacings range from 0.317 to 0.382 nm different from that of pure graphite (0.335 nm). The orientation of the layers in activated carbons is such that a turbostratic structure is resulted. Furthermore, there are crystal lattice defects and the presence of built in heteroatoms (Do, 1998).

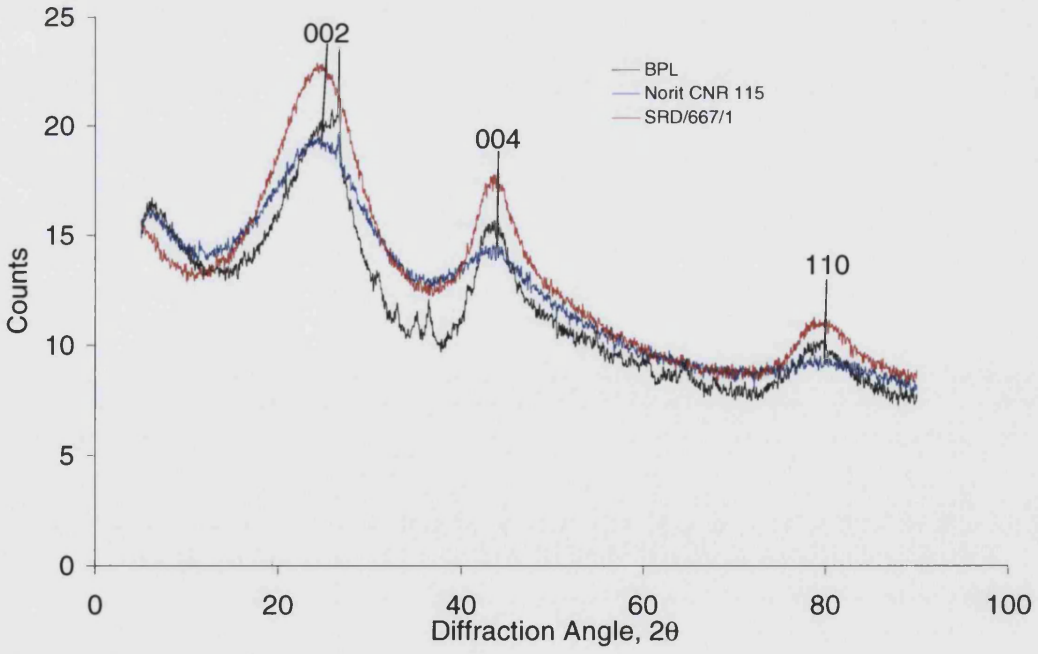

Figure 4.7-1: XRD patterns for the activated carbons

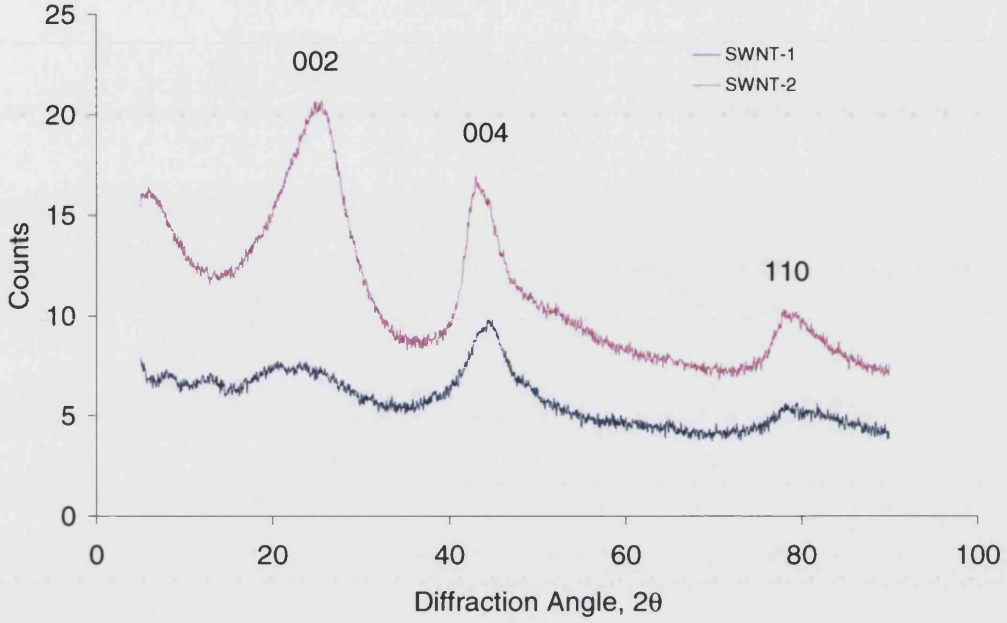

Figure 4.7-2: XRD patterns for SWNT-1 and SWNT-2

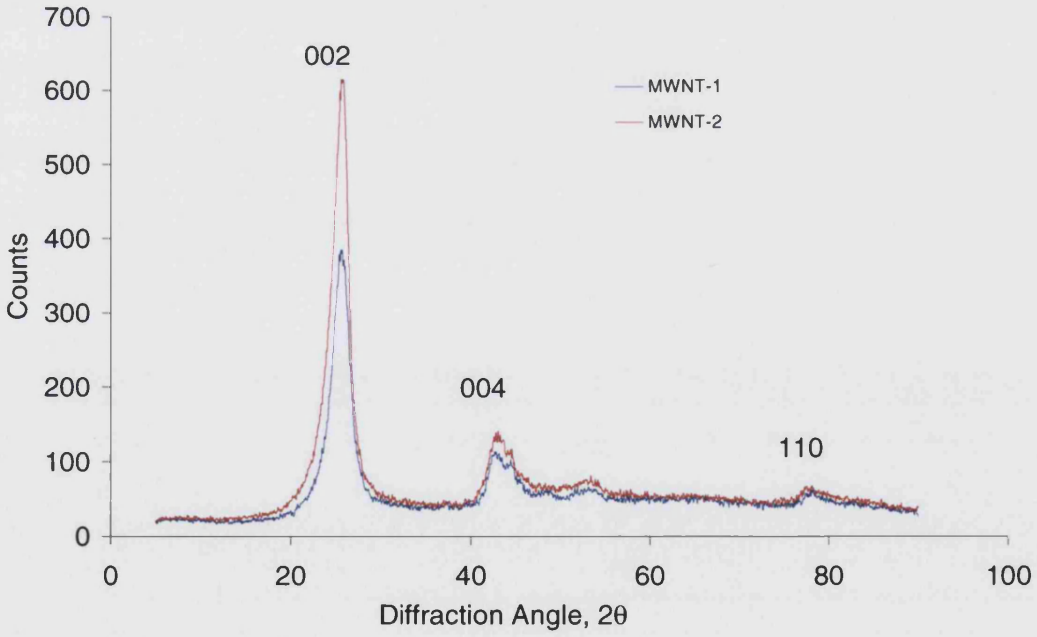

Figure 4.7-3: XRD patterns for MWNT-1 and MWNT-2

Table 4.7-2: X-Ray diffraction results at the *002* peaks of the nanoporous carbons

	BPL	
Diffracted Angle, 2θ (*002*)	23.22	°
Interlayer Spacing, d_{002}	3.82	Å
Lattice Constant, c_0	7.66	Å
	Norit CNR 115	
Diffracted Angle, 2θ (*002*)	23.52	°
Interlayer Spacing, d_{002}	3.78	Å
Lattice Constant, c_0	7.56	Å
	SRD/667/1	
Diffracted Angle, 2θ (*002*)	23.62	°
Interlayer Spacing, d_{002}	3.77	Å
Lattice Constant, c_0	7.06	Å
	SWNT-1	
Diffracted Angle, 2θ (*002*)	22.21	°
Interlayer Spacing, d_{002}	-	-
Lattice Constant, c_0	-	-
	SWNT-2	
Diffracted Angle, 2θ (*002*)	23.46	°
Interlayer Spacing, d_{002}	-	-
Lattice Constant, c_0	-	-
	MWNT-1	
Diffracted Angle, 2θ (*002*)	25.57	°
Interlayer Spacing, d_{002}	3.48	Å
Lattice Constant, c_0	6.92	Å
	MWNT-2	
Diffracted Angle, 2θ (*002*)	25.54	°
Interlayer Spacing, d_{002}	3.49	Å
Lattice Constant, c_0	6.89	Å

Chapter Five

Gravimetric Sorption Results

5.1 Introduction

This chapter is a report on a selection of hydrogen isotherms from the large volume of data obtained using the Intelligent Gravimetric Analyser (IGA) described in Chapter 3. The main findings are discussed and linked to the characterisation results obtained in Chapter 4. Detailed analysis of these gravimetric results are presented in Chapter 6.

Section 5.2 discusses how the experimental data are corrected for buoyancy, a major source of error in gravimetric experiments and shows the importance of the equation of state chosen to quantify the hydrogen gas properties. Excess hydrogen adsorption and desorption isotherms are presented in Section 5.3 with the effect of temperature and hydrogen gas purity on the amount adsorbed presented in Section 5.3.1and 5.3.2 respectively. This is followed in Section 5.4 by the results of cycling the materials at 77 K using ultrahigh purity (UHP) H_2.

5.2 Buoyancy Correction

The data obtained from the IGA equipment are raw mass data uncorrected for buoyancy. Gravimetric isotherm measurements are seriously affected by buoyancy, which can be defined as an upward force on an object immersed in a fluid (liquid or gas), enabling it to float or appear lighter. The effect of buoyancy is not constant along the sorption isotherm and may become significant at high pressures. Buoyancy correction is therefore paramount in the reporting of gravimetric adsorption data. The two main contributions to buoyancy are the contribution due to the volume of the adsorbent, sample holder and components subject to displacement by the fluid; i.e. its variation due to the change in gas density and the contribution due to the volume of the adsorbed phase (Frere and De Weireld, 2002).

The first buoyancy correction can be calculated by:

$$W_e = W - W_s + \rho_b V_s \qquad \textbf{Equation 5.2-1}$$

Where W_e is the excess adsorbed weight, W is the detected weight of the adsorbent with increasing pressure, P, W_s is the 'dry' weight of the adsorbent when $P = 0$, that is at vacuum, ρ_b is the bulk density of the gas which is a function of pressure, P and temperature, T calculated using the Peng-Robinson equation of state (Peng and Robinson, 1976) and V_s is the volume of the sample, which can be calculated from its density ρ_s obtained from helium pycnometry; $V_s = {W_s}/{\rho_s}$. It is generally assumed that helium penetrates all pores of the solid and it is not adsorbed at the experimental conditions (room temperature and pressure) (Sircar, 2001; Maggs *et al.*, 1960; Myers *et al.*, 1996; Springer *et al.*, 1969) for all the nanoporous carbon materials. For volumetric adsorption measurements, helium has also been applied for the measurement of the dead space for isotherm data correction.

The experimental measurement of adsorption either by gravimetric or volumetric methods gives the surface excess (Sircar, 1999; Myers *et al.*, 1996) that can be

calculated using equation 5.2-1. This is known as the Gibbs surface excess, which can be defined as the actual or absolute amount of gas contained in the adsorbent pores less the amount of gas that would be present in the pores in the absence of gas-solid intermolecular interactions (Myers *et al.*, 1996).

The second contribution can then be calculated by:

$$W_t = W_e + \rho_b V_a \qquad \textbf{Equation 5.2-2}$$

Where W_t is the total adsorption (the total amount of fluid in pores) and V_a is the volume of the adsorbate with $V_a = {W_a}/{\rho_a}$, which is the weight of the adsorbed phase, W_a is divided by the adsorbed phase density, ρ_a. Equation 5.2-2 represents the total or absolute hydrogen adsorption in this case and is calculated using the experimental excess derived from equation 5.2-1. For the calculation of the total adsorption, the volume of the Gibbs interface (Sircar, 1999) is assumed to be equal to the micropore volume obtained from N_2 adsorption measurements at 77 K or can be evaluated during curve fitting of the experimental excess isotherm to an adsorption model such as the Langmuir-Freundlich or the Toth equation as shown in Chapter 6. At high gas pressures and/or low gas temperatures, the buoyancy correction is increasingly sensitive to the calculated gas density and therefore to the gas compressibility factor, *Z (P, T, V)*.

$$Z(P,T,V) = \frac{PV}{RT} \quad . \qquad \textbf{Equation 5.2-3}$$

Where V is the molar volume of the gas; R is the molar gas constant = 8.3145 J mol^{-1} K^{-1}.

The change in the adsorptive density in the bulk phase as a function of pressure and temperature is calculated using the Peng-Robinson equation of state (Peng and Robinson, 1975) shown in equation 5.2-4.

$$P = \frac{RT}{V-b} - \frac{a(T)}{V(V+b)+b(V-b)}$$ **Equation 5.2-4**

Where b is a constant related to the size of the hard spheres assumed for molecules, a is a parameter which is a measure of the intermolecular attraction force, P, T and V are as defined above. Equation 5.2-4 can be rewritten as Equation 5.2-5.

$$Z^3 - (1-B)Z^2 + (A - 3B^2 - 2B)Z - (AB - B^2 - B^3) = 0$$ **Equation 5.2-5**

Where $A = \frac{aP}{R^2T^2}$ and **Equation 5.2-6**

$$B = \frac{bP}{RT}$$ **Equation 5.2-7**

At temperatures excluding the critical;

$$a(T) = a(T_c)\alpha(T_{r,\omega})$$ and **Equation 5.2-8**

$$b(T) = b(T_c)$$ **Equation 5.2-9**

Where $\alpha(T_{r,w})$ is a dimensionless function of reduced temperature, T_r and acentric factor, ω and equals unity at the critical temperature. The relationship between α and T_r can be linearised to give Equation 5.2-10.

$$\alpha^{1/2} = 1 + \kappa(1 - T_r^{1/2}) \qquad \Rightarrow \alpha = [1 + \kappa(1 - T_r^{1/2})]^2$$ **Equation 5.2-10**

Where κ is a constant and can be correlated against the acentric factor, to give Equation 5.2-11.

$$\kappa = 0.37464 + 1.54226\omega - 0.26992\omega^2$$ **Equation 5.2-11**

The Peng-Robinson equation of state was chosen for the calculation of the thermodynamic properties of the adsorptive because being a 3-parameter equation of state it provides a more accurate prediction of the volumetric behaviour of single component systems (Peng and Robinson, 1975). The equation provides simplicity and accuracy and performs as well or better than the Redlich-Kwong-Soave (RKS) equation (Peng and Robinson, 1975). This equation of state is valid for hydrogen gas within the experimental conditions being applied in this study. The Peng-Robinson equation of state has been incorporated into an EXCEL macro containing a series of calculations for the buoyancy correction of the hydrogen adsorption-desorption experimental results and is shown in Appendix A. The excess % mass uptake is calculated using Equation 5.2-12.

$$\%wt = \frac{W_e}{W_s} \times 100 \qquad \textbf{Equation 5.2-12}$$

Figure 5.2-1 and Figure 5.2-2 below are illustrations of the observed significance of correcting the 'raw' experimental gravimetric data for effects due to buoyancy. It is observed that the buoyancy correction leading to the excess isotherm becomes relevant at pressures greater than about 500 kPa, showing that this correction starts to become quantitatively significant above this pressure region for the adsorption isotherms shown in Figure 5.2-1 and Figure 5.2-2.

The total isotherm is largely influenced by the magnitude of the adsorbed phase, V_a considered to be equivalent to the pore volumes obtained from nitrogen adsorption experiments at 77 K. For materials with high pore volume the deviation of the total isotherm from the excess isotherm has been observed to be greater. The pore volumes obtained for each of the nanoporous carbons have been reported in Table 4.4-2 and 4.4-3.

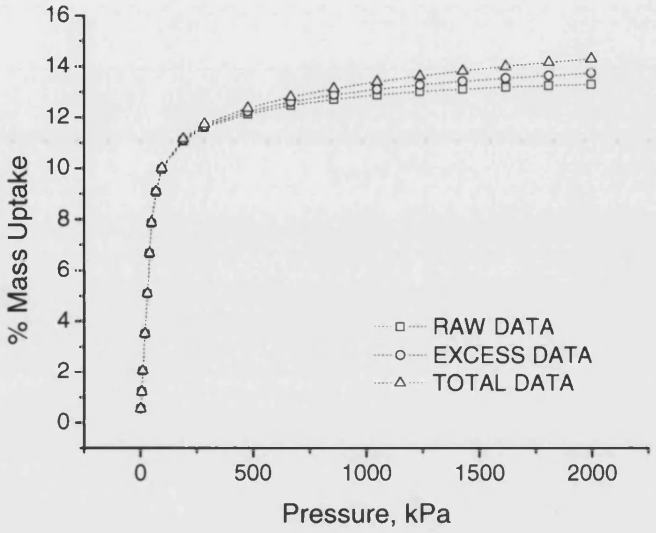

Figure 5.2-1: Graph comparing raw, excess and total experimental adsorption isotherms on Norit CNR 115 activated carbon using ultra high purity hydrogen at 77 K.

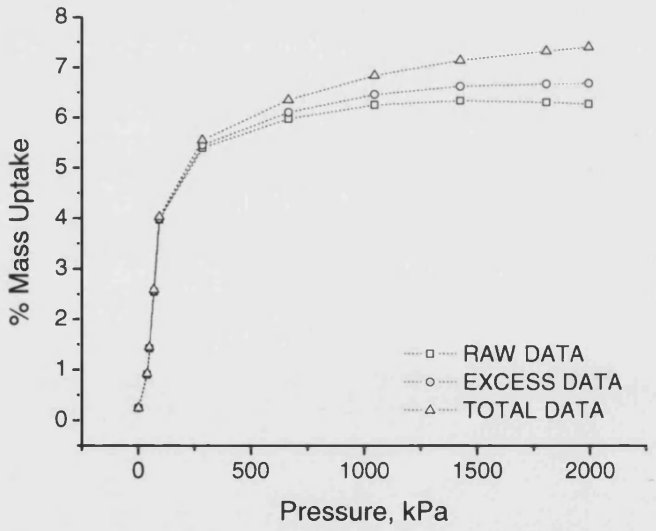

Figure 5.2-2: Graph comparing raw, excess and total experimental adsorption isotherms on SWNT-1 using ultra high purity hydrogen at 77 K.

5.3 Gravimetric Hydrogen Isotherms on the Activated Carbon Materials

The gravimetric hydrogen adsorption-desorption isotherms obtained for the activated carbon samples are presented in this section. The isotherms reported are excess data, which have been corrected for buoyancy effects as described in Section 5.2. Figure 5.3-1 to Figure 5.3-3 are graphs comparing the % mass adsorbed on each activated carbon for the different grades of hydrogen at different temperatures, 77 K, 195 K and 303 K.

The isotherms obtained for the activated carbons show Type I behaviour according to the BDDT classification (Sing *et al.*, 1985). In all materials, the amount adsorbed increased with increasing pressure, and no excess behaviour, which is characterised by the reduction in the amount adsorbed in regions of high pressure, has been observed for these materials in the pressure range (0 – 2000 kPa) used. The uptake at low pressures (Henry's law region) is linear with a steep rise and then approaches saturation when the pressure is high. In these materials, hydrogen uptake is believed to take place via physisorption, such that all of the adsorbed hydrogen is released when the temperature is increased and/or pressure is decreased. Evidence of this is based on the reported values of adsorption energy (isosteric heat) measured on nanoporous carbons in the literature and also as a part of this work. This is further described in Section 6.2.3.

The adsorption isotherms at 77 K are accompanied by the appearance of hysteresis in the low pressure region of the desorption cycle. This implies that the sorption isotherms obtained under these conditions are not fully reversible. When the system temperature is raised above 77 K, all of the hydrogen originally left behind has been observed to fully desorb. In an ideal storage system, it is a requirement that a large proportion, if not all of the stored hydrogen should be dischargeable. This is an interesting observation and is discussed in more detail in Section 6.3.3.

In Figure 5.3-1, the isotherms obtained at 77 K are shown. It is observed that when low grade (LG) hydrogen is used, the amount of hydrogen adsorbed is 5.15, 5.50 and 6.98 wt-% on BPL, SRD/667/1 and Norit CNR 115 respectively. For high grade (HG) hydrogen, the amount adsorbed is 7.45 wt-% on BPL, 5.67 wt-% on SRD/667/1 and 12.1 wt-% on Norit CNR 115. In the case of ultra high purity (UHP) hydrogen, values of 10.04, 9.47 and 13.7 wt-% have been obtained on BPL, SRD/667/1 and Norit CNR 115 respectively. Norit CNR 115 appears to have the highest uptake of the three activated carbons at 77 K. This may be linked to its high DR (N_2) micropore volume (0.62 cm^3 g^{-1}) and BET surface area of 1624 m^2 g^{-1} in comparison to the other carbons. This is fully discussed in Section 6.5. Similarly, high adsorption capacities (8 wt-%) at 77 K have been observed by Schwarz on a Norit sample (Schwarz, 1994) although no specification on the purity of the hydrogen gas used is stated in the publication. This indicates that the high uptake observed here is not unheard of. It is worth noting that the Norit activated carbon is the only chemically activated sample (phosphoric acid), while BPL and SRD have both been activated by steam. The adsorption isotherms measured at temperatures higher than 77 K, that is, at 195 and 303 K as shown in Figure 5.3-2 and Figure 5.3-3 reveal much lower values of hydrogen uptake, with values in the range of 0.2 wt-% - 1.0 wt-% observed. The use of higher purity hydrogen does not provide an improvement in the amount adsorbed by the activated carbons as observed at 77 K.

The process of adsorption in these nanoporous carbon materials is by van der Waals forces at the adsorbent surface. These binding forces are weak, implying that the process of physisorption at room temperature is almost impeded by thermal motion (Rzepka *et al.*, 1998). It has been observed that in order to store significant amounts of hydrogen, the carbon materials need to be cooled to liquid nitrogen temperatures. This is in agreement with the work of other authors (Zhou *et al.*, 2003; Benard and Chahine, 2001). The amount of hydrogen stored at much higher temperatures is significantly reduced.

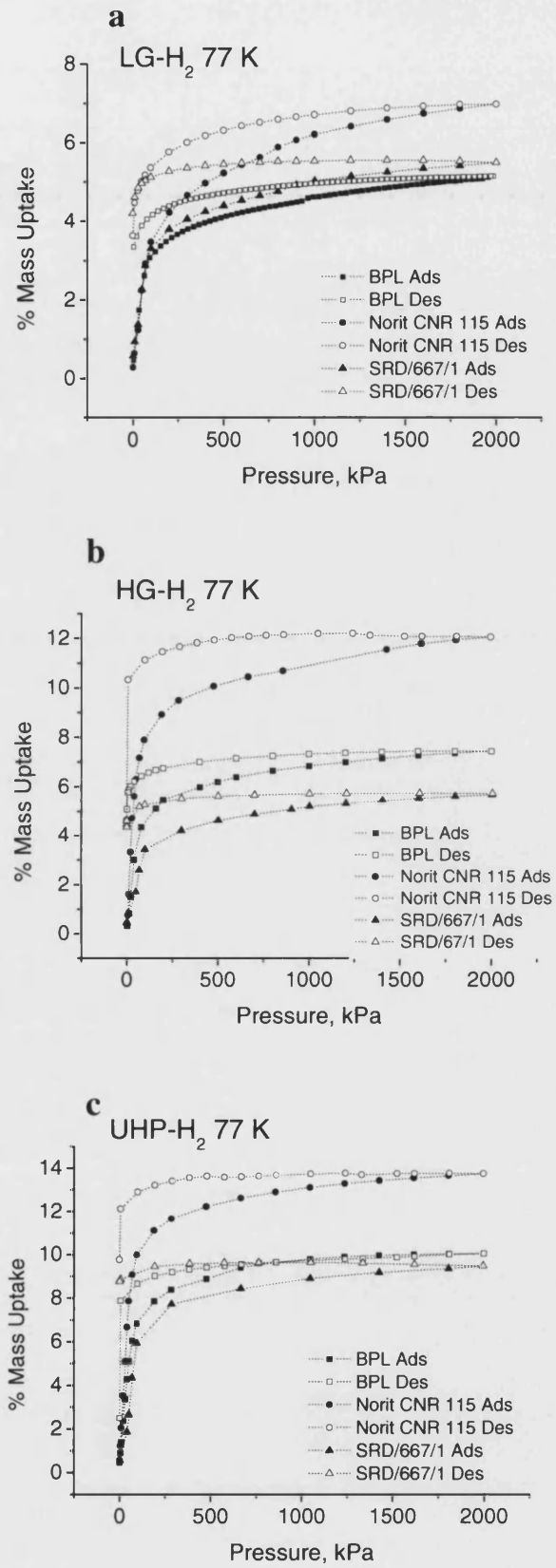

Figure 5.3-1: Graphs comparing the sorption isotherms of BPL, Norit CNR 115 and SRD/667/1 activated carbons at 77 K using (a) Low Grade H_2; (b) High Grade H_2; (c) Ultra High Purity H_2.

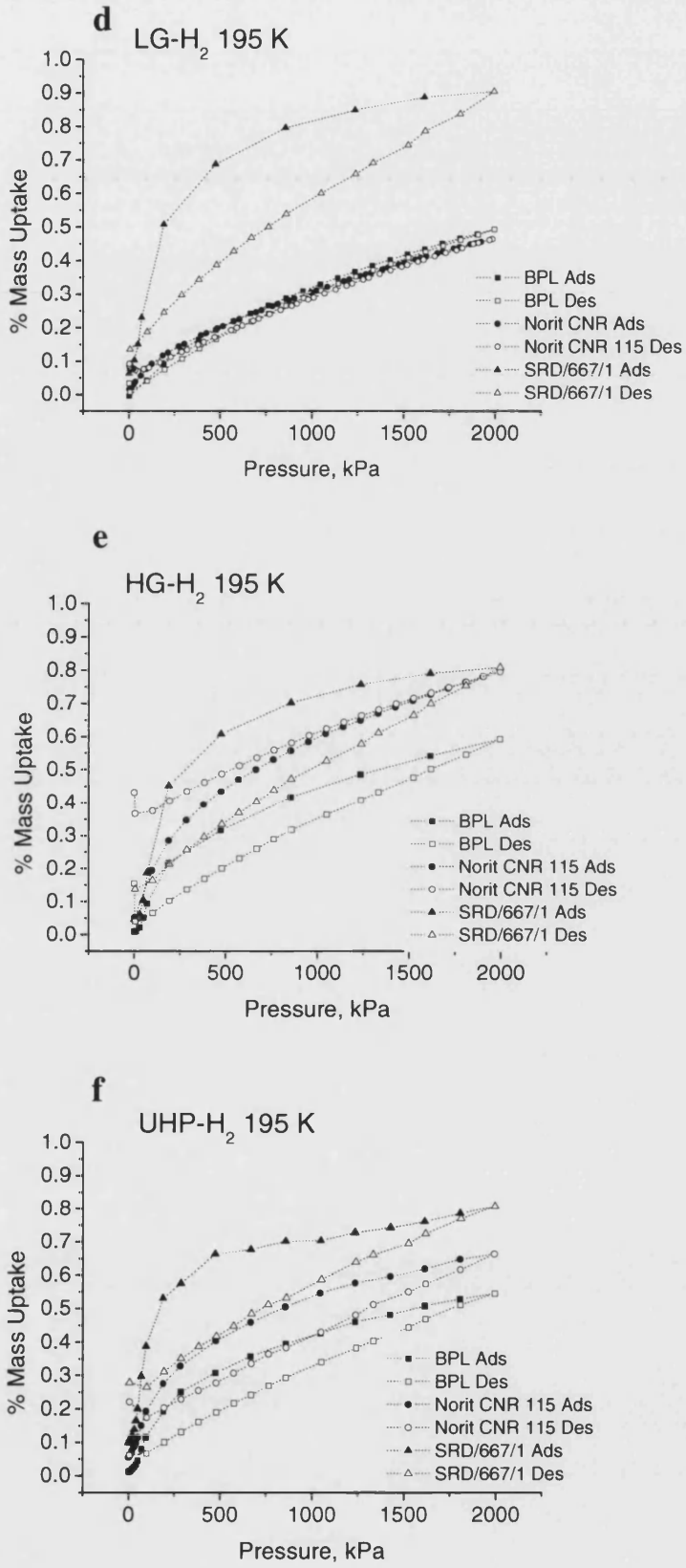

Figure 5.3-2: Graphs comparing the sorption isotherms of BPL, Norit CNR 115 and SRD/667/1 activated carbons at 195 K using (d) Low Grade H_2; (e) High Grade H_2; (f) Ultra High Purity H_2.

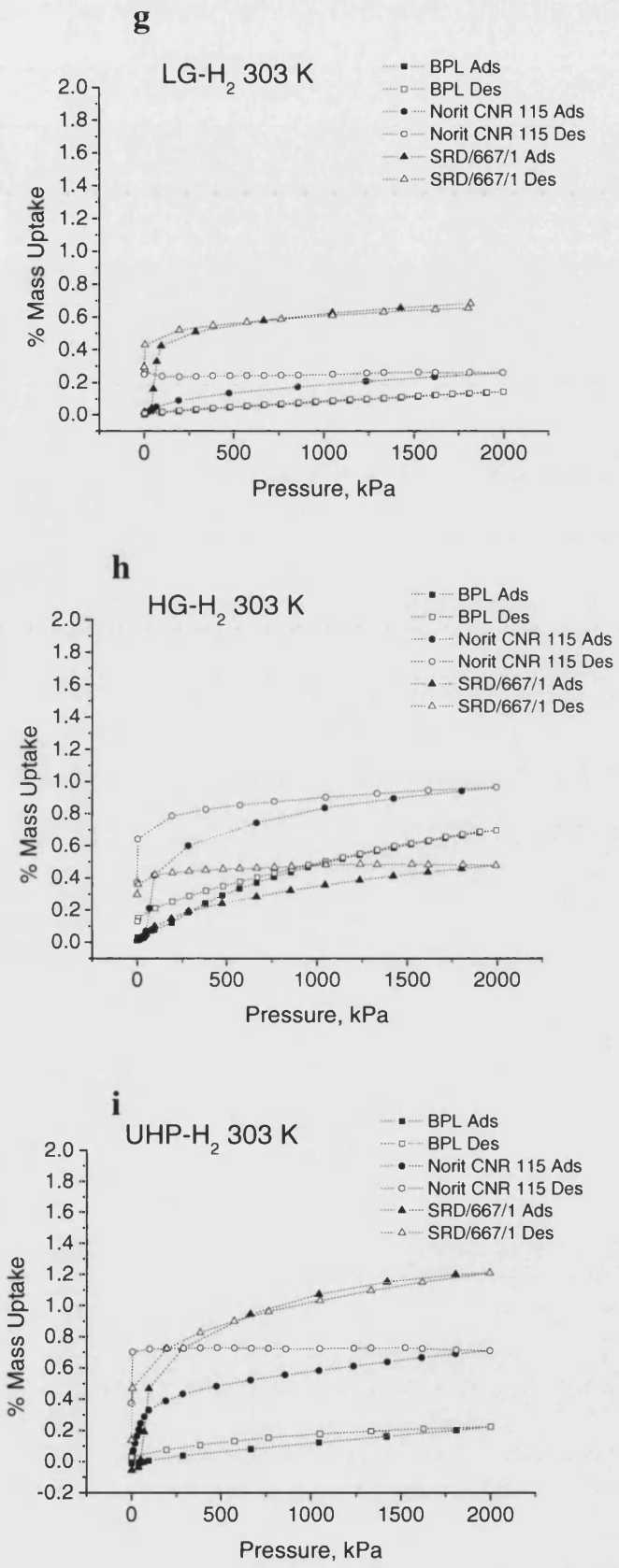

Figure 5.3-3: Graphs comparing the sorption isotherms of BPL, Norit CNR 115 and SRD/667/1 activated carbons at 303 K using (g) Low Grade H_2; (h) High Grade H_2; (i) Ultra High Purity H_2.

5.3.1 Effect of Temperature on Hydrogen Uptake in the Activated Carbons

The amount of hydrogen adsorbed on the nanoporous carbon materials studied has been observed to be dependent on the adsorption temperature, as expected. Figure 5.3-4 to Figure 5.3-6 are plots of the adsorption isotherms for the respective samples at varying temperatures. It is observed that BPL has an uptake of 10.04 wt-% at 77 K and 0.22 wt-% at 303 K, Norit CNR 115 has an uptake of 13.74 wt-% at 77 K compared to 0.71 wt-% at 303 K, while SRD/667/1 has an uptake of 9.47 wt-% at 77 K and 0.40 wt-% at 303 K using UHP-H_2. The shapes of the observed isotherms are analogous to that of the standard Langmuir isotherm. As mentioned previously, the highest uptakes have been measured at 77 K with a significant reduction in the uptake observed at higher temperatures. It is clear that low temperature favours the adsorption process.

The semblance of the shape of the isotherms obtained here to that of the Langmuir (1918) model appear to be coincidental since the Langmuir model describes adsorption onto a flat surface as a continuous process of bombardment of adsorbate molecules onto the surface of the adsorbent and a corresponding desorption of molecules from the surface. It is important to note that the surfaces of the nanoporous carbon materials studied are not flat, but the Langmuir model provides a preliminary qualitative analysis of their isotherms. This is further developed in Chapter 6. According to Do (1998), when the affinity parameter or Langmuir constant (based on its dependency on temperature) is larger, the surface of the adsorbent is covered with more adsorbate molecules as a result of the stronger affinity of these molecules towards the surface. Similarly, when the heat of adsorption increases, the amount adsorbed increases as a result of the higher energy barrier in which the gas molecules have to overcome to desorb back into the gas phase (Do, 1998).

Increasing the adsorption temperature will decrease the amount adsorbed at a given pressure. This is due to the greater energy acquired by the adsorbate molecules to desorb from the adsorbed phase. The affinity parameter decreases with temperature because the heat of adsorption is positive, that is, adsorption is an exothermic process.

Hence it is commonly observed that lower temperatures favour adsorption. Semi-empirical models for describing the hydrogen sorption isotherms are considered in more detail in Chapter 6 as well as the heat of adsorption and its significance.

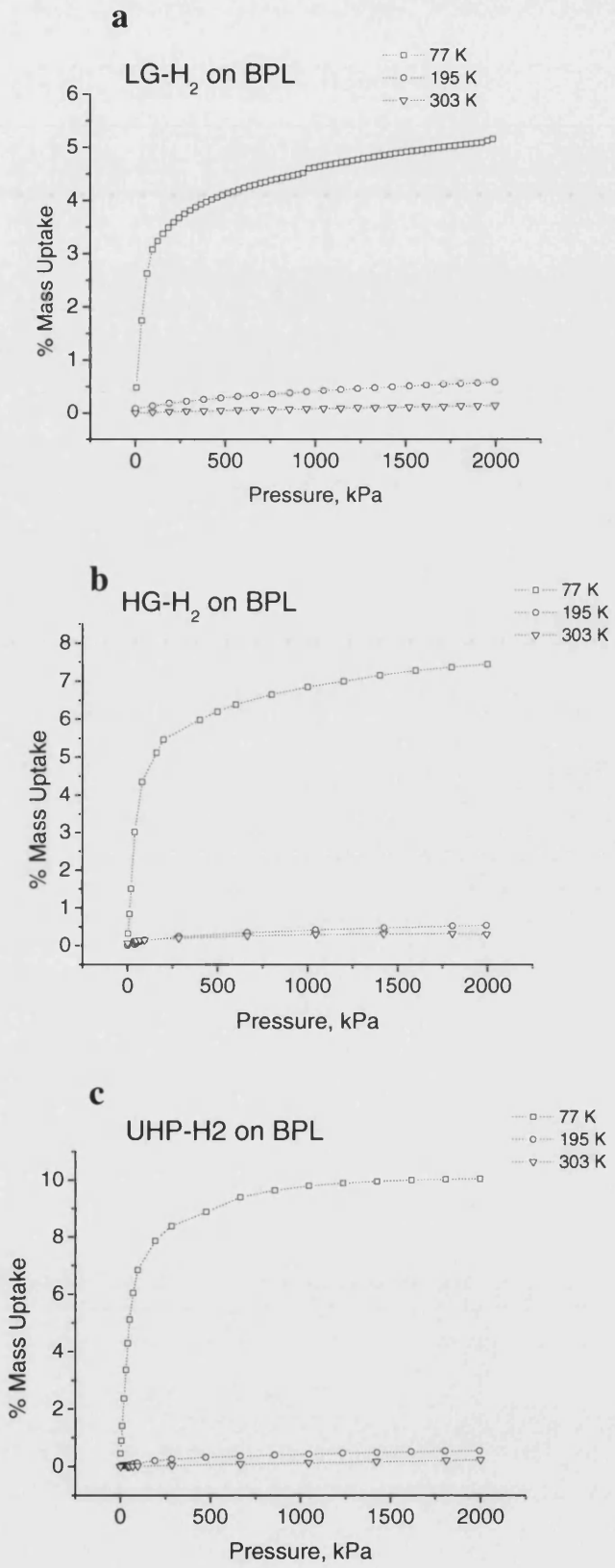

Figure 5.3-4: Graph showing the effect of temperature on the amount adsorbed on BPL using (a) Low-Grade H_2; (b) High Grade H_2; (c) Ultra High Purity H_2.

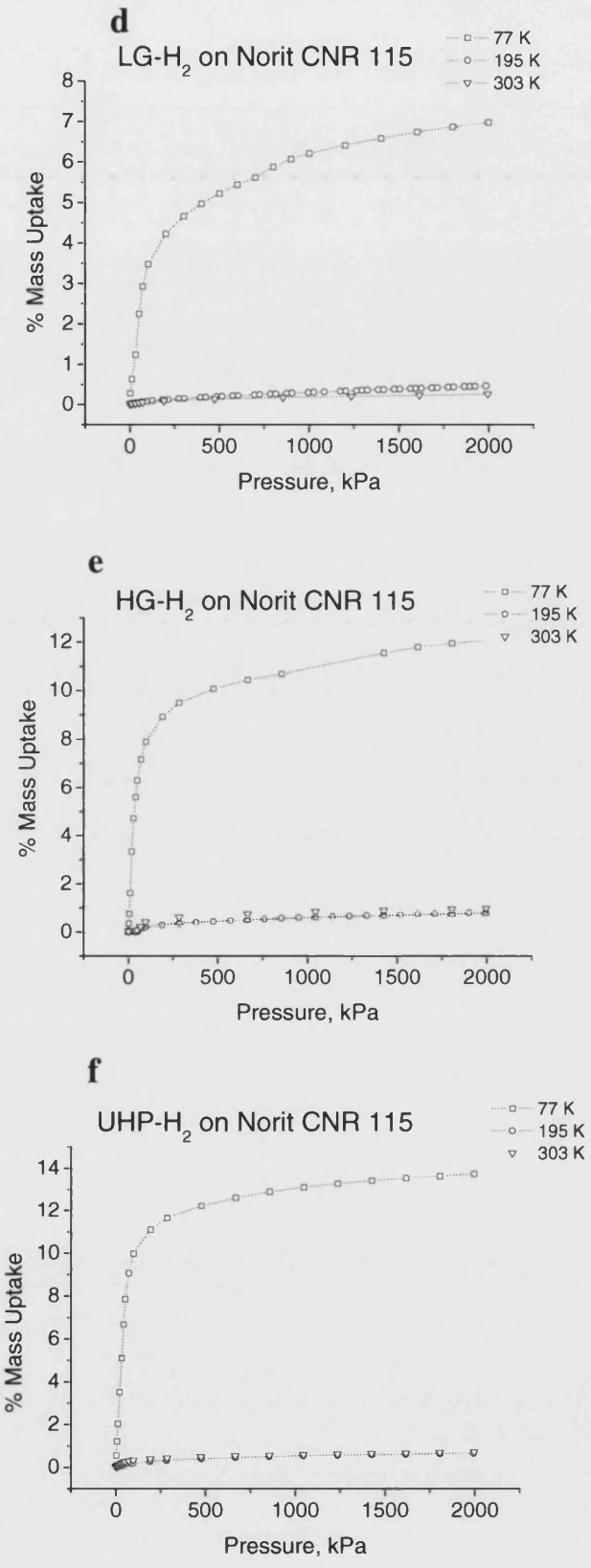

Figure 5.3-5: Graph showing the effect of temperature on the amount adsorbed on Norit CNR 115 using (d) Low-Grade H_2; (e) High Grade H_2; (f) Ultra High Purity H_2.

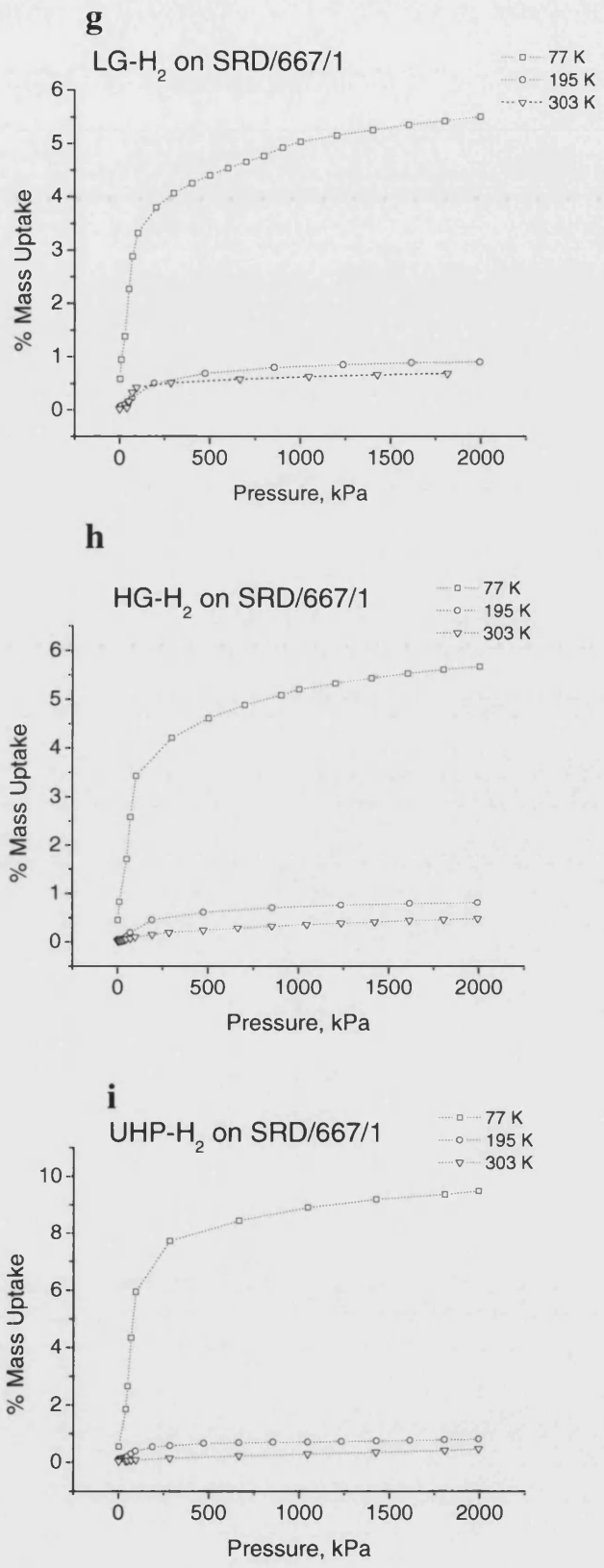

Figure 5.3-6: Graph showing the effect of temperature on the amount adsorbed on SRD/667/1 using (g) Low-Grade H_2; (h) High Grade H_2; (i) Ultra High Purity H_2.

5.3.2 Effect of Hydrogen Gas Purity on the Amount Adsorbed on the Activated Carbons

There appears to be a relationship between the amount of hydrogen adsorbed and the purity of the adsorptive. Therefore, adsorption isotherms have been carried out on the activated carbons using hydrogen gas with varying purity levels as shown in Table 3.3-2. The low grade hydrogen contains approximately 50 ppm impurities, the high grade hydrogen contains 5 ppm impurities, while the ultra high purity hydrogen contains 1 ppm impurities as specified by the respective manufacturers.

The results showing the purity effects are presented in Figure 5.3-7 to Figure 5.3-9. For the activated carbons at 77 K the amount of hydrogen adsorbed is observed to increase as the purity of the hydrogen gas is increased. At the other temperatures, the use of higher purity hydrogen appears to have a greatly reduced significance on the amount adsorbed. For example, from the isotherms measured on BPL at 195 K, 0.58 wt-% is observed for LG-H_2, 0.59 wt-% for HG-H_2, and 0.55 wt-% for UHP-H_2. The adsorption capacity of the material is not improved. In the case of Norit CNR 115 at 303 K it is observed that the high grade hydrogen results gives higher uptake than the isotherms obtained with ultra high purity hydrogen. This is also observed to be the case for BPL at 303 K. These observations can be possibly attributed to the adsorption of the impurities in the gas stream. The adsorption isotherms for SRD/667/1 at 77 K show interesting behaviour. There appears to be only a small difference in the amount adsorbed using low grade hydrogen and high grade hydrogen (5.50 to 5.67 wt-%) when compared to the differences observed with the other activated carbons (5.15 to 7.45 wt-% for BPL and 6.98 to 12.10 wt-% for Norit CNR 115).

These observations highlight the importance of specifying the purity concentration of the hydrogen gas used when reporting this kind of data. It is evident that the gas phase impurities play an important role in hydrogen storage in activated carbons. The observations are in agreement with the observations of Amankwah and Schwarz (1991) who studied the impurity effect in hydrogen storage and calculated that for a superactivated carbon, the reduction in the adsorbed amount of hydrogen due to the prescence of impurities mainly nitrogen will not exceed 30 %. Findings from

experiment and Grand Canonical Monte Carlo (GCMC) simulation on this subject have been published by Odunsi *et al.*, (2005).The findings suggest the presence of a pore blocking phenomenon in the activated carbons, such that the impurities in the gas stream with higher molecular weights and higher adsorption affinity in comparison to hydrogen compete for adsorption sites on these materials. It is suggested that on exposure of the clean adsorbent sample to lower grade hydrogen gases, the impurities (N_2, O_2, H_2O, CO, CO_2), as reported by the manufacturers adsorb preferentially onto the activated carbons blocking access to the interconnected/complex pore structure of the material. In the case of the ultra high purity hydrogen, the concentration of impurities in the gas stream is much less than that in the lower grade gas. This implies that more of the accessible adsorption sites are available for occupation by hydrogen molecules.

In the work by Odunsi *et al.*, (2005), simulation results based on a slit-pore model suggest that the differences between the molecular sizes and interaction energies of hydrogen and the impurites are influenced by the range of pore sizes in the material invariably affecting hydrogen uptake. For small pores (0.74 nm), the uptake of nitrogen is found to reduce the amount of hydrogen adsorbed even at sufficiently high pressures, while for large pores (2.664 nm), the presence of N_2 is said not to influence the amount adsorbed. Pore sizes for the activated carbons in Section 4.5-1 using DFT reveal that there is a varied distribution of pores. The pore sizes range from 0.45 – 10 nm for Norit CNR 115 with a significant peak observed at 1.18 nm, 0.50 – 10 nm for BPL with a significant peak at 0.54 nm and 0.42 – 2 nm for SRD/667/1 showing a significant peak at 0.59 nm. These pores size distributions suggest that when low grade hydrogen is used the available adsorption sites will be competed for by H_2 and the balance impurities in comparison to when higher purity gas is used.

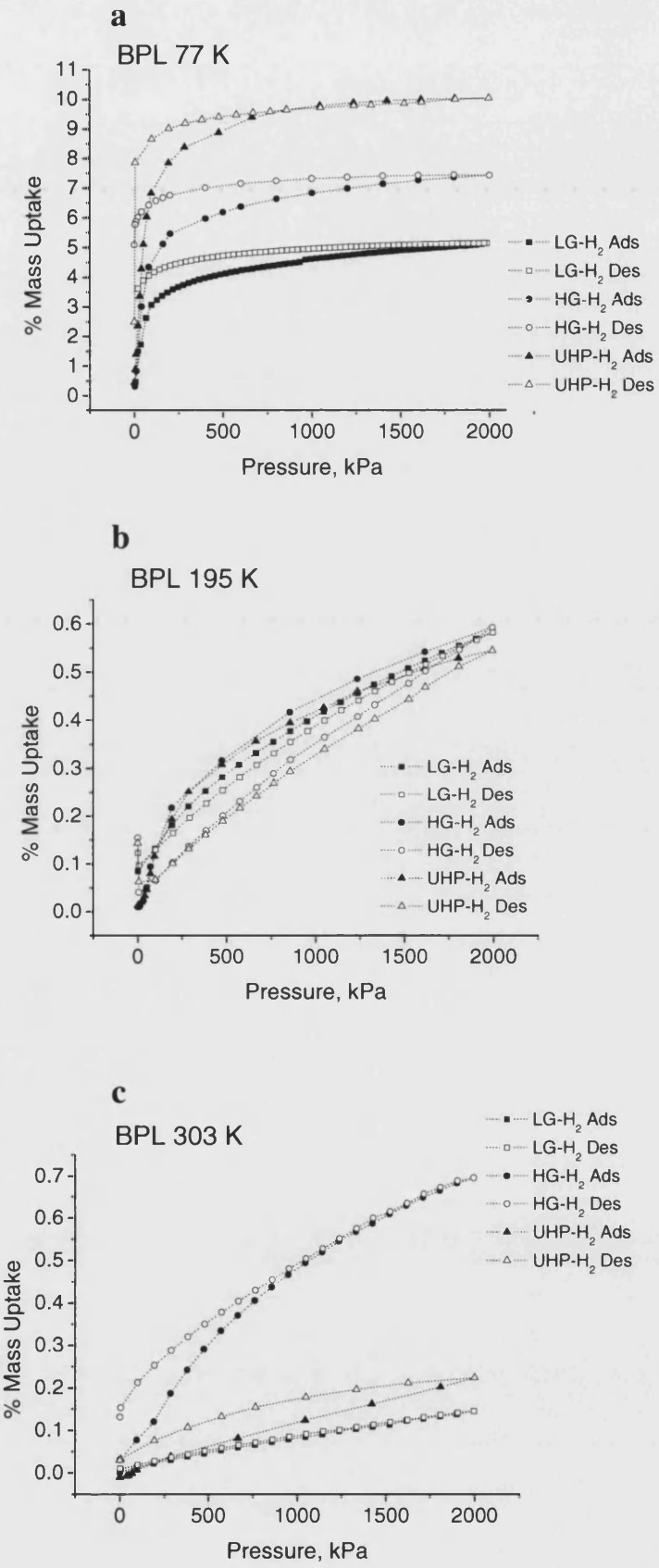

Figure 5.3-7: Graph showing the effect of hydrogen purity on the adsorption capacity of BPL at different temperatures (a) 77 K; (b) 195 K; (c) 303 K.

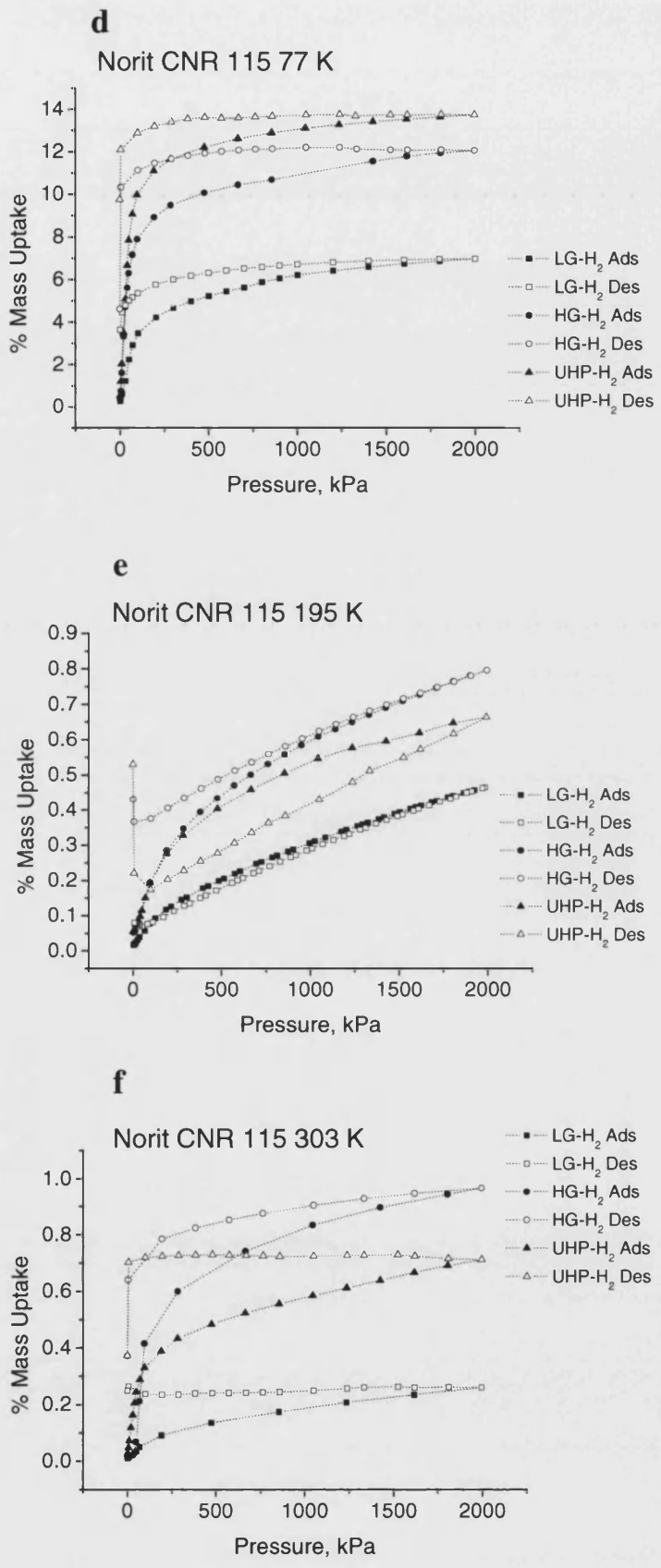

Figure 5.3-8: Graph showing the effect of hydrogen purity on the adsorption capacity of Norit CNR 115 at different temperatures (d) 77 K; (e) 195 K; (f) 303 K.

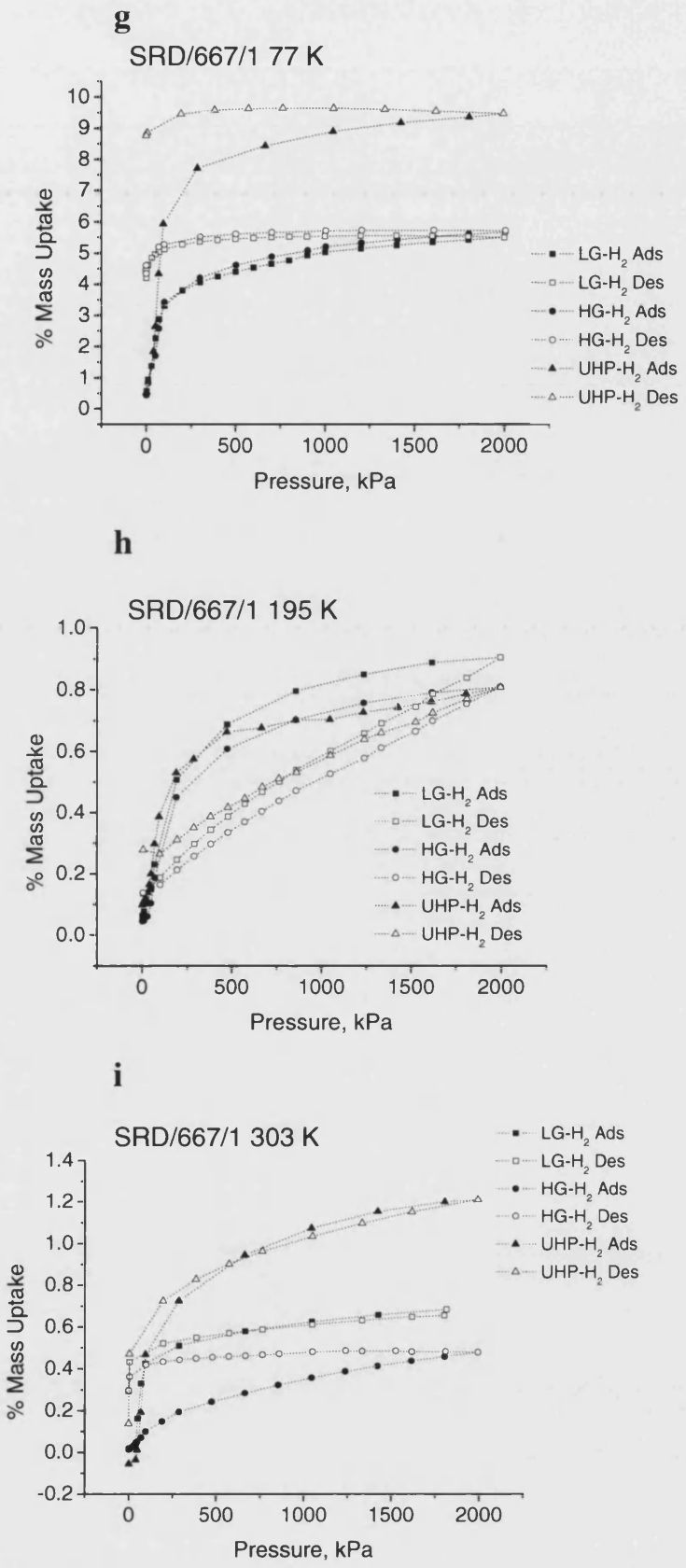

Figure 5.3-9: Graph showing the effect of hydrogen purity on the adsorption capacity of SRD/667/1 at different temperatures (g) 77 K; (h) 195 K; (i) 303 K.

5.3.3 Gravimetric Hydrogen Isotherms on the Carbon Nanotubes

The carbon nanotubes labelled SWNT-1, SWNT-2, MWNT-1 and MWNT-2 have been investigated for their hydrogen storage potential to complement the work on activated carbons. The isotherms on these materials were measured solely at 77 K due to high demand on machine time and a realisation that the amount adsorbed at this temperature represents a good approximation of the optimum amount of hydrogen storable on these materials.

All isotherms exhibit Type 1 behaviour as observed with the activated carbon materials but the surface excess of hydrogen in MWNT-1 increases with increasing pressure. At low pressures, it goes through a maximum value and then it decreases with increasing pressure. This follows the definition of the surface excess of a pure gas as described by Sircar (1999). The extent of reversibility and hysteresis observed on these materials is discussed in detail in Section 6.3.3.

Figure 5.3-10 and Figure 5.3-11 show the sorption curves obtained. It is observed that SWNT-2 has the highest uptake of carbon nanotubes with 11.98 wt-% obtained from the LG-H_2 experiments and 7.63 wt-% obtained from the UHP-H_2 experiment. SWNT-1 has a measured uptake of 7.24 and 6.68 wt-% for LG and UHP H_2 respectively. MWNT-1 exhibits uptake values of 4.24 wt-% for LG-H_2 and 2.95 wt-% for UHP-H_2. MWNT-2, on the other hand, shows the lowest uptake adsorbing only 0.83 wt-% for LG-H_2 and 0.85 wt-% on the UHP-H_2. This is an interesting observation because SWNT-2 has the highest BET surface area (807.6 $m^2\ g^{-1}$) of the carbon nanotubes with MWNT-2 having the lowest (16.3 $m^2\ g^{-1}$). Also interesting is that MWNT-2 is the only carbon nanotube studied here that has been opened on the ends (manufacturer communication) and as observed by TEM. The observed low values of uptake observed for MWNT-2 is contrary to the work of Darkrim and Levesque (2000) and Hou *et al.*, 2002. They report that carbon nanotubes with open ends have a higher capacity for hydrogen storage. A comparison between the storage amounts observed for SWNT-2 and the results of Ye *et al.*, (1999) quoting a storage capacity of 8.25 wt-% at 77 K for single walled nanotubes suggests that the value

obtained in this work is in agreement with literature data. The GCMC simulation results of Darkrim and Levesque (2000) of hydrogen storage at 77 K in carbon nanotubes quote a hydrogen storage capacity of 11.24 wt-%, which is also in agreement with the amounts reported here. Lueking and Yang (2002), also report that the residual metal content of the single walled nanotube samples from their preparation may enhance their uptake of hydrogen through the spillover from the metal to the carbon surface (Lueking and Yang, 2002). This is interesting because SWNT-2 with the highest uptake has been produced via catalytic chemical vapour deposition (CVD) with a residual metal content of 4.2 wt-% (comprising 4 wt-% Fe and 0.2 wt-% Mg). The high uptake values observed at 77 K may be linked partially to the metal content of this material.

Both single and multi-walled carbon nanotubes assemble to form bundles as a result of the van der Waals forces between tubes. In a bundled sample, there are several sites where hydrogen can be adsorbed, such as in the tubes (if the tubes are open), in the interstitial sites between the tubes and or on the outer surface of the bundle (Atkinson and Roth, 2003; Liu and Cheng, 2005, Levesque *et al.*, 2002). Cheng *et al.*, 2001 discussed the work of Dresselhaus (1999), stating that a hydrogen molecule adsorbed in the interstitial space undergoes much stronger surface attraction than on a single planar graphene surface, since it is in close proximity to three graphene surfaces. This implies that the hydrogen adsorbed in that space would be expected to be denser that on the single graphene sheet (Cheng *et al.*, 2001).

According to Levesque *et al.*, (2002) due to the limited range of the attractive van der Waals interactions between hydrogen molecules and the carbon atoms, the adsorption is not very much increased if the nanotubes are multi-walled. This is in agreement with the observation in this work that the capacity to store hydrogen is clearly not improved by the use of multi-walled nanotubes. This can be supported with the fact that the interlayer separation distance between the tube layers is 0.34 nm (distance between two graphitic layers). If the tubes are open, most of the hydrogen will be stored in the hollow centre of the tubes as opposed to between the layers, but if the tube ends are capped, the multilayer structure provides an insignificant improvement to the hydrogen storage capacity of the nanotube. The surface and pore structure of carbon nanotubes determine their storage performance in gas adsorption.

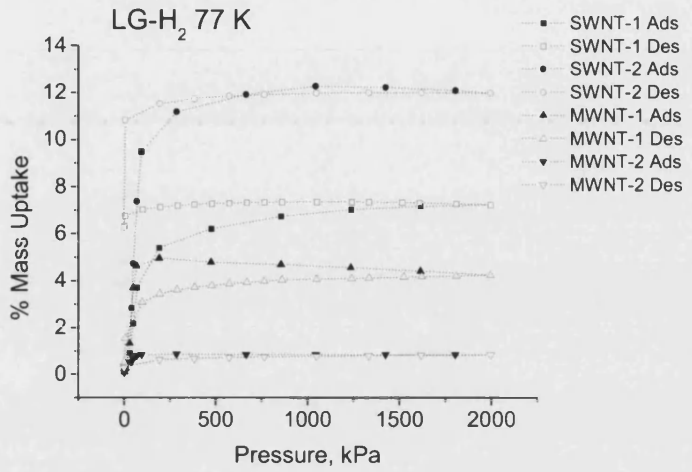

Figure 5.3-10: Overlay of hydrogen sorption isotherms on the carbon nanotubes using LG-H_2 at 77 K

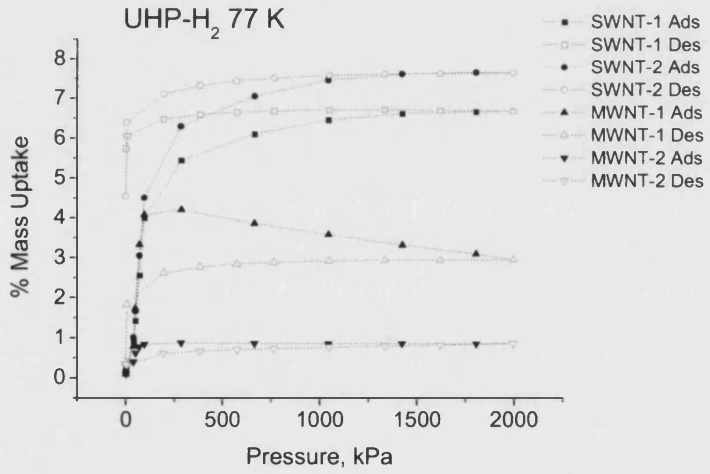

Figure 5.3-11: Overlay of hydrogen sorption isotherms on the carbon nanotubes using UHP-H_2 at 77 K

5.3.4 Effect of Gas Purity on Adsorption in Nanotubes

In this section, the effect of hydrogen purity on the amount of gas adsorbed onto the nanotubes at 77 K is reported. The results are shown in Figure 5.3-12 (a – d). It is observed that the amount of gas adsorbed using LG-H_2 is higher than the amount adsorbed with UHP-H_2 and is evident for SWNT-1, SWNT-2 and MWNT-1. This observation is contrary to the findings of the measurements with the activated carbons. On MWNT-2, the amounts adsorbed are marginally different, 0.83 and 0.85 wt-% is adsorbed for the LG and UHP H_2 respectively. It can be deduced that for MWNT-2, H_2 purity has a minimal effect on the quantity adsorbed.

Hysteresis is observed on the isotherms of SWNT-1 and SWNT-2, shown in Figure 5.3-12 (a, b) whereas for the multi-walled nanotubes it is negligible and considered fully reversible (Figure 5.3-12 (c) and (d)). The inclination towards chemisorption can be eliminated because the heat of adsorption for a carbon nanotube hydrogen gas system, although not measured in this work is reported to be ~ 6.3 kJ mol^{-1} (Cheng *et al.*, 2001). This value is not high enough for chemisorption to be considered feasible. The presence of residual metal in SWNT-1 and 2 can also be linked to the observed hysteresis following the suggestions of Lueking and Yang (2002). The difference in the observed maximum uptake for SWNT-1 for both grades of hydrogen is 0.56 wt-%, for SWNT-2, this difference is 4.35 wt-%, while for MWNT-1 and MWNT-2 this difference is 1.29 and 0.02 wt-% respectively.

The observed difference in the behaviour of the activated carbons and the carbon nanotubes to sorption using different grades of hydrogen such that in the case of the activated carbons, the uptake increases with enhanced hydrogen purity and for the nanotubes the uptake decreases with enhanced hydrogen purity at 77 K is not surprising since the mechanisms of adsorption in both materials are different. Studies have been done on the molecular selectivity of carbon nanotubes by Arab *et al.*, (2004) to suggest that there are adsorption sites in single walled nanotubes that selectively adsorb molecules such as nitrogen and carbon dioxide based on the potential energy. This mechanism of adsorption in these nanoporous carbons using kinetic hydrogen sorption data is further developed in Section 6.4.

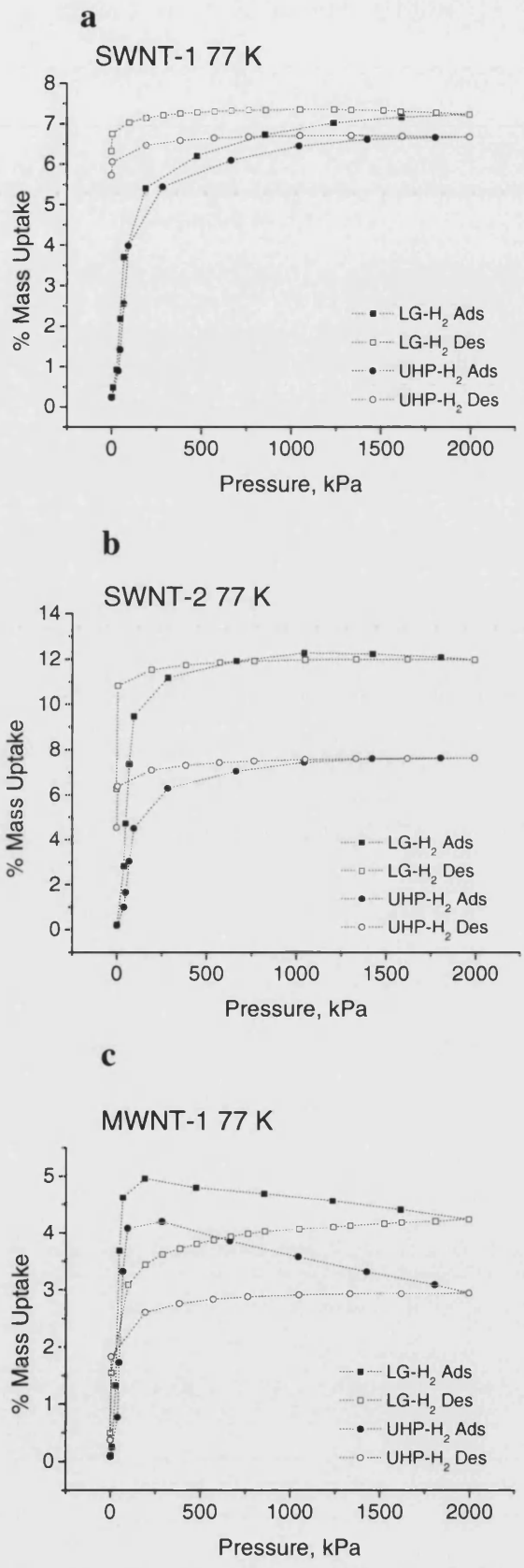

Figure 5.3-12: Graph showing the effect of gas purity on the amount adsorbed at 77 K on (a) SWNT-1; (b) SWNT-2; (c) MWNT-1.

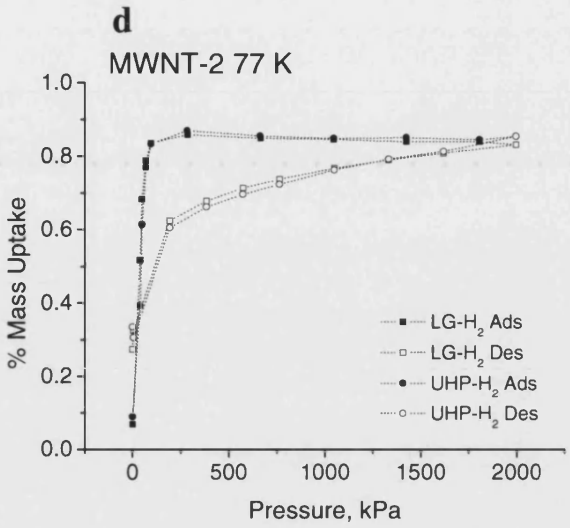

Figure 5.3-12: Graph showing the effect of gas purity on the amount adsorbed at 77 K on (d) MWNT-2.

5.4 Gravimetric Material Cycling Results

Cyclic isotherms at 77 K have been measured for the three activated carbons and the carbon nanotube observed to have the highest uptake (SWNT-2) using UHP-H_2. The results obtained form an essential part of determining the practical application of these materials for storage purposes. In practise, the viability of these materials will depend on the ability to charge and discharge hydrogen readily at predefined temperature and pressure conditions. Hence measuring their cyclability is one way of achieving this along with an understanding of their stability on recycling.

At first glance, the measured cyclic uptakes appear to increase with increasing number of cycles for the carbon materials as shown in Figure 5.4-1 (a), (b), (c) and (d). On closer inspection, this appears not to be the case. The cyclic isotherms have been recalculated using the weight at the end of each desorption run to get the values of the actual uptake for the subsequent cycles and are shown in Figure 5.4-1 (e), (f), (g) and (h). Hence they are replots of the same data. This reveals that the amount that can be stored on these materials reduces significantly after the first cycle. On the second and subsequent adsorption-desorption cycles, the amount adsorbed appears to be more stable.

These results indicate that the amounts observed on the subsequent cycles are likely to be a representation of the real adsorption capacity of each of these materials. In practical terms, the use of any of these nanoporous carbons as hydrogen storage media will require a system whereby a fresh batch of the material is loaded for each charge of hydrogen. High uptake of hydrogen will only be achievable if the storage system is maintained at 77 K hence maximising the adsorbent capacity. In a case where the nanoporous carbon is to be recycled, regeneration of the material will be required as an intermediate stage. These results are further analysed in Section 6.3.2.

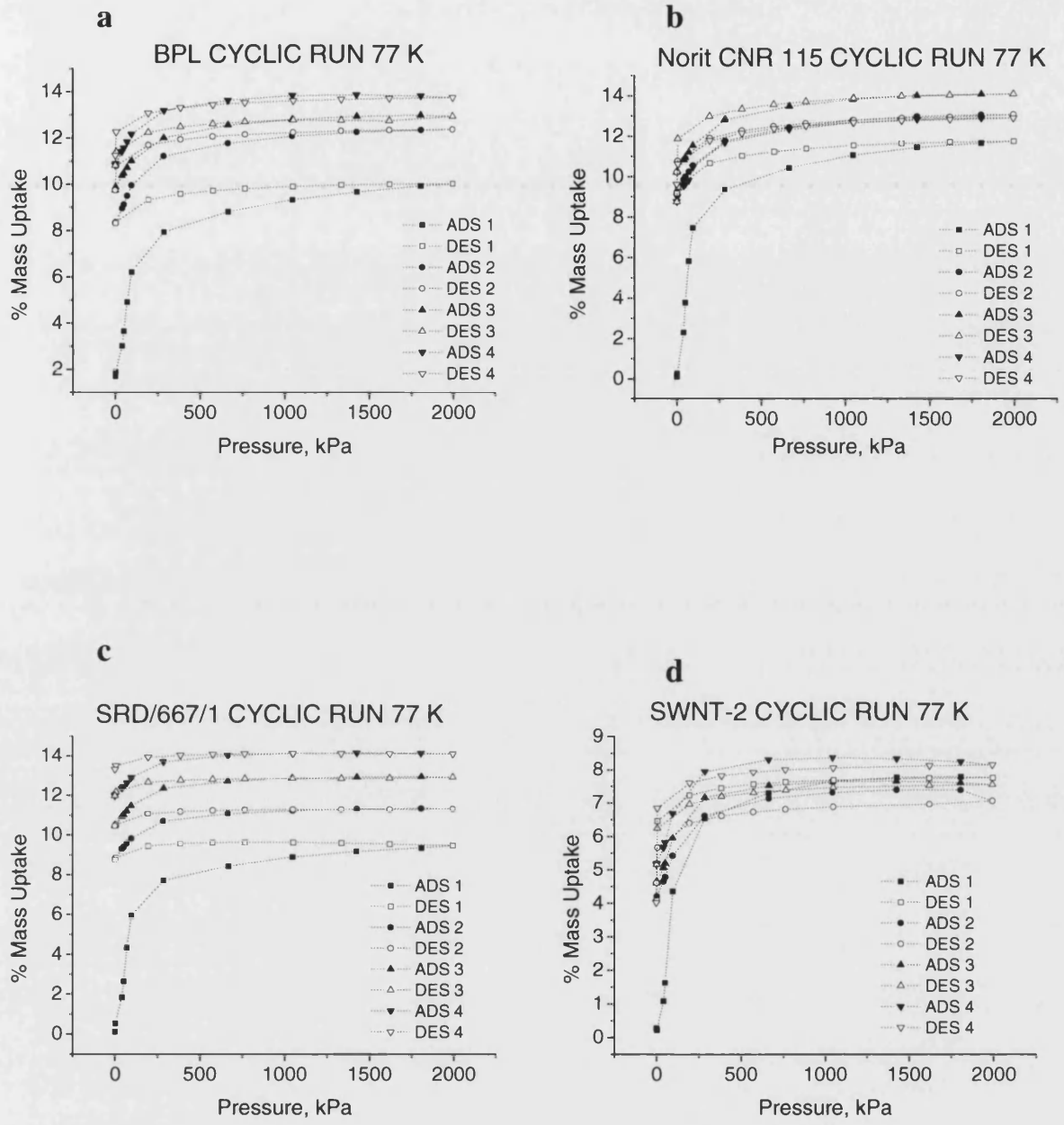

Figure 5.4-1: Graph showing the adsorption and desorption cyclic isotherms for the carbon materials using UHP-H_2 at 77 K on (a) BPL; (b) Norit CNR 115; (c) SRD/667/1 and (d) SWNT-2.

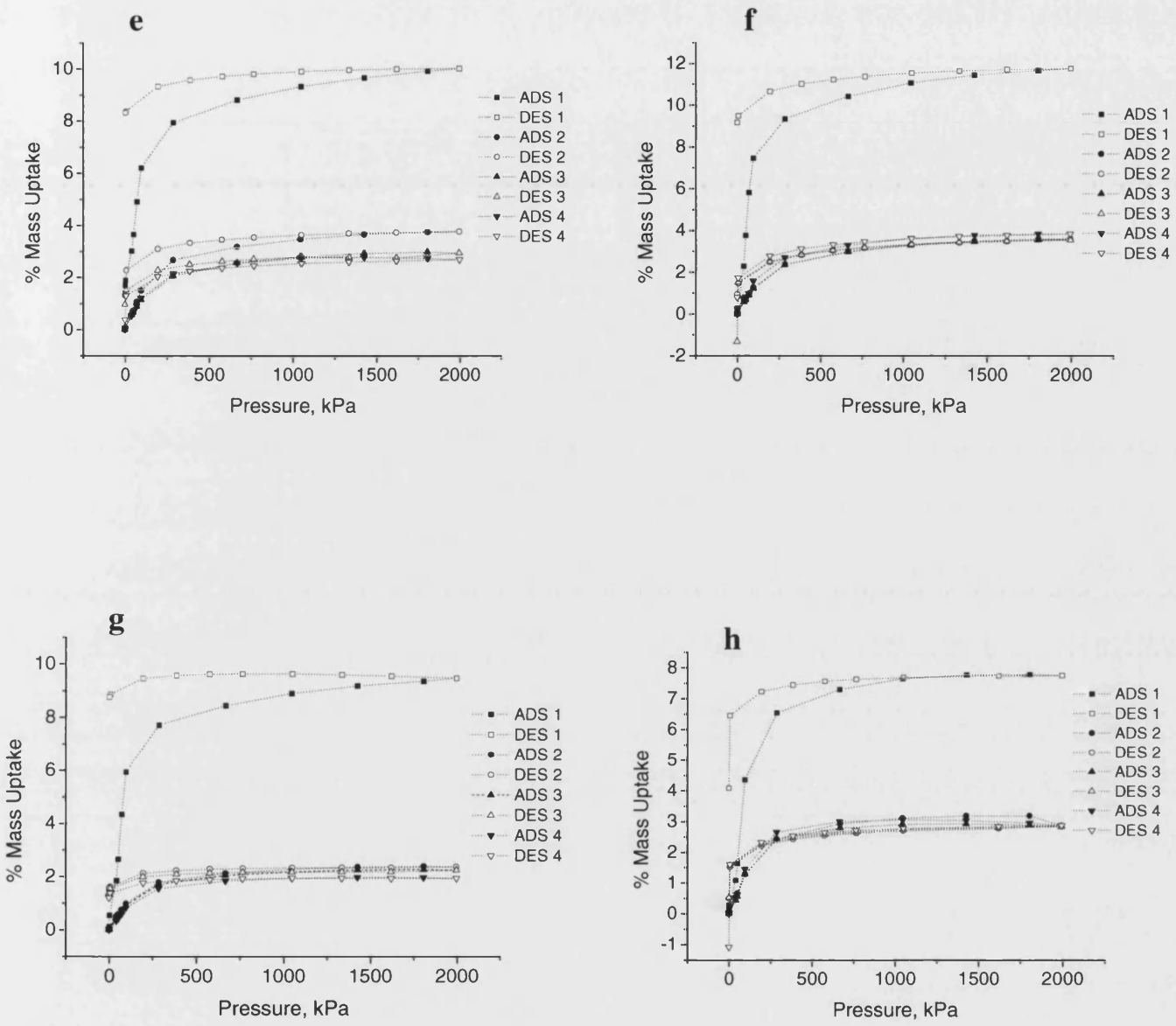

Figure 5.4-1: Graph showing the re-plots (using dry sample mass) of the adsorption and desorption cyclic isotherms on the carbon materials using UHP-H_2 at 77 K on (e) BPL; (f) Norit CNR 115; (g) SRD/667/1 and (h) SWNT-2.

Chapter Six

Gravimetric Data Analysis and Discussion

6.1 Introduction

In this chapter, the analysis of the gravimetric experimental data reported in Chapter 5 will be presented. Empirical adsorption models are used to fit the experimental data to obtain parameters useful for the study of the hydrogen-carbon adsorption system. This chapter is divided into four main sections as described below.

In Section 6.2, the equilibrium hydrogen adsorption isotherms are fitted to empirical adsorption models such as the Toth equation. The resulting model parameters are presented and discussed. A detailed analysis of the errors associated with the fits is also carried out. Section 6.3 deals with the analysis of the sample gravimetric cycling results and the sorption hysteresis observed. The assessment of the hydrogen storage mechanism in the nanoporous carbons is then evaluated in Section 6.4 by analysing the kinetic data using diffusion approximating equations. Section 6.5 is an analysis of the relation between the structural characterisation results presented in Chapter 4 to the hydrogen storage capacity observed in the respective nanoporous carbons as discussed in Chapter 5.

6.2 Hydrogen Sorption Data Analysis

In this section, the gravimetric adsorption data obtained and presented in Chapter 5 have been analysed using empirical adsorption models such as the Langmuir-Freundlich and Toth equations. The results obtained are representative of the characteristics of the hydrogen-carbon adsorption system. The model parameters are then used to calculate quantities such as the heat of adsorption.

6.2.1 Semi-Empirical Adsorption Models

In chapter five, gravimetric hydrogen sorption results were presented for the respective nanoporous carbons. According to the BDDT classification (Sing *et al.*, 1985), the isotherms of these materials are observed to exhibit Type 1 isotherm behaviour at lower temperatures (77 K). It is evident that at higher adsorption temperatures (195 - 303 K), the results exhibit a somewhat 'early Type 1' behaviour such that at higher pressures (approaching 2000 kPa) the graphs still appear to be linear, i.e. within the Henry's law region. The Type 1 behaviour was originally attributed to subcritical systems, i.e. systems where the adsorption temperature (T) is lower than the critical temperature (T_c) of the adsorptive gas so that condensation occurs at saturation. In the case of the hydrogen-carbon adsorption system of interest here, the adsorption conditions are supercritical implying that the temperature of adsorption is above the critical temperature of the adsorptive gas (hydrogen; 33.3 K). Hence there is no condensation taking place, rather the process of adsorption is likely due to gradual densification of the adsorptive near the adsorbent surface.

Several semi-empirical models have been developed following the Langmuir model, which is unsuitable for describing the experimental data of practical solids (Do, 1998) as a result of their complex pore and surface structure. These empirical equations have been applied to a wide range of equilibrium adsorption data with success and hence will be applied in this work. Some of these equations include the Freundlich, Langmuir-Freundlich or Sips equations, the Toth, Unilan and Keller, *et al.* equations.

These equations are not without their respective limitations and are described in Sections 6.2.1.1 to 6.2.1.7 and summarised in Table 6.2-1.

6.2.1.1 Langmuir Model

The basic theory of the Langmuir model (Langmuir, 1916) considers adsorption onto a flat surface such that the adsorptive molecules continuously bombard the surface of the adsorbent and there is subsequent desorption such that there is a zero rate of accumulation at the surface at equilibrium (Do, 1998). This model assumes that the surface of the adsorbent is energetically homogeneous, that is constant over all adsorption sites, it also assumes that adsorption occurs at definite localised sites on the surface of the adsorbent and finally that each site can accommodate only one molecule (Langmuir, 1916, Jaroneic and Madey, 1988; Do, 1998, Yang, 2003).

The Langmuir equation written in terms of the amount adsorbed is shown in Equation 6.2-1 below.

$$n = n_o \frac{b(T)P}{1 + b(T)P}$$ **Equation 6.2-1**

Where n is the total amount adsorbed (% mass); n_0 is the maximum amount that can be adsorbed on the adsorbent, corresponding to complete monolayer coverage; b is the affinity constant (a measure of how strongly the adsorbate is attracted to the adsorbent surface) and P is the pressure. This equation reduces to the Henry's law when the pressure is very low implying that the amount adsorbed increases linearly with pressure, a constraint demanded by statistical thermodynamics (Do, 1998). The oversimplified nature of this model as a result of the governing assumptions limits its application for certain adsorption systems.

6.2.1.2 The Freundlich Model

The Freundlich equation being one of the earliest empirical equations used to describe equilibrium adsorption data is very popular and applicable to gas phase systems, its range of validity relies on the pressure range used in measurement and is described by Equation 6.2-2. It assumes that the surface of the adsorbent is heterogeneous in the sense that the adsorption energy is distributed, with sites having the same energy grouped into one patch (Do, 1998) and there is no interaction between patches. It also assumes that on each patch the adsorbate molecule only adsorbs onto one adsorption site making the Langmuir equation applicable on each patch.

$$n = KP^{1/c} \qquad \textbf{Equation 6.2-2}$$

This equation is applicable to gas phase systems having energetically heterogeneous surfaces, when the pressure range is not too wide since it does not have a proper Henry's law behaviour at low pressures and also does not have a finite limit at high pressures. It is thus only valid in the narrow range of the adsorption data. Its parameters K and c are generally temperature dependent with c being a constant that characterises the heterogeneity of the system.

6.2.1.3 The Langmuir-Freundlich Model

The Langmuir-Freundlich (LF) equation was formulated in an attempt to solve the problem of infinite uptake as pressure (P) is increased as observed with the Freundlich equation. This equation is based on the assumption that the energy distribution along the surface of the adsorbent exhibits a Gaussian shape such that when the energy is either larger or smaller than the maximum energy, the distribution exhibits an exponential decay (Do, 1998). The LF equation is similar to the Langmuir equation with the exception of the additional parameter c and is shown in Equation 6.2-3.

$$n = n_0 \frac{(bP)^{1/c}}{1+(bP)^{1/c}}$$ **Equation 6.2-3**

When c equals 1, the LF equation reduces to the Langmuir equation, as P tends to 0 with c equals 1, it reduces to Henry's law and when c is not equal to 1 but P tends to 0, the Freundlich equation is obtained. The other LF parameters, n_0 and b represent the maximum capacity of the adsorbent and the adsorption affinity respectively. The LF equation though having a finite limit at high values of pressure still does not give the correct Henry's law limit (Do, 1998).

6.2.1.4 The Toth Model

In contrast to the aforementioned models, the Toth equation assumes that there is an energy distribution on the surface of the adsorbent, such that its surface is energetically heterogeneous. This equation satisfies both limits at either end of the pressure range, that is, Henry's law and saturation, and is popularly used as shown in Equation 6.2-4.

$$n = n_0 \frac{(bP)}{[1+(bP)^t]^{1/t}}$$ **Equation 6.2-4**

In this equation, the parameter, t is usually less than 1 and is specific for adsorbate-adsorbent pairs along with the affinity parameter, b. The parameters b and t in Toth equation are temperature dependent. When t equals 1, the Toth isotherm reduces to the Langmuir equation; hence like the LF equation, this parameter is said to characterise the heterogeneity of the system. The further it deviates from 1, the more energetically heterogeneous the system is. The Toth equation has correct limits when P approaches 0 or infinity. Being a three-parameter model, the Toth equation can describe well a range of adsorption data (Do, 1998). This model is recommended as the ideal choice of isotherm equations for fitting experimental data on hydrogen adsorption on activated carbon (Do, 1998; Valenzuela and Myers, 1989).

6.2.1.5 The Unilan Model

The Unilan equation is obtained by assuming a patchwise distribution on the adsorbent surface with each patch being ideal such that the Langmuir model is applicable on each of them, similar to the Freundlich. The energy distribution here is assumed to be uniform and the equation is expressed as shown Equation 6.2-5.

$$n = \frac{n_0}{2s} \ln\left(\frac{1+\bar{b}e^{s}P}{1+\bar{b}e^{-s}P}\right)$$ **Equation 6.2-5**

The parameter s characterises the heterogeneity of the system, the larger it is the more heterogeneous is the system. When $s = 0$, the Unilan equation reduces to the classical Langmuir equation because in this limit the range of energy distribution is 0. The Unilan equation has the correct behaviour at low and high pressures but its assumption of uniform energy distribution is probably too constraining.

6.2.1.6 The Keller, Staudt and Toth Model

The Keller *et al.* model (1996) is similar to the Toth model with the exception that the exponent α is a function of pressure rather than a constant as in the Toth equation. Also the saturation capacities of different species are different. The form of the equation is shown in Equation 6.2-6.

$$n = n_0 \alpha_m \frac{bP}{[1+(bP)^{\alpha}]^{1/\alpha}};$$
$$\alpha = \frac{1+\alpha_m \beta P}{1+\beta P}$$ **Equation 6.2-6**

Where the parameter α_m is expressed as $\alpha_m / \alpha_m^* = \left(r / r^*\right)^{-D}$; r is the molecular radius and D is the fractal dimension of the adsorbent surface. This equation contains more

parameters than the aforementioned models (Keller *et al.*, 1996) and has a Henry's law limit and a finite saturation limit.

Other empirical models such as the Dubinin-Radushkevich (DR), Jovanovich and Temkin equations are also available, but the models described above have been considered for further data analysis. The DR model has been discussed and applied to the nitrogen and carbon dioxide subcritical adsorption data obtained for the carbon materials in Chapter 4. It is necessary to bear in mind that the DR equation applies mainly to subcritical systems and does not satisfy the requirements of the data obtained here, it does not have a Henry's law limit but reaches a finite limit when P approaches P^0. The Temkin equation was originally proposed for chemisorption systems while the Jovanovich equation is an unpopular yet useful empirical equation having a Henry's law limit and a finite saturation limit (Do, 1998). Table 6.2-1 below is a summary of the different empirical model equations and their respective parameters as described in the above sections.

6.2.1.7 The Modified Toth Model

The adsorption isotherms of SWNT-2, MWNT-1 and MWNT-2 show 'excess' effects, characterised by a downturn in the amount adsorbed at higher pressures. This can be explained using the Gibbs Surface Excess (GSE) theory described in Chapter 5. These isotherms cannot be easily described with a standard Toth model as it predicts the total amount adsorbed as opposed to the excess and require the inclusion of an additional term shown in Equation 6.2-7 below. This equation is being called the 'Modified Toth' equation for purposes of distinguishing it from the original Toth equation.

$$n = n_0 \frac{(bP)}{[1+(bP)^t]^{1/t}} - \rho_b V_a \qquad \textbf{Equation 6.2-7}$$

The parameters have the same meaning as specified above, ρ_b is the bulk density of hydrogen (mol cm^{-3}) at the measurement conditions (the ideal gas equation of state

may be assumed to be valid for the range of measurement) and V_a is the volume (cm^3 g^{-1}) of the adsorbed phase comparable with the pore volumes of the adsorbents obtained from nitrogen and carbon dioxide in Chapter 4. During fitting, this parameter can be set as a variable or defined as a constant. In this work, it was chosen to be a variable to see how the values obtained compare with the pore volumes obtained from nitrogen. The fitted isotherms are shown in Figure 6.2-3.

Table 6.2-1: Table showing the different semi-empirical equations (Equations sourced from Do, 1998)

Model	Equation	Parameters
Langmuir	$n = n_0 \frac{b(T)P}{1+b(T)P}$	n_0, b
Freundlich	$n = KP^{1/c}$	K, c
Langmuir-Freundlich	$n = n_0 \frac{(bP)^{1/c}}{1+(bP)^{1/c}}$	n_0, b, c
Toth	$n = n_0 \frac{(bP)}{[1+(bP)^t]^{1/t}}$	n_0, b, t
Unilan	$n = \frac{n_0}{2s} \ln\left(\frac{1+\bar{b}e^{s}P}{1+\bar{b}e^{-s}P}\right)$	n_0, $\bar{b}$, s
Keller, Staudt and Toth	$n = n_0 \alpha_m \frac{bP}{[1+(bP)^{\alpha}]^{1/\alpha}}$; $\alpha = \frac{1+\alpha_m \beta P}{1+\beta P}$	n_0, b, β, α

6.2.1.8 General Discussion

Each of the adsorption models described above has been used to fit a set of gravimetric hydrogen adsorption data for Norit CNR 115 at 77 K, as an example, to determine which model is most suitable for the description of the experimental data. A decision on the most suitable adsorption model will be based on the following.

i. *The governing assumptions of the model;*
ii. *The quality (or goodness) of the fit determined by visual examination, residual and error analysis.*

The determination of the goodness of fit and error analysis has been carried out using the methods described in Section 6.2.2. The commercial graphing and data fitting software, ORIGIN has been used for fitting the empirical equations to the experimental data. A nonlinear least square fitting (NLSF) tool incorporated into ORIGIN is used. The selected adsorption model equation is entered into the tool and the model parameters to be calculated are defined. The nonlinear regression method used is based on the Levenberg-Marquadt (LM) algorithm, which is the most widely used algorithm in nonlinear least square fitting. Given a set of experimental data points, it optimises the parameters of the adsorption model so that the sum of the squares of the deviation becomes minimal. Since it is a numeric minimisation algorithm, the LM algorithm is an iterative procedure. Initially, best starting values of the required parameters are entered and then iterations (typically 100) are performed to give optimal values of the required parameters with minimal error.

Figure 6.2-1 shows the respective plots and fits to the same experimental data set. It is evident by an initial visual assessment of the plots that the Langmuir and Freundlich models give poor fits of the experimental data. The Langmuir model tends to underestimate the adsorption capacity close to saturation while the Freundlich model overestimates these values. The oversimplified assumptions of the 2-parameter models also add to their inadequacy in representing the experimental data. While the Langmuir model assumes that the surface of the adsorbent is energetically homogeneous, such that the distribution of energy is the same on every site on the

surface, the Freundlich model assumes surface heterogeneity applicable to activated carbon adsorption systems. As previously mentioned, the Freundlich model is only valid within a limited pressure range and as it does not have the appropriate Henry's law behaviour at low pressures and also a finite saturation limit at higher pressures, hence the inadequacy of these models in fitting the experimental data. Therefore, the system parameters obtained from using these two models can be considered as inaccurate.

The quality of the fit obtained, on the other hand, using the Langmuir-Freundlich, Toth, Unilan and Keller *et al.*, equations is an improvement on the other two models. This might be as a result of the additional parameters in their equations. The LF model provides an improvement compared to the 2-parameter models but still slightly underestimates the values of adsorption close to saturation. Although this model is applicable to heterogeneous systems, it is worth noting that it does not reduce to the Henry's law at low pressures. The Toth model provides an even better fit of the experimental data; it reduces to the Henry's law at low pressures and has a finite limit at higher pressures. The Unilan and Keller *et al.* method also give good fits of the data, they both have the correct Henry's law limit and a finite limit at high pressures. The choice on which of these three models best fits the data requires a closer examination of the data by plotting the residuals of each fit and calculating the root mean square error. The results are presented in Section 6.2.2.1.

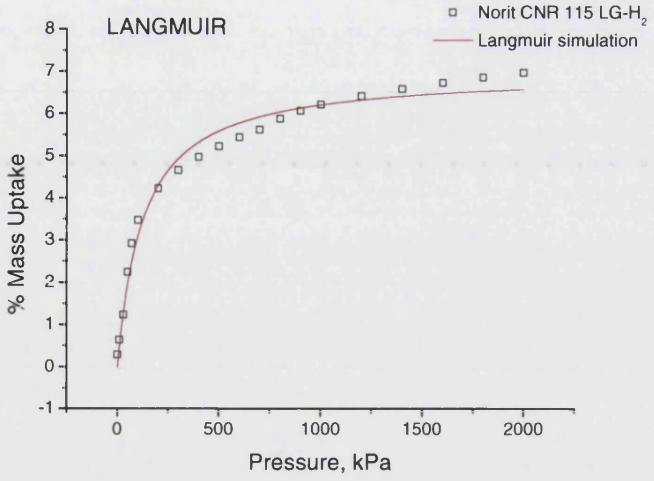

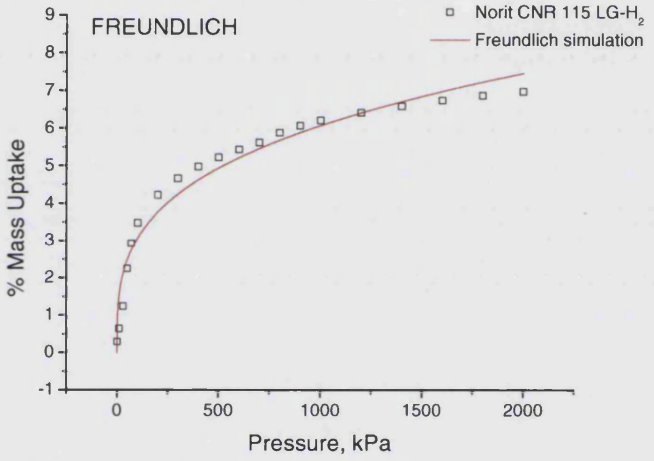

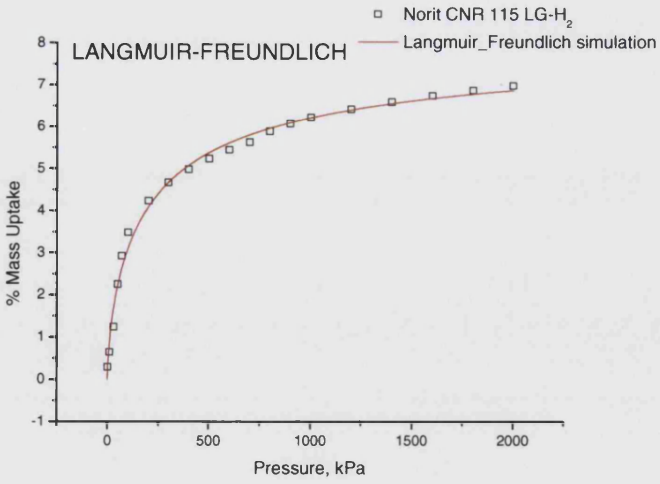

Figure 6.2-1: Fits of the different adsorption models to gravimetric hydrogen uptake data obtained at 77 K on Norit CNR 115 using LG-H_2.

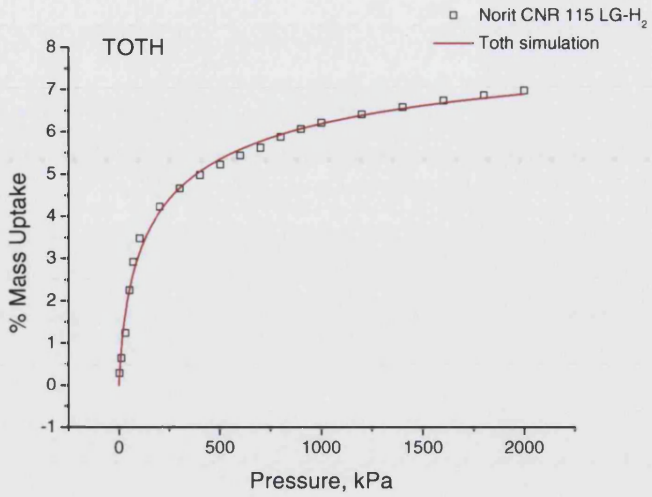

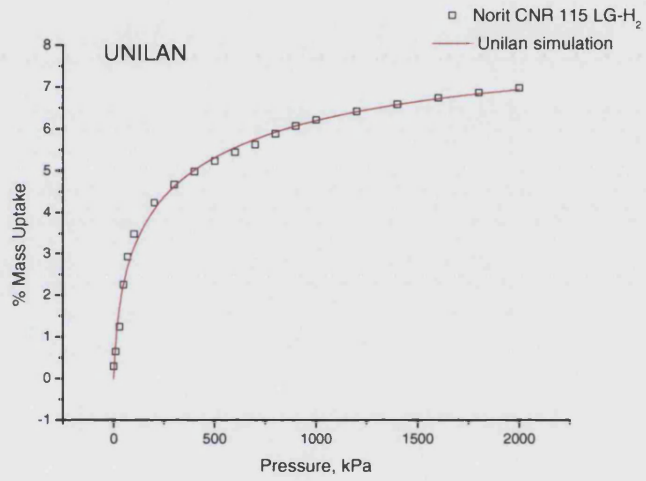

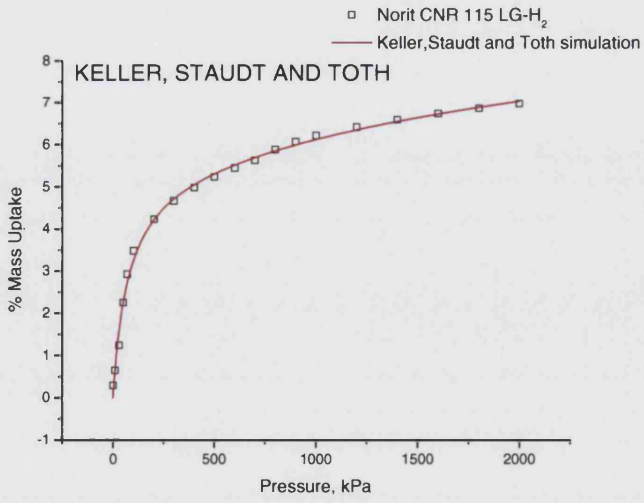

Figure 6.2-1: Continued from previous page (Fits of the different adsorption models to gravimetric hydrogen uptake data obtained at 77 K on Norit CNR 115 using LG-H_2).

6.2.2 Goodness of Fit and Error Analysis

In this section, the evaluation of the 'goodness of fit' and analysis of the error associated with the fits carried out with the different adsorption models to ascertain their suitability for fitting the experimental data is reported.

When experimental data has been fitted to a model, it is important to assess the quality or 'goodness' of the fit. This assessment allows for the determination of the model parameters with minimal uncertainty and provides a good description of the experimental observation. There are a number of ways in which this can be accomplished. Initially, a visual examination of the fit to the experimental data provides preliminary information on the quality of the fit, following on from this, the residual and the root mean square error (RMSE) can be calculated.

6.2.2.1 Residual

The residual, r, from a fitted model is defined as the difference between the experimental observation and the predicted observation obtained from the model. Mathematically,

$$r = y - y_i^{'} \qquad \textbf{Equation 6.2-8}$$

where y is the experimental observation (% mass uptake) and $y_i^{'}$ is the model prediction (% mass uptake). If the model used is a good representation of the experimental data, the residual will be an approximation of the random errors associated with the fit. That is, if the residuals appear random, then the model is a good fit of the experimental data. However, the appearance of a systematic pattern in the observed residual indicates a bias in the fit. Figure 6.2-2 shows the residual plots for the different adsorption models fitted to a sample set of data on Norit CNR 115 at 77 K using low-grade hydrogen. The residual appears randomly distributed around zero for the fits carried out using the Toth, Langmuir-Freundlich, Unilan and Keller *et*

al., models. The residuals of the Langmuir and Freundlich fits are not randomly distributed around zero indicating that these models are a poor fit for the data.

At this point, it is obvious that a choice of either one of the Toth, Unilan or the Keller *et al.* method will be suitable for describing the experimental adsorption data. This fact is further highlighted by the comparison of the R^2 values obtained from each fit shown in Table 6.2-2.

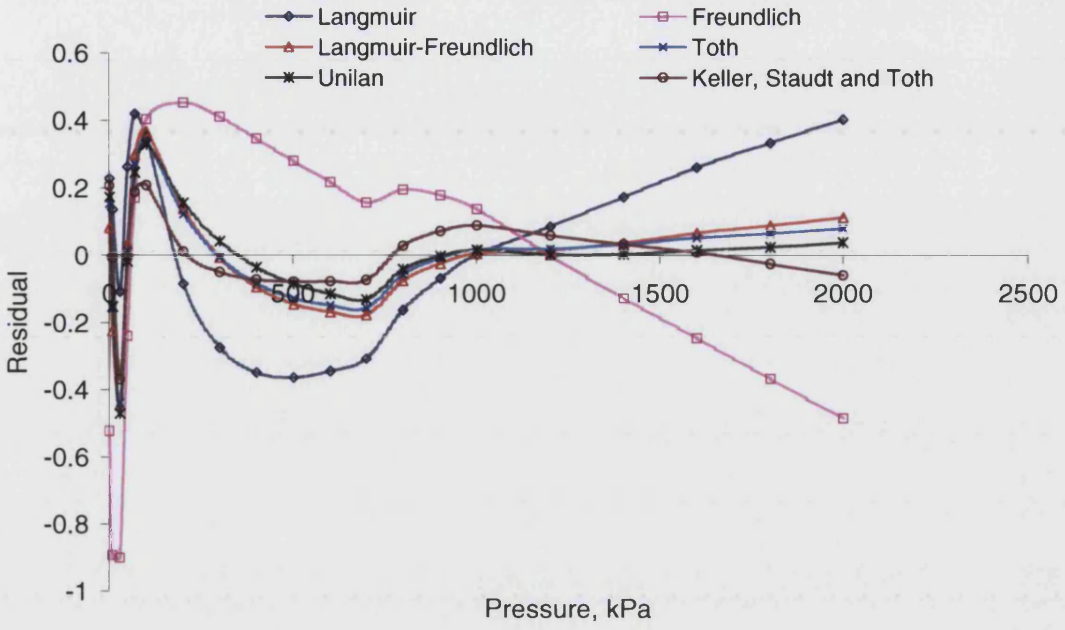

Figure 6.2-2: Residual plots for the fitted isotherm to different adsorption models.

Table 6.2-2: R^2 for the Langmuir, Freundlich, Langmuir-Freundlich, Toth, Unilan and Keller *et al.* fits to the adsorption isotherm of Norit CNR 115 using LG-H_2

	Langmuir	Freundlich	LF	Toth	Unilan	Keller *et al.*
R^2	0.98370	0.96173	0.99282	0.99388	0.99408	0.99648

6.2.2.2 The Root Mean Square Error (RMSE)

The RMSE is being employed here as a statistic for assessing the quality of a fit of the empirical isotherm models to the experimental data. The RMSE is also known as the fit standard error or the standard error of regression. It is calculated using the mathematical relationship below.

$$RMSE = \sqrt{\frac{\sum (y - y_i')^2}{N_d - N_p}} \qquad \textbf{Equation 6.2-9}$$

The denominator in the above equation refers to the degrees of freedom, where N_d is the number of data points to be fitted and N_p is the number of parameters in the model equation used. The parameters of each of the adsorption models are listed in Table 6.2-1. The respective RMSE have been calculated in relation to how the different models fit the experimental data and are shown in Table 6.2-3.

The Langmuir model has an average error of 5.3 %, the Freundlich, 7.5 %, the LF, 3.0 %, the Toth, 2.7 % with the Unilan and Keller *et al.*, models having an average error of 2.5 and 2.1 % respectively. The RMSE associated with the Toth, Unilan and Keller *et al.* methods are generally of the same order of magnitude. Therefore, a choice of using the Toth model to represent the experimental data is reasonable. This is based on the evidence that it has the correct limits at high and low pressure as previously mentioned, it is the simplest model with the minimal number of parameters providing an adequate fit of the experimental data with minimal error and does not give a biased fit based on the assessments of the residual plots.

Table 6.2-3: Table showing the root mean square error on the fits to Norit CNR 115 adsorption data at 77 K

Pressure, kPa	Experimental % Mass	RMSE Langmuir	RMSE Freundlich	RMSE LF	RMSE Toth	RMSE Unilan	RMSE Keller *et al.*
1.17	0.29	0.05	0.12	0.02	0.04	0.04	0.05
9.84	0.65	0.03	0.20	0.05	0.04	0.03	0.002
29.96	1.24	0.02	0.20	0.10	0.10	0.11	0.09
49.84	2.25	0.06	0.05	0.008	0.004	0.004	0.001
70.12	2.93	0.09	0.04	0.07	0.06	0.06	0.04
101.46	3.48	0.08	0.09	0.08	0.08	0.08	0.05
201.82	4.23	0.02	0.10	0.03	0.03	0.04	0.003
301.32	4.66	0.06	0.09	0.001	0.001	0.01	0.01
401.00	4.98	0.08	0.08	0.02	0.02	0.01	0.02
501.32	5.23	0.08	0.06	0.03	0.03	0.02	0.02
601.24	5.44	0.08	0.05	0.04	0.03	0.03	0.02
700.93	5.62	0.07	0.04	0.04	0.04	0.03	0.02
801.04	5.88	0.04	0.04	0.02	0.01	0.01	0.01
901.17	6.07	0.02	0.04	0.006	0.002	0.0004	0.02
1001.19	6.22	5.77e-04	0.03	0.001	0.004	0.004	0.02
1201.22	6.42	0.02	3.39e-05	0.003	0.004	0.0005	0.01
1401.19	6.59	0.04	0.03	0.008	0.007	0.0008	0.01
1601.58	6.74	0.06	0.05	0.02	0.01	0.004	0.002
1801.07	6.87	0.07	0.08	0.02	0.01	0.006	0.006
1999.80	6.98	0.09	0.11	0.03	0.02	0.009	0.01

6.2.2.3 Fitting of Equilibrium Hydrogen Adsorption Isotherms to the Toth Model

The respective Toth fits of the gravimetric equilibrium data on the nanoporous carbons are presented in Figure 6.2-3 and 6.2-4. The model predicts the data well and provides parameters with minimal errors. The parameter n_0 corresponds to the maximum uptake on the adsorbent (% mass), b is the affinity constant with a temperature dependency (kPa^{-1}), while t is the dimensionless parameter that characterises the heterogeneity (energetic) of the adsorption system. Table 6.2-4, Table 6.2-6, Table 6.2-8 and Table 6.2-10 show the parameter results obtained from the 'unconstrained' fit of the Toth model to the equilibrium data. They are called 'unconstrained' because the parameter n_0 has been allowed to vary during the fit. Strictly speaking, this parameter might be expected to be constant for a specific adsorbent such that it is independent of the adsorption temperature. Allowing this parameter to vary leads to inconclusive values of the t parameter and hence an inability to assess the extent of heterogeneity of the adsorption system.

In Table 6.2-5, Table 6.2-7 and Table 6.2-9, the parameter values obtained from the constrained Toth fits of the adsorption isotherms of the activated carbons are shown. The parameter n_0 is kept constant at the values obtained experimentally at 77 K using ultra high purity (UHP) H_2. This amount is assumed to be representative of the maximum amount of hydrogen that can be adsorbed onto each of the carbon materials studied. The other Toth parameters b and t are allowed to vary.

In both fits (constrained and unconstrained), it is observed that the value of the parameter b decreases as the temperature of adsorption increases for all the activated carbons, which is intuitively correct. This is because the larger the affinity constant, b, the more the surface of the adsorbent is covered with adsorbate molecules as a result of the stronger affinity of the adsorbate molecules to the surface of the adsorbent. This is verified by the decrease in the amount of hydrogen adsorbed as the adsorption temperature increased as observed from the equilibrium data shown in Figure 6.2-3

and 6.2-4. The values of the heterogeneity parameter t, on the other hand show no certain trend at different temperatures for the unconstrained fits but a definite upward trend is observed with temperature with its value approaching 1 at high temperatures for the constrained fits as shown in Figure 6.2-9. Recalling that the Toth equation reduces to the Langmuir model when $t = 1$, it could be said that the more t deviates from unity the more heterogeneous the system is. It is important to note that the system has the same heterogeneity at all temperatures but the effects of this are less noticeable at high temperature since the thermal energy of the molecules dominate over the surface energy. This surface heterogeneity is an important factor in adsorption systems as stated by Do (1998), that adsorbate molecules prefer to adsorb onto sites of high energy at the initial stages and as adsorption progresses they then adsorb onto sites of decreasing energy, resulting in the slower rise in the amount adsorbed (Do, 1998).

In the case of the carbon nanotubes insufficient machine time prevented measurements to be carried out at higher temperatures therefore, a direct comparison of the Toth parameters based on the effect of temperature cannot be made. The modified Toth fits of the equilibrium data for the carbon nanotubes, SWNT-2, MWNT-1 and MWNT-2 are shown in Figure 6.2-4. It is observed that this equation is a good fit of the equilibrium data. The average errors of the fits are in the range of 0.4 to 9.0 %. The values of the parameters obtained are presented in Table 6.2-10, the value of the heterogeneity parameter t is observed in all cases to be greater than 1 indicating that the adsorption system is heterogeneous for all the nanotubes. The affinity parameter b is observed to be small and within the same order of magnitude as observed with the activated carbons.

It is important to note that for all the nanoporous carbons, the magnitude of the parameter t does not reveal the source of the heterogeneity, that is, whether it is structural or surface related. The values of the additional parameter, the adsorbate volume V_a are observed to be consistent with the pore volumes obtained from the nitrogen experiments for MWNT-2, in the case of SWNT-2 and MWNT-1, these values appear much larger. It could be suggested that the use of the modified Toth equation could be an alternative method for predicting the adsorbate volume (V_a) provided that an excess isotherm is available.

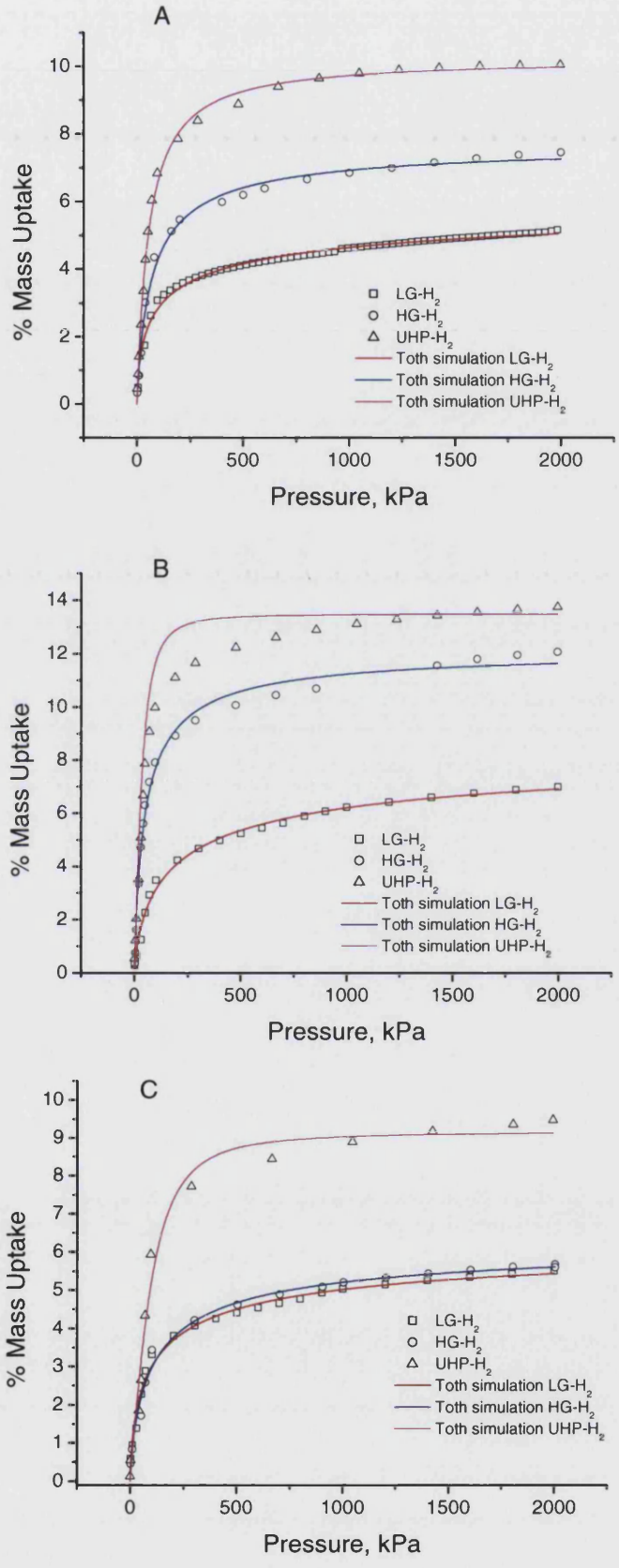

Figure 6.2-3: Toth model fits of gravimetric equilibrium data for the activated carbons; (A) BPL at 77 K; (B) Norit CNR 115 at 77 K; (C) SRD/667/1 at 77 K.

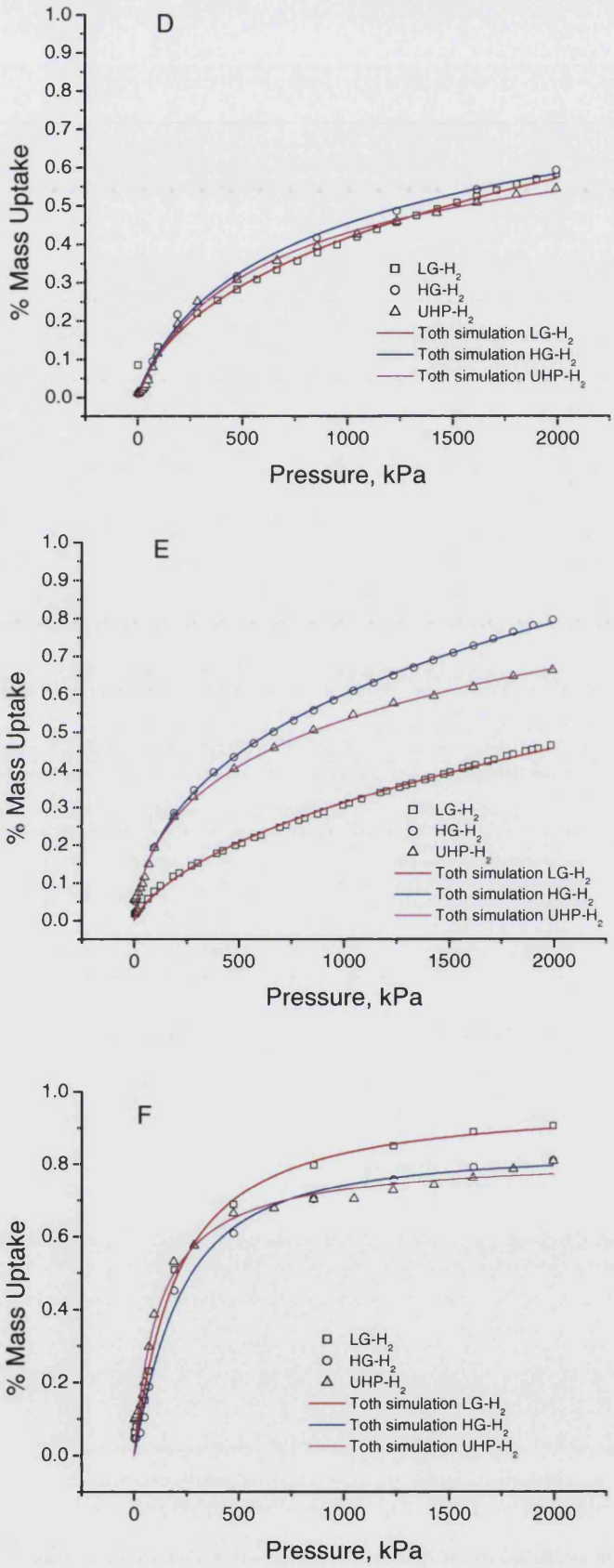

Figure 6.2-3: (D) BPL at 195 K; (E) Norit CNR 115 at 195 K; (F) SRD/667/1 at 195 K.

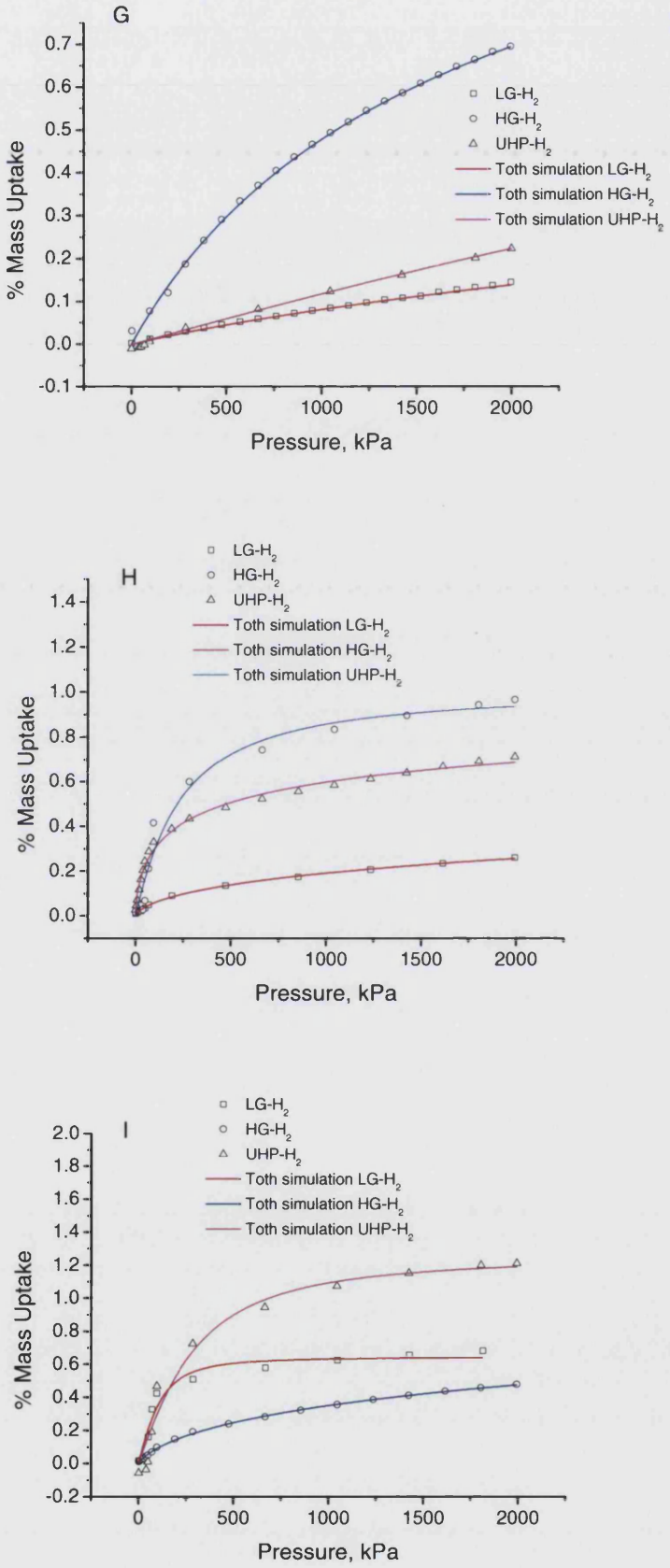

Figure 6.2-3: (G) BPL at 303 K; (H) Norit CNR 115 at 303 K; (I) SRD/667/1 at 303 K.

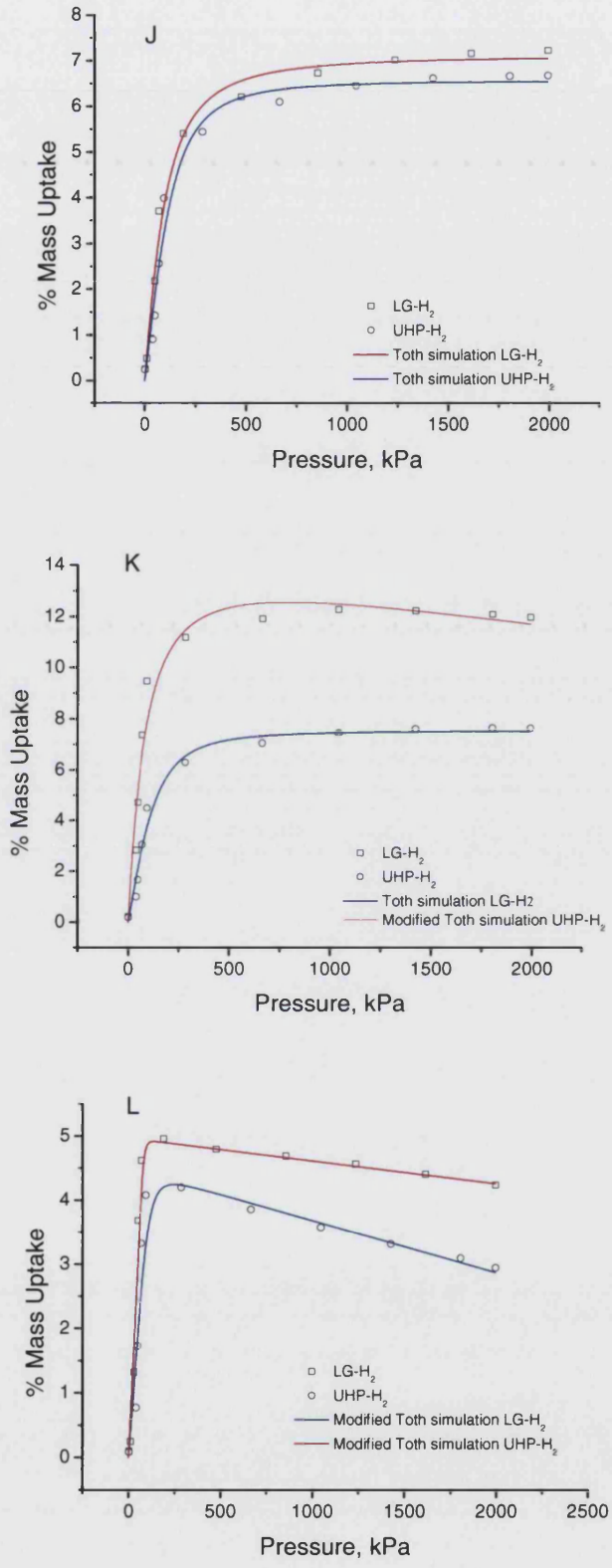

Figure 6.2-4: Toth model fits of gravimetric equilibrium data for the carbon nanotubes; (J) SWNT-1 at 77K; (K) SWNT-2 at 77 K; (L) MWNT-1 at 77 K.

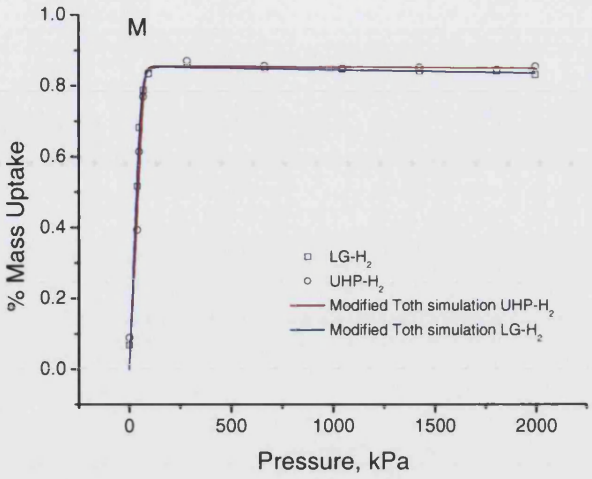

Figure 6.2-4: (M) MWNT-2 at 77 K.

Table 6.2-4: Table showing the 'unconstrained' Toth model parameters (± absolute error) for BPL at different temperatures on the three grades of hydrogen ($\rho_b.V_a$ assumed to be approximately 0)

Temperature, K	n_0, % Mass	b, kPa^{-1}	t
		BPL LG-H_2	
77	6.570 ± 0.223	0.074 ± 1.8E-03	0.427 ± 0.031
195	3.514 ± 5.591	0.001 ± 4.00E-04	0.311 ± 0.223
303	1.024 ± 1.129	0.0001 ± 1.00E-04	0.654 ± 0.299
		BPL HG-H_2	
77	7.743 ± 0.247	0.019 ± 3.00E-03	0.802 ± 0.094
195	1.088 ± 0.338	0.002 ± 3.00E-04	0.607 ± 0.179
303	1.382 ± 0.215	0.0006 ± 5.00E-05	0.904 ± 0.136
		BPL UHP-H_2	
77	10.223 ± 0.139	0.018 ± 2.00E-03	1.027 ± 0.077
195	0.823 ± 0.099	0.019 ± 2.00E-04	0.741 ± 0.110
303	0.670 ± 4.037	0.0002 ± 1.00E-03	1.854 ± 8.079

Table 6.2-5: Table showing the 'constrained' Toth model parameters (± absolute error) for BPL at different temperatures on the three grades of hydrogen ($\rho_b.V_a$ assumed to be approximately 0)

Temperature, K	n_0, % Mass	b, kPa $^{-1}$	t
		BPL LG-H_2	
77	6.570 ± 0.223	0.074 ± 1.8E-03	0.427 ± 0.031
195	6.570 ± 0	0.0001 ± 6.38E-06	0.429 ± 0.027
303	6.570 ± 0	0.00002 ± 4.80E-06	0.501 ± 0.169
		BPL HG-H_2	
77	7.743 ± 0.247	0.019 ± 3.00E-03	0.329 ± 0.220
195	7.743 ± 0	0.0003 ± 1.00E-04	0.396 ± 0.087
303	7.743 ± 0	0.0002 ± 6.44E-06	0.790 ± 0.094
		BPL UHP-H_2	
77	10.223 ± 0.13943	0.018 ± 0.002	0.397 ± 0.162
195	10.223 ± 0	0.0002 ± 1.00E-05	0.540 ± 0.105
303	10.223 ± 0	0.00002 ± 4.00E-05	0.728 ± 1.240

Table 6.2-6: Table showing the 'unconstrained' Toth model parameters (± absolute error) for Norit CNR 115 at different temperatures on the three grades of hydrogen ($\rho_b.V_a$ assumed to be approximately 0)

Temperature, K	n_0, % Mass	b, kPa^{-1}	t
	Norit CNR 115 LG-H_2		
77	8.975 ± 0.708	0.016 ± 3.94E-03	0.540 ± 0.073
195	6.902 ± 5.128	0.0003 ± 1.00E-04	0.276 ± 0.064
303	2.645 ± 3.035	0.003 ± 8.00E-04	0.224 ± 0.087
	Norit CNR 115 HG-H_2		
77	12.185 ± 0.365	0.026 ± 4.67E-03	0.821 ± 0.099
195	5.517 ± 3.568	0.004 ± 1.00E-03	0.241 ± 0.067
303	1.677 ± 0.045	0.0005 ± 1.00E-05	4.681 ± 0.455
	Norit CNR 115 UHP-H_2		
77	13.483 ± 0.189	0.019 ± 2.00E-03	1.186 ± 0.009
195	2.141 ± 0.821	0.007 ± 2.00E-03	0.311 ± 0.070
303	1.200 ± 0.222	0.036 ± 1.60E-02	0.354 ± 0.067

Table 6.2-7: Table showing the 'constrained' Toth model parameters (± absolute error) for Norit CNR 115 at different temperatures on the three grades of hydrogen ($\rho_b.V_a$ assumed to be approximately 0)

Temperature, K	n_0, % Mass	b, kPa^{-1}	t
	Norit CNR 115 LG-H_2		
77	8.975 ± 0.708	0.016 ± 3.94E-03	0.525 ± 0.034
195	8.975 ± 0	0.0001 ± 3.98E-06	0.578 ± 0.114
303	8.975 ± 0	0.0001 ± 2.00E-05	0.616 ± 0.363
	Norit CNR 115 HG-H_2		
77	12.185 ± 0.365	0.026 ± 4.67E-03	0.379 ± 0.201
195	12.185 ± 0	0.0003 ± 7.00E-05	0.396 ± 0.791
303	12.185 ± 0	0.00007 ± 8.30E-04	0.322 ± 0.106
	Norit CNR 115 UHP-H_2		
77	13.483 ± 0.189	0.019 ± 0.002	0.674 ± 0.109
195	13.483 ± 0	0.002 ± 3.30E-04	0.395 ± 0.015
303	13.483 ± 0	0.0003 ± 4.00E-05	0.589 ± 0.054

Table 6.2-8: Table showing the 'unconstrained' Toth model parameters (± absolute error) for SRD/667/1 at different temperatures on the three grades of hydrogen ($\rho_b.V_a$ assumed to be approximately 0)

Temperature, K	n_0, % Mass	b, kPa^{-1}	t
	SRD/667/1 LG-H_2		
77	6.646 ± 0.537	0.038 ± 1.50E-02	0.511 ± 0.085
195	0.966 ± 0.056	0.004 ± 6.00E-04	1.133 ± 0.219
303	0.645 ± 0.051	0.007 ± 2.03E-03	1.747 ± 1.142
	SRD/667/1 HG-H_2		
77	6.445 ± 0.485	0.019 ± 7.03E-03	0.647 ± 0.132
195	0.837 ± 0.045	0.004 ± 5.00E-04	1.339 ± 0.294
303	2.014 ± 0.581	0.001 ± 1.00E-04	0.365 ± 0.053
	SRD/667/1 UHP-H_2		
77	9.161 ± 0.308	0.007 ± 1.00E-03	1.822 ± 0.626
195	0.823 ± 0.045	0.008 ± 2.00E-03	0.975 ± 0.188
303	8.552 ± 13.261	0.0005 ± 4.00E-04	0.369 ± 0.237

Table 6.2-9: Table showing the 'constrained' Toth model parameters for (± absolute error) SRD/667/1 at different temperatures on the three grades of hydrogen ($\rho_b.V_a$ assumed to be approximately 0)

Temperature, K	n_0, % Mass	b, kPa^{-1}	t
	SRD/667/1 LG-H_2		
77	6.646 ± 0.537	0.038 ± 7.97E-03	0.511 ± 0.023
195	6.646 ± 0	0.002 ± 8.70E-04	0.345 ± 0.051
303	6.646 ± 0	0.0001 ± 8.21E-06	1.089 ± 0.412
	SRD/667/1 HG-H_2		
77	6.445 ± 0.485	0.019 ± 7.03E-03	0.329 ± 0.220
195	6.445 ± 0	0.042 ± 1.80E-02	0.475 ± 0.082
303	6.445 ± 0	0.0002 ± 1.00E-05	0.790 ± 0.094
	SRD/667/1 UHP-H_2		
77	9.161 ± 0.308	0.007 ± 0.001	0.397 ± 0.208
195	9.161 ± 0	0.001 ± 1.80E-04	0.416 ± 0.025
303	9.161 ± 0	0.0003 ± 5.00E-05	0.553 ± 0.051

Table 6.2-10: Table showing the 'unconstrained' Toth and Modified Toth model parameters (± absolute error) for the carbon nanotubes at 77 K

Sample	H_2 Grade	Temperature, K	n_0, % Mass	b, kPa $^{-1}$	t	V_a, cm^3 g^{-1}	R^2
SWNT-1	LG-H_2	77	7.126 ± 0.254	0.008 ± 0.001	1.543 ± 0.408	-	0.98784
	UHP-H_2		6.569 ± 0.233	0.006 ± 0.001	2.011 ± 0.734	-	0.97986
SWNT-2	LG-H_2	77	14.239 ± 3.484	0.009 ± 0.003	1.271 ± 0.902	0.733 ± 1.024	0.96283
	UHP-H_2		7.546 ± 0.245	0.006 ± 0.001	2.057 ± 0.708	-	0.98268
MWNT-1	LG-H_2	77	4.969 ± 0.319	0.012 ± 0.002	9.143 ± 26.868	0.227 ± 0.166	0.96923
	UHP-H_2		4.497 ± 0.500	0.009 ± 0.002	4.000 ± 6.107	0.521 ± 0.232	0.90511
MWNT-2	LG-H_2	77	0.854 ± 0.019	0.016 ± 0.001	5.949 ± 2.320	0.006 ± 0.009	0.99326
	UHP-H_2		0.856 ± 0.034	0.013 ± 0.001	9.677 ± 10.681	0.002 ± 0.017	0.97993

6.2.2.4 Residual and RMSE Analysis of the Toth and Modified Toth Fits

In this section, the residual plots for the Toth and modified Toth fits of the equilibrium hydrogen adsorption data on the nanoporous carbons are presented. The plots are shown in Figure 6.2-5 to Figure 6.2-7. It is evident that both models provide good fits to the data without a bias in the fit such that the residuals are distributed evenly around zero.

Percentage root mean square error values have also been obtained for the fits of the adsorption isotherms of the respective nanoporous carbons as shown in Table 6.2-11 for the activated carbons and Table 6.2-12 for the carbon nanotubes. These values are generally within acceptable limits with percentage errors ranging from 0.04 – 4.41 % for Toth fits to the adsorption isotherms for BPL. The range of values for Norit CNR 115 and SRD/667/1 are 0.09 – 8.3 % and 0.36 – 12.1 % respectively. In the case of the carbon nanotubes, there is an error of ~ 9 % associated with the Toth fit to the SWNT-1 and SWNT-2 adsorption isotherms. For MWNT-1 and MWNT-2 adsorption isotherms, which have been fitted with a modified Toth model, percentage root mean square errors of ~ 8 % and 0.8 % are obtained respectively.

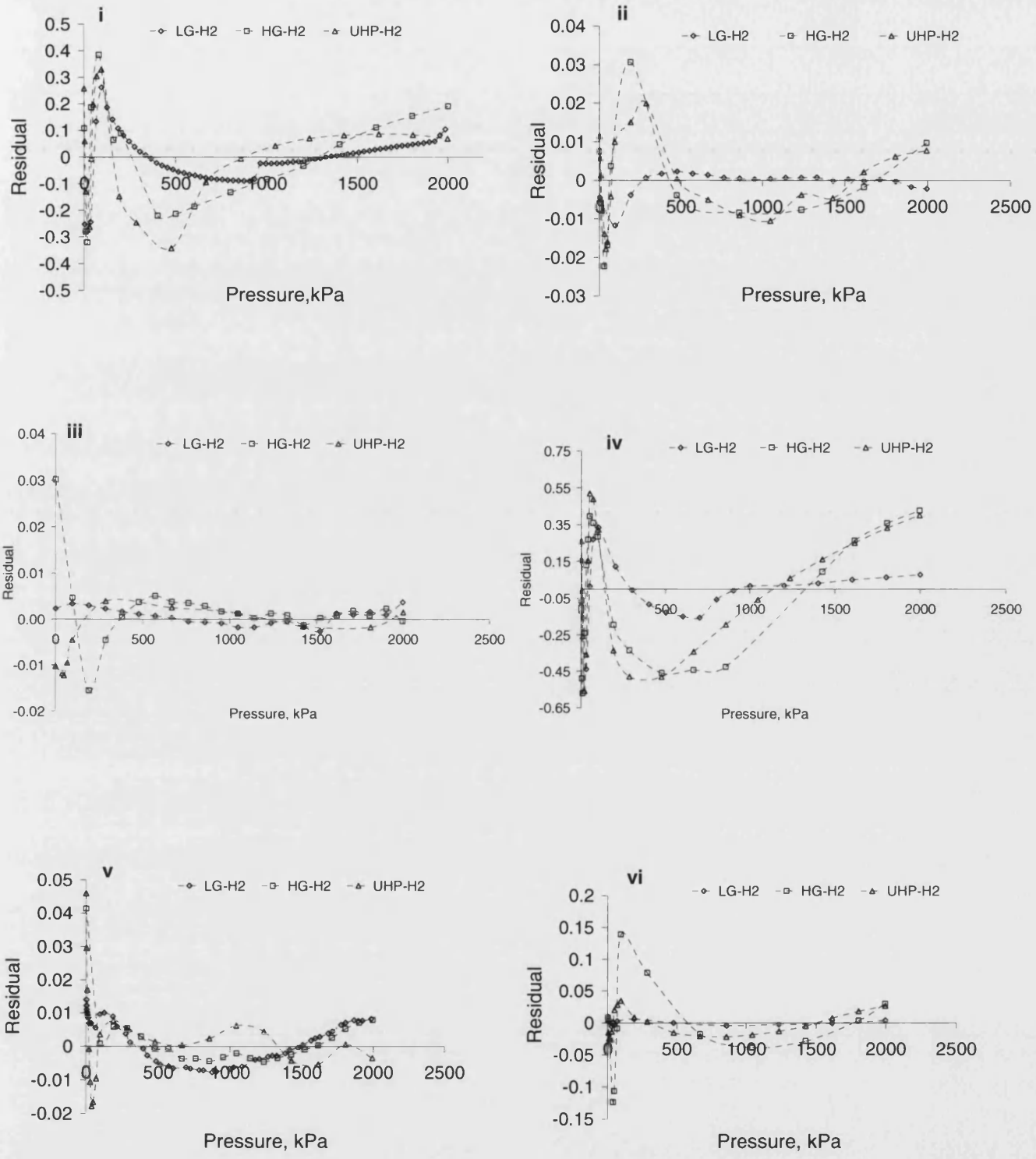

Figure 6.2-5: Residual plots for the activated carbons; (i) BPL at 77 K; (ii) BPL at 195 K; (iii) BPL at 303 K; (iv) Norit CNR 115 at 77 K; (v) Norit CNR 115 at 195 K; (vi) Norit CNR 115 at 303 K. Residuals all in wt-%.

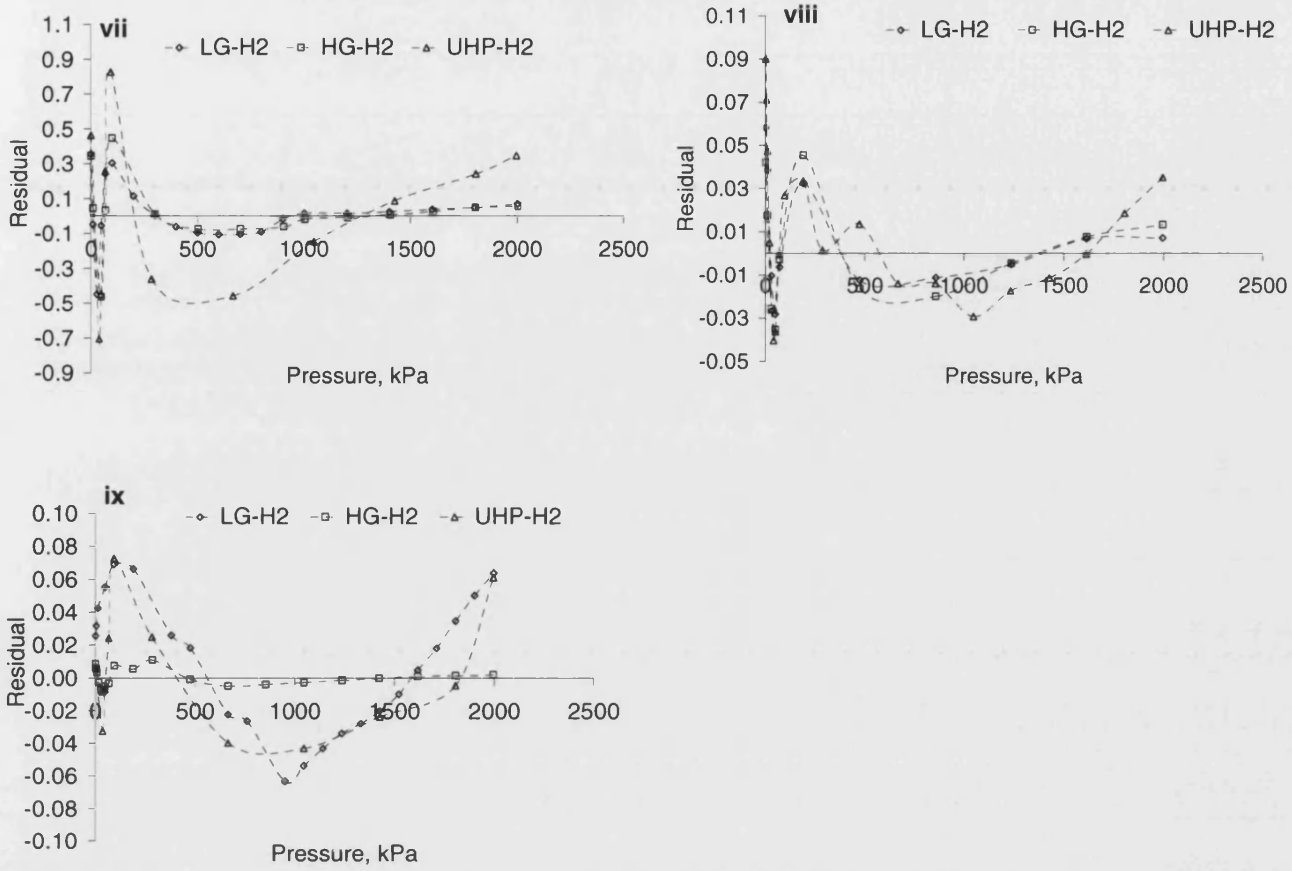

Figure 6.2-6: Residual plots for the activated carbons; (vii) SRD/667/1 at 77 K; (viii) SRD/667/1 at 195 K; (ix) SRD/667/1 at 303 K. Residuals all in wt-%.

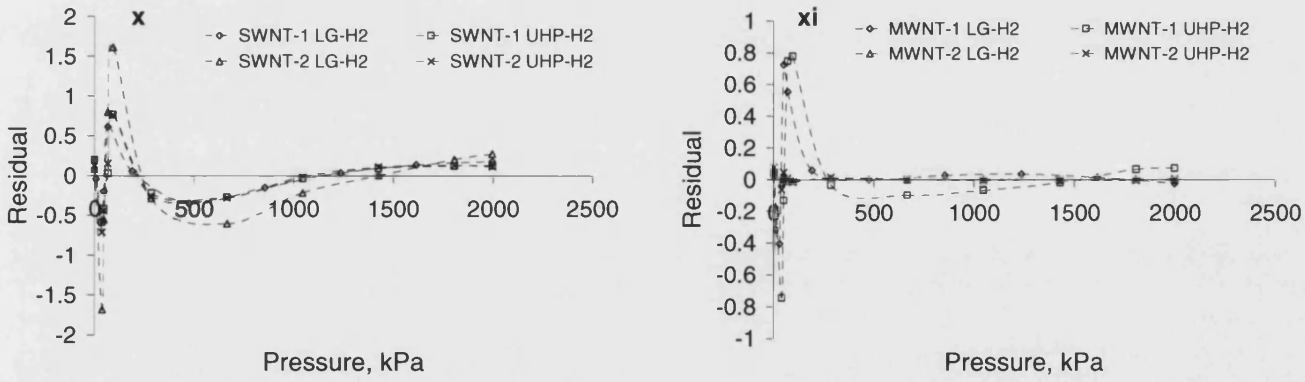

Figure 6.2-7: Residual plots for the carbon nanotubes; (x) SWNT-1 and SWNT-2 at 77 K; (xi) MWNT-1 and MWNT-2 at 77 K. Residuals all in wt-%.

Table 6.2-11: Table showing the % root mean square error based on the Toth Fits of the BPL adsorption isotherms

Temperature, K	H_2 Grade	% RMSE BPL	% RMSE Norit	% RMSE SRD
77	LG-H_2	0.724	2.841	2.741
195		0.038	0.085	0.696
303		0.036	0.126	0.842
77	HG-H_2	4.411	8.329	3.305
195		0.379	0.118	0.740
303		0.091	1.874	0.106
77	UHP-H_2	3.748	7.301	12.062
195		0.209	0.234	0.644
303		0.196	0.394	1.093

Table 6.2-12: Table showing the % root mean square error based on the Toth Fits of the adsorption isotherms for the carbon nanotubes

Sample	Temperature, K	H_2 Grade	% RMSE Toth	% RMSE Modified Toth
SWNT-1	77	LG-H_2	8.141	-
		UHP-H_2	9.224	-
SWNT-2	77	LG-H_2	-	20.351
		UHP-H_2	9.936	-
MWNT-1	77	LG-H_2	-	7.022
		UHP-H_2	-	8.999
MWNT-2	77	LG-H_2	-	0.410
		UHP-H_2	-	0.780

6.2.3 The Isosteric Heat of Adsorption

The knowledge of the isosteric heat of adsorption is important in the study of adsorption kinetics and the temperature dependence of equilibrium adsorption. According to Do (1998), during adsorption some of the heat released is absorbed by the solid adsorbent while some is dissipated to the surroundings. The amount absorbed by the solid causes a rise in its temperature leading to a reduction in the rate at which adsorption takes place (Do, 1998). This phenomenon has been observed during the adsorption carried out in this work. The time taken to reach equilibrium has been observed to be faster at 77 K in comparison to measurements taken at much warmer temperatures of 303 K.

The heat of adsorption provides a measure of the change in enthalpy before and after adsorption (Zhou *et al.*, 2004), and is therefore a quantitative description of the interaction strength between the surface of the adsorbent (carbon) and the adsorbate (hydrogen) molecules (Zhou *et al.*, 2006; Zhou *et al.*, 2004; Benard and Chahine, 2001) . The measurement of the heat of adsorption can provide information about the surface heterogeneity of the nanoporous carbons. Since these materials have a complex texture, they exhibit sites having a distribution of adsorption energies. The magnitude of this energy (heat of adsorption) is indicative of adsorption process taking place (physical or chemical). The isosteric heat of adsorption can be calculated from the van't Hoff equation (Do, 1998, Zhou *et al.*, 2004 and Choi *et al.*, 2003).

$$\frac{\Delta H}{RT^2} = \left(\frac{\partial \ln P}{\partial T}\right)_n \qquad \textbf{Equation 6.2-10}$$

Where ΔH is the heat of adsorption in J mol^{-1}, R is the molar gas constant (J mol^{-1} K^{-1}), T is the temperature of adsorption (K) and P is the pressure (kPa). The value of the heat of adsorption may vary with the amount adsorbed and it is this relationship that explains the surface structure (Choi *et al.*, 2003) of the adsorbent. The heat of adsorption has been calculated for the ultra high purity hydrogen equilibrium data obtained for the three activated carbons as shown in Table 6.2-13. This has not been

carried out for the carbon nanotubes because their adsorption isotherms have been obtained only at 77 K due to time constraints.

6.2.3.1 Heat of Adsorption from the Affinity Constant

As stated in Section 6.2.1.4, the adsorbate-adsorbent affinity parameter, *b*, in the Toth equation is dependent on temperature. This relationship can be exploited to give an initial indication of the energy of adsorption as shown in Equation 6.2-11.

$$b = b_0 \exp\left(\frac{E}{RT}\right) \qquad \textbf{Equation 6.2-11}$$

where b_0 is a pre-exponential constant and E is a measure of the heat of adsorption. By plotting ln *b* against *1/RT*, a linear plot is obtained as shown in Figure 6.2-8 with a slope E and a y-intercept $ln\ b_0$. A linear regression of the data has been obtained to give values of the adsorption energy and the affinity constant for the three activated carbons.

The adsorption energies obtained for the activated carbons are shown in Table 6.2-13. These values range from 2.61 kJ mol^{-1} to 5.26 kJ mol^{-1} for the activated carbons. These figures are within the range expected for physical adsorption of hydrogen on activated carbons and are consistent with values reported in the literature (Benard and Chahine, 2001; Zhou *et al.*, 2006). According to Do (1998), the measured values of the adsorption energy using the temperature dependence of the Toth parameter, *b* gives the value of the isosteric heat when the amount adsorbed (or loading) is zero. These values therefore do not provide a full picture of the change in the heat of adsorption with changes in the amount adsorbed, that is, the surface energetic heterogeneity of the carbons. Values of the heat of adsorption as the amount adsorbed changes are thus required. This is obtained by plotting adsorption isosteres as described in the Section 6.2.3.2.

From Figure 6.2-8, it is observed that the affinity constant, b decreases with temperature for the activated carbons. This is because the heat of adsorption is positive, that is, adsorption is an exothermic process. Since the free energy must decrease for adsorption to occur and the change in entropy is negative. Therefore,

$$\Delta G = \Delta H - T\Delta S \quad < 0 \qquad \textbf{Equation 6.2-12}$$

The negative nature of the enthalpy change means that heat is released from the adsorption process.

The temperature dependence of the heterogeneity parameter t is also shown in Figure 6.2-9. This parameter is found to depend on temperature such that as temperature increases, its value also increases.

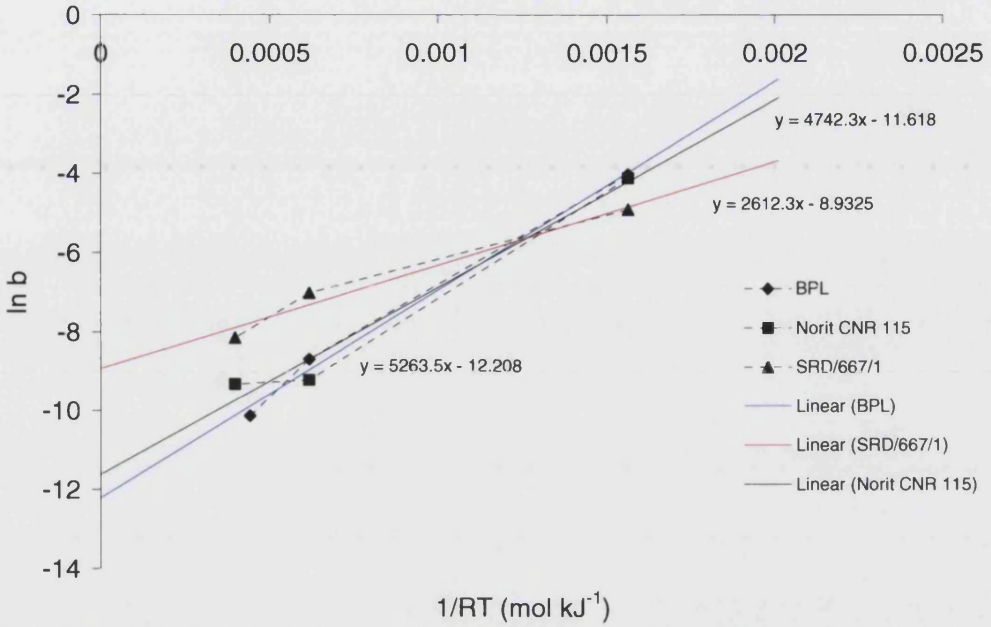

Figure 6.2-8: A plot showing the temperature dependence of the affinity parameter, *b* for BPL, Norit CNR 115 and SRD/667/1.

Table 6.2-13: Table showing the adsorption energies of the activated carbons

Sample	b_0 (kPa^{-1})	E (kJ mol^{-1})
BPL	3.39E-06	5.26
Norit CNR 115	9.00E-06	4.74
SRD/667/1	1.32E-04	2.61

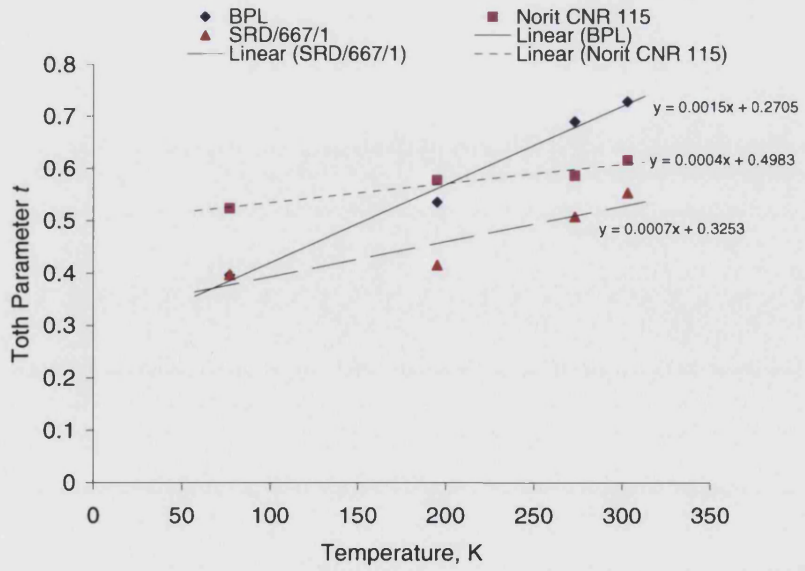

Figure 6.2-9: Variation of the Toth parameter *t* with temperature

6.2.3.2 Adsorption Isosteres

In this section, the results of the adsorption isosteres for the nanoporous carbons are reported. Adsorption isosteres are obtained when curves of pressure as a function of temperature at a constant value of the amount adsorbed are plotted. The slope of each curve corresponds to the isosteric heat ($-\Delta H$). As mentioned above, the values of the isosteric heat when plotted against the amount adsorbed gives a measure of the surface energetic heterogeneity.

The adsorption isosteres for the activated carbons, BPL, Norit CNR 115 and SRD/667/1 are shown in Figure 6.2-10 to Figure 6.2-12. The amount adsorbed is varied at the values of 0.05, 0.15, 0.3, 0.35, 0.38, 0.1 and 0.5 %. The plots are observed to be linear in each case with a change in the slope as the amount adsorbed is varied. The slope of each curve is calculated by linear regression and the observed change in the isosteric heat with the amount adsorbed is shown in Figure 6.2-13. The values of the isosteric heat is observed to decrease as the amount adsorbed increases with values in the range of 6.7 to 1.38 kJ mol^{-1} for BPL, 8.73 to 2.24 kJ mol^{-1} for Norit CNR 115 and 3.49 to 1.92 kJ mol^{-1} for SRD/667/1. These values lie within the range observed by several authors for activated carbons (see Zhou *et al.*, 2004; Bernard and Chahine, 2001; Zhou *et al.*, 2006). According to Bhatia and Myers, values within this range imply that the energy of interaction between hydrogen and the activated carbons is too weak for storing hydrogen at ambient temperature (Bhatia and Myers, 2006), analogous with the low values of uptake measured in this work at ambient temperature (303 K).

The observed decrease in the isosteric heat with the increase in the amount adsorbed further points to the heterogeneity of the surface of the activated carbon materials such that the adsorption energy is different on varying sites on the adsorbent surface. This has also been suggested by Choi *et al.*, (2003) and Do, (1998). Constant values of the isosteric heat on the other hand would point to a homogeneous system analogous with the Langmuir model. Bhatia and Myers also point out that the ideal adsorbent is energetically homogeneous, that is, the isothermal heat of adsorption should be constant with loading for optimal delivery. Energetic heterogeneity in any

form is believed to be detrimental to the adsorptive storage of gas (Bhatia and Myers, 2006).

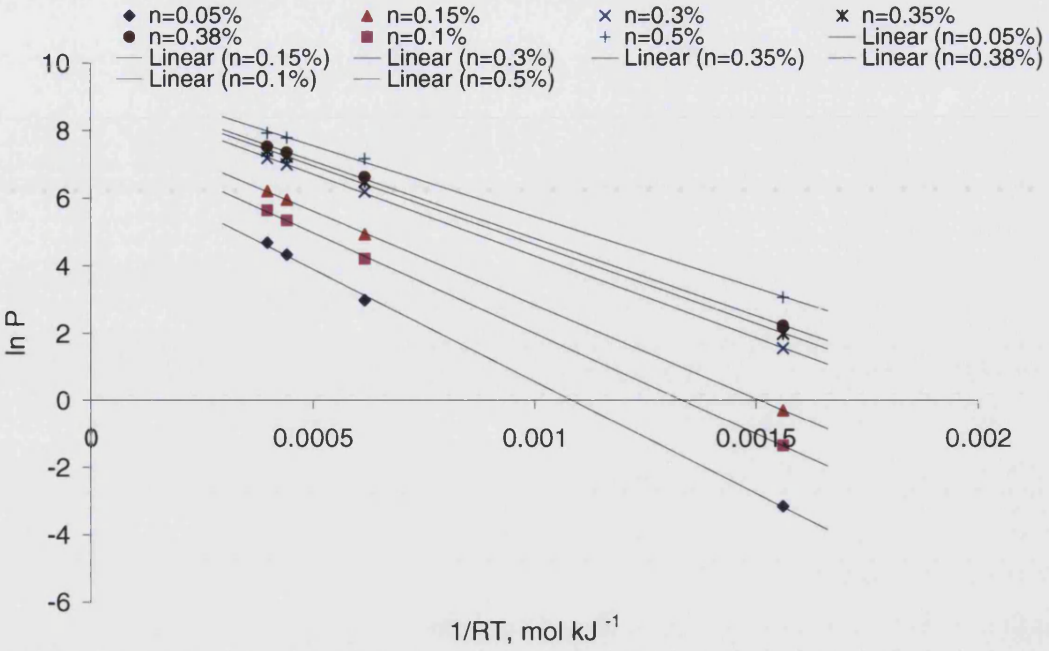

Figure 6.2-10: Graphs showing the adsorption isosteres for BPL activated carbon. Pressure (*P*) in kPa.

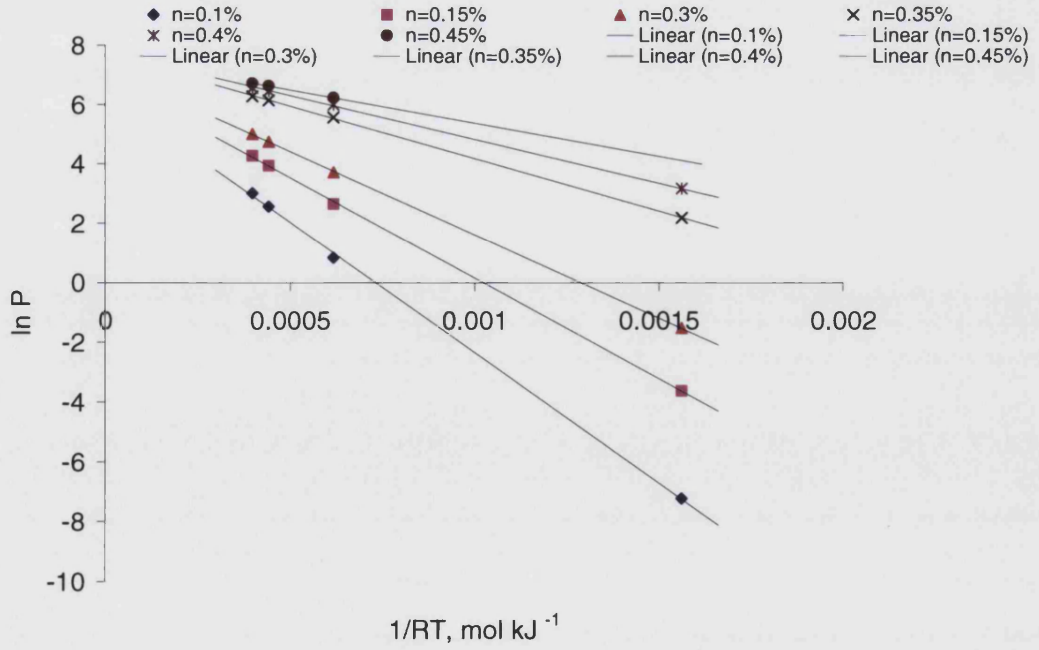

Figure 6.2-11: Graphs showing the adsorption isosteres for Norit CNR 115 activated carbon. Pressure (*P*) in kPa.

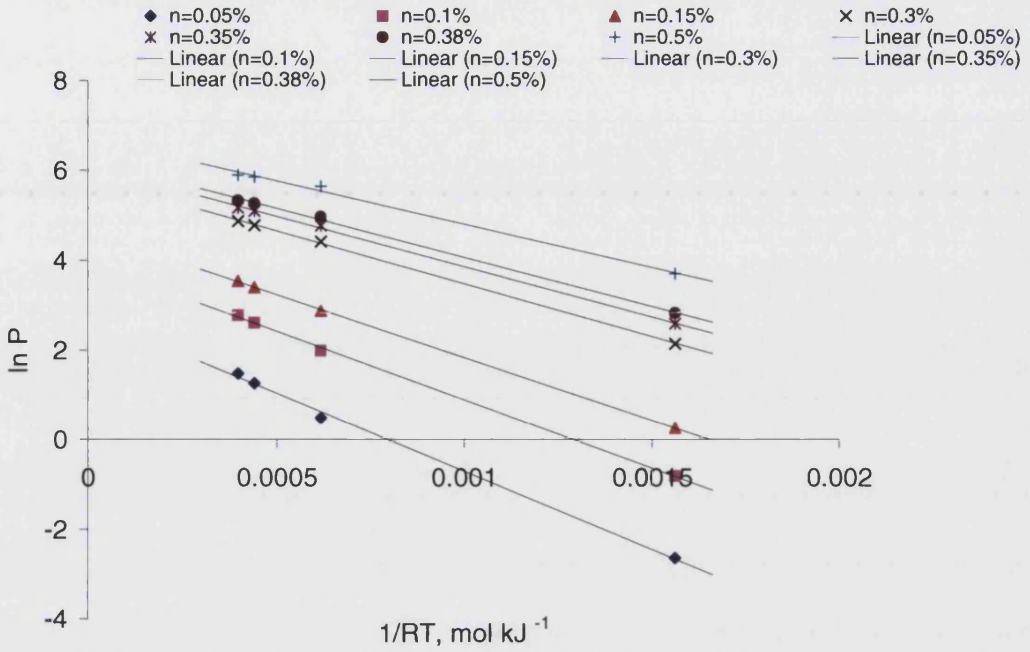

Figure 6.2-12: Graphs showing the adsorption isosteres for SRD/667/1 activated carbon. Pressure (*P*) in kPa.

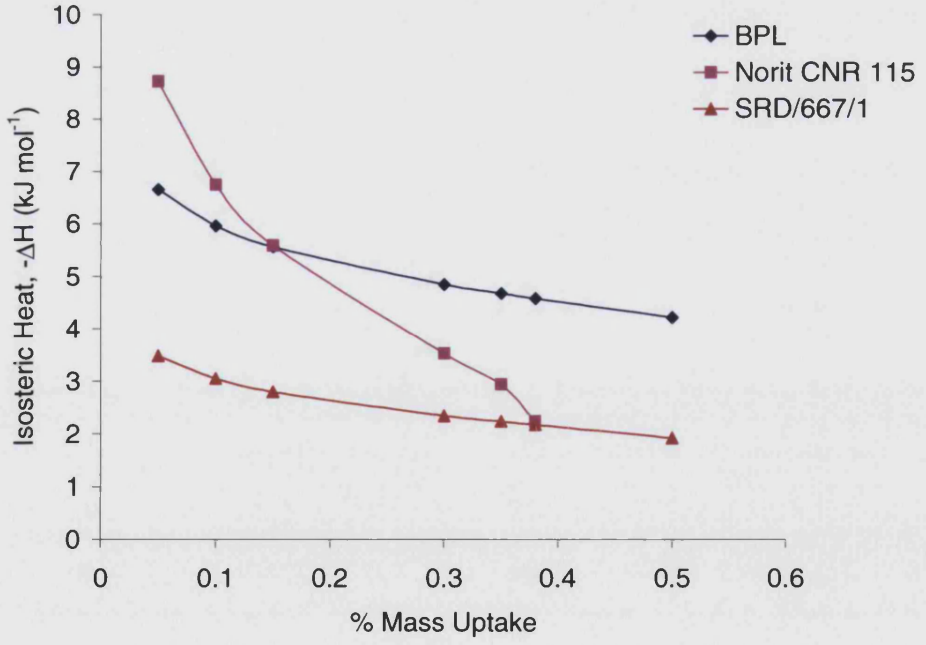

Figure 6.2-13: Graph showing the variation of the isosteric heat with the amount adsorbed for the activated carbons.

6.3 Sample Variation, Cyclability and Adsorption Hysteresis

This section of the thesis is a description of the experimental findings based on the observed variation in the amount of hydrogen adsorbed by a nanoporous carbon sample at a particular temperature. The effect of cycling a loaded quantity of carbon on the amount adsorbed and desorbed and the extent of the sorption hysteresis in these materials is also presented. These effects are found to be mainly significant at low temperatures, that is, at 77 K. The results are presented here along with a discussion on their implications in this work.

6.3.1 Variation in the Amount Adsorbed on BPL

BPL activated carbon has proven to be very variable in terms of determining its hydrogen storage capacity. The value of the amount of hydrogen adsorbed has been observed to change during reproducibility checks making it difficult to ascertain its true capacity as a hydrogen storage material. The results presented in the preceding sections for this material are based on an average taken on the range of data measured under exactly similar experimental conditions. Experiments were carried out as described in Chapter 3 involving weighing and loading a fresh sample of BPL into the gravimetric apparatus on each occasion to assess the range and extent of its variability.

The results obtained are shown in Figure 6.3-1. A comparison between the data obtained for BPL has been made with another activated carbon material, Norit CNR 115, which appears to be more stable based on results shown in Figure 6.3-2. The main factors found to be responsible for the variation in this material are discussed in Section 6.3.1.1 to 6.3.1.3.

6.3.1.1 Effect of Sample Degassing Conditions

One of the factors discovered to have an effect on the magnitude of the amount adsorbed on BPL is the degassing conditions used. When the sample was degassed at 250 °C for 4 hours, the amount adsorbed is higher in comparison to the values obtained when degassing is done at 150 °C for 16 hours. This is evident from the data shown in Figure 6.3-1 for experiments carried out using LG H_2. It is important to note that even when the degassing conditions for BPL are kept the same, the amount adsorbed still varies. The reason for the change in the degassing conditions was to speed up the degassing process since at higher temperatures the rate of removal of the surface contaminants is improved. It is believed that the degassing temperature has an effect on the accessible porosity of the material influencing the materials' gas adsorption properties.

A comparison between the plots obtained for Norit CNR 115 and BPL show that the extent of variation in the adsorption isotherms of Norit CNR 115 is reduced when the degassing conditions are kept the same such that it is possible to get reproducible isotherms using this material (See Table 6.3-1).

6.3.1.2 Effect of Sample Cycling

Sample cycling is another factor that has been observed to have an effect on the amount of hydrogen adsorbed by BPL. This factor is discussed in detail for the other materials in Section 6.3.2. Cycling is achieved by loading a quantity of material for testing and after preparation, running a sequence of isotherms without intermediate regeneration following the desorption run. The results obtained at 77 K using UHP H_2 are shown in Figure 6.3-3. For BPL, it is observed that, the amount adsorbed on the first scan (10.03 %) is the highest of all the adsorption cycles as compared to 3.77 % on the second scan, 2.98 % on the third scan and 2.74 % on the fourth scan. The amount adsorbed decreases as the number of cycles increases. This finding is interesting because it enables the assessment of the true storage capacity of this

material. In the case of the amount of desorbed (or discharged) hydrogen, it is observed that on the first desorption scan only 1.71 % of the amount adsorbed is released. This can be attributed to the small hydrogen molecules burrowing deeply into the porosity of the carbon and getting stuck in pores of molecular dimensions such that they cannot be released easily. On the second desorption scan, 2.46 % of hydrogen is released while on the third and fourth desorption scans 2.00 % and 2.36 % are desorbed respectively. It is evident that as the number of cycles increase, the % mass of hydrogen desorbed is improved. These amounts represent the real or useable amount of hydrogen in BPL. The desorption scan also has interesting implications such that coupled with the adsorption scan they are representative of the desired characteristics of a potentially good hydrogen storage material.

6.3.1.3 Other Factors

Some other factors that may be responsible for the variation in the amount adsorbed on BPL when the conditions of measurement are kept the same include its porous structure, its raw material source and preparation and activation method. While BPL is a physically activated (steam) bituminous coal based activated carbon, Norit CNR 115 is a chemically activated (phosphoric acid) activated carbon. The preparation and activation methods supplied by the manufacturer have been reported in Chapter 3. The extent of the preparation and precursor effects are not studied in this work.

Table 6.3-1 is a summary of the calculated % mass adsorbed for the activated carbons based on the observed variation in their measurements. The variation of each value of the % mass uptake from the mean, that is, the standard deviation has been calculated and is also presented in the table. The number of repeats carried out for BPL is larger than the other two activated carbons because of the variability observed in the data. Norit CNR 115 and SRD/667/1 appear to have a smaller deviation from the mean in comparison to BPL, implying that the adsorption isotherms have an improved reproducibility when compared to BPL. This is very important when considering the practical application of these materials.

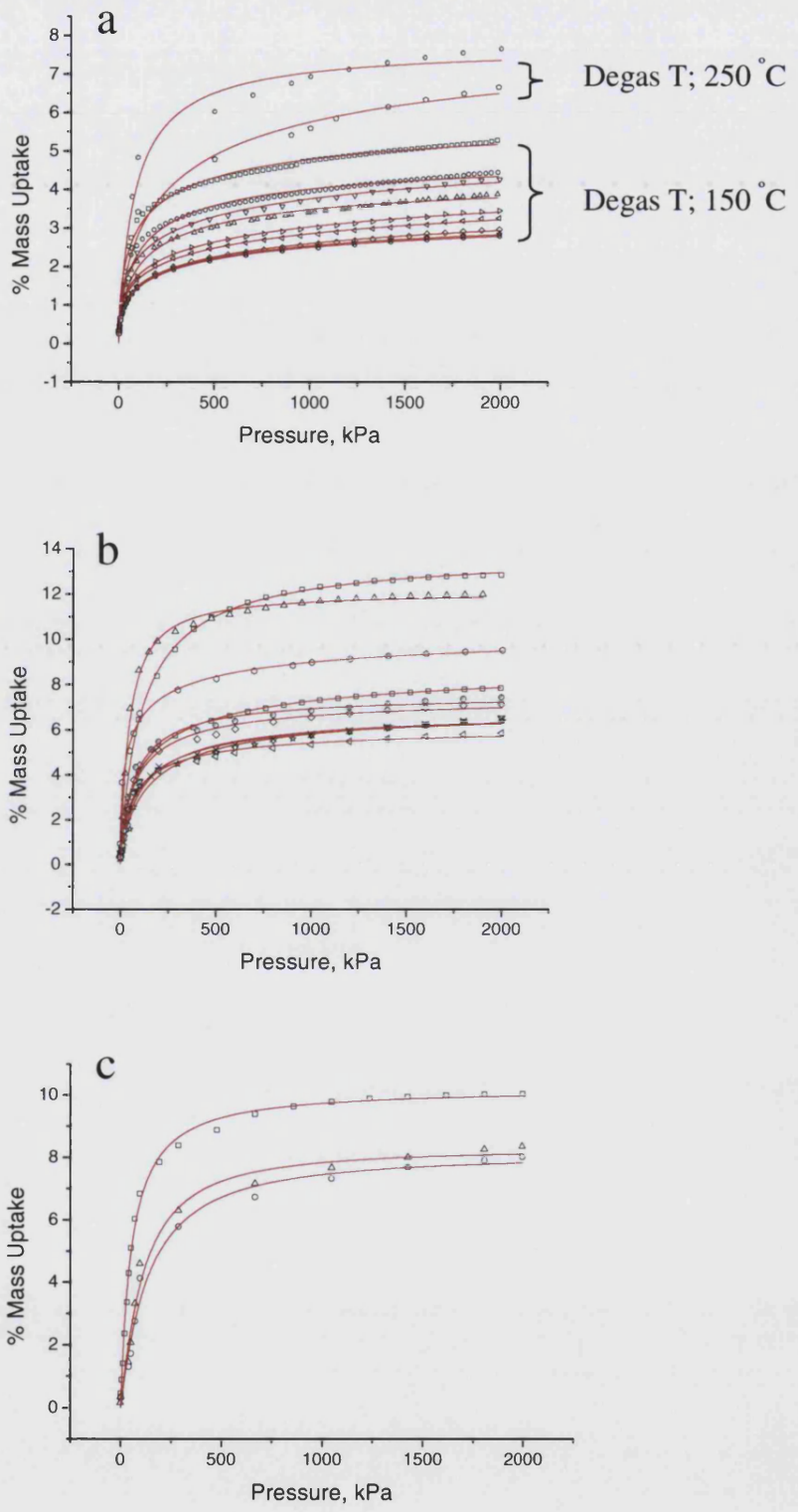

Figure 6.3-1: Variation in % mass adsorbed on BPL at 77 K using (a) Low grade H_2; (b) High Grade H_2; (c) Ultra high purity H_2.

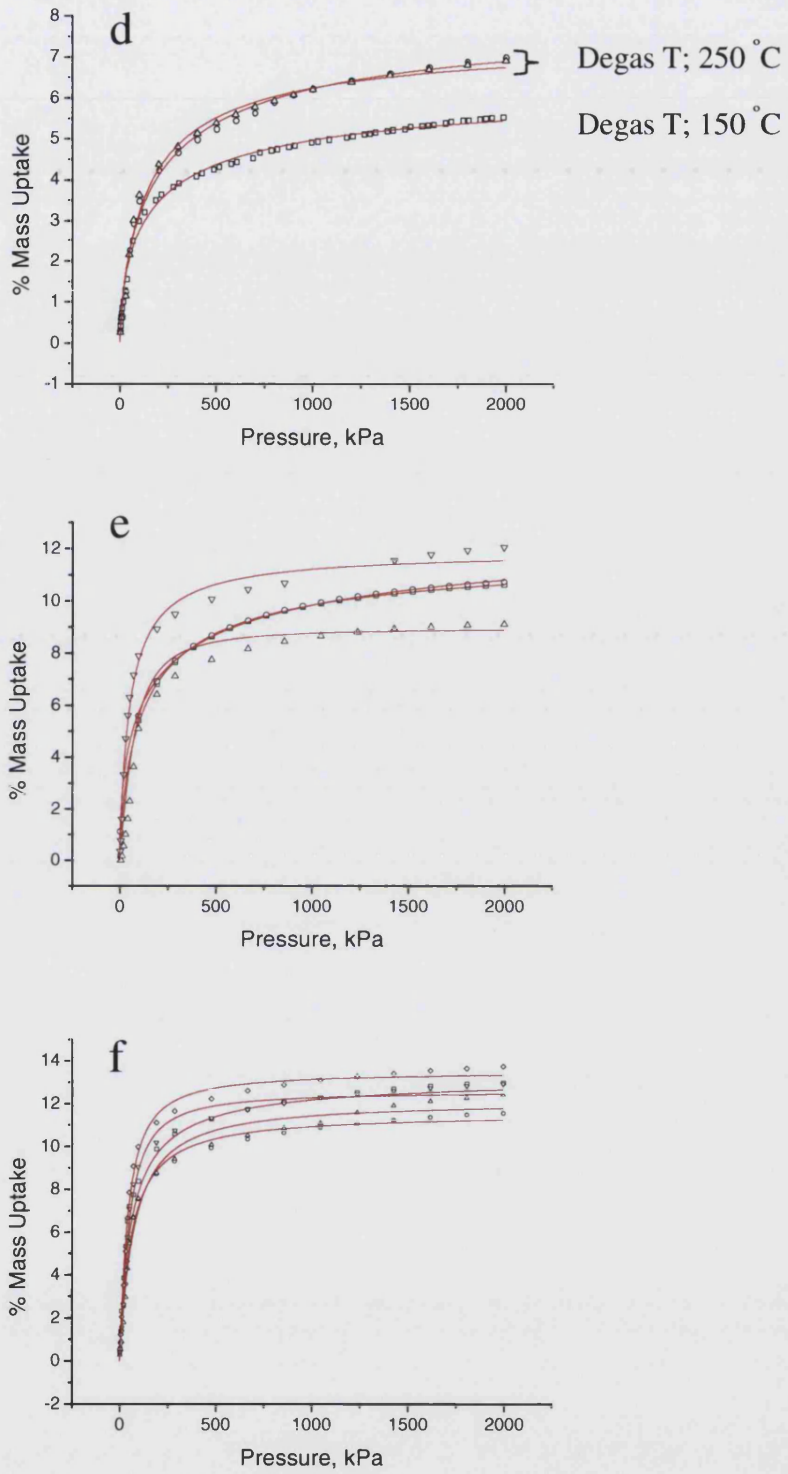

Figure 6.3-2: Variation in % mass adsorbed on Norit CNR 115 at 77 K using (d) Low grade H_2; (e) High Grade H_2; (f) Ultra high purity H_2.

Table 6.3-1: Summary of the results showing the extent of variation in the amount adsorbed on the activated carbons at 77 K

Sample	H_2 Grade	No. of Experiments	Average % Mass Uptake at 2000 kPa	Standard Deviation (±)
BPL	LG	11	5.33	± 1.39
	HG	9	7.70	± 1.94
	UHP	3	8.80	± 1.08
Norit CNR 115	LG	3	6.46	± 0.81
	HG	4	10.40	± 1.27
	UHP	5	12.56	± 0.82
SRD/667/1	LG	4	5.23	± 0.38
	HG	2	5.27	± 0.57
	UHP	2	10.43	± 1.36

6.3.2 Sample Cycling

The activated carbons and the carbon nanotube with the highest observed % mass uptake (SWNT-2) of hydrogen have been cycled using ultra high purity hydrogen. Eight scans comprising of four adsorption and four desorption isotherms have been obtained for each material. The excess adsorption and desorption isotherms for each material have been presented in Chapter 5. Here, the adsorption isotherms obtained for each cycle are shown in Figure 6.3-3 along with their respective fits to the Toth model equation. Each scan of the equilibrium isotherms will be discussed in relation to the carbon material and the implications for its use as a hydrogen storage material.

The results for BPL have been discussed in Section 6.3.1.2. For the Norit CNR 115, SRD/667/1 and SWNT-2 cyclic adsorption isotherms, it is observed that the amount adsorbed on the first scan showed the highest values of the entire adsorption scans. % mass uptakes of 11.75, 9.47 and 7.79 wt-% have been obtained for each carbon respectively. The subsequent adsorption scans show a significantly reduced uptake, less than half of the original value in all cases as summarised in Table 6.3-2.

In the first adsorption scan, hydrogen is introduced to a carbon sample that has been degassed at vacuum and high temperature and is therefore assumed to be void of any pre-adsorbed species. The introduction of hydrogen into the system leads to the adsorption on the higher energy sites followed by sites with weaker energy, resulting in the filling of the easily accessible sites or pores. This is followed by adsorption in the pores buried deeper in the structure of the carbon leading to the higher uptake values observed in the case of the activated carbon materials. On the desorption scan, all of the adsorbed hydrogen is not released such that on the next adsorption cycle, some of the adsorption sites are still occupied by the originally adsorbed hydrogen leading to much lower uptake as observed. If all the hydrogen adsorbed on the second scan is reversibly stored (all the adsorbed hydrogen is desorbed), it is possible to find the real or useable amount of hydrogen for a particular carbon. In the case of Norit activated carbon, only 2.57 % mass hydrogen was released on the first desorption scan, compared to the 11.75 % adsorbed. It would be expected that the amount

adsorbed on the next (second) scan would be equal to this value assuming all the accessible pores were filled on the first adsorption scan. This is observed not to be the case implying that there were still some pores left unfilled with a value of 3.60 % mass uptake observed on the second adsorption scan. 2.66 % mass of hydrogen was desorbed on the next (second) desorption scan indicating irreversible storage. On the third adsorption scan, 3.55 % hydrogen was adsorbed but 4.87 % was desorbed. This on initial inspection proved to be impossible but a closer look suggests that some of the originally adsorbed hydrogen was desorbed in addition to the additional amounts adsorbed in the subsequent scans. On the final (fourth) adsorption scan, 3.84 % hydrogen was adsorbed and 3.05 % desorbed. These results point to the presence of adsorption hysteresis, which will be discussed in the Section 6.3.3. The amounts adsorbed and desorbed on the different scans for SRD/667/1 and SWNT-2 follow similar trends as described above and the results are also presented in Figure 6.3-3 and Table 6.3-2.

In the case of SWNT-2, similar trends associated with the observations for the activated carbons are evident. That is, the amount adsorbed on the first scan is high while the subsequent scans show a much reduced hydrogen storage capacity. From TEM, it is observed that this material consists of single walled nanotubes arranged into bundles. The hydrogen adsorption taking place in this material is believed to be on the outer surface of the bundles, in the interstices between tubes and possibly in the hollow centre of the tubes that are accessible as a result of surface defects associated with purification methods. It is likely that the loss of capacity on cycling may be due to the chemisorption of hydrogen with the residual metal impurities present.

In summary, from the results of the cyclic adsorption isotherms, it can be concluded that the useable amount of hydrogen from the carbon materials at 77 K is ~ 2 % for BPL; ~ 3 % for Norit CNR 115, ~ 0.9 % for SRD/667/1 and ~ 3 % for SWNT-2.

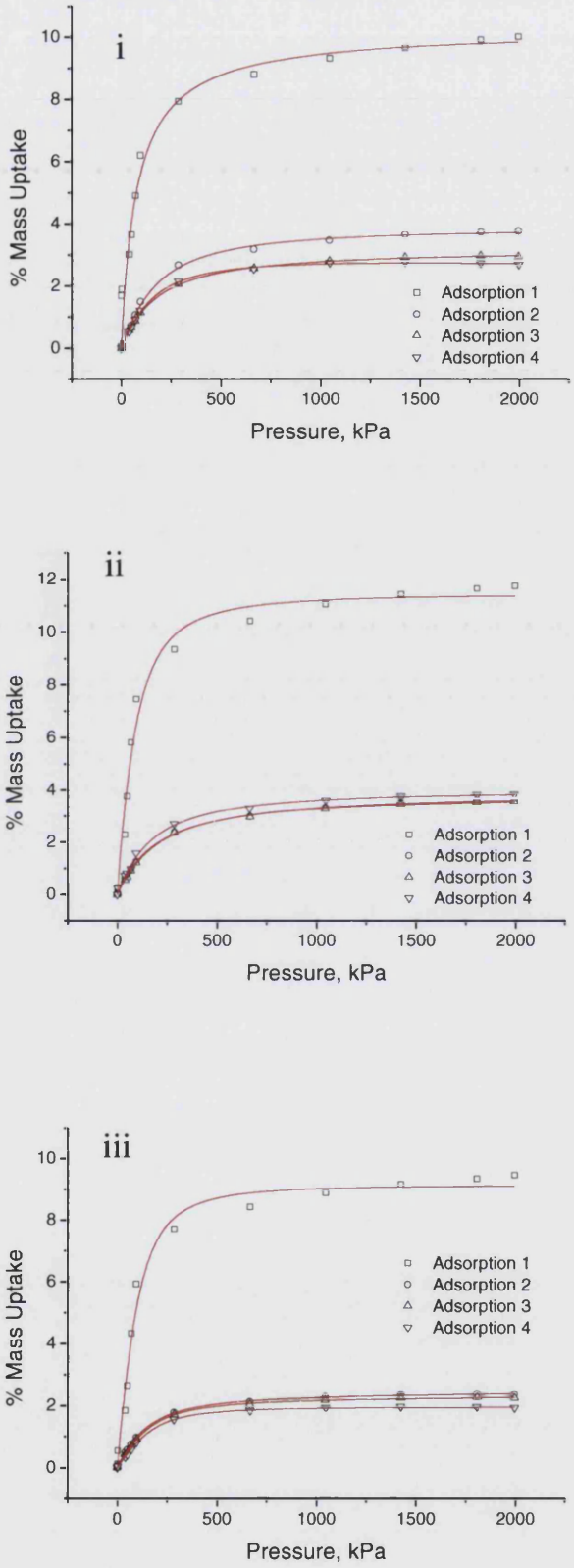

Figure 6.3-3: Figure showing the cyclic adsorption isotherms of (i) BPL; (ii) Norit CNR 115; (iii) SRD/667/1.measured at 77 K using ultra high purity H_2.

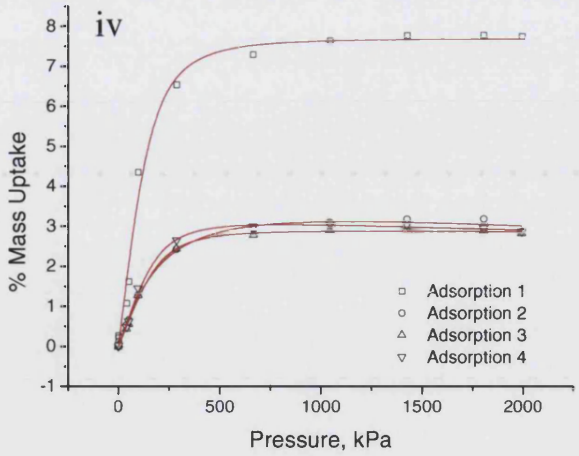

Figure 6.3-3: Continued for (iv) SWNT-2

Table 6.3-2: Summary of the cyclic hydrogen sorption amounts for the nanoporous carbons at 77 K

Sample	Scan	% Mass Adsorbed	% Mass Desorbed
BPL	1, 2	10.03	1.71
	3, 4	3.77	2.46
	5, 6	2.98	2.00
	7, 8	2.74	2.36
Norit CNR 115	1, 2	11.75	2.57
	3, 4	3.60	2.66
	5, 6	3.55	4.87
	7, 8	3.84	3.05
SRD/667/1	1, 2	9.47	0.71
	3, 4	2.39	0.83
	5, 6	2.27	0.90
	7, 8	1.96	0.77
SWNT-2	1, 2	7.79	3.70
	3, 4	3.19	2.69
	5, 6	2.93	2.40
	7, 8	3.06	4.14

6.3.3 Adsorption Hysteresis of Hydrogen in the Nanoporous Carbon Materials

This section is a discussion on the adsorption hysteresis observed in the sorption isotherms of the nanoporous carbons, mainly evident at low temperature (77 K). Hysteresis occurs when the adsorbed amount is not fully recovered on desorption such that the amount adsorbed is not equal to the desorbed amount. According to Thommes *et al.*, (2006), the factors that determine hysteretic behaviour are: hysteresis on the level of a single pore of a given shape and cooperative effects reflecting aspects of connectivity of the pore network (Thommes *et al.*, 2006).

Throughout this work, significant hysteresis is only observed at cryogenic temperatures. At temperatures closer to ambient this effect is insignificant. At 77 K, the adsorbed hydrogen is difficult to recover even when the pressure is dropped very low to varying extents in the different nanoporous carbons. It has been observed that when the cryogenic system is removed, all of the hydrogen held onto the material is released as the temperature returns to room temperature, such that the inclination towards the presence of chemisorption that may be associated with the presence of impurities in the gas supply or a change in the material surface can be negated to an extent in the case of the activated carbons. For the carbon nanotubes, suggestions by Lueking and Yang that some of the adsorption capacity of these materials may be enhanced by the chemisorption of hydrogen on the metal impurities (Lueking and Yang, 1999) is likely. This can be linked to the hysteresis observed in these materials at 77 K.

Table 6.3-3 is a summary of the gravimetric hydrogen sorption results obtained at 77 K for the nanoporous carbons. The graphs have been shown in Chapter 5. This is separate from the results presented for the sample cycling. It shows the % amount adsorbed and desorbed for each material to highlight the extent of the hysteresis observed under these conditions. It can be seen that as observed in the cyclic isotherms, only a proportion of the amount adsorbed is released on desorption. The presence of hysteresis in carbon materials although mainly associated with adsorption in subcritical systems is present in the supercritical adsorption system studied here at

cryogenic conditions. The main reasons highlighted for this observation is the possibility of the desorption process being very slow such that the time allowed for equilibration may be insufficient; the molecules of hydrogen could be trapped in the porous structure of the carbon materials; the measurement temperature (77 K) is too low whereby the process of adsorption is favoured over the desorption process such that even the reduction in pressure is incapable of enhancing desorption.

At this point, it is important to reiterate that when the sample temperature is gradually increased (on removal of the cryogenic system), all of the hydrogen is released. This is verified by the observation that the sample weight returns to its original value. This implies that by raising the system temperature from cryogenic to room temperature all the hydrogen "stuck" in the material is desorbed. Therefore, for system applications, a suggestion might be to store the hydrogen in these nanoporous carbon materials at 77 K and release it for use at some optimised temperature and pressure close to ambient conditions.

Table 6.3-3: Summary of gravimetric H_2 sorption results at 77 K for the nanoporous carbons

Sample	H_2 Grade	% Mass Adsorbed	% Mass Desorbed
BPL	LG	5.15	1.80
	HG	7.45	2.36
	UHP	10.04	7.54
Norit CNR 115	LG	6.98	3.34
	HG	12.06	7.44
	UHP	13.74	3.98
SRD/667/1	LG	5.50	1.29
	HG	5.67	1.32
	UHP	9.47	0.31
SWNT-1	LG	7.24	0.91
	UHP	6.68	0.94
SWNT-2	LG	11.98	5.72
	UHP	7.63	3.09
MWNT-1	LG	4.24	3.74
	UHP	2.95	2.57
MWNT-2	LG	0.83	0.56
	UHP	0.85	0.51

6.4 Assessment of Hydrogen Storage Mechanism

In this section, the adsorption kinetic data obtained from the gravimetric isotherms on the nanoporous carbons is analysed and the subsequent findings discussed. The kinetic data will be used to assess whether the equilibrium conditions were met for the adsorption points on the equilibrium adsorption isotherm. The kinetic data has been fitted to a diffusion approximation model called the linear driving force (LDF) as applied by the IGA computer algorithm described in Chapter 3. The application of the LDF equation will provide values of rate constants, which can be used to estimate the mechanism of adsorption taking place in the nanoporous carbon materials.

6.4.1 Kinetics of Adsorption

In order to fully understand the adsorption process taking place in a particular system, it is important to carefully consider the kinetics involved. A closer look at the kinetics involved in a particular system can provide valuable information about the mechanism of adsorption. Adsorption kinetics are complex and studies have shown that it may follow the linear driving force (LDF), combined barrier resistance/diffusion or Fickian diffusion model (Fletcher *et al.*, 2004), which provide a satisfactory description of the adsorption kinetics of various gases and vapours on activated carbons. This is dependent on the nature of the adsorptive and the adsorbent (porous structure, structural and electronic properties), and the experimental conditions applied (Fletcher and Thomas, 1999).

According to Buzanowski and Yang, (1989), the design and modelling of adsorption processes requires the numerical solution of a set of partial differential equations involving time and spatial variables. These computations can be greatly simplified by using approximations for the intraparticle diffusion rates. According to several

authors, the most powerful form of such approximations is the linear driving force model (LDF) proposed by Glueckauf and Coates in 1947 (Glueckauf and Coates, 1947). This model is conventionally written as shown in Equation 6.4-1 for isothermal adsorption of a pure gas onto a single adsorbent particle (Sircar and Hufton, 2000; Glueckauf and Coates, 1947).

$$\frac{dn}{dt} = k(n_1 - n) \qquad \textbf{Equation 6.4-1}$$

With boundary conditions: $t = t_0$; $n = n_0$ and where k is the kinetic rate constant or the mass transfer coefficient, n is the % mass uptake at time t, n_1 is the equilibrium uptake at the limit $t \rightarrow \infty$ and n_o is the equilibrium uptake at $t = t_0$. The solution to Equation 6.4-1 may be written as

$$n = n_o + (n_1 - n_o)[1 - \exp(-k(t - t_0)] \qquad \textbf{Equation 6.4-2}$$

The term $(n_1 - n)$ in Equation 6.4-1 refers to the "driving force", since the rate of mass transfer of adsorbate to the adsorbent is expressed as a function of the overall driving force for diffusion.

For spherical particles, it can be shown that (Sircar and Hufton, 2000);

$$k = \frac{15D}{R_p^2} \qquad \textbf{Equation 6.4-3}$$

Where D is the diffusion coefficient of the adsorbate gas in the adsorbent and R_p is the adsorbent particle radius.

The LDF equation as shown in Equation 6.4-2 has thus been applied for analysis of the kinetic data obtained from the hydrogen adsorption isotherms on the nanoporous carbons. An example of kinetic data obtained on an activated carbon is shown in Figure 3.3-10. The graphing software ORIGIN was used to compute the variable LDF model parameters k and n_1. It was observed that the kinetic data deviates from the LDF model as shown in Figure 6.4-1 (1a to 7a). This deviation occurred for the whole range of pressure for the nanoporous carbons. A look at the residual plots in Figure 6.4-2 also indicates that the fit is biased towards the positive.

It is proposed in this work that there are two mechanisms present in the nanoporous carbons. For the activated carbons, the mechanisms could be due to diffusion from the bulk gas phase to the solid surface and diffusion of the gas molecules through the interconnecting network of pores. This observation is analogous to that observed by Rao *et al.*, (1985) in his work on the kinetics of adsorption on carbon molecular sieves and Fletcher *et al.*, (2004) on metal organic frameworks. In the case of the nanotubes, the adsorption mechanisms can be potentially described as the diffusion from the bulk gas phase to the outer surface adsorption sites on the closed nanotubes (SWNT-1, 2 and MWNT-1) and adsorption in the interstitial spaces between bundles of the nanotubes. MWNT-2 is opened on the ends with surface defects as observed by TEM shown in Figure 4.6-1, therefore, the mechanism of adsorption in this material can also be attributed to adsorption inside the tube, on the outer surface of the nanotubes and interstitial sites.

The mechanisms discussed above can be described by a modified linear driving force (MLDF) equation:

$$n = n_0 + (n_1 - n_0)[1 - \exp(-k_1(t - t_0))] + (n_2 - n_0)[1 - \exp(-k_2(t - t_0))] \quad \textbf{Equation 6.4-4}$$

Where k_1 and k_2 are kinetic rate constants and the terms $(n_1 - n_0)$ and $(n_2 - n_0)$ define the contributions of the two mechanisms to the overall adsorption process. It is apparent from Figure 6.4-1 that the adsorption kinetic plots of all the nanoporous carbons follow the MLDF model. The residual plots are presented in Figure 6.4-2 as a comparison with the LDF model. It is evident that the MLDF model provides a much more improved fit of the data because the residuals are randomly distributed around zero as opposed to the LDF model residuals, which are evidently biased as mentioned previously. The % root mean square errors of the fits have also been calculated and are shown in Table 6.4-1. The values range from 0.005 to 0.126 % and 0.0003 to 0.024 % for the LDF and MLDF fits respectively.

Figure 6.4-3 shows the variation of the respective rate constants with pressure obtained for the nanoporous carbons at 77 K. Kinetic data obtained at other

temperatures, 195 and 303 K have also been analysed and the data is presented in Appendix C. The variation of the kinetic rate constant with hydrogen uptake is also shown in Figure 6.4-4. For the activated carbons, the rate constant, k_1, appears to have higher values at low pressures and then decrease with increasing pressure. Its values are generally higher in magnitude than the values of the rate constant, k_2, which also starts high and reduces as the pressure increases. Similar trends are observed in the case of the carbon nanotubes. The difference in the rate constants obtained for the nanoporous carbons can also be linked to the difference in geometry of each of the materials, that is, their particle sizes as defined by Equation 6.4-3. Knowledge of the material mean particle size and its rate constant can be used to estimate the diffusion coefficient of hydrogen in each carbon. The mean diffusion coefficient for the activated carbons is in the range of 1.1×10^{-5} to 5.1×10^{-5} m^2 s^{-1} while for the carbon nanotubes, it is in the range of 3.6×10^{-11} to 8.7×10^{-11} m^2 s^{-1} at 77 K. In the case of the activated carbons, the values are within the same range at higher temperatures. This implies that the rate of diffusion of hydrogen in the activated carbons is faster than in the carbon nanotubes. Graphs showing the variation of the diffusion coefficient for the materials with pressure are included in Appendix D.

Furthermore, the parameter k_1 can be said to refer to the faster of the two adsorption mechanisms taking place in the nanoporous carbons. For the activated carbons this can be linked to the diffusion of hydrogen gas molecules from the bulk to the pores of the carbon material. This leads to faster adsorption kinetics since this process is accompanied by a rise in the temperature of the system associated with the adsorption exotherm. The hydrogen molecules move faster making the process of adsorption faster. The parameter k_2 on the other hand can be related to the slower adsorption mechanism, which is the movement of the hydrogen molecules in the porous carbon network. For the carbon nanotubes, the fast component of adsorption relates to adsorption of hydrogen on the outer surface of the tubes, while the slow component can be attributed to the adsorption in the spaces between the tube bundles.

For pores with a wide opening, large enough for hydrogen molecules to diffuse easily, but narrow endings such that the diameter decreases with length, hydrogen molecules will diffuse faster from the bulk gas phase into the pore, but as they travel deeper into the pore, the rate of diffusion slows down making this process the rate determining

step. When the reverse is the case, that is, a pore with a narrow opening but with diameter that widens with length, the transfer of hydrogen from the bulk to the pore entry will be much slower than the diffusion inside the length of the pore making this the rate determining step.

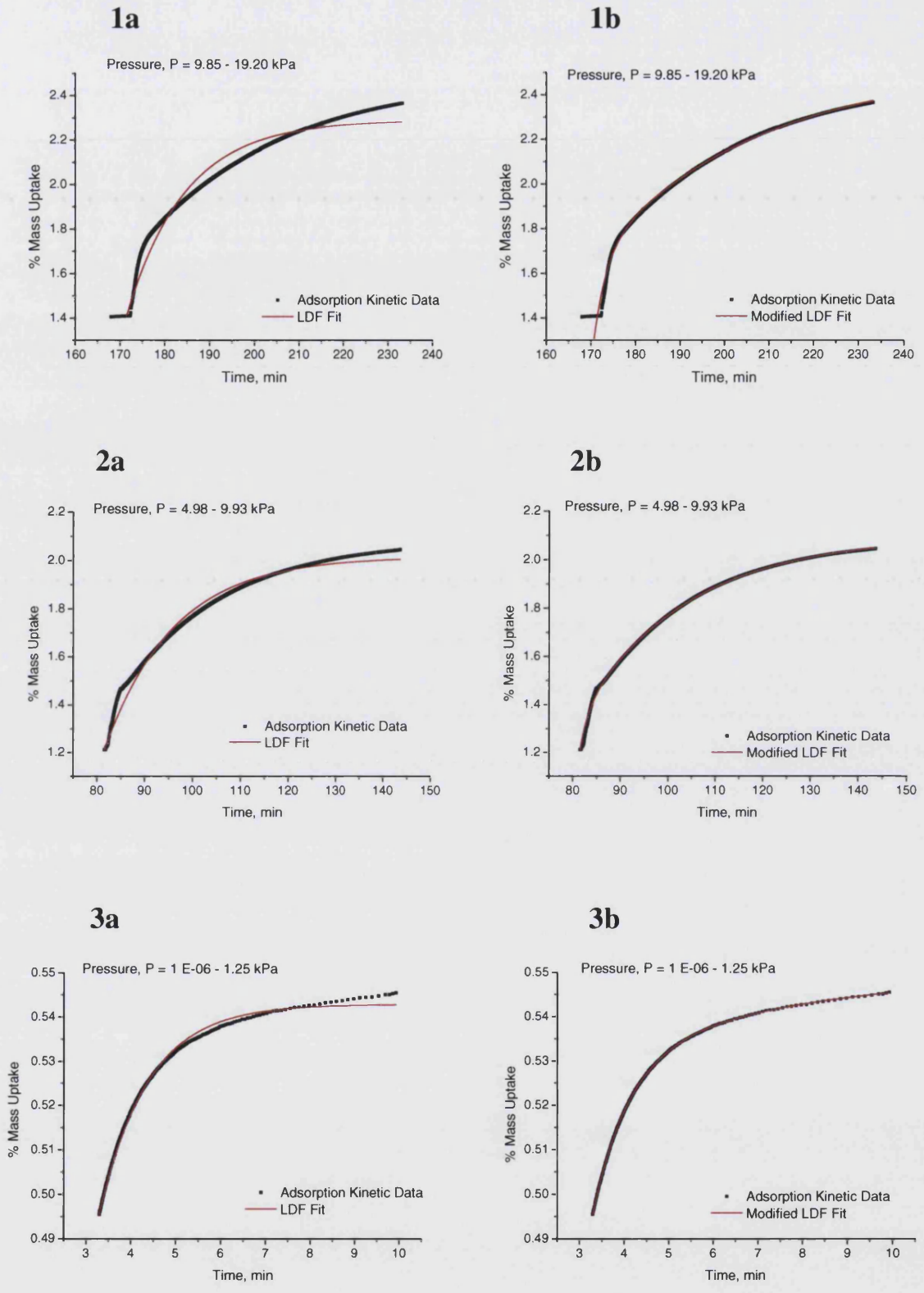

Figure 6.4-1: Plots of the ultra high purity hydrogen adsorption kinetic data showing the Linear Driving Force and Modified Linear Driving Force fits for (1a, b) BPL; (2a, b) Norit CNR 115; (3a, b) SRD/667/1.

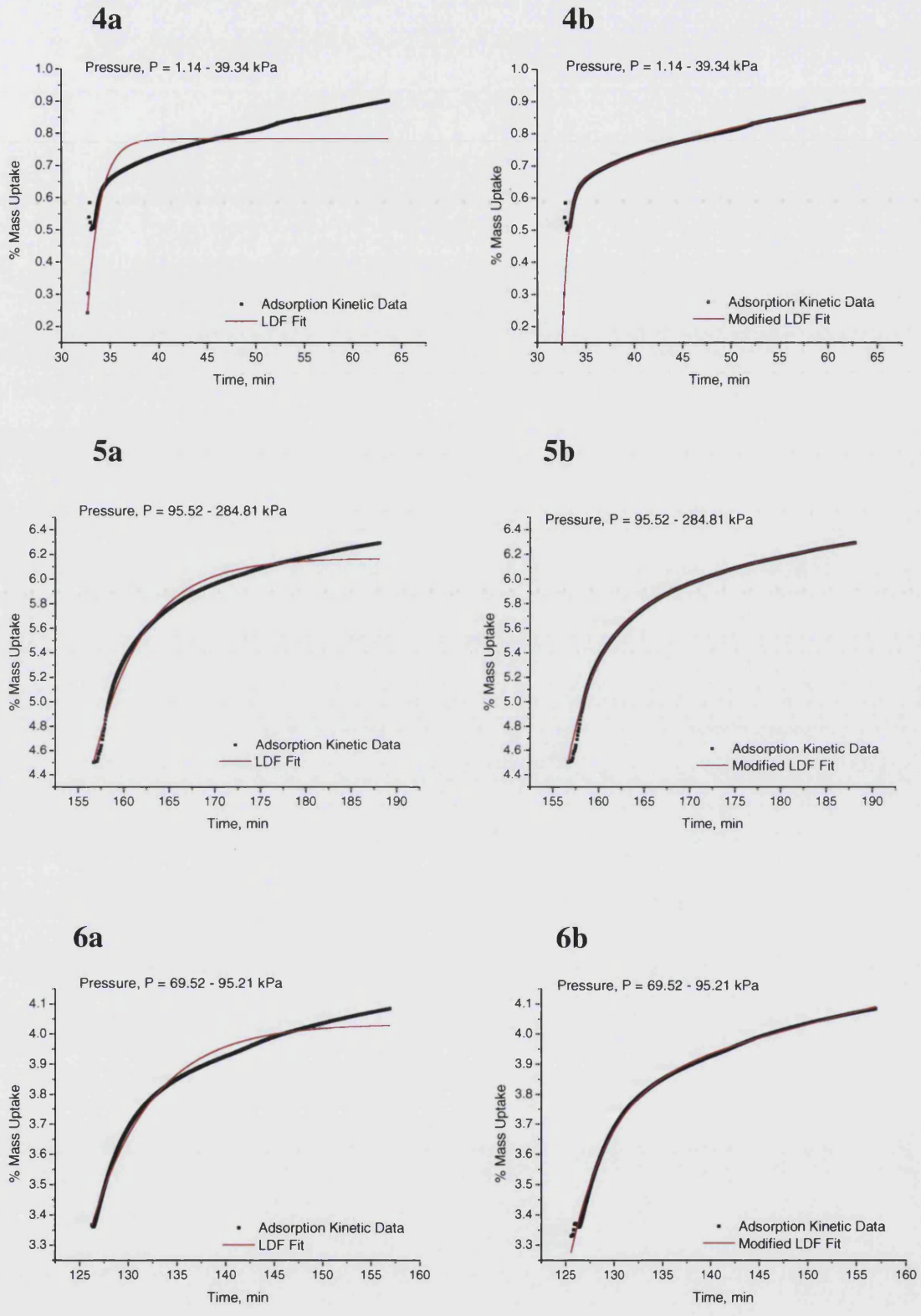

Figure 6.4-1: Plots of the ultra high purity hydrogen adsorption kinetic data showing the Linear Driving Force and Modified Linear Driving Force fits for (4a, b) SWNT-1; (5a, b) SWNT-2; (6a, b) MWNT-1.

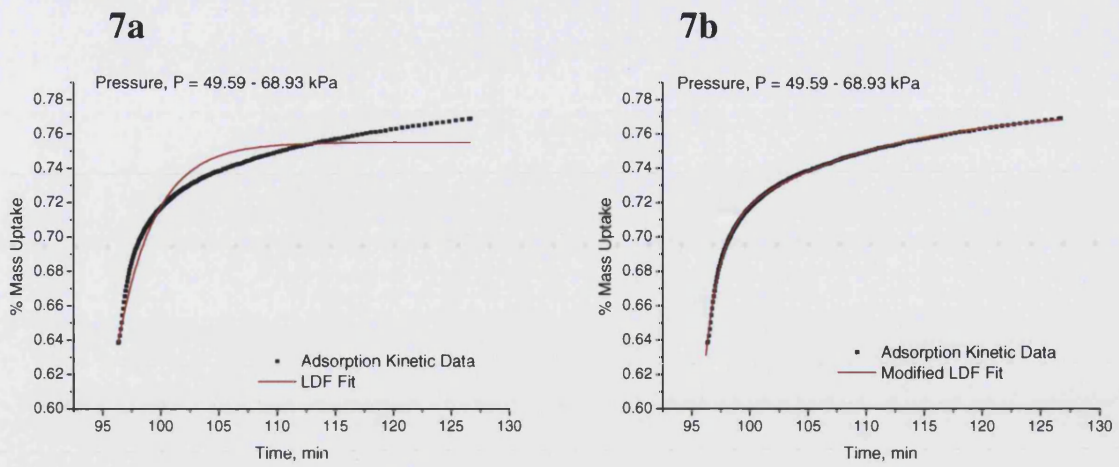

Figure 6.4-1: Plots of the ultra high purity hydrogen adsorption kinetic data at 77 K showing the Linear Driving Force and Modified Linear Driving Force fits for (7a, b) MWNT-2.

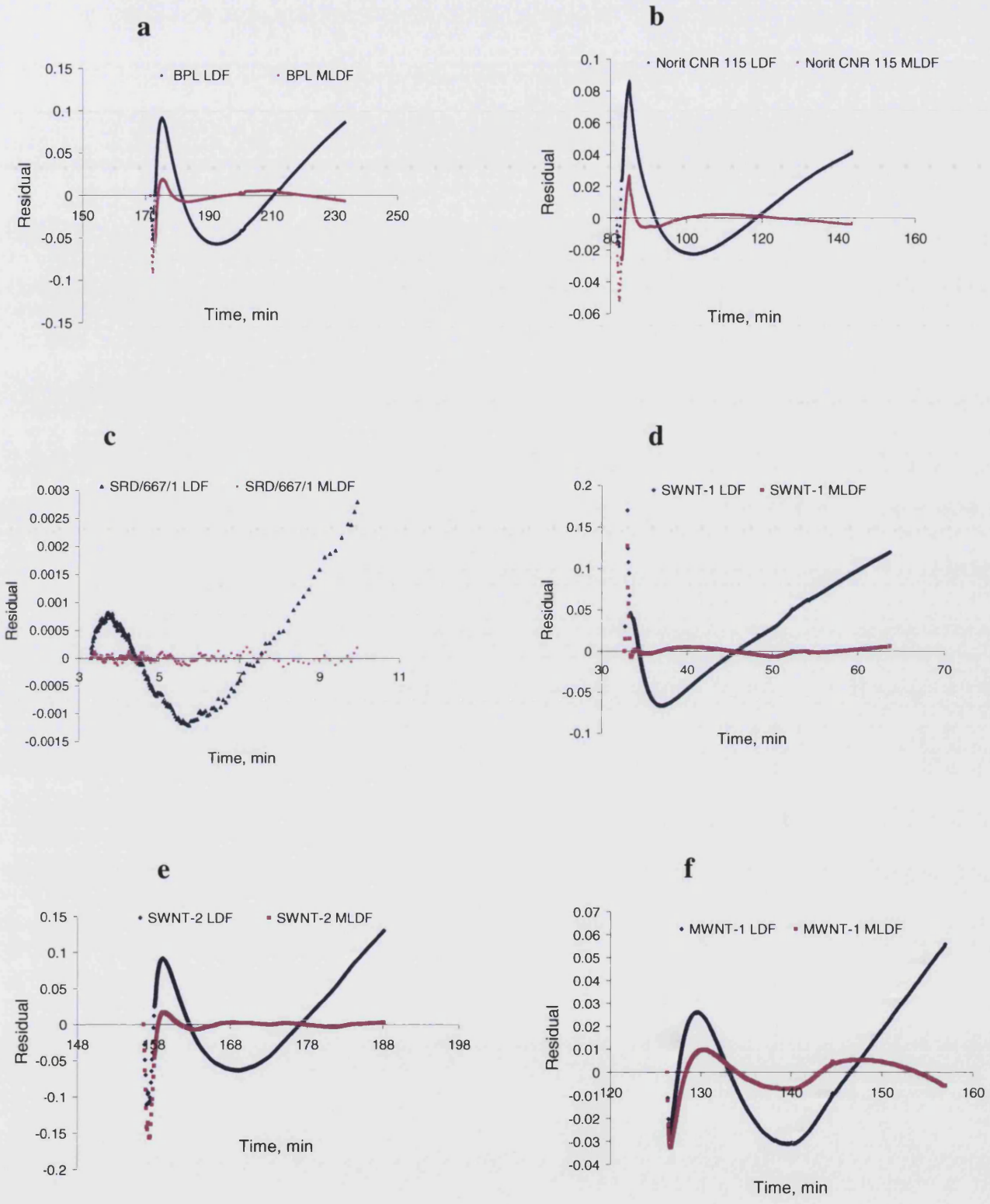

Figure 6.4-2: Residual plots of the linear driving force and modified linear driving force model fits to the adsorption kinetic data for the nanoporous carbons. (a) BPL; (b) Norit CNR 115; (c) SRD/667/1; (d) SWNT-1; (e) SWNT-2; (f) MWNT-1.

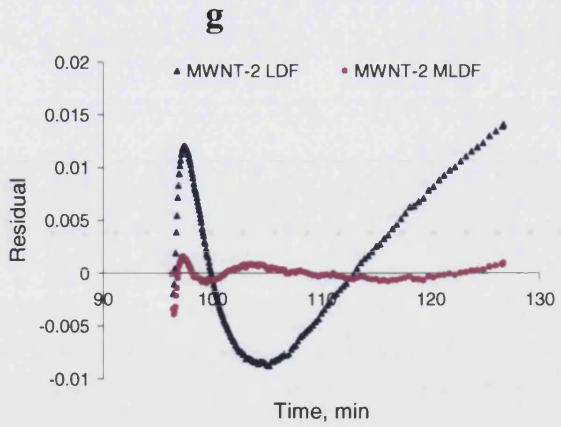

Figure 6.4-2: Residual plots of the linear driving force and modified linear driving force model fits to the adsorption kinetic data for the nanoporous carbons. (g) MWNT-2.

Table 6.4-1: Table showing the % Root Mean Square Error based on the LDF and MLDF Fits of the Adsorption Kinetic Data

Sample	% RMSE LDF	% RMSE MLDF
BPL	0.087	0.014
Norit CNR 115	0.052	0.009
SRD/667/1	0.005	0.0003
SWNT-1	0.126	0.010
SWNT-2	0.086	0.009
MWNT-1	0.055	0.024
MWNT-2	0.049	0.005

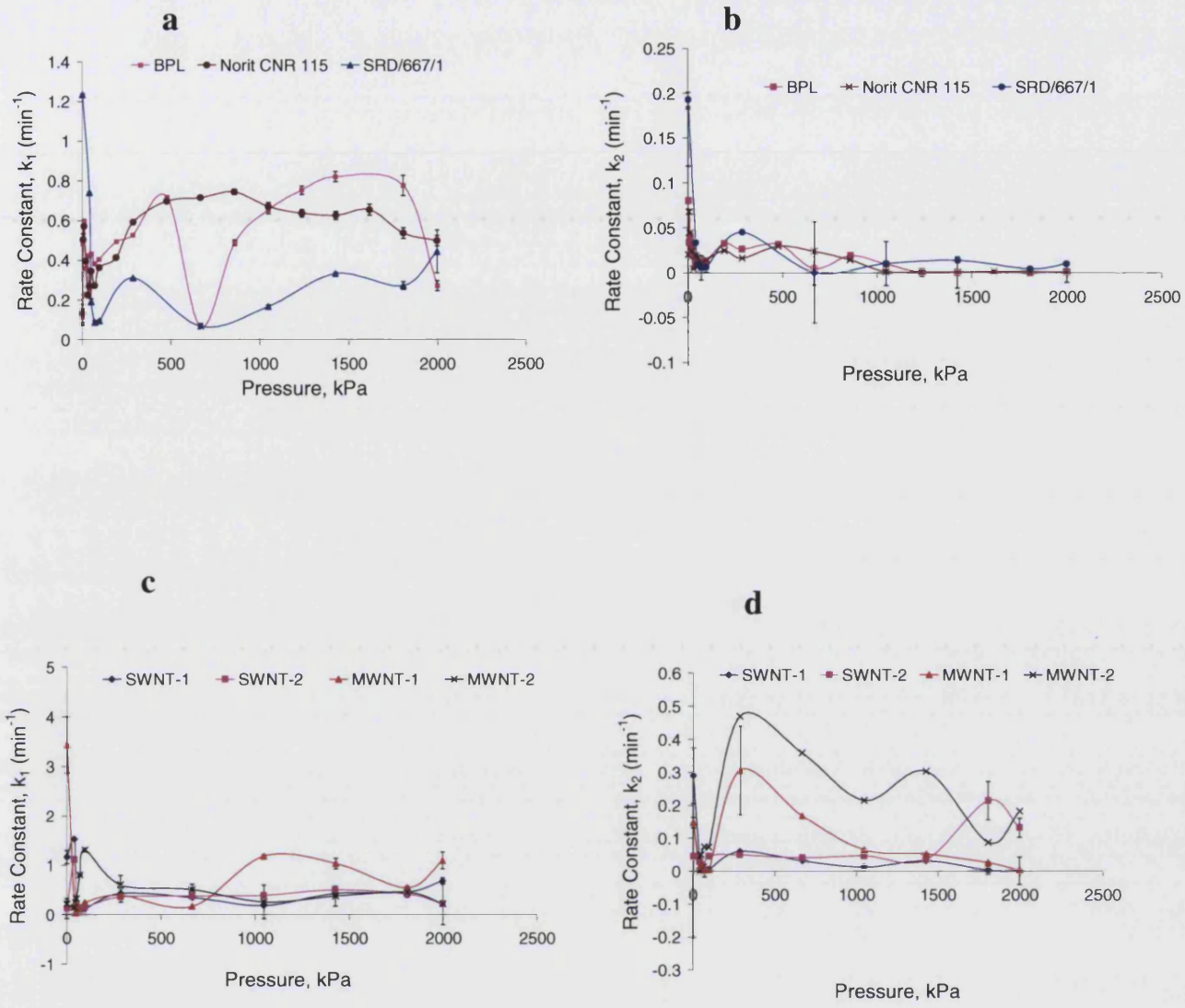

Figure 6.4-3: Graphs showing the variation of the adsorption rate constants with pressure for the nanoporous carbons. (a) Variation of k_1 for BPL, Norit CNR 115 and SRD/667/1; (b) Variation of k_2 for BPL, Norit CNR 115 and SRD/667/1; (c) Variation of k_1 for SWNT-1, SWNT-2, MWNT-1 and MWNT-2; (d) Variation of k_2 for SWNT-1, SWNT-2, MWNT-1 and MWNT-2.

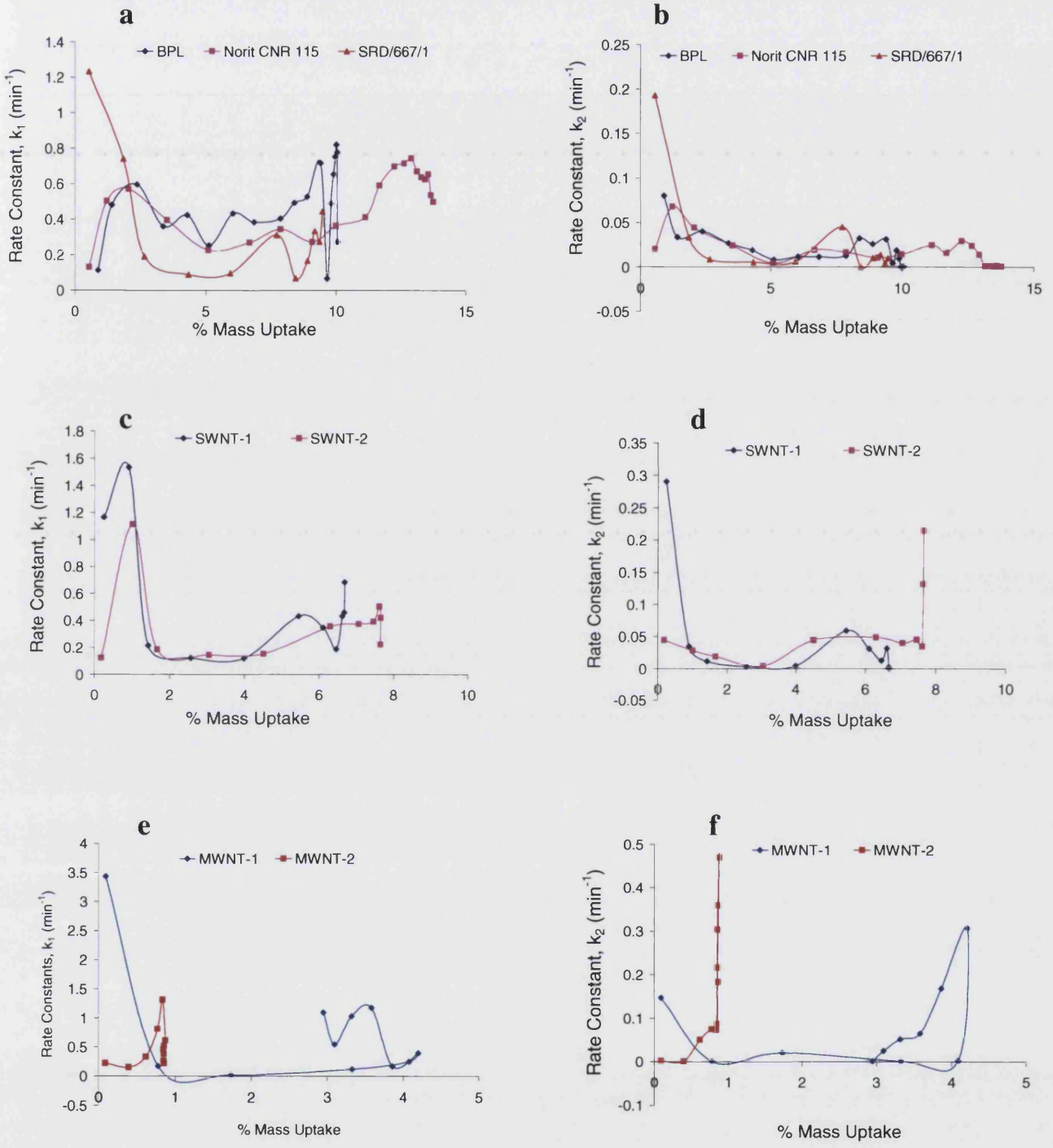

Figure 6.4-4: Graphs showing the variation of the adsorption rate constants with the experimental % mass uptake for the nanoporous carbons. (a) Variation of k_1 for BPL, Norit CNR 115 and SRD/667/1; (b) Variation of k_2 for BPL, Norit CNR 115 and SRD/667/1; (c) Variation of k_1 for SWNT-1, SWNT-2; (d) Variation of k_2 for SWNT-1, SWNT-2; (e) Variation of k_1 for MWNT-1 and MWNT-2; (f) Variation of k_2 for MWNT-1 and MWNT-2.

6.5 Relationship between Material Structure and Hydrogen Storage Capacity

This section of the thesis is a presentation and discussion on how the structural properties of the nanoporous carbon materials measured in the preceding chapters affect the hydrogen storage amounts observed. Structural properties such as the BET equivalent surface area, pore volume as obtained from nitrogen and carbon dioxide gas adsorption experiments, and pore size distribution results will be considered in this section. The findings are then compared to results available in the literature.

6.5.1 Surface Area, Pore Volume and Hydrogen Uptake

The experimental structural characterisation results for the nanoporous carbons have been presented in Chapter 4. The results obtained, such as the BET equivalent surface area and pore volumes measured from nitrogen and carbon dioxide, have been suggested by many authors (Gadiou *et al.*, 2005; Texier-Mandoki *et al.*, 2004; Zuttel *et al.*, 2001; Schlapbach and Zuttel, 2001; Nijkamp *et al.*, 2001; Strobel *et al.*, 1999; Takagi *et al.*, 2004) to correlate to the hydrogen storage capacity of these materials. According to Kayiran *et al.*, (2004), the main characteristic of carbon nanotubes and activated carbons is their specific surface area, defined as the area of the pore walls per gram of material, where gas molecules can be adsorbed and their pore volume (Kayiran *et al.*, 2004).

Figure 6.5-1 and Figure 6.5-2 show the plots of the BET equivalent surface area and pore volume in relation to the maximum uptake of hydrogen measured using ultra-high purity hydrogen at 77 K. It is evident from Figure 6.5-1 that the % mass of

hydrogen adsorbed increases with increasing equivalent BET surface area. This is analogous to the findings of many authors. Nijkamp *et al.*, (2001) carried out surface area and pore volume measurements on a wide range of carbon materials and found a rough correlation between the equivalent surface area and the hydrogen adsorption capacities at 77 K and 1 MPa (Nijkamp *et al.*, 2001). It is important to note that this correlation cannot be used as the sole representation of the potential capacity of a porous adsorbent especially when they are microporous. It can provide an initial idea or direction on the potential hydrogen storage capacity of the material but the extent does not depend completely on the magnitude of this value. Factors such as the pore size distribution and pore volume are also important. According to Gadiou *et al.*, (2005), the ability to adsorb hydrogen at 77 K is related to the range of accessible micropores present in a particular material (Gadiou *et al.*, 2005). Figure 6.5-2 shows that the amount of adsorbed hydrogen by weight at 77 K seems to be linearly related to the micropore volume of the sample. It can also be observed that the values of the nitrogen micropore volume are much higher than that of carbon dioxide. This finding is an indication that the range of micropore size distribution of the materials is wide also including supermicropores. This is consistent with the findings of the pore size distribution analysis discussed in Section 4.5. Despite the low pore volumes of SRD/667/1, SWNT-1 and SWNT-2, they adsorb high amounts of hydrogen than expected at 77 K. This indicates that the pore size may have a large influence on the amount adsorbed. This is in agreement with the observations of de la Casa-Lillo *et al.*, (2002) who studied the adsorption of hydrogen on a wide range of microporous materials (de la Casa-Lillo *et al.*, 2002).

According to de la Casa-Lillo *et al.*, (2002) there exists an optimum pore size and optimum pore geometry (slit pore) for hydrogen adsorption. The experiments they carried out demonstrated that the density of adsorbed hydrogen is strongly dependent on the pore size and that there exists an optimum pore size where the hydrogen adsorption is greater because of the enhanced adsorbate-adsorbent interactions (de la Casa-Lillo *et al.*, 2002). The optimum pore size seems to be able to accommodate two layers of hydrogen. These results pointed out that the amount of hydrogen adsorbed at room temperature is dependent on the volume of micropores in the adsorbent. Moreover his experiments show that the adsorption of hydrogen depends on the

micropore volume and pore size, but is not affected by the preparation method of the activated carbon (physical or chemical) or the shape of the material (powder or fibre). Rzepka *et al.*, (1998), on the other hand concluded in their study that the optimum pore size can hold one layer of adsorbed hydrogen, proposing a pore size close to 0.35 nm (Rzepka *et al.*, 1998). Their results were contrary to Wang and Johnson, who reported that the optimum pore size can hold two layers of hydrogen with the proposed pore size close to 0.56 nm (Wang and Johnson, 1999). Values similar this have been observed for BPL (0.54 nm) and SRD/667/1 (0.59 nm).

The pore size distribution results obtained for the nanoporous carbons as outlined in Section 4.5 can be correlated to the hydrogen uptake observed on these materials. It is found that BPL and Norit CNR 115 have a distribution of pore sizes in the range of ~ 0.42 – 10 nm, while SRD/667/1 has a distribution in the range of ~ 0.4 – 1.5 nm. This clearly shows that SRD/667/1 has the narrowest range of pore sizes all of which are in the microporous range. This is also evident from its nitrogen sorption isotherm shown in Figure 4.3-2. This provides a supporting explanation for the high uptake observed for this material at 77 K (9.47 %) using ultra high purity hydrogen inspite of its low BET equivalent surface area. The range of pore sizes observed for BPL and Norit CNR 115 show that the porosity of these materials extends into the mesoporous range, which may limit their hydrogen storage capacity as suggested by McEnaney *et al.*, (1987). In spite of this, their high BET equivalent surface areas coupled with these distribution of pores give them a high enough uptake of 10.04 and 13.74 % with ultra high purity hydrogen respectively. For the carbon nanotubes, pore sizes in the range of ~ 0.9 – 98 nm, ~ 0.9 – 80 nm, ~ 2 – 110 nm and ~ 25 – 40 nm are observed for SWNT-1, SWNT-2, MWNT-1 and MWNT-2 respectively. SWNT-1 and SWNT-2, clearly have a wide distribution of pores extending from the microporous range into mesoporous and macroporous range while MWNT-1 and MWNT-2 consist of pores mainly in the mesoporous and macroporous range. These observations are consistent with the hydrogen uptake amounts measured on these materials at 77 K. SWNT-2 with the highest surface area of the nanotubes and narrower range of pore sizes has the highest uptake of ultra high purity hydrogen (7.63 %) followed by SWNT-1 (6.68 %), MWNT-1 (2.95 %) and then MWNT-2 (0.85 %).

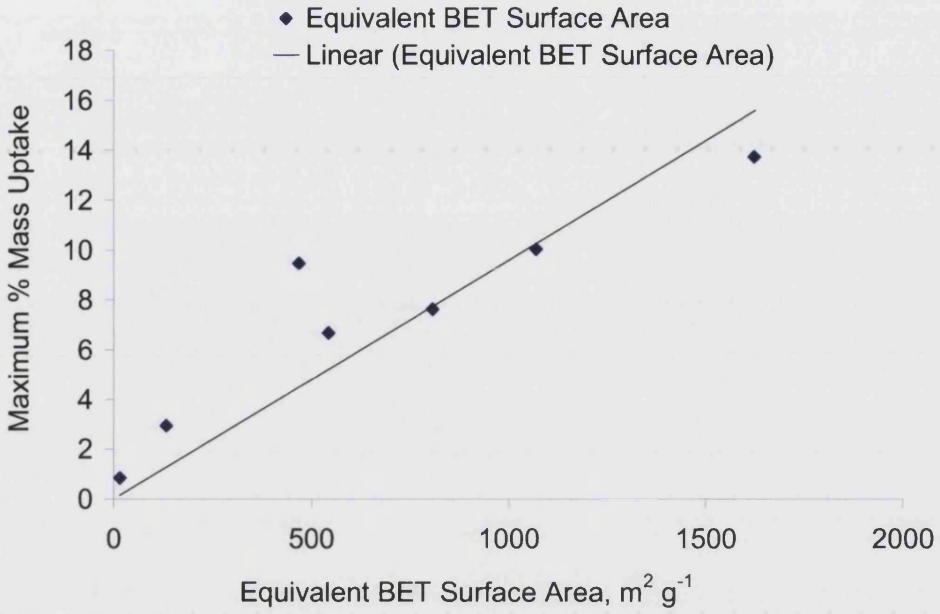

Figure 6.5-1: Graph showing the relationship between the equivalent BET surface area and hydrogen gas uptake obtained for the nanoporous carbons.

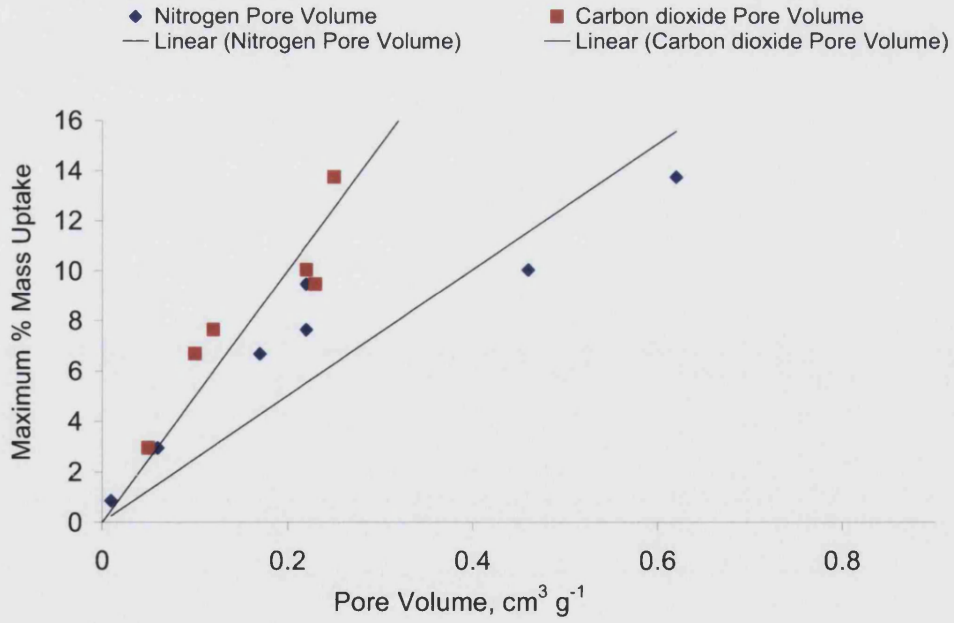

Figure 6.5-2: Graph showing the variation of the pore volume with the % mass adsorbed on the nanoporous carbons.

Chapter Seven

Concluding Remarks

7.1 Introduction

In this chapter a brief summary of the work detailed in this investigation will be presented. This chapter is divided into three main sections. Section 7.2 is a summary of the thesis background and the work carried out in this investigation. In section 7.3, the overall conclusions of this work are highlighted followed by suggestions for future work in section 7.4.

7.2 Background and Thesis Summary

This work has been focussed on bringing into context the issue of hydrogen storage with regards to advancing the introduction of hydrogen as a future energy carrier. It has been highlighted that a suitable method for storing hydrogen is required to make this possible. The storage system should be able to hold and discharge 4.5 wt % H_2 by 2007, 6 wt % H_2 by 2010 and 9 wt % H_2 by 2015, according to the targets set by the United States Department of Energy (DOE), which is applied worldwide. In this work, studies on the potential of a selection of nanoporous carbon materials to store hydrogen have been carried out leading to a number of interesting findings:

1. High maximum weight uptakes of hydrogen have been observed on the activated carbons, BPL (10.04 wt-%), Norit (13.74 wt-%) and SRD (9.47 wt-%) and the single-walled carbon nanotubes, SWNT-1 (6.68 wt-%) and SWNT-2 (7.63 wt-%) at 77 K using UHP-H_2. The multi-walled nanotubes, MWNT-1 (2.95 wt-%) and MWNT-2 (0.85 wt-%) are observed to have much lower uptake.

2. The storage capacity of the activated carbons has been observed to be dependent on the sorption temperature, such that when the temperature is low (77 K), the amount of hydrogen adsorbed is higher than when the adsorption temperature is high (195, 303 K). This can be linked to the observed reduction in the value of affinity constant, *b*, obtained from the Toth adsorption model as the temperature increases.

3. The gas purity has been found to affect the hydrogen storage capacities of all the nanoporous carbons studied. The effects are significantly noticeable at 77 K but have been observed to diminish as the temperature is increased.

4. The storage capacity of these materials has a dependence on their respective BET equivalent surface areas, therefore the materials with high surface areas such as Norit CNR 115 (1624.3 $m^2 g^{-1}$), BPL (1069.6 $m^2 g^{-1}$), SRD/667/1 (468.1 $m^2 g^{-1}$), SWNT-1 (543.5 $m^2 g^{-1}$) and SWNT-2 (807.6 $m^2 g^{-1}$)) were observed to have higher uptakes of hydrogen at 77 K. The multi-walled carbon nanotubes, MWNT-1 (133.9 $m^2 g^{-1}$) and MWNT-2 (16.3 $m^2 g^{-1}$) with lower surface areas had much lower capacities for hydrogen storage at this temperature.

5. Measurements also reveal that the hydrogen storage capacity is dependent on the pore volume and distribution of pore sizes in the materials. The activated carbons and single-walled nanotubes with higher pore volumes are observed to have higher capacity for hydrogen.

6. There is the evidence of hysteresis at 77 K for hydrogen sorption isotherms obtained for the activated carbons and the single-walled nanotubes. The

sorption isotherms for the multi-walled nanotubes on the other hand are reversible. The hysteresis effects are found to diminish as the sorption temperature is increased from cryogenic to room temperature.

7. Cyclic studies carried out on the activated carbons and SWNT-2 show that the storage capacity of the materials is reduced to less than half of the originally observed uptake as the number of cycles increases. The amount of discharged (desorbed) hydrogen is also found to increase on subsequent cycles.

8. Transmission electron microscopy reveals the alignment and arrangement of the carbon nanotubes. All the carbon nanotubes are observed to be intertwined long tubules, which are arranged into bundles in the case of the single-walled nanotubes. The presence of residual catalyst particles from the preparation of SWNT-1 & 2 is also observed. The presence of surface defects linked to the purification of MWNT-2 is also revealed.

9. X-ray diffraction studies reveal that the structure of the nanoporous carbon materials studied differ from that of perfect graphite resulting in wider interlayer spacings. This can be linked to the tubostratic stacking of graphitic sheets, defects in their crystal lattice and possibly the presence of heteroatoms in their structure.

10. The heterogeneity of the activated carbons, derived from the heterogeneity parameter, t of the Toth adsorption model is found to increase with temperature. This parameter does not indicate the source of the heterogeneity, (structural or surface). The affinity constant b, decreases with temperature.

11. The heat of adsorption obtained at zero surface coverage for the activated carbons show values of 5.26, 4.74 and 2.61 kJ mol^{-1} for BPL, Norit and SRD respectively.

12. Calculation of the Isosteric heat of adsorption for the activated carbons revealed that its value reduces with increase in the amount adsorbed (surface coverage). This implies that the surfaces of these materials are energetically

heterogeneous such that different sites exhibit varying extents of adsorption energy.

13. Two mechanisms of adsorption for the nanoporous carbons have been proposed. For the activated carbons, the mechanisms are due to diffusion from the bulk gas phase to the solid surface and the diffusion of the gas molecules through the network of pores. For the nanotubes, the dominating mechanisms are based on diffusion from the bulk gas phase to the outer surface if the tubes, adsorption in the interstitial spaces between the nanotube bundles or inside the tubes in the case of the opened nanotube, MWNT-2.

7.3 Overall Conclusions

From the main research findings reported in section 6.2, the following conclusions have been reached.

1. The nanoporous carbon materials studied in this work can only be useful for hydrogen storage at 77 K and 20 bar. The uptake values obtained meet and exceed the US DOE 2010 hydrogen storage target for systems as stated above. It is important to note that the release of hydrogen from the system will have to be at a temperature different from the storage conditions due to the hysteresis observed at this temperature.

2. Activated carbon materials are not able to store sufficient amounts of hydrogen at room temperature based on the weak adsorption affinity between hydrogen and their respective surfaces at this temperature. It is believed that high temperature impedes hydrogen storage. The relatively low heat of adsorption observed combined with the reduction of the heat of adsorption as surface coverage increases, play contributory roles in the low uptakes measured.

3. Gravimetric sorption cycling of the nanoporous carbon materials shows that in practical applications, a new load of sample must be used with every application to meet the storage requirements.

4. Correlation of the structural characterisation data with the storage capacity of the nanoporous carbons shows that several factors dictate their hydrogen storage capacity. These include; surface area, pore size distribution, pore volume, purity of the carbon material and the hydrogen gas.

7.4 Suggestions for Further Work

The work carried out in this investigation has led to a series of interesting observations. The following suggestions are proposed as interesting future directions for this work.

1. Design and construction of a hydrogen storage prototype based on nanoporous carbon materials. The system would be supplied with hydrogen either from a compressed gas cylinder or an in house production system. An activated carbon such as Norit CNR 115, which has been proposed to have good capacity for hydrogen storage at 77K will be utilised as the storage media. The material would be encased in a storage vessel which would be evacuated and immersed in a cryogenic bath prior to hydrogen loading. This would be followed by the delivery of the hydrogen to power a piece(s) of equipment via a fuel cell or internal combustion engine (ICE). Critical aspects of the design would include thermal management of system, pressure control, safety and optimisation of the system delivery conditions. Figure 7.4-1 shown below represents a schematic of the proposed system. Such a system would improve knowledge on the practical application of nanoporous carbon systems for hydrogen storage.

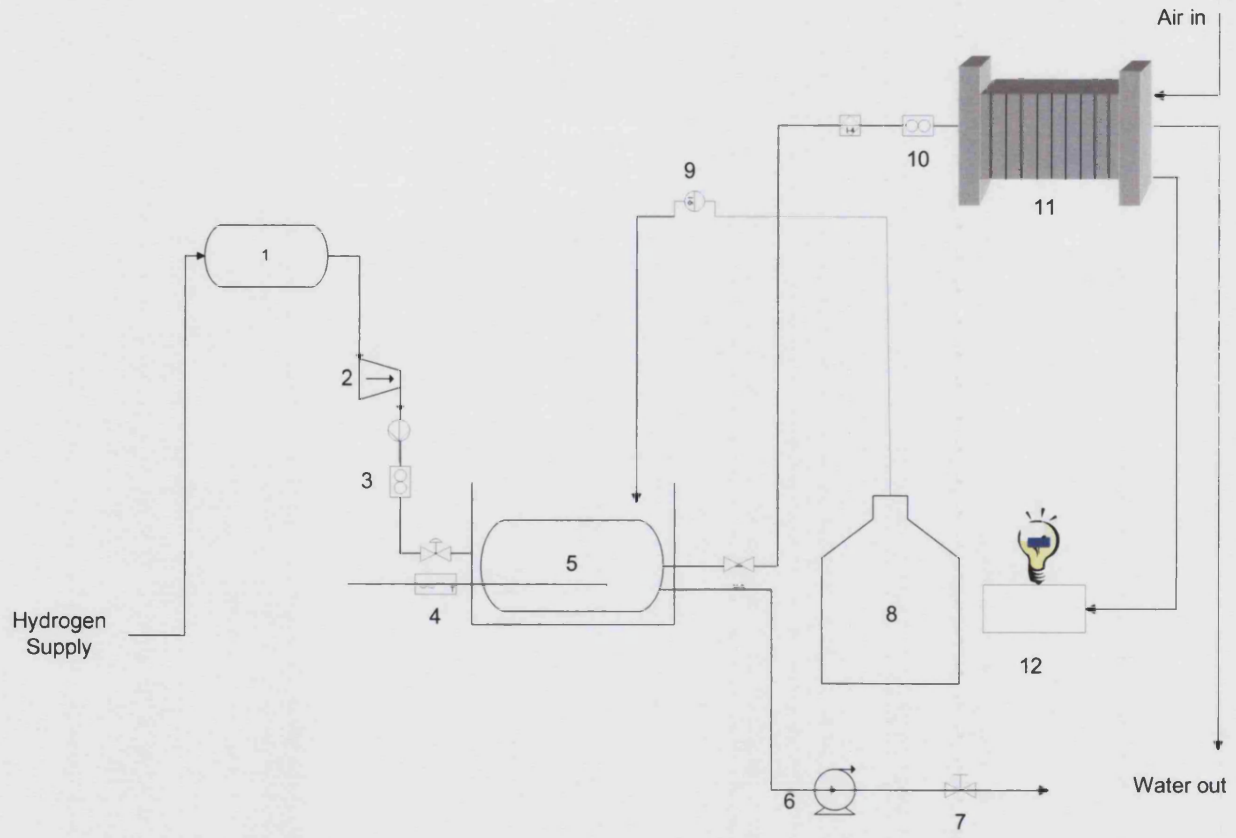

Figure 7.4-1: Schematic of a H_2 storage system based on the use of nanoporous carbon. 1) H_2 gas dehumidifier and cleaner; 2) Gas compressor; 3) FeedH_2 pressure controller; 4) Liquid N_2 level meter; 5) H_2 storage vessel; 6) Liquid N_2 pump; 7) Manual Valve; 8) Liquid N_2 supply dewar; 9) Flow controller; 10) Discharge H_2 pressure controller; 11) H_2 fuel cell and 12) Light bulb.

2. Preparation and characterisation of nanoporous carbons with very high surface area, stable cycling properties, high pore volume in the microporous range and optimum pore sizes in the range suitable for hydrogen storage.

3. Precise measurement of the hysteresis critical point for each material, that is, measuring exactly the point (temperature) where hysteresis disappears. Thereby optimising the hydrogen delivery conditions.

4. Use of hydrogen storage measurement equipment attached to a mass spectrometer to determine the composition of the gas desorbed from a nanoporous carbon material. Thereby deducing what quantity of the gas adsorbed by the material is actually hydrogen.

5. Carry out high pressure hydrogen storage measurements on the materials studied in this work to investigate their hydrogen storage properties at pressures in excess of 2000 kPa (20 bar).

6. A detailed economic analysis of the cost of implementing a H_2 storage system based on the use of nanoporous carbon materials for mobile and stationary applications in comparison to currently available technologies using the United Kingdom initially as a benchmark.

7. Carry out hydrogen storage measurements on the ash contained in the nanoporous carbons to assess their contribution to uptake.

References

Abdel-Aal, H. K., Sadik, M., Bassyouni, M., Shalabi, M., (2005). A New Approach to Utilize Hydrogen as a Safe Fuel. *International Journal of Hydrogen Energy*, 30 (13-14), pp.1511-1514.

Adamson, K.-A., (2004). Hydrogen from Renewable Resources – The Hundred Year Commitment. *Energy Policy*, 32 (10), pp.1231-1242.

Agrawal, R., Offutt, M., Ramage, M. P., (2005). Hydrogen Economy – An Opportunity for Chemical Engineers. *AIChE Journal*, 51, pp.1582- 1589.

Ahmed S., and Krumpelt, M., (2001). Hydrogen from Hydrocarbon Fuels for Fuel Cells. *International Journal of Hydrogen Energy*, 26, pp.291-301.

Ahmadpour, A., and Do, D. D., (1996). The preparation of active carbons from coal by chemical and physical activation. *Carbon*, 34 (4), pp.471-479.

Ahn, C. C., Ye, Y., Ratnakumar, B. V., Witham, R. C., Bowman, Jr., and Fultz, B., (1998). Hydrogen Desorption and Adsorption Measurements on Graphite Nanofibers. *Applied Physics Letters*, 73 (23), pp.3378-3380.

Aiello, R., Matthews, M. A., Reger, D. L., and Collins, J. E., (1998). Production of Hydrogen Gas from Novel Chemical Hydrides *International Journal of Hydrogen Energy*, 23 (12), pp.1103-1108.

Aiello, R., Sharp, J. H., Matthews, M. A., (1999). Production of Hydrogen from Chemical Hydrides via Hydrolysis with Steam. *International Journal of Hydrogen Energy*, 24(12), pp.1123-1130.

Ajayan, P. M., Ebbesen, T. W., Ichihashi, T., Iijima, S., Tanigaki, K., and Hiura, H., (1993). Opening Carbon Nanotubes with Oxygen and Implications for Filling. *Nature*, 362, pp.522-525.

Amankwah, K. A. G. and Schwarz, J. A., (1991). Assessment of the Effect of Impurity Gases on the Storage Capacity of Hydrogen on Activated Carbon using the Concept of Effective Adsorbed Phase Molar Volume. *International Journal of Hydrogen Energy*, 16(5), pp.339-344.

Amendola, S. C., Sharp-Goldman, S. L., Janjua, M. S., Spencer, N. C., Kelly, M. T., Petillo, P. J., Binder, M., (2000a). A Safe, Portable, Hydrogen Gas Generator using Aqueous Borohydride Solution and Ru Catalyst. *International Journal of Hydrogen Energy*, 25 (10), pp.969-975.

Amendola, S. C., Sharp-Goldman, S. L., Janjua, M. S., Kelly, M. T., Petillo, P. J., Binder, M., (2000b). An Ultrasafe Hydrogen Generator: Aqueous, Alkaline Borohydride Solutions and Ru Catalyst. *Journal of Power Sources*, 85, pp.186-189.

Andrews, C. J., and Weiner, S. A., (2004). Visions of a Hydrogen Future. In *IEEE Power and Energy Magazine*, 2 (2), pp. 26-34.

Arab, M., Picaud, F., Devel, M., Ramseyer, C., and Giradet, C., (2004). Molecular Selectivity due to Adsorption Properties in Nanotubes. *Physical Review B*, 69, 165401-1 - 165401-11.

Arriagada, R., Garcia, R., Molina-Sabio, M., Rodriguez-Reinoso, F., (1997). Effect of Steam Activation on the Porosity and Chemical Nature of Activated Carbons from Eucalyptus Globulus and Peach Stones. *Microporous Materials*, 8 (3), pp.123-130.

Atkinson, K., Roth, S., Hirscher, M. and Grunwald, W., (2001). Carbon Nanostructures: An Efficient Hydrogen Storage Medium for Fuel Cells. In *Fuel Cells Bulletin*, 4 (38), pp. 9-12.

Bandosz, T. J., Jagiello, J., and Schwarz, J. A., (1993). Effects of Surface Chemical Groups on Energetic Heterogeneity of Activated Carbons. *Langmuir*, 9 (10), pp.2518-2522.

Barreto, L., Makihira, A., and Riahi, K., (2003). The Hydrogen Economy in the 21st Century: A Sustainable Development Scenario. *International Journal of Hydrogen Energy*, 28 (3), pp.267-284.

Barrett, E. P., Joyner, L. G., and Halenda, P. P., (1951). The Determination of Pore Volume and Area Distributions in Porous Substances. I. Computations from Nitrogen Isotherms. *Journal of American Chemical Society*, 73, pp.373-380.

BBC, (2004).The Hydrogen Bomb. Access Date: 02/10/2006. http://news.bbc.co.uk/onthisday/hi/dates/stories/march/1/newsid_2781000/2781419.stm

Benard, P., and Chahine, R., (2001). Determination of the Adsorption Isotherms of Hydrogen on Activated Carbons above the Critical Temperature of the

Adsorbate over Wide Temperature and Pressure Ranges. *Langmuir*, 17, pp.1950-1955.

Benard, P., and Chahine, R., (2001). Modelling of Adsorption Storage of Hydrogen on Activated Carbons. *International Journal of Hydrogen Energy*, 26 (8), pp.849-855.

Bhatia, S. K., Myers, A. L., (2006). Optimum Conditions for Adsorptive Storage. *Langmuir*, 22, pp.1688-1700.

Brewer, G.D., (1991). *Hydrogen Aircraft Technology*, CRC Press. (http://www.crcpress.com).

BS4539-1: (1996). Determination of the Specific Surface Area of Powders – Part 1: BET Method of Gas Adsorption for Solids (including Porous Materials). British Standards.

BS7591-2: (1992). Porosity and Pore Size Distribution of Materials – Part 2: Method of Evaluation by Gas Adsorption. British Standards.

Bucky Balls, Diamond and Graphite, (2006). Wisconsin. http://www.chem.wisc.edu/~newtrad/CurrRef/BDGTopic/BDGtext/BDGtoc.html

Buzanowski, M. A., Yang, R. T., (1989). Extended Linear Driving-Force Approximation for Intraparticle Diffusion Rate Including Short Times. *Chemical Engineering Science*, 44 (11), pp.2683-2689.

Cagnon, B., Py, X., Guillot, A., Stoeckli, F., (2003). The Effect of the Carbonization/Activation Procedure on the Microporous Texture of the Subsequent Chars and Active Carbons. *Microporous and Mesoporous Materials*, 57 (3), pp.273-282.

Carpetis, C., and Peschka, W., (1980). A study on hydrogen storage by use of cryoadsorbents .*International Journal of Hydrogen Energy*. 5(4) pp.539-554

Carzorla-Amoros, D., Alcaniz-Monge, J., de la Casa-Lillo, M. A., and Linares-Solano, A., (1998). CO_2 as an Adsorptive to Characterize Carbon Molecular Sieves and Activated Carbons. *Langmuir*, 14 (16), pp.4589-4596.

Cazorla-Amoros, D., Alcaniz-Monge, J., and Linares-Solano, A., (1996). Characterization of Activated Carbon Fibers by CO_2 Adsorption. *Langmuir*, 12 (11), pp.2820-2824.

Chambers, A., Park, C., Baker, T. K., Rodriguez, N. M., (1998). Hydrogen Storage in Graphite Nanofibers. *Journal of Physical Chemistry B*, 102, pp.4253-4255.

Chen, P., Wu, X., Lin, J., and Tan, K. L., (1999). High H_2 Uptake by Alkali-Doped Carbon Nanotubes under Ambient Pressure and Moderate Temperatures. *Science*, 285 (5424), pp.91-93.

Chen, Y., Liu, C., Li, F., Cheng, H.-M., (2006). Pore structures of multi-walled carbon nanotubes activated by air, CO_2 and KOH. *Journal of Porous Materials*, 13 (2), pp.141-146.

Cheng, H.-M., Yang, Q.-H. and Liu, C., (2001). Hydrogen Storage in Carbon Nanotubes. *Carbon*, 39 (10), pp.1447-1454.

Cherry, R. S., (2004). A Hydrogen Utopia? *International Journal of Hydrogen Energy*, 29 (2), pp.125-129.

Choi, B.-U., Choi, D.-K., Lee, Y.-W., and Lee, B.-K., (2003). Adsorption Equilibria of Methane, Ethane, Ethylene, Nitrogen, and Hydrogen onto Activated Carbon. *Journal of Chemical Engineering Data*, 48, pp.603-607.

Choma, J., Jaroneic, M., Kloske, M., (2002). Improved Pore-size Analysis of Carbonaceous Adsorbents. *Adsorption Science and Technology*, 20, pp.307-315.

Conte, M., Iacobazzi, A., Ronchetti, M., and Vellone, R., (2001). Hydrogen Economy for a Sustainable Development: State-of-the-art and Technological Perspectives. *Journal of Power Sources*, 100, pp.171-187.

Conte, M., Prosini, P. P., Passerini, S., (2004). Overview of Energy/Hydrogen Storage: State-of-the-Art of the Technologies and Prospects for Nanomaterials. *Materials Science and Engineering*, B108, pp.2-8.

Cullity, B. D., and Stock, S. R., (2001). *Elements of X-ray Diffraction*. London: Prentice Hall.

Darkrim, F., and Levesque, D., (2000). High Adsorptive Property of Opened Carbon Nanotubes at 77 K. *Journal of Physical Chemistry B*, 104, pp.6773-6776.

Darkrim, F. L., Malbrunot, P., and Tartaglia, G. P., (2002). Review of Hydrogen Storage by Adsorption in Carbon Nanotubes. *International Journal of Hydrogen Energy*, 27 (2), pp.193-202.

Das, L. M., (1996). On-board Hydrogen Storage Systems for Automotive Application. *International Journal of Hydrogen Energy*, 21 (9), pp.789-800.

de la Casa-Lillo, M. A., Lamari-Darkrim, F., Cazorla-Amoros, D., and Linares-Solano, A., (2002). Hydrogen Storage in Activated Carbon and Activated Carbon Fibers. *Journal of Physical Chemistry B*, 106, pp.10930-10934.

DeLuchi, M. A., (1989). Hydrogen vehicles: An Evaluation of Fuel Storage, Performance, Safety, Environmental Impacts, and Cost. *International Journal of Hydrogen Energy*, 14 (2), pp.81-130.

DeLuchi, M.A., Larson, E.D., Williams, R.H. (1991). "Hydrogen and Methanol: Production from Biomass and Use in Fuel Cell and Internal Combustion Engine Vehicles, A Preliminary Assessment," The Centre for Energy and Environmental Studies, Princeton University, PU/CEES Report No. 263, August.

Dillon, A. C., Jones, K. M., Bekkedahl, T. A., Kiang, C. H., Bethune, D. S., and Heben, M. J., (1997). Storage of Hydrogen in Single-walled Carbon Nanotubes. *Nature*, 386, pp.377-378.

Dillon, A. C., and Heben, M. J., (2001). Hydrogen Storage using Carbon Adsorbents: Past, Present and Future. *Applied Physics A: Materials Science and Processing*, 72, pp.133-142.

Divisek, J., Oetjen, H-F., Peinecke, V., Schmidt, V. M., Stimming, U. (1998).Components for PEM fuel cell systems using hydrogen and CO containing fuels. *Electrochimica Acta.* 43(24), pp. 3811-3815.

Do, H. D., and Do, D. D., (1995). A description of adsorption in activated carbon using a hybrid isotherm equation. *Langmuir*, 11(7), pp.2639-2647.

Do, D. D., and Do, H. D., (2003). Refined Method of Potential Enhancement in the Equilibria Characterization of Activated Carbon. Comparison with GCMC and DFT. *Langmuir,* 19 (20), PP.8302 -8315.

Do, D. D., and Do, H. D., (2003). Adsorption of supercritical fluids in non-porous and porous carbons: analysis of adsorbed phase volume and density. *Carbon*, 41(9), pp. 1777-1791.

Do, D. D., and Wang, K., (1998). A New Model for the Description of Adsorption Kinetics in Heterogeneous Activated Carbon. *International Journal of Hydrogen Energy*, 36, pp.1539-1554.

Do, D. D., (1998). *Adsorption Analysis: Equilibria and Kinetics*, London: Imperial College Press.

Dubinin, M. M., (1989). Fundamentals of the Theory of Adsorption in Micropores of Carbon Adsorbents: Characteristics of their Adsorption Properties and Microporous Structure. *Pure and Applied Chemistry*, 61, pp.1841-1843.

M.M. Dubinin, L.V. Radushkevich, Proceedings of the National Academy of Science USSR 55 (1947) 331.

Dunn, S., (2002). Hydrogen Futures: Toward A Sustainable Energy System. *International Journal of Hydrogen Energy*, 27 (3), pp.235-264.

Ebbesen, T. W., and Ajayan, P. M., (1992). Large Scale Synthesis of Carbon Nanotubes. *Nature*, 358, pp.220-222.

Ebbesen , T. W., Hiura, H., Fujita, J., Ochiai, Y., Matsui, S., and Tanigaki., K., (1993). Patterns in the Bulk Growth of Carbon Nanotubes. *Chemical Physics Letters*. 209 (1-2), pp.83-90.

Ebbessen, T. W., (1994). Purification of Nanotubes. *Nature*. 367, pp.519.

Ebbessen, T. W., (1997). Production and Purification of Carbon Nanotubes: In Carbon Nanotubes: Preparation and Properties. CRC Press Inc.

Ehrburger-Dolle, F., Gonzalez, M. T., Molina-Sabio, M., Rodriguez-Reinoso, F. (1997). *In Characterisation of Porous Solids IV*(Ed, McEnaney, B., et al.) Elsevier, Bath, pp. 237-244.

Endo, M., Takeuchi, K., Igarashi, S., Korbori, K., Shiraishi, M., Kroto, H. W., Production and Structure of Pyrolytic Carbon Nanotubes (PCNTs). *Journal of Physics and Chemistry of Solids*. 54(12), pp. 1841-1848. (1993).

Endo et al., 1995

Fan, Y., Liao, B., Wei, Y., Lu, M. and Cheng, H.-M., (1999). *Carbon*, 37, pp.1649-1652.

Fletcher, A. J., and Thomas, K. M., (1999). Adsorption and Desorption Kinetics of *n*-Octane and *n*-Nonane Vapors on Activated Carbon. *Langmuir*, 15 (20), pp.6908-6914.

Fletcher, A. J. and Thomas, K. M., (2000). Compensation Effect for the Kinetics of Adsorption/Desorption of Gases/Vapors on Microporous Carbon Materials. *Langmuir*, 16, pp.6253-6266.

Fletcher, A. J., Cussen, E. J., Bradshaw, D., Rosseinsky, M. J. and Thomas, K. M., (2004). Adsorption of Gases and Vapors on Nanoporous Ni_2(4-4'-Bipyridine)$_3(NO_3)_4$ Metal-Organic Framework Materials Templated with Methanol and Ethanol: Structural Effects in Adsorption Kinetics. *JACS Articles*, 126, pp.9750-9759.

Frere, M. G., De Weireld, G. F., (2002). High Pressure and High Temperature Excess Adsorption Isotherms of N_2, CH_4, and C_3H_8 on Activated Carbon. *Journal of Chemical Engineering Data*, 47, pp.823-829.

Gadiou, R., Saadallah, S.-E., Piquero, T., David, P., Parmentier, J., Vix-Guterl, C., (2005). The Influence of Textural Properties on the Adsorption of Hydrogen on Ordered Nanostructures Carbons. *Microporous and Mesoporous Materials*, 79, pp.121-128.

Glueckauf, E., and Coates, J. I., (1947). Theory of Chromatography. Part IV. The Influence of Incomplete Equilibrium on the Front Boundary of Chromatograms and on the Effectiveness of Separation. *Journal of the Chemical Society*, pp.1315-1321.

Goltsov, V. A. and Veziroglu, T. N., (2001). From Hydrogen Economy to Hydrogen Civilisation. *International Journal of Hydrogen Energy*, 26 (9), pp.909-915.

Gosselink, J. W., (2002). Pathways to a more Sustainable Production of Energy: Sustainable Hydrogen—A Research Objective for Shell. *International Journal of Hydrogen Energy*, 27 (11-12), pp.1125-1129.

Goswami, D. Y., Goel, N., (2003). *Fuel Cell Science, Engineering and Technology*, pp.61-74.

Gregg, S. J., Sing, K. S. W., (1982). *Adsorption Surface Area and Porosity*, London: Academic Press.

Guillot, A., Stoeckli, F., (2001). Reference Isotherm for High Pressure Adsorption of CO_2 by Carbons at 273 K. *Carbon*, 39 (13), pp.2059-2064.

Harris, P. J. F., (1999). *Carbon Nanotubes and Related Structures: New Materials for the Twenty-first Century*, Cambridge: Cambridge University Press.

Hirscher, M., and Becher, M., (2003). Hydrogen Storage in Carbon Nanotubes. *Journal of Nanoscience and Nanotechnology*, 3, pp.3-17.

Hiura, H., Ebbesen, T. W., and Tanigaki, K., (1995). Opening and Purification of Carbon Nanotubes in High Yields. *Advanced Materials*. 7, pp.275-283.

Horvath, G., Kawazoe, K., (1983). Method for the Calculation of Effective Pore Size Distribution in Molecular Sieve Carbon. *Journal of Chemical Engineering Japan*, 16, pp.470-476.

Hou, P.-X., Liu, C., Tong, Y., Xu, S., Liu, M., and Cheng, H., (2001). Purification of single-walled carbon nanotubes synthesized by the hydrogen arc-discharge method. *Journal of Materials Research*. 16 (9), pp.2526-2529.

Hou, P.-X., Yang, Q.-H., Bai, S., Xu, S.-T., Liu, M. and Cheng, H.-M., (2002). Bulk Storage of Hydrogen in Purified Multiwalled Carbon Nanotubes. *Journal of Physical Chemistry B*, 106, pp.963-966.

Hu, Z., and Srinivasan, M. P., (1999). Preparation of High Surface-Area Activated Carbons from Coconut Shell. *Microporous and Mesoporous Materials*, 27, pp.11-18.

Iijima, S., (1991). Helical Microtubules of Graphitic Carbon. *Nature*, 354, pp.56-58.

Iwashita, N., Park, C. R., Fujimoto, H., Shiraishi, M., Inagaki, M., (2004). Specification for a Standard Procedure of X-Ray Diffraction Measurements on Carbon Materials. *Carbon*, 42 (4), pp.701-714.

Jaroniec, M., Madey, R., (1988). *Physical Adsorption on Heterogeneous Solids*, Oxford: Elsevier.

Jaroniec, M., (1995). In: *Access in Nanoporous Materials* (T. J. Pinnavaia, M. F. Thorpe, ed. New York : Plenum Press, pp. 441.

Johnston, B., Mayo, M. C. and Khare, A., (2004). Hydrogen: The Energy Source for the 21st Century. *Technovation*, pp.1-17.

Kajiura, H., Tsutsui, S., Kadono, K., Kakuta, M., Ata, M. and Murakami, Y., (2003). Hydrogen Storage Capacity of Commercially Available Carbon Materials at Room Temperature. *Applied Physics Letters*, 82, pp.1105-1107.

Journet, C., Maser, W. K., et al. (1997) Large-scale production of single-walled carbon nanotubes by the electric-arc technique. *Nature.* 388 pp.756-758.

Kayiran, S. B., Lamari, F. D., and Levesque, D., (2004). Adsorption Properties and Structural Characterisation of Activated Carbons and Nanocarbons *Journal of Physical Chemistry B*, 108, pp.15211-15215.

Kidnay, A. J., Hiza, M. J., (1967). High Pressure Adsorption Isotherms of Neon, Hydrogen and Helium at 76K. *Advances in Cryogenic Engineering.* 12, pp.730.

Kojima, Y., Kawai, Y., Nakanishi, H., and Matsumoto, S., (2004). *Journal of Power Sources*, 135, pp.36-41.

Kong, V. C. Y., Foulkes, F. R., Kirk, D. W., Hinatsu, J. T., (1999). Development of Hydrogen Storage for Fuel Cellgenerators. I: Hydrogen Generation Using Hydrolysishydrides. *International Journal of Hydrogen Energy*, 24 (7), pp.665-675.

Kroto, H. W., Heath, J. R., Obrien, S. C., Curl, R. F., Smalley, R. E., (1985). C(60): Buckminsterfullerene (carbon molecule formation in space and stellar envelopes). *Nature*. 318, pp. 162-163.

Kreith, F., West, R., (2004). Fallacies of a Hydrogen Economy: A Critical Analysis of Hydrogen Production and Utilisation. *Journal of Energy Resources Technology*, 126, pp.249-257.

Kruk, M., Jaroneic, M., Olivier, J. P., (1997). Assessment of the Validity of Horvath-Kawazoe Method for Micropore Analysis on the Basis of Adsorption Isotherms Obtained from Density Functional Theory. http://acs.omnibooksonline.com/papers/1997_i106.pdf#search=%22ASSESSMENT%20OF%20THE%20VALIDITY%20OF%20THE%20HORVATH-KAWAZOE%22

Kruk, M., Jaroneic, M., Choma, J., (1998). Comparative Analysis of Simple and Advanced Sorption Methods for Assessment of Microporosity in Activated Carbons. *Carbon*, 36 (10), pp.1447-1458.

Langmuir, I., (1918). The Evaporation of Small Spheres. *Physical Review*. 12(5), pp.368-370.

Langmuir, I., (1916). The Evaporation, Condensation and Reflection of Molecules and the Mechanism of Adsorption. *Physical Review*. 8(4), pp.149-176.

Lastokie, C., Gubbins, K. E., Quirke, N., (1994). In: *Studies in Surface Science and Catalysis III*, Vol. 87 (Ed, Rouquerol, F., Rodriguez-Reinoso, F., Sing, K. S. W., and Unger, K. K.) Elsevier, pp. 51-60.

Levesque, D., Gicquel, A., Dakrim, F.-L., and Kayiran, S. B., (2002). Monte Carlo simulations of Hydrogen Storage in Carbon Nanotubes. *Journal of Physics: Condensed Matter*, 14, pp.9285-9293.

Li, F., Wang, Y., Wang, D., Wei, F., (2004). Characterization of Single-Wall Carbon Nanotubes by N_2 Adsorption. *Carbon*, 42 (12-13), pp.2375-2383.

Lillo-Rodenas, M. A., Cazorla-Amoros, D., Linares-Solano, A. (2003). Understanding Chemical Reactions between Carbons and NaOH and KOH. An Insight into the Chemical Activation Mechanism. *Carbon*, 41 (2), 267-275.

Liu, C., Fan, Y. Y., Liu, M., Cong, H. T., Cheng, H. M., Dresselhaus, M. S., (1999). Hydrogen Storage in Single-Walled Carbon Nanotubes at Room Temperature. *Science*, 286(5442), pp.1127-1129.

Liu, C., Cheng, H.-M., (2005). Carbon Nanotubes for Clean Energy Applications. *Journal of Physics D: Applied Physics*, 38, pp.R231-R252.

Lua, A. C., Guo, J., (2001). Preparation and Characterisation of Activated Carbons from Oil-Palm Stones for Gas-Phase Adsorption. *Colloids and Surfaces A: Physicochemical and Engineering Aspects*, 179, pp.151-162.

Lueking, A., and Yang, R. T., (2002). Hydrogen Spillover from a Metal Oxide Catalyst onto Carbon Nanotubes—Implications for Hydrogen Storage. *Journal of Catalysis*, 206, pp.165-168.

Lueking, A., and Yang, R. T., (2003). Hydrogen Storage in Carbon Nanotubes: Residual Metal Content and Pretreatment Temperature. *AIChE Journal*, 49, pp.1556-1568.

Maggs, F. A., Schwabe, P. H., Williams, J. H., (1960). Adsorption of Helium on Carbons: Influence on Measurement Density. *Nature*, 186, pp.956-958.

Manitoba Energy, Science and Technology, Energy Development Initiative, (2003). Hydrogen Fuel. http://www.gov.mb.ca/est/energy/hydrogen/abouthyd.html.

Manitoba Energy Development Initiative. Department of Energy, Science and Technology. Preliminary hydrogen opportunities report. Available from: http://www.manitobaenergy.com, April 2003.

Manocha, S. M., (2003). Porous Carbons. *Sahana*, 28, pp.335-348.

McEnaney, B., Mays, T., and Causton, P. D., (1987). Heterogeneous Adsorption on Microporous Carbons. *Langmuir*, 3, pp.695-699.

Midilli, A., Ay, M., Dincer, I., Rosen, M. A., (2005). On Hydrogen and Hydrogen Energy Strategies I: Current Status and Needs. *Renewable and Sustainable Energy Reviews*, 9, pp.255-271.

Milne, T.A., C.C. Milne, and R.J. Evans (2002), *Hydrogen From Biomass: State of the Art and Research Challenges*, National Renewable Energy Laboratory for the International Energy Agency, IEA/H2/TR-02/001.

Momirlan, M., Veziroglu, T., (1999). Recent Direction of World Hydrogen Production, *Renewable and Sustainable Energy Reviews*, 3, pp.219-231.

Momirlan, M., and Veziroglu, T. N., (2005). The Properties of Hydrogen as Fuel Tomorrow in Sustainable Energy System for a Cleaner Planet. *International Journal of Hydrogen Energy*, 30 (7), pp.795-802.

Moore, R. B., Raman, V., (1998). Hydrogen Infrastructure for Fuel Cell Transportation. *International Journal of Hydrogen Energy*, 23 (7), pp.617-620.

Myers, A. L., Calles, J. A., Calleja, G., (1997). Comparison of Molecular Simulation of Adsorption with Experiment. *Adsorption*, 3, pp.107-115.

Nijkamp, M. G., Raaymakers, J. E. M. J., van Dillen, A. J., de Jong, K. P., (2001). Hydrogen Storage using Physisorption-Materials Demands. *Applied Physics A: Materials Science and Processing*, 72, pp.619-623.

C. Nutzenadel, A. Zuttel, D. Chartouni, L. Schlapbach, Electrochemical Storage of Hydrogen in Nanotube Materials. *Electrochemical and Solid State Letters* 2, 30-32 (1999).

Odunsi, O. Y., He, Y., Mays, T. J., (2005). Hydrogen Storage in Nanoporous Carbons - Effects of Gas Phase Impurities. *Journal of Material Chemistry*, in preparation.

Odunsi, O. Y., He, Y., Mays, T. J., (2005). Hydrogen Storage on Nanoporous Carbons. In: *7th World Chemical Engineering Conference*, 11th – 14th July 2005, Glasgow. Place of publication: Elsevier, page numbers of paper.

Odunsi, O. Y., He, Y., Mays, T. J., (2006). Hydrogen Storage on Nanoporous Carbons. *Studies in Surface Science and Catalysis*, 160, pp.423-430.

Ogden, J.M., (1999). Prospects for building a hydrogen energy infrastructure, *Annual Review Energy Environment*. 24, pp.227-279.

Olivier, J. P., (1995). Modeling physical adsorption on porous and nonporous solids using density functional theory. *Journal of Porous Materials*, 2, pp. 9–17.

Oney, F., Veziroglu, T. N., Dulger, Z., (1994). Evaluation of Pipeline Transportation of Hydrogen and Natural Gas Mixtures, *International Journal of Hydrogen Energy*, 19(10) pp. 813-822.

Pace, E. L., and Siebert, A. R., (1959). Heat of Adsorption of Parahydrogen and Orthodeuterium on Graphon. *Journal of Physical Chemistry B*, 63, pp.1398-1400.

Peng, D.-Y., and Robinson, D. B., (1976). A New Two-Constant Equation of State. *Industrial and Engineering Chemistry Fundamentals*, 15, pp.59-64.

Pinkerton, F. E., Wicke, B. G., Olk, C. H., Tibbetts, G. G., Meisner, G. P., Meyer, M. S. and Herbst, J. F., (2000). Thermogravimetric Measurement of Hydrogen

Absorption in Alkali-Modified Carbon Materials. *Journal of Physical Chemistry B*, 104, pp.9460-9467.

Poirier, E., Chahine, R., Benard, P., Cossement, D., Lafi, L., Melancon, E., Bose, T. K., and Desilets, S., (2004). Storage of Hydrogen on Single-walled Carbon Nanotubes and other Carbon Structures. *Applied Physics A: Materials Science and Processing*, 78, pp.961-967.

Raman V. Hydrogen infrastructure-market development. Allentown (PA) USA: Air products and Chemicals Inc., Available from: http://www.cleanair.org, 2003.

Reich, S. T., C., Maultzch, J., (2004). *Carbon Nanotubes, Basic Concepts and Physical Properties*, Weinheim: Wiley-VCH.

Reznik, D., Olk, C. H., Neumann, D. A., Copley, J. R. D., (1994). X-ray Powder Diffraction from Carbon Nanotubes and Nanoparticles. *Physical Review B*, 52, pp.116-124.

Rodriguez, N. M., Chambers, A., and Baker, K., (1995). Catalytic Engineering of Carbon Nanostructures. *Langmuir*, 11 (10), pp.3862-3866.

Rodriguez-Reinoso, F., Martin-Martinez, J. M., Prado-Burgete, C., (1987). A Standard Adsorption Isotherm for the Characterisation of Activated Carbons. *Journal of Physical Chemistry*, 91, pp.515-516.

Rodriguez-Reinoso, F., (1989). An Overview of Methods for the Characterisation of Activated Carbons. *Pure and Applied Chemistry*, 61, pp.1859-1866.

Rodriguez-Reinoso, F., Molina-Sabio, M., Gonzalez (1995). The Use of Steam and CO_2 as Activating Agents in the Preparation of Activated Carbons. *Carbon*, 33 (1), pp.15-23.

Rosen, M. A., and Scott, D. S., (1998). Comparative Efficiency Assessments for a Range of Hydrogen Production Processes. *International Journal of Hydrogen Energy*, 23 (8), pp.653-659.

Rouquerol, J., Avnir, D., Fairbridge, C. W., Everett, D. H., Haynes, J. H., Pernicone, N., Ramsay, J. D. F., Sing, K. S. W., Unger, K. K., (1994). Recommendations for the Characterisation of Porous Solids. *Pure and Applied Chemistry*, 66, pp.1739-1758.

Rouquerol, F., Rouquerol, J., and Sing, K. S. W., (1999*). Adsorption by Powders and Porous Solids, Principles, Methodology and Applications*, London: Academic Press.

Rzepka, M., Lamp, P., and de la Casa-Lillo, M. A., (1998). Physisorption of Hydrogen on Microporous Carbon and Carbon Nanotubes. *Journal of Physical Chemistry B*, 102, pp.10894-10898.

Saito, A., Foley, H. C., (1995). Argon Porosimetry of the Selected Molecular Sieves: Experiments and Examination of the Adapted Horvath-Kawazoe Model. *Microporous Materials*, 3, pp.531-542.

Saito, R., Dresselhaus, G., Dresselhaus, M. S., (1998). *Physical Properties of Carbon Nanotubes*, London: Imperial College Press.

Sarkar, A., Kroto, H. W., Endo, M., (1995). Hemi-Toroidal Networks in Pyrolytic Carbon Nanotubes. *Carbon*, 33, pp.51–55.

Scaife, S. J., Kluson, P., Quirke, N., (2000). Characterisation of Porous Materials by Gas Adsorption: Do Different Molecular Probes give Different Pore Structures? *Journal of Physical Chemistry B*, 104, pp.313-318.

Schlapbach, L. A. Zuttel., A. (2001). Hydrogen Storage - Materials for Mobile Applications. *Nature*, 414, pp.23-30.

Schuth, F., Sing, K. S. W., Weitkamp, J., Ed. (2002). *Handbook of Porous Solids*, Weinheim: Wiley-VCH.

Schwarz, J. A., (1994). Hydrogen Storage on Activated Carbon. Syracuse University, pp. 1-18.

Sherif, S. A., Barbir, F., Veziroglu, T. N., (2005). Wind Energy and the Hydrogen Economy - Review of the Technology. *Solar Energy*, 78, pp.647-660.

Sima-Ella, E., Yuan, G., and Mays, T., (2005). A simple kinetic analysis to determine the intrinsic reactivity of coal chars. *Fuel*, 84 1920.

Simbeck, D. R., (2004). CO2 Capture and Storage-The Essential Bridge to the Hydrogen Economy. *Energy*, 29, pp.1633-1641.

Sing, K. S. W., Everett, D. H., Haul, R. A. W., Moscou, L., Pierotti, R. A., Rouquerol, J., Siemieniewska, T., (1985). Reporting Physisorption Data for Gas/Solid Systems with Special Reference to the Determination of Surface Area and Porosity. *Pure and Applied Chemistry*, 57 (4), pp.603-619.

Sing, K. S. W., Williams, R. T., (2004). Physisorption Hysteresis Loops and the Characterisation of Nanoporous Materials. *Adsorption Science and Technology*, 22, pp.773-782.

Sing, K. S. W., Williams, R. T., (2005). Empirical Procedures for the Analysis of Physisorption Isotherms. *Adsorption Science and Technology*, 23, pp.839-853.

Sircar, S., (1999). Gibbsian Surface Excess for Gas Adsorption – Revisited. *Industrial and Engineering Chemistry Research*, 38, pp.3670-3682.

Sircar, S., and Hufton, J. R., (2000). Why Does the Linear Driving Force Model for Adsorption Kinetics Work? *Adsorption*, 6, pp.137-147.

Sircar, S., and Hufton, J. R., (2000). Intraparticle adsorbate concentration profile for linear driving force model. *AIChE Journal*, 46, pp.659-660.

Sircar, S., (2001). Measurement of Gibbsian Surface Excess. *AIChE Journal*, 47, pp.1169-1176.

Steinberg, M., and Cheng, H. C., (1989). Modern and Prospective Technologies for Hydrogen Production from Fossil Fuels. *International Journal of Hydrogen Energy*, 14 (11), pp.797-820.

Stiegel, G. J., Ramezan, M., (2006). Hydrogen from coal gasification: An economical pathway to a sustainable energy future. *International Journal of Coal Geology*, 65, pp.173-190.

Stoeckli, F., Guillot, A., Slasli, A. M., Hugi-Cleary, D., (2002). Microporosity in Carbon Blacks. *Carbon*, 40 (2), pp.211-215.

Strobel, R., Jorissen, L., Schliermann, T., Trapp, V., Schutz, W., Bohmhammel, K., Wolf, G., and Garche, J., (1999). Hydrogen Adsorption on Carbon Materials. *Journal of Power Sources*, 84, pp.221-224.

Takagi, H., Hatori, H., Soneda, Y., Yoshizawa, N., Yamada, Y., (2004). Adsorptive Hydrogen Storage in Carbon and Porous Materials. *Materials Science and Engineering*, B108, pp.143-147.

Tam, M. S., Antal, M. J., (1999). Preparation of Activated Carbons from Macadamia Nut Shell and Coconut Shell by Air Activation. *Industrial and Engineering Chemistry Research*, 38, pp.4268-4276.

Tanaka, H., El-Merraoui, M., Steele, W. A., Kaneko, K., (2002). Possibility of quantum effect in micropore filling of Neon AlPO4-5. *Chemical Physics Letters*, 351, pp.417-423.

Texier-Mandoki, N., Dentzer, J., Piquero, T., Saadallah, S., David, P., Vix-Guterl, C., (2004). Hydrogen Storage in Activated Carbon Materials: Role of the Nanoporous Texture. *Carbon*, 42, pp.2735-2777.

Thess, A., Lee, R., Nikolaev, P., Dai, H., Petit, P., Robert, J., Xu, C., Lee, Y.H., Kim, S.G., Rinzler, A.G., Colbert, D.T., Scuseria, G.E., Tomanek, D., Fischer, J.E.

& Smalley, R.E. (1996) Crystalline ropes of metallic carbon nanotubes. Science, 273, 483-487.

Thommes, M., Smarsly, B., Groenewolt, M., Ravikovitch, P. I., and Neimark, A. V., (2006). *Langmuir*, 22, pp.756-764.

Tsang, S. C., Harris, P. J. F., Green, M. L. H., (1993). Thinning and Opening of Carbon Nanotubes y Oxidation using Carbon dioxide. *Nature*, 362, pp.520–22.

Turner, J. A., (2004). Sustainable Hydrogen Production. Sustainable Hydrogen Production. *Science*, 305, pp.972-974.

Tzimas, E., Filiou, C., Peteves, S. D., and Veyret, J.-B., (2003). Hydrogen Storage: State-of-the-Art and Future Perspective. *European Commission Directorate General Joint Research Centre*, Petten, pp. 57.

Tzimas, E., Peteves, S. D., (2005). The impact of carbon sequestration on the production cost of electricity and hydrogen from coal and natural-gas technologies in Europe in the medium term *Energy*, 30, pp.2672-2689.

Uhrig, R. E., (2004). Engineering Challenges of the Hydrogen Economy. Iowa, pp. 10-19.

US-Department of Energy, (2002). *National Hydrogen Energy Roadmap.*

US-Department of Energy, (2002). A National Vision of America's Transition to a Hydrogen Economy - To 2030 and beyond.

Utgikar, V., and Thiesen, T., (2006). Life Cycle Assessment of High Temperature Electrolysis for Hydrogen Production via Nuclear Energy. *International Journal of Hydrogen Energy*, 31 (7), pp.939-944.

Valenzuela, D. P., and A. L. Myers. (1989). *Adsorption Equilibrium Data Handbook.* Prentice Hall: Englewood Cliffs, New Jersey.

Valladares, D. L., Rodriguez-Reinoso, F., and Zgrablich, G., (1998). Characterization of Active Carbons: The Influence of the Method in the Determination of the Pore Size Distribution. *Carbon*, 36 (10), pp.1491-1499.

Veziroglu, T. N., and Barbir, F., (1992). Hydrogen: The Wonder Fuel. *International Journal of Hydrogen Energy*, 17 (6), pp.391-404.

Vijayaraghavan, K., Mohd Soom, A. A., (2004). Trends in Biological Hydrogen Production – A Review. *International Journal of Hydrogen Energy*, Article in Press.

Wang, Q., and Johnson, J. K., (1999). Optimization of Carbon Nanotube Arrays for Hydrogen Adsorption. *Journal of Physical Chemistry B*, 103, pp.4809-4813.

Webb, P. A., (2001). *Micromeritics Instrument Corporation*, pp. 1-16.

Wigmans, T., Industrial Aspects of Production and Use of Activated Carbons. ***Carbon*** 1989, 7, pp.13-22.

Wu, X. B., Chen, P., Lin, J., and Tan, K. L., (2000). Hydrogen Uptake by Carbon Nanotubes. *International Journal of Hydrogen Energy*, 25 (3), pp.261-265.

Yalcin, S., (1989). A Review of Nuclear Hydrogen Production. *International Journal of Hydrogen Energy*, 14 (8), pp.551-561.

Yang, R. T., (2000). Hydrogen Storage By Alkali-Doped Carbon Nanotubes–Revisited. *Carbon*, 38 (4), pp.623-641.

Ye, Y., Ahn, C. C., Witham, C., Fultz, B., Liu, J., Rinzler, A. G., Colbert, D., Smith, K. A., and Smalley, R. E., (1999). Hydrogen Adsorption and Cohesive Energy of Single-walled Carbon Nanotubes. *Applied Physics Letters*, 74, pp.2307-2309.

Zhao, Y., Kim, Y.-H., Dillon, A. C., Heben, M. J., Zhang, S. B., (2005). Hydrogen Storage in Novel Organometallic Buckyballs. *Physical Review Letters*, 94, pp.155504-1 - 155504-4.

Zhao, X. B., Xiao, B., Fletcher, A. J., and Thomas, K. M., (2005). Hydrogen Adsorption on Functionalised Nanoporous Activated Carbons. *Journal of Physical Chemistry B*, 109, pp.8880-8888.

Zhou, O., Fleming, R. M., Murphy, D. W., Chen, C. H., Haddon, R. C., Ramirez, A. P., Glarum, S. H., (1994). Defects in Carbon Nanostructures. *Science*, 263, pp.1744-1747.

Zhou, L., Zhou, Y. and Sun, Y., (2003). Enhanced Storage of Hydrogen at the Temperature of Liquid Nitrogen. *International Journal of Hydrogen Energy*, 29 (3), pp.319-322.

Zhou, L., Zhou, Y., and Sun, Y., (2004). A Comparative Study of Hydrogen Adsorption on Superactivated Carbon versus Carbon Nanotubes. *International Journal of Hydrogen Energy*, 29 (5), pp.475-479.

Zhou, L., (2005). Progress and Problems in Hydrogen Storage Problems. *Renewable and Sustainable Energy Reviews*, 9, pp.395-408.

Zhou, L., (2005). Progress in Fundamental Research into Supercritical Adsorption and its Impacts on Clean Energy Technology. *Adsorption Science and Technology*, 23, pp.509-518.

Zhou, L., Zhou, Y., Sun, Y., (2006). Studies on the Mechanism and Capacity of Hydrogen Uptake by Physisorption-Based Materials. *International Journal of Hydrogen Energy*, 31 (2), pp.259-264.

ZutteL, A., Nutzenadel, C., Sudan, P., Mauron, P., Emmenegger, C., Rentsch, S., Schlapbach, L., Weidenkaff, A., and Kiyobayashi, T., (2001). Hydrogen Sorption by Carbon Nanotubes and other Carbon Nanostructures. *Journal of Alloys and Compounds*, 330-332, pp.676-682.

ZutteL, A., (2003). Materials for Hydrogen Storage. *Materials Today*, pp.24-33.

ZutteL, A., Wenger, P., Sudan, P., Mauron, P., Orimo, S.-I., (2004). Hydrogen Density in Nanostructured Carbon, Metals and Complex Materials. *Materials Science and Engineering*, B108, pp.9-18

Appendices

Appendix A:

Excel Macro for Buoyancy Correction

```
Sub H2_Gravimetric()
'
' H2_Gravimetric_Data_Macro

Dim Counter%

MolWt = Cells(2, 4)
PoreVol = Cells(48, 2)

VacVolt = Cells(14, 2)
TransFactor = Cells(7, 8)

InitBal = Cells(14, 3)
SamWtmg = Cells(9, 5)

SamWt = Cells(9, 4)
CwtWt = Cells(10, 4)
SamT = Cells(3, 8)
CwtT = Cells(4, 8)

SamDens = Cells(7, 4)
CwtDens = Cells(8, 4)
PanDens = Cells(8, 4)
LWHDens = Cells(6, 15)
UPHDens = Cells(7, 15)

SPanWt = Cells(5, 13)
SLWHWt = Cells(6, 13)
SUPHWt = Cells(7, 13)
CPanWt = Cells(8, 13)
CUPHWt = Cells(9, 13)
```

```
AdDens = Cells(9, 8)

GasC = Cells(5, 8)
CrT = Cells(3, 4)
CrP = Cells(4, 4)
AccFac = Cells(5, 4)

PoreVol = Cells(78, 2)

Cells(4, 1).Value = (Date)

Cells(10, 4).Value = CPanWt + CUPHWt - SPanWt - SLWHWt - SUPHWt


For Counter% = 0 To 75

 'Pressure kPa
 Cells((Counter% + 15), 6).Value = (Cells((Counter% + 15), 2)) / 10

 'Mass increase mg
 Cells((Counter% + 15), 7).Value = (Cells((Counter% + 15), 3) - SamWtmg)

 'Uptake mg/g sample, uncorrected results
 Cells((Counter% + 15), 8).Value = (Cells((Counter% + 15), 7) / SamWt)

'for sample side, calculation of Z
fw = 0.37464 + 1.54226 * AccFac - 0.26992 * (AccFac ^ 2)
alphaT = (1 + fw * (1 - (SamT / CrT) ^ 0.5)) ^ 2
Aa = 0.45724 * ((GasC * CrT) ^ 2) * alphaT / CrP
Bb = 0.0788 * GasC * CrT / CrP

A = Aa * Cells((Counter% + 15), 6).Value * 1000 / ((GasC * SamT) ^ 2)
B = Bb * Cells((Counter% + 15), 6).Value * 1000 / GasC / SamT

'Now calculate the c1, c2, c3 parameters
c1 = B - 1
c2 = A - 3 * B * B - 2 * B
c3 = -A * B + B * B + B * B * B

Z2 = 1
Do
  Z1 = Z2
  Z2 = Z1 - (Z1 * Z1 * Z1 + c1 * Z1 * Z1 + c2 * Z1 + c3) / (3 * Z1 * Z1 + 2 * c1 *
Z1 + c2)
Loop While Abs(Z2 - Z1) > 0.000001

Cells((Counter% + 15), 9) = Z1

'Now calculate the c1, c2, c3 parameters
```

```
A = Aa * Cells((Counter% + 15), 6).Value * 1000 / ((GasC * CwtT) ^ 2)
B = Bb * Cells((Counter% + 15), 6).Value * 1000 / GasC / CwtT

'Now calculate the c1, c2, c3 parameters
c1 = B - 1
c2 = A - 3 * B * B - 2 * B
c3 = -A * B + B * B + B * B * B

Z2 = 1
Do
  Z1 = Z2
  Z2 = Z1 - (Z1 * Z1 * Z1 + c1 * Z1 * Z1 + c2 * Z1 + c3) / (3 * Z1 * Z1 + 2 * c1 *
Z1 + c2)
Loop While Abs(Z2 - Z1) > 0.000001

Cells((Counter% + 15), 10) = Z1

Next Counter

'for buoyancy effect: volume on each side
VolSam = SamWt / SamDens + SPanWt / PanDens + SLWHWt / LWHDens +
SUPHWt / UPHDens
VolCwt = CPanWt / PanDens + CUPHWt / UPHDens

'n = PV / zrt

For Counter% = 0 To 75
 NH2Sam = Cells((Counter% + 15), 6).Value * 1000 * VolSam / 10 ^ 6 /
Cells((Counter% + 15), 9).Value / GasC / SamT
 NH2Cwt = Cells((Counter% + 15), 6).Value * 1000 * VolCwt / 10 ^ 6 /
Cells((Counter% + 15), 10).Value / GasC / CwtT

If Cells(9, 8) = ("") Then
 Cells((Counter% + 15), 11) = (NH2Sam - NH2Cwt) * 1000 * MolWt
Else
 Cells((Counter% + 15), 11) = ((NH2Sam - NH2Cwt) + (Cells((Counter% + 15), 7)) /
1000 / AdDens / 10 ^ 6 * (Cells((Counter% + 15), 6).Value * 1000) /
(Cells((Counter% + 15), 9).Value) / GasC / SamT) * 1000 * MolWt
End If


'Corrected Mass Uptake mg/g
Cells((Counter% + 15), 12).Value = ((Cells((Counter% + 15), 7)) + (Cells((Counter%
+ 15), 11))) / SamWt

'Corrected Mass Uptake mmol/g
Cells((Counter% + 15), 13).Value = (Cells((Counter% + 15), 12)) / MolWt

'Ideal Gas Equation of State Calculations
'Density (kg/m3)
```

```
Cells((Counter% + 15), 14).Value = MolWt * 0.001 * 1000 * Cells(Counter% + 15, 6) / GasC / SamT

'Number of moles of hydrogen in the sample and counterweight side (mol)
NH2Sam = Cells((Counter% + 15), 6).Value * 1000 * VolSam / 10 ^ 6 / 1 / GasC / SamT
NH2Cwt = Cells((Counter% + 15), 6).Value * 1000 * VolCwt / 10 ^ 6 / 1 / GasC / CwtT

'Amount of displaced Hydrogen (mg)
Cells((Counter% + 15), 15).Value = (NH2Sam - NH2Cwt) * 1000 * MolWt

'Corrected Excess Weight (mg)
Cells((Counter% + 15), 16).Value = Cells((Counter% + 15), 7).Value + (Cells((Counter% + 15), 11))

'Excess % Mass Uptake
Cells((Counter% + 15), 17).Value = (Cells((Counter% + 15), 16).Value / SamWtmg) * 100

'Peng-Robinson % Mass
Cells((Counter% + 15), 18).Value = ((Cells((Counter% + 15), 7).Value + Cells((Counter% + 15), 11).Value) / SamWtmg) * 100

'Uncorrected % Mass
Cells((Counter% + 15), 19).Value = (Cells((Counter% + 15), 7).Value / SamWtmg) * 100

  If Cells((Counter% + 15), 2) = ("") Then
   Cells((Counter% + 15), 3) = ("")
   Cells((Counter% + 15), 5) = ("")
   Cells((Counter% + 15), 6) = ("")
   Cells((Counter% + 15), 7) = ("")
   Cells((Counter% + 15), 8) = ("")
   Cells((Counter% + 15), 9) = ("")
   Cells((Counter% + 15), 10) = ("")
   Cells((Counter% + 15), 11) = ("")
   Cells((Counter% + 15), 12) = ("")
   Cells((Counter% + 15), 13) = ("")
   Cells((Counter% + 15), 15) = ("")
   Cells((Counter% + 15), 16) = ("")
   Cells((Counter% + 15), 17) = ("")
   Cells((Counter% + 15), 30) = ("")
   Cells((Counter% + 15), 31) = ("")
   Cells((Counter% + 84), 2) = ("")
   Cells((Counter% + 84), 3) = ("")
   Cells((Counter% + 84), 4) = ("")
   Cells((Counter% + 84), 5) = ("")
   Cells((Counter% + 84), 6) = ("")
   Cells((Counter% + 84), 7) = ("")
```

```
    Cells((Counter% + 84), 8) = ("")
    Cells((Counter% + 84), 9) = ("")
    Cells((Counter% + 84), 10) = ("")
    Cells((Counter% + 84), 11) = ("")

  End If
Range("A3").Select
Next Counter
End Sub
```

Appendix B:

X-Ray Diffraction Results for the Nanoporous Carbons

Figure 1: X-ray diffraction results at the 004 peaks of the nanoporous carbons

	BPL	
Diffracted Angle, 2θ (*004*)	44.44	°
Interlayer Spacing, d_{004}	2.04	Å
Lattice Constant, c_0	8.16	Å
	Norit CNR 115	
Diffracted Angle, 2θ (*004*)	42.71	°
Interlayer Spacing, d_{004}	2.12	Å
Lattice Constant, c_0	8.47	Å
	SRD/667/1	
Diffracted Angle, 2θ (*004*)	43.86	°
Interlayer Spacing, d_{004}	2.06	Å
Lattice Constant, c_0	8.26	Å
	SWNT-1	
Diffracted Angle, 2θ (*004*)	44.68	°
Interlayer Spacing, d_{004}	2.03	Å
Lattice Constant, c_0	8.11	Å
	SWNT-2	
Diffracted Angle, 2θ (*004*)	44.21	°
Interlayer Spacing, d_{004}	2.05	Å
Lattice Constant, c_0	8.19	Å
	MWNT-1	
Diffracted Angle, 2θ (*004*)	43.57	°
Interlayer Spacing, d_{004}	2.08	Å
Lattice Constant, c_0	8.31	Å
	MWNT-2	
Diffracted Angle, 2θ (*004*)	43.64	°
Interlayer Spacing, d_{004}	2.07	Å
Lattice Constant, c_0	8.30	Å

Figure 2: X-ray diffraction results at the 110 peaks of the nanoporous carbons

	BPL	
Diffracted Angle, 2θ (*110*)	79.51	°
Interlayer Spacing, d_{110}	1.21	Å
Lattice Constant, a_0	2.41	Å
	Norit CNR 115	
Diffracted Angle, 2θ (*110*)	78.49	°
Interlayer Spacing, d_{110}	1.22	Å
Lattice Constant, a_0	2.44	Å
	SRD/667/1	
Diffracted Angle, 2θ (*110*)	79.91	°
Interlayer Spacing, d_{110}	1.20	Å
Lattice Constant, a_0	2.40	Å
	SWNT-1	
Diffracted Angle, 2θ (*110*)	80.17	°
Interlayer Spacing, d_{110}	1.20	Å
Lattice Constant, a_0	2.39	Å
	SWNT-2	
Diffracted Angle, 2θ (*110*)	79.86	°
Interlayer Spacing, d_{110}	1.20	Å
Lattice Constant, a_0	2.40	Å
	MWNT-1	
Diffracted Angle, 2θ (*110*)	79.00	°
Interlayer Spacing, d_{110}	1.21	Å
Lattice Constant, a_0	2.42	Å
	MWNT-2	
Diffracted Angle, 2θ (*110*)	79.02	°
Interlayer Spacing, d_{110}	1.21	Å
Lattice Constant, a_0	2.42	Å

APPENDIX C:

Modified Linear Driving Force Parameters at Different Temperatures

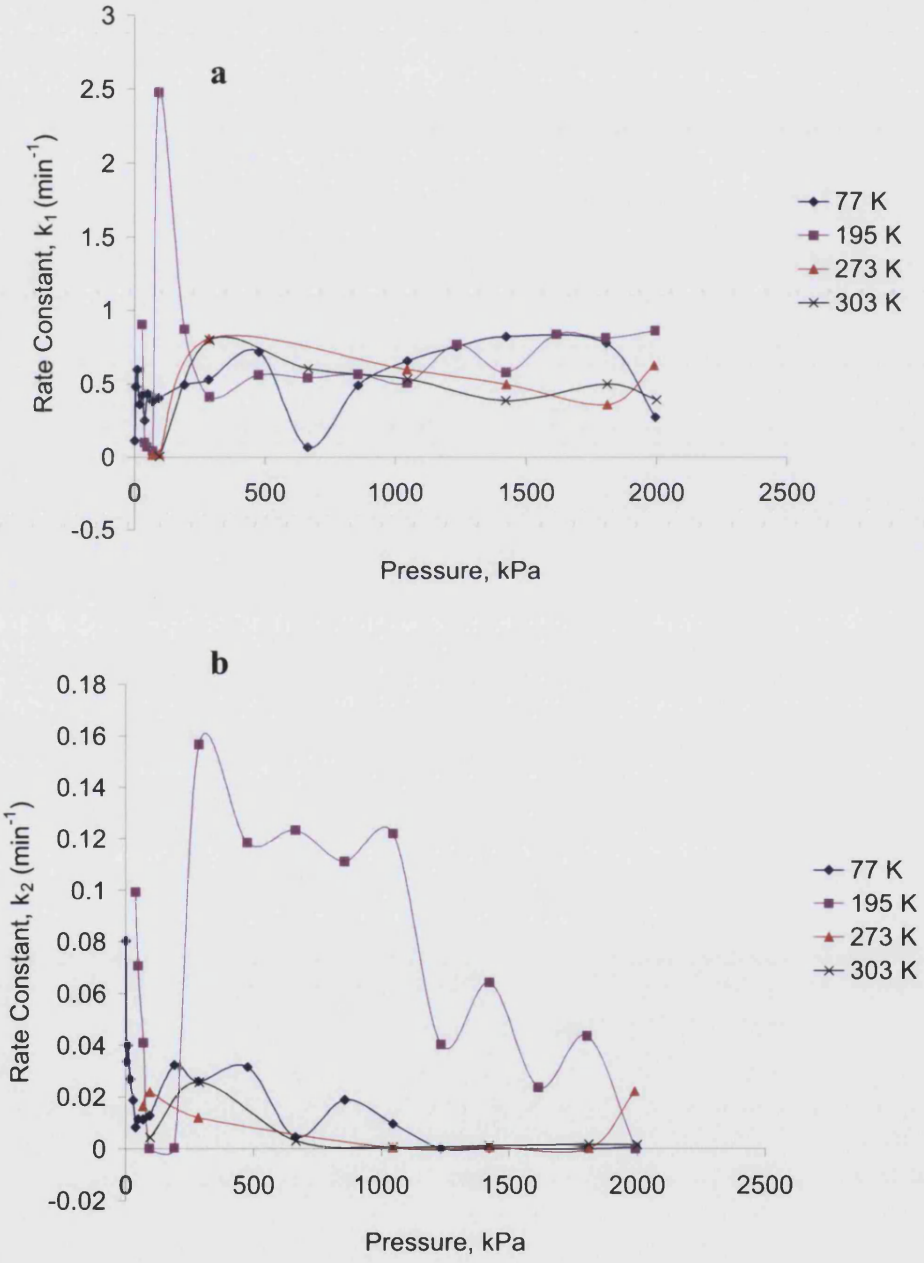

Figure 3: Graph showing the variation of the adsorption rate constants at different temperatures with pressure for the nanoporous carbons. (a) Variation of k_1 for BPL; (b) Variation of k_2 for BPL.

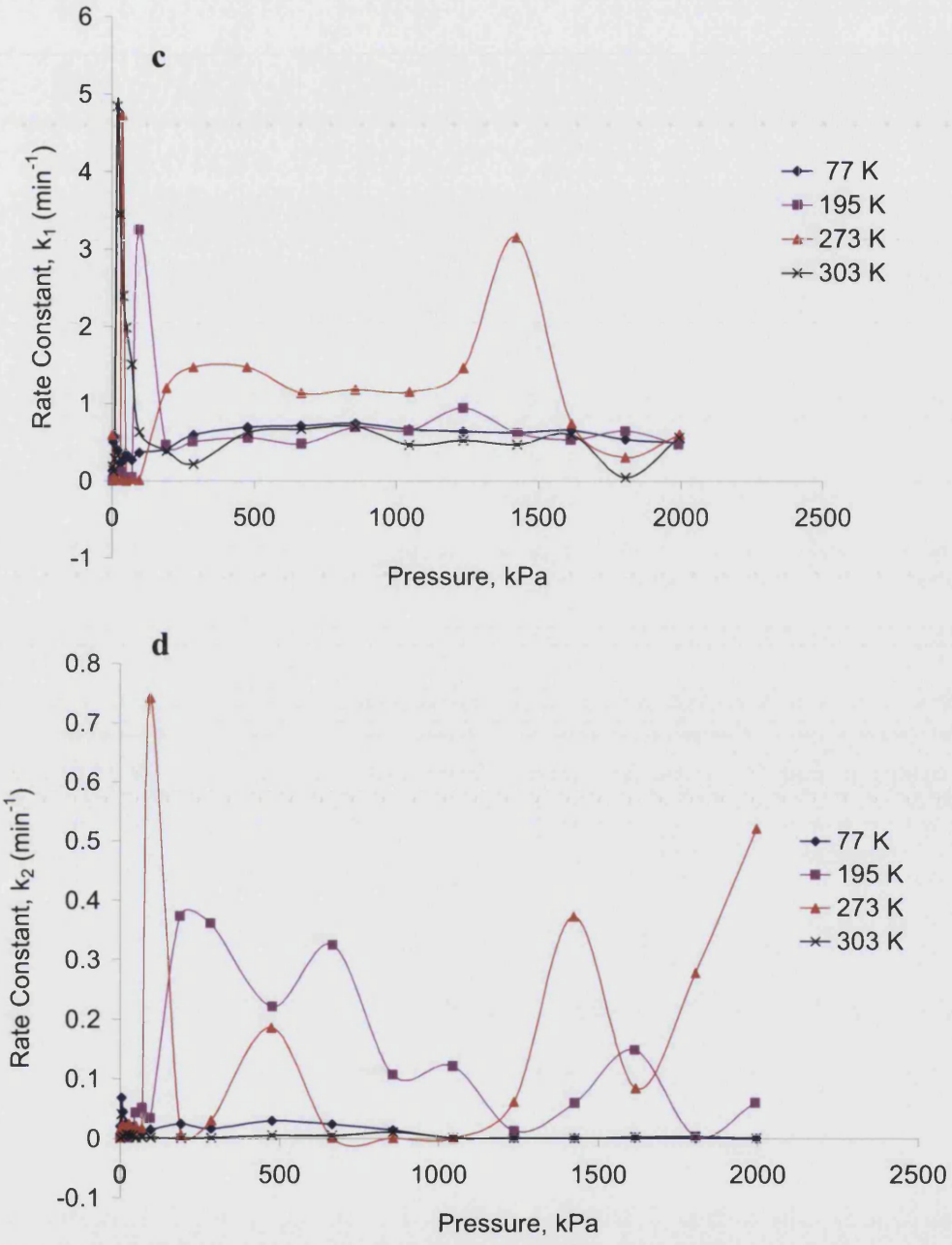

Figure 4: Graph showing the variation of the adsorption rate constants at different temperatures with pressure for the nanoporous carbons. (a) Variation of k_1 for Norit CNR 115; (b) Variation of k_2 for Norit CNR 115.

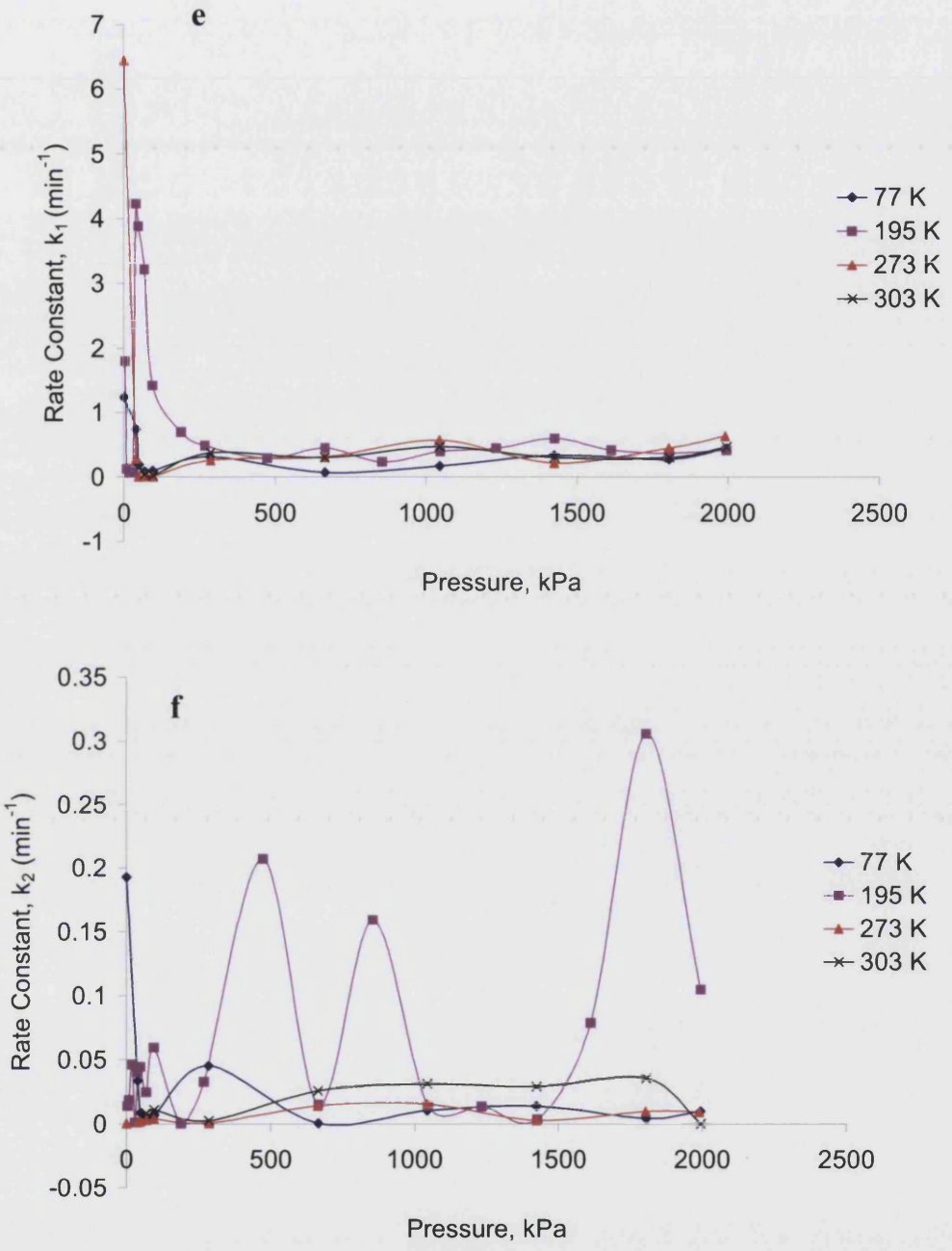

Figure 5: Graph showing the variation of the adsorption rate constants at different temperatures with pressure for the nanoporous carbons. (a) Variation of k_1 for SRD/667/1; (b) Variation of k_2 for SRD/667/1.

APPENDIX D:

Variation of the hydrogen diffusion coefficient with pressure

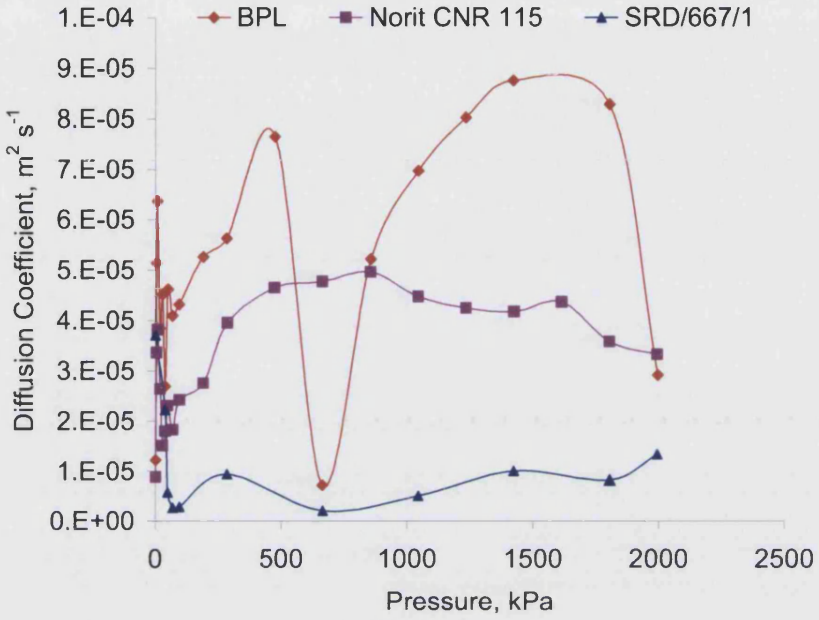

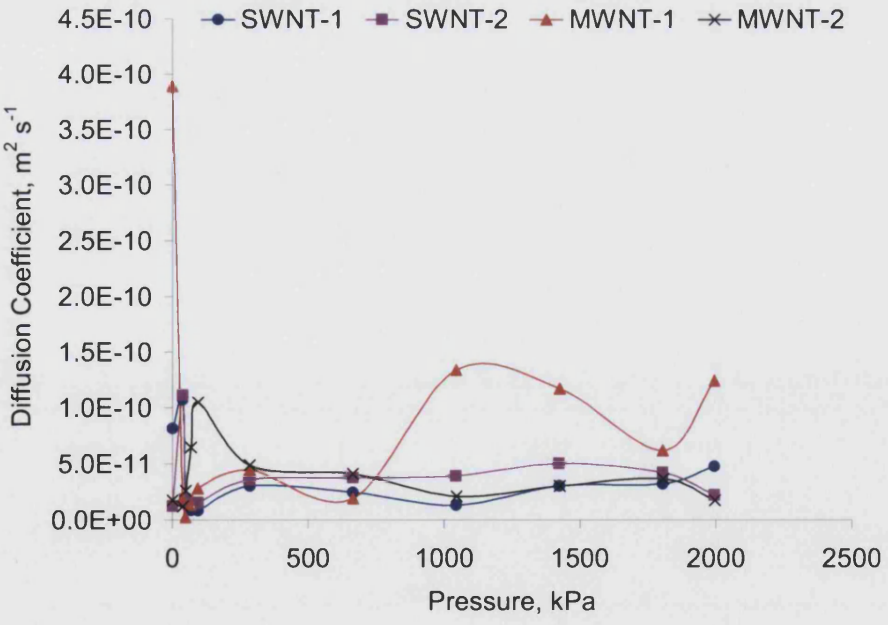

Figure 6: Graph showing the variation of hydrogen diffusion coefficient with pressure at 77 K. (a) For the activated carbons and (b) For the carbon nanotubes.

APPENDIX E: Dissemination

Paper Presented at the 7th World Congress of Chemical Engineering, Glasgow, U. K. (10th – 14th July, 2005)

HYDROGEN STORAGE ON NANOPOROUS CARBONS

OY Odunsi, Y He and TJ Mays*

Department of Chemical Engineering, University of Bath, Bath BA2 7AY, UK.

* Tel: +44(0)1225 386528, Fax: +44(0)1225 385713, E-mail: t.j.mays@bath.ac.uk

Abstract

Sustainable hydrogen (e.g., produced from biomass) is of much current interest as an energy store and/or carrier. Attractions are that H_2 generates ~143 MJ kg^{-1} when it reacts with O_2, with only H_2O as the product. This compares to fossil fuels, which generate 10–50 MJ kg^{-1}, plus environmentally–damaging CO_2. However, there are many challenges to be met before energy systems based on H_2 are technically feasible or socially/economically acceptable. One of the main challenges is to store H_2 safely, effectively and at low–cost. This paper presents the results of a mainly experimental study of H_2 sorption in nanoporous carbons. This is part of a broad examination of the potential of these materials as storage media for H_2 in low volume and low mass energy systems, in comparison with other storage media such as light metal hydrides, and with liquid and high–pressure gas storage. Note that the new term nanoporous refers to pores in the size range 0.1 to 100 nm.

We have measured kinetic and equilibrium H_2 sorption isotherms on a wide range of carbons for temperatures in the range 77 to 298 K and for pressures in the range 0 to 20 bar using a gravimetric system. Initial conclusions are that reasonable amounts of H_2 (up to 5 wt.%) are adsorbed at 77 K on many different carbons, but that amounts adsorbed at 298 K are at least an order of magnitude lower. There is some evidence that at 77 K adsorption is not fully equilibrated even over periods of many hours at a given pressure, and comprises an irreversible component (*i.e.*, there is some desorption hysteresis) possibly arising from impurities in the H_2 used in experiments.

1. Introduction

Hydrogen storage technologies have drawn a wide research interest to help in tackling the problem faced in advancing technology for a proposed 'hydrogen economy'. Hydrogen being the lightest element has a very low density under normal conditions and is difficult to store at atmospheric pressure and room temperature. It can currently be stored as a compressed gas or a liquid with advantages and

disadvantages. Porous carbon materials have been recognised as having the potential to store hydrogen and have thus been the subject of research for several years.

This report is focused on the measurement of adsorption isotherms on two commercially available activated carbons using industrial grade hydrogen and research grade hydrogen to determine whether the concentration of impurities in the gas has an effect on the adsorption capacity of these materials. Grand Canonical Monte Carlo (GCMC) simulations are also performed to investigate these effects.

2. Experimental Method

The adsorbents used in this work are AC-1 (supplied by Calgon Carbon Corporation) and AC-2 (supplied by Norit Activated carbon). AC-1 is a bituminous coal based granular material activated at high temperature in steam. AC-2 is a pelletised chemically activated carbon, produced from a renewable raw material source via a version of the phosphoric acid process. It is a high activity, medium density grade carbon. These materials have surface areas of about 1000 and 1262 m^2/g respectively obtained from nitrogen adsorption measurements at 77 K using a Micromeritics ASAP 2010, which is a volumetric system. The hydrogen gas used was of two grades: 99.995 % and 99.9995 % purity supplied by BOC Special Gases Division. The lower grade hydrogen has no more than 50 ppm of impurities while the higher-grade hydrogen has about 5 ppm, see table 1.

The hydrogen gas adsorption isotherms were obtained gravimetrically using an Intelligent Gravimetric Analyser (IGA) supplied by Hiden Analytical Ltd., Warrington, U.K. The instrument combines computer-control and measurement of weight change, pressure and temperature to enable determination of gas adsorption-desorption isotherms in a wide range of operating conditions. The mass uptake is measured as a function of time and the approach to equilibrium monitored in real time with a computer algorithm. After equilibrium is established, the pressure is increased to the next set pressure value and the subsequent uptake is measured until equilibrium is re-established.

The experiments were carried out at 77 K, 195 K, 273 K and 303 K over a pressure range of 0 – 20 bar. Any temperature fluctuation was kept below 1 K by constant monitoring and setting of the temperature controls. Prior to the measurement of each isotherm the adsorbent sample (~ 150 mg) was outgassed to a constant weight at 423 K and 10^{-6} mbar for 16 hours. For the isotherms measured with ultrapure hydrogen on AC-2, the sample was prepared by heating to 523 K for 4 hours. The pressure was monitored using three pressure transducers with ranges of 0 – 1 bar, 0 – 10 bar and 0 – 20 bar and maintained at the relevant set-point by active computer control of the feed and exhaust valves throughout the duration of the experiments to an accuracy of +/- 0.02 % of the range used. The isotherms generated are reproducible when the experimental set-up is kept the same as described above. The hydrogen adsorption amount (% mass uptake) is calculated as shown below.

$$\% \text{ Mass Uptake} = \frac{wt_{H_2}}{wt_{H_2} + wt_{Carbon}} \times 100 \qquad (1)$$

Where wt_{H_2} is the weight of hydrogen, wt_{Carbon} is the weight of the dried carbon sample.

Table 1: Hydrogen Gas Specification (supplied by BOC Special Gases)

Grade	Purity (% min)	O_2 ppm	N_2 ppm	THC ppm	CO_2 ppm	H_2O ppm	CO ppm
N 4.5	99.995	Total impurities 50 ppm maximum					
N 5.5	99.9995	1	2	0.5	0.5	1	-

3. Molecular Models for the Adsorptive and the Adsorbent

The effect of impurities in the storage of hydrogen on activated carbons has been studied using Grand Canonical Monte Carlo (GCMC) simulations. In GCMC simulations, the temperature, the volume of the simulation cell and the chemical potential of the adsorbate are kept constant. Details of

the GCMC simulations can be found in the work of Frenkel and Smit (1996). Hydrogen molecules are modelled as two-site Lennard-Jones (LJ) spheres which interact via the 12-6 Lennard-Jones potential. The impurities are modelled to be nitrogen, as is the dominant content and oxygen and CO_2 have similar effects as nitrogen. Nitrogen molecules are modelled also as two-site Lennard-Jones (LJ) spheres. The Lennard-Jones parameters for the adsorptive species are given in Table 2.

Table 2: Summary of Lennard-Jones parameters for the adsorptive species

Adsorptive	σ, Å	ε/k_B, K	Bond Length, Å
Hydrogen (Cracknell, 2001)	2.59	12.5	0.74
Nitrogen (Turner et al., 1998)	3.31	37.3	1.098

The pores in the activated carbon adsorbent are modelled as slits, and each pore wall consists of an infinite number of structureless graphitic layers composed of Lennard-Jones sites. The interaction between a site on an adsorptive molecule and a single semi-infinite slab of graphite is given by Steele's 10-4-3 potential (Steele, 1974):

$$u_{sf}^{*}(z_i) = 2\pi\varepsilon_{sf}\rho_s\sigma_{sf}^2\Delta\left[\frac{2}{5}\left(\frac{\sigma_{sf}}{z_i}\right)^{10} - \left(\frac{\sigma_{sf}}{z_i}\right)^{4} - \frac{\sigma_{sf}^4}{3\Delta(z_i + 0.61\Delta)^3}\right], \quad (2)$$

Where ρ_s is the number of carbon atoms per unit volume in the graphitic layer (0.114 $Å^{-3}$), Δ is the separation distance between layers of graphitic carbon (3.35 Å), and z_i is the distance between the site and the surface. The values of σ and ε/k_B for the carbon are 3.40 Å and 28.0 K, respectively. The solid-fluid Lennard-Jones parameters are calculated by applying the Lorentz-Berthelot combining rules: $\sigma_{sf} = (\sigma_s + \sigma_f)/2$ and $\varepsilon_{sf} = \sqrt{\varepsilon_s\varepsilon_f}$. The overall interaction between an adsorbate site and the two pore walls is given by Equation (2).

$$u_{sf} = u_{sf}^{*}(z_i) + u_{sf}^{*}(w - z_i) \quad (3)$$

All the simulations were carried out in a rectangular simulation cell, which is bounded in the *z* direction by the pore walls and replicated in the *x* and *y* directions. The cell length in the *x* and *y* directions is 44.4 Å and periodic boundary conditions are applied in these directions.

Slit-shaped pore junction model (Maddox et al. 1996) was generated and applied to study the pore-blocking effects in the ink-bottle-shaped pores. The model consists of partial atomistic graphite layers on top and bottom (in the z direction) of the structure-less slit-shaped pores, as shown in Figure 1.

Similar to the structure-less slit model, this pore junction model is also bounded in the *z* direction by the pore walls and replicated in the *x* and *y* directions. The interaction between an adsorbate site with the adsorbent is the Steele's 10-4-3 potential (using Equations 2 and 3), and its interaction with each carbon atom in the atomistic region of the pore, which is given by the 12-6 LJ equation. The distance between the two structure-less walls is called the body pore width, and the distance between the two innermost atomistic layers is called the neck pore width, which is 20.1 Å less the body pore width. The cut-off distance, beyond which the potential is neglected, in the two models is set to be 15.24 Å. The system is equilibrated with 6×10^6 Monte Carlo cycles, then the variables of interest are averaged over another 1×10^7 sampling steps.

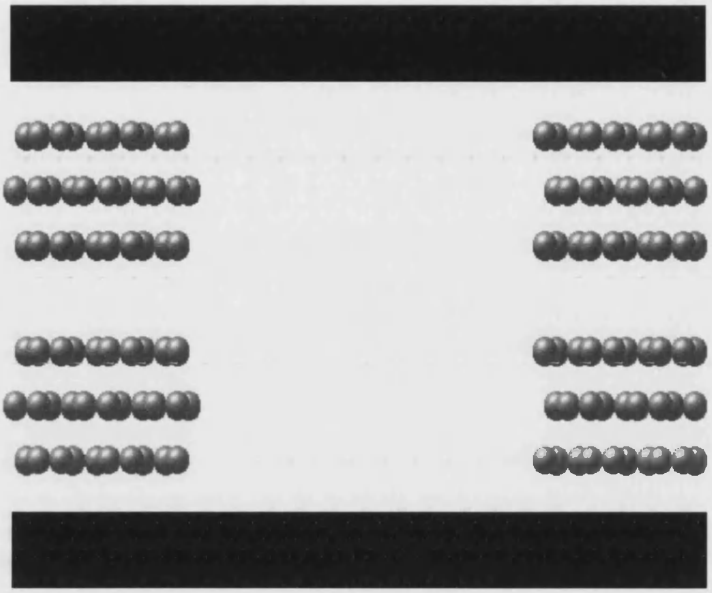

Figure 7: Schematic representation of the slit-shaped pore junction model

4. Results and Discussion

Figure 2 and 3 show the adsorption isotherms measured on the two activated carbon samples studied. It can be observed that for both samples the % mass uptake increases when the high grade hydrogen is used, irrespective of the temperature of adsorption. It implies that the lower the concentration of impurities in the gas the higher the mass uptake. This is in agreement with the work of Amankwah and Schwarz (1991), which predicts that the amount of hydrogen adsorbed by an activated carbon is reduced due to the presence of nitrogen as an impurity in the gas. The isotherms obtained are generally type 1 (according to the IUPAC classification) characteristic of the physisorption of supercritical gases. As the isotherms obtained are supercritical there is no condensation of hydrogen in the pores of the sample.

Initial speculation suggests that depending on the type of pores present in the carbon samples the reduction in the adsorption capacity of the adsorbent caused by impurities in the hydrogen gas may be due to a pore blocking phenomenon, such that hydrogen molecules are in competition with nitrogen ones for the available adsorption sites. This stems from the fact that nitrogen molecules are bigger in size than hydrogen ones, resulting in a higher molecular attraction of nitrogen to the internal pore surfaces in preference to hydrogen, which has an even weaker interaction with the pores of the adsorbent.

If we look at the impurity specification of the high-grade hydrogen, which can be found in table 1, N_2 is present in the highest concentration (2 ppm) in comparison to the other impurities, for the purpose of simplification it is reasonable to model all the impurities present as N_2, similar to the study of Amankwah and Schwarz (1991).

GCMC simulations of pure H_2 and H_2 with different concentrations of N_2 were carried out in slit pores with pore sizes of 7.40 and 26.64 Å, respectively, at 77 K and at pressures up to 1 bar. The results are presented in figure 4 and 5, which show the weight uptake of H_2 and total weight uptake in these two slit models. In a 7.40 Å slit pore, H_2 uptake decreases drastically even when only 5 ppm of N_2 was included in the gas phase; when the content of N_2 was increased to 100 ppm, H_2 weight uptake is nearly negligible at pressures up to 1 bar. In the 26.64 Å slit pore, H_2 uptake decreases gradually as the content of N_2 increases. The reason is that N_2 adsorbs much stronger than H_2 in a 7.40 Å slit pore, it fills the pore instantly even when its partial pressure is very low. Figure 4 shows a snapshot of adsorption of 5 ppm N_2 in H_2 in 7.40 Å slit at 77 K and at 50 pa. This strong adsorption of N_2 in 7.40 Å is due to the strong overlap of the interaction of N_2 with the two opposite walls. However, this overlap decreases drastically as the pore size increases, so this pore filling as low pressures cannot happen in 26.64 Å slit pores.

Although H_2 weight uptake decreases as the content of impurities increases in both the pores, the total weight uptake, which includes the weight uptake of H_2 and N_2 (as we cannot distinguish them in our gravimetric apparatus), increases as the content of impurities increases. The reason is because N_2 adsorbs much stronger than H_2. This seems contrary to our experimental observations, therefore, we proposed the slit pore junction model, as shown in Figure 1, to clarify the difference. GCMC simulations of H_2 with 100 ppm of N_2 were carried out in a junction model with a neck pore width of 7.40 Å at 77 K and at pressures up to 1 bar. Figure 7 shows a snapshot of the adsorption of H_2 with 100 ppm N_2 in this junction model at 50 pa. Clearly, N_2 molecules fill the neck pores quickly, and blocks the bigger body pore for of H_2 with 100 ppm N_2 in this junction model at 50 pa. Clearly, N_2 fills the neck pores quickly, and blocks the bigger body pore for hydrogen adsorption.

According to Rezpka et al (1998), for hydrogen storage in porous activated carbons, the hydrogen weight uptake increases as the micropore volume of the activated carbon increases. If there is certain amount of ink-bottle pores in our activated carbons, as the content of impurities increases, more and more neck pores are filled with the impurities, causing the blocking of the pores. Therefore the available micropore volume for hydrogen storage decreases, so does the total weight uptake. Although the total amount in the neck pores in these ink-bottle pores increases with the impurities (see Figure 5), however, the contribution of these neck pores to the total micropore volume is trivial, so the increase of the total weight uptake in these neck pores will not cancel the decrease of the total weight uptake as the content of impurities increases. However, this is at the moment just a hypothesis, and more experimental and theoretical investigations are needed for confirmation.

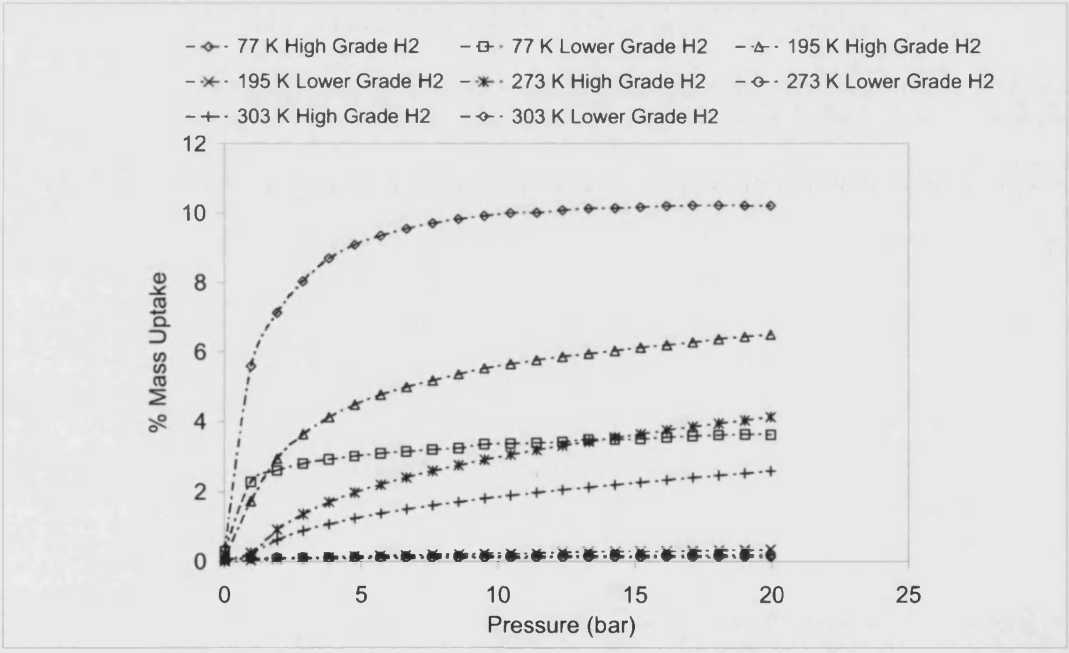

Figure 8: Adsorption isotherms for AC-1 at different temperatures

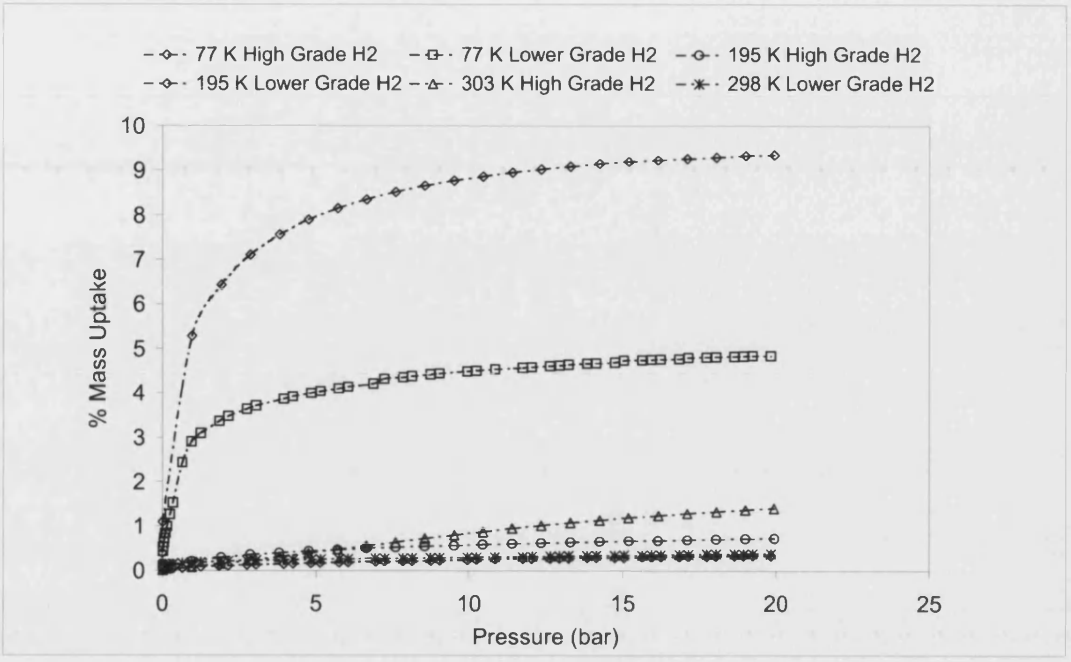

Figure 9: Adsorption isotherms for AC-2 at different temperatures

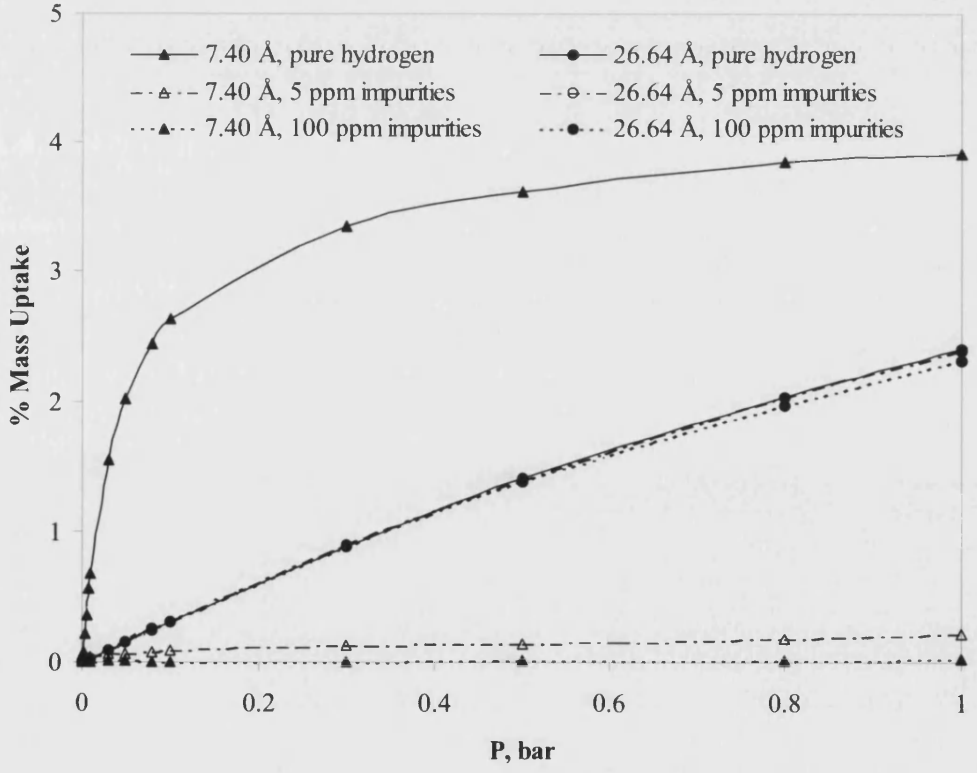

Figure 10: Simulated Hydrogen weight uptake in slit pores at 77 K

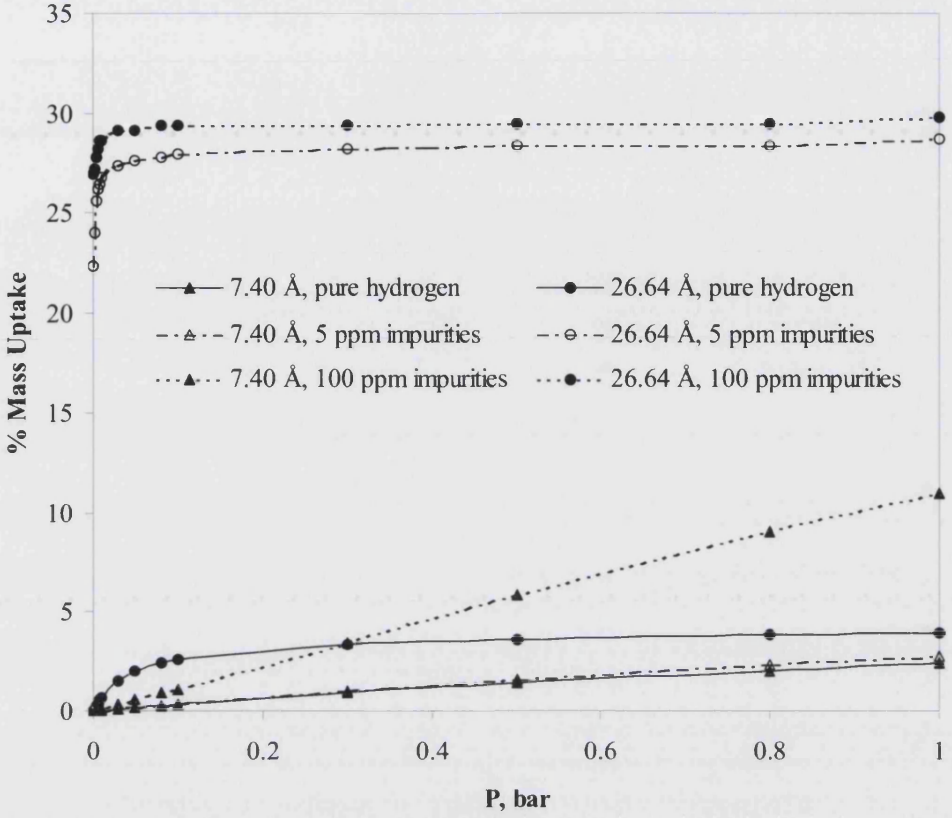

Figure 11: Simulated total weight uptake in slit pores at 77 K

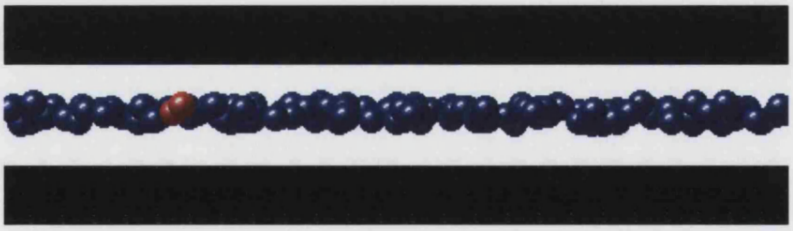

Figure 12: A snapshot of simulated adsorption of H_2 with 5 ppm N_2 in a slit pore at 77 K and 50 pa (Red: H_2; Blue: N_2)

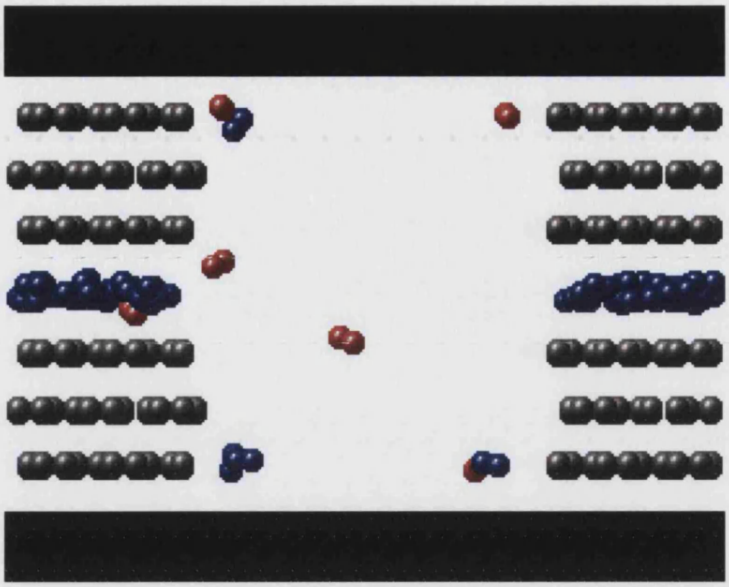

Figure 13: A snapshot of the simulated adsorption of H_2 with 100 ppm N_2 in a slit pore at 77 K and 50 pa (Red: H_2; Blue: N_2)

Conclusions

We have observed experimentally an increase in the % mass uptake of gas when high grade hydrogen is used in comparison to the standard grade within the specifications provided. This % mass uptake increase is observed on both of the activated carbons tested. Molecular simulations suggest that the mass uptake is dependent on the type of pores present in the samples, the size of these pores and on the concentration of impurities present in the gas.

More work still needs to be done in terms of experiments and molecular simulations to further test our present ideas.

Acknowledgements

The authors will like to acknowledge the financial support of the EPSRC, and thank the members of the United Kingdom Sustainable Hydrogen Energy Consortium (UK-SHEC) for their support.

References

Amankwah, K. A. G., Schwarz J. A., 1991. *Int. J. Hydrogen* Energy, 16(5): 339-344.

Cracknell, R.F., 2001. *Phys. Chem. Chem. Phys.*, 3, 2091-2097.

Frenkel, D., Smit, B., 1996. *Understanding Molecular Simulation, from Algorithms to Applications*. London: Academic Press.

Maddox, M. W., Quirke, N., Gubbins, K.E., 1996. *Simulation of Pore Blocking Hysteresis in Model Porous Carbon Networks*, Fundamentals of Adsorption, Proceedings of the Fifth International Conference on Fundamentals of Adsorption: p 571-578.

Rzepka, M., Lamp, P., de la Casa-Lillo, M. A., 1998. *J. Phys. Chem. B*, 102(52): 10894-8.

Steele, W. A., 1974. Interaction of Gases with Solid Surfaces. *International Encyclopaedia of Phys. Chem. Chem. Phys.* 3.

Turner, A. R., Quirke, N., 1998. Carbon, 36(10): 1439-1446

Paper Presented at the Conference on the Characterisation of Porous Solids VII, Aix-en-Provence, France (25^{th} – 28^{th} May, 2005)

Hydrogen storage in nanoporous carbons

O.Y. Odunsi, Y. He and T.J. Mays*

Department of Chemical Engineering, University of Bath, Bath BA2 7AY, United Kingdom

ABSTRACT

Hydrogen is of much current interest as an energy store and/or carrier in sustainable energy conversion systems. The attractions are that H_2 generates ~143 MJ kg^{-1} when it reacts with O_2, with only H_2O as the product. This compares to fossil fuels, which have lower specific energy densities (in the range 10–50 MJ kg^{-1}), and which generate environmentally–damaging CO_2. However, there are many challenges to be met before energy systems based on H_2 are technically feasible or socially/economically acceptable. One of the main challenges is to store H_2 safely, effectively (principally at low volume) and at low cost.

This paper presents the results of an experimental study of supercritical H_2 adsorption in nanoporous carbons plus some supporting data from molecular simulations of adsorption. This is part of a broad examination of the potential of these materials as storage media for H_2 in sustainable energy systems, in comparison with other proposed storage media such as carbon nanofibres and metal hydrides, and with other storage systems such cryogenic liquid and high–pressure gas. Note that the new term nanoporous refers to pores in the size range 0.1 to 100 nm, as proposed in another Mays paper at COPS-VII.

Recent results of this work appear to show high H_2 uptakes in certain nanoporous carbons, but that these uptakes only occur for very pure hydrogen. We propose a pore blocking mechanism to account for this. While at present high uptakes only appear possible at liquid nitrogen temperatures, the pressures are 'reasonable' (below 2000 kPa).

1. INTRODUCTION

Sustainable energy supply is crucial in helping to tackle issues related to fossil fuels such depleting energy resources, decreasing energy security, reducing air quality and global warming. Hydrogen is a suitable and likely candidate as an energy vector to help in combating these issues because the products of its combustion are environmentally benign (water vapour). However, one challenge on the road to a 'hydrogen economy' is that as the lightest element hydrogen is difficult to store in small volumes. This is unsuitable if hydrogen is to be used for mobile applications where on-board space is a premium. For example, 5 kg of H_2 could provide enough energy for a standard saloon car to cruise for 500 km. However, in ambient conditions this would occupy a spherical vessel of about 5 m internal diameter, which is impractical. By contrast 5 kg of liquid H_2 would occupy a spherical vessel of only 0.5 m internal diameter, which is potentially more manageable.

* Corresponding author: Tel: +44 (0)1225 386528, Fax: +44 (0)1225 385713, E-mail: t.j.mays@bath.ac.uk

Currently, hydrogen can be stored as a liquid (its most energy dense form) and as a compressed gas at very high pressures and in solid-state systems such as metal hydrides. There are issues surrounding these methods such as the energy intensive nature of the hydrogen liquefaction process and problems due to boil-off, and the associated high pressures for gas storage, which can pose safety issues on board a vehicle. Metal hydride storage systems require high desorption temperatures and may only store hydrogen irreversibly.

Nanoporous carbons have been identified as potentially good hydrogen storage media as they are widely available, are low cost, they have high surface areas and pore volumes and may be easily regenerated for recycling purposes. Hydrogen storage in these materials is the main focus of this paper. We have measured adsorption isotherms on these materials using industrial or low-grade and research or high-grade grade hydrogen to determine whether the concentration of impurities in the gas has an impact on the storage capacity of these materials. We have also carried out grand canonical Monte Carlo simulations to investigate these effects.

2. EXPERIMENTAL DETAILS

The adsorbents used in this work are AC-1 (supplied by Calgon Carbon Corporation) and AC-2 (supplied by Norit Activated carbon). AC-1 is a bituminous coal based granular material activated at high temperature in steam. AC-2 is a pelletised chemically activated carbon, produced from a renewable raw material source via a version of the phosphoric acid process. It is a high activity, medium density grade carbon. These materials have surface areas of 1,000 and 1,262 $m^2\ g^{-1}$ respectively obtained from BET analysis of nitrogen adsorption measurements at 77 K below relative pressures of 0.4 using a Micromeritics ASAP 2010 volumetric system. The hydrogen gas used was of two grades: 99.995 % (low grade, LG-H_2) and 99.9995 % (high grade, HG-H_2) purity supplied by BOC Special Gases Division. The lower grade hydrogen has no more than 50 ppm of impurities while the high-grade hydrogen has about 5 ppm impurities, see Table 1.

Table 1:Hydrogen gas specification (supplied by BOC Special Gases)

Grade	Purity (% min)	O_2 ppm	N_2 ppm	THC* ppm	CO_2 ppm	H_2O ppm	CO ppm
LG-H_2	99.995	Total impurities 50 ppm maximum					
HG-H_2	99.9995	1	2	0.5	0.5	1	-

* Total hydrocarbons

Equilibrium hydrogen gas adsorption isotherms were obtained gravimetrically using an Intelligent Gravimetric Analyser (IGA) (Hiden Analytical Ltd.). This instrument combines computer-control and measurement of weight change, pressure and temperature to enable determination of gas adsorption-desorption isotherms in a wide range of operating conditions. After equilibrium is established at a particular pressure, the pressure is increased to the next set value and the subsequent uptake is measured over time until equilibrium is re-established. We have carried out experiments at 77 K, 195 K, 273 K and 303 K over a pressure range of 0 – 2000 kPa.

Prior to the measurement of each isotherm samples of AC-1 (~150 mg) were degassed to a constant weight at 423 K and 10^{-6} bar for 16 hours. For the isotherms measured with high-grade hydrogen on AC-2, the sample was prepared by heating to 523 K and 10^{-6} bar for 4 hours; the higher temperature having being determined to achieve similar degassing weight losses but over a shorter time. The pressure was monitored using three pressure transducers with ranges of 0 – 1 bar, 0 – 10 bar and 0 – 20 bar and maintained at the relevant set-point by active computer control of the feed and exhaust valves throughout the duration of the experiments to an accuracy of +/- 0.02 % of the range used. The isotherms generated are reproducible when the experimental set-up is kept the same as described above. The hydrogen adsorption amount (% mass uptake) is calculated as follows

$$\% \text{ mass uptake} = (w_E / w_S) \times 100 \quad (1)$$

where w_E is the excess uptake (weight of adsorbate less the weight of adsorptive that would occupy the same volume as the adsorptive at the same pressure and temperature) and w_S is the weight of the sample in vacuum after degassing. The excess uptake is calculated as follows

$$w_E = w - w_S + \rho_B V_S \quad (2)$$

where w is the detected weight of the sample, ρ_B is the bulk mass density of the adsorptive and V_S is the inaccessible volume of the sample (which displaces the bulk gas). The bulk mass density of the adsorptive is calculated using the Peng-Robinson equation of state, while V_S is obtained in ambient conditions using a He pycnometer (AccuPyc 1330, Micromeritics) assuming no He uptake.

3. MONTE CARLO SIMULATION

Grand canonical Monte Carlo (GCMC) simulations, in which the temperature, the volume of the simulation cell and the chemical potential of the adsorbate-adsorptive system are kept constant, have been carried out to probe the effect of impurities on the storage of hydrogen on nanoporous carbons. Details of the GCMC simulations can be found in the work of Frenkel and Smit [1]. The impurities are taken as nitrogen, since it is the dominant balance gas and oxygen and carbon dioxide have similar effects as nitrogen. Nitrogen molecules are modelled also as two-site Lennard-Jones (LJ) spheres, which interact via the 12-6 LJ potential. A two-site LJ spheres model is also applied to hydrogen. The Lennard-Jones parameters (collision diameter, σ, energy parameter, ε / k_B, where k_B is Boltzmann's constant, and bond length) for the adsorptive species are given in Table 2.

Table 2:Lennard-Jones parameters for the adsorptive species in the molecular simulations

Adsorptive		σ / nm	(ε / k_B) / K	Bond length / nm
Hydrogen	[2]	0.259	12.5	0.074
Nitrogen	[3]	0.331	37.3	0.1098

The pores in the activated carbon adsorbent are modelled as structureless slits, and each pore wall consists of an infinite number of structureless graphitic layers composed of Lennard-Jones sites. The interaction between a site on an adsorptive molecule and a single semi-infinite slab of graphite is given by Steele's 10-4-3 potential [4]:

$$u_{sf}^{*}(z_i) = 2\pi\varepsilon_{sf}\rho_s\sigma_{sf}^2\Delta\left[\frac{2}{5}\left(\frac{\sigma_{sf}}{z_i}\right)^{10} - \left(\frac{\sigma_{sf}}{z_i}\right)^{4} - \frac{\sigma_{sf}^4}{3\Delta(z_i + 0.61\Delta)^3}\right] \quad (3)$$

where ρ_s is the number of carbon atoms per unit volume in the graphitic layer (114 nm^{-3}), Δ is the separation distance between layers of graphitic carbon (0.3354 nm), and z_i is the distance between the site and the surface. All the simulations were carried out in a rectangular simulation cell, which is bounded in the z direction by the pore walls and replicated in the x and y directions. The cell length in the x and y directions is 4.44 nm and periodic boundary conditions are applied in these directions. The cut-off distance, beyond which the potential is neglected, is set to be 1.524 nm. The system is equilibrated with 6×10^6 Monte Carlo cycles, then the variables of interest are averaged over another 1×10^7 sampling steps. Output of the simulations is the total number of molecules of each gas species in a pore at a specified pressure and temperature. This can easily be converted to excess uptake as the pore volume in known. Further details of the GCMC simulations can be found in the work of Frenkel and Smit [1].

4. RESULTS AND DISCUSSION

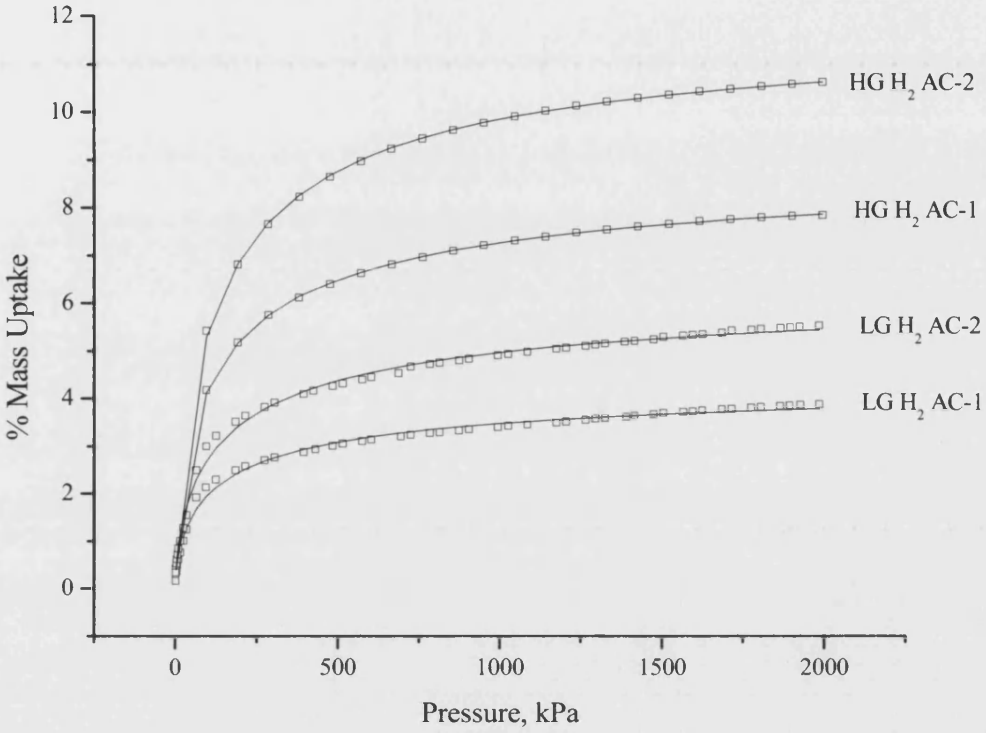

Fig.1. Adsorption isotherms at 77 K for the two activated carbons and for the two grades of hydrogen.

Fig. 1. shows the excess adsorption isotherms measured gravimetrically at 77 K on the two activated carbon samples for the two grades of hydrogen. All isotherms are of Type I in the IUPAC classification - this is typical of supercritical adsorption (where there is no condensation in pores) at pressures where the density of the bulk gas is very much lower then the adsorbate. For both samples the % mass uptake increases when high-grade hydrogen is used, with AC-2 always showing a higher uptake than AC-1. The latter can be linked to the higher BET surface area of AC-2 (1,262 $m^2 g^{-1}$) compared to AC-1 (1,000 $m^2 g^{-1}$). Isotherms at higher temperatures were similar, but reached much lower maximum uptakes (< 2 %).

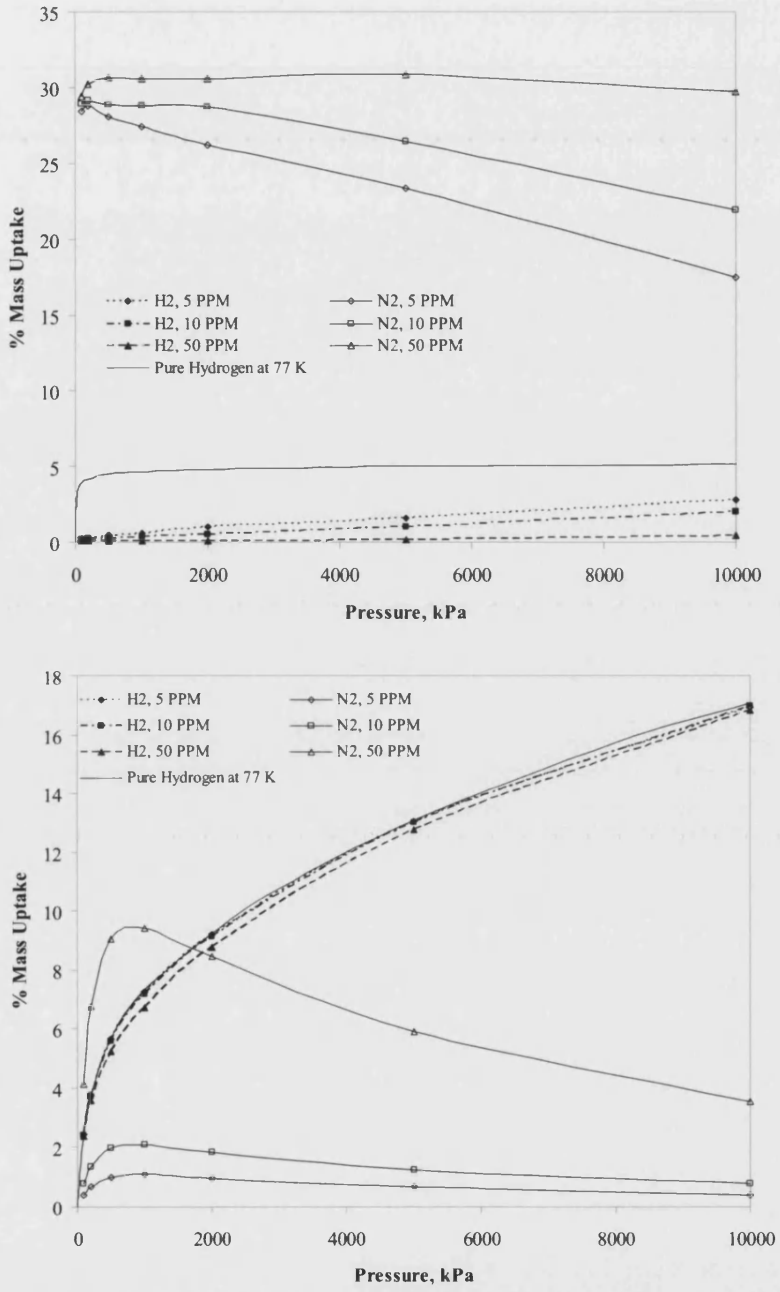

Fig. 2 GCMC simulation of the adsorption of H_2/N_2 mixtures in slit-shaped carbon pores at 77 K. Top: 0.74nm ; bottom: 2.664 nm.

The main observation from Fig. 1 is the very high maximum uptakes for both carbons (~10 % for AC-2 and ~7.5% for AC-1) in the HG-H_2 compared with capacities about half these values for the LG-H_2, which are commonly observed for activated carbons. This implies that the storage of hydrogen in porous carbons may be affected by the purity of the gas used and that these carbons may be sensitive to ppm amounts of impurities such as nitrogen, which therefore may compromise their storage capacity. This is in agreement with the work of Amankwah and Schwarz [5], where the amount of hydrogen adsorbed by an activated carbon appeared to be reduced in the presence of nitrogen impurities.

The difference between uptakes for the two adsorptive grades may be due to differences between the molecular sizes and interactions energies of the hydrogen and impurities (see Table 1) and how these affect uptake in pores of different sizes. Results from the simulations clarify this.

Fig. 2 shows the GCMC simulation results of the adsorption of binary H_2/N_2 mixtures (including HG-H_2, 5ppm N_2, and LG-H_2, 50 ppm N_2, see Table 1) in slit-shaped pores of size 0.74 nm and 2.664 nm. Those simulated isotherms are the total adsorption isotherms in the pore as opposed to excess isotherms determined experimentally. However, we have found that in experimental measurements, the difference between total and excess hydrogen adsorption isotherms in activated carbon is insignificant on the conditions studied. The simulated pure hydrogen adsorption isotherms are also shown in Fig. 2 as a comparison. In the 0.74 nm pore, the existence of trace amounts of N_2 greatly reduces the amount of H_2 adsorbed in the pore, and the amount of H_2 adsorbed is less than 10% in comparison to pure H_2 adsorption at 2000 kPa. The adsorbed phase still contains N_2 even when using HG-H_2 where the amount of N_2 in the gas phase is only 5 ppm, though the amount is less than for 50 ppm. For LG-H_2, the amount adsorbed for hydrogen is small even at high pressures. In the 2.664 nm pore, the existence of N_2 seems not to influence the adsorption of H_2, which decreases only marginally as the content of N_2 increases from 5 ppm to 50 ppm, and is quite similar to pure hydrogen adsorption. The amount of N_2 adsorbed is considerably reduced as the N_2 content in the gas phase decreases from 50 ppm to 5 ppm. The adsorbed phase is mainly H_2, especially at high pressures and with HG-H_2.

Fig. 3 shows the adsorbed-phase density for hydrogen adsorption in slit-shaped pores at 77 K by GCMC simulations. Small pores with pore sizes of less than 1 nm are filled with hydrogen at quite low pressure while the adsorbed-phase density approaches liquid hydrogen density at high pressure in bigger pores. The maximum density at 2000 kPa is obtained in a pore with a pore size of about 0.9 nm, which is sonly just less than the density of liquid hydrogen (0.071 g cm^{-3}). Fig. 4 shows a relationship between the adsorbed-phase density and the accessible pore volume of an adsorbent sample for fixed weight uptake. The dotted line parallel to the *y*-axis represents the liquid hydrogen density. Clearly, for a 'reasonable' high hydrogen weight uptake, a large accessible pore volume or a high adsorbed phase density of hydrogen or both is needed. For example, a combination of 1.0 cm^3 g^{-1} accessible pore volume and 0.063 g cm^{-3} of adsorbed hydrogen density will lead to 6-wt% of hydrogen in a carbon sample.

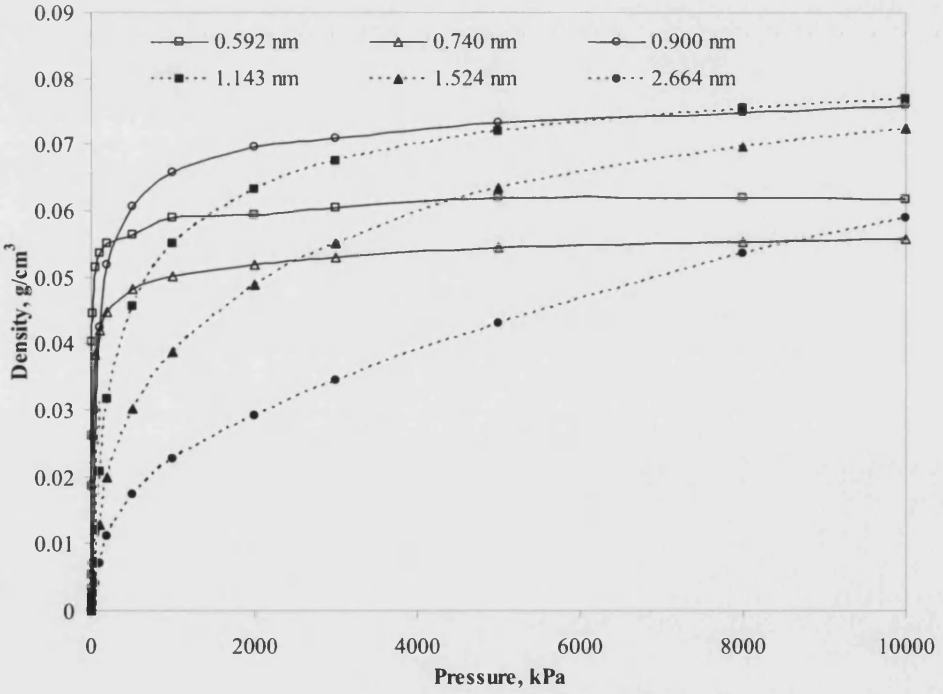

Fig. 3. Adsorbed-phase density of hydrogen in slit pores at 77 K from GCMC simulations.

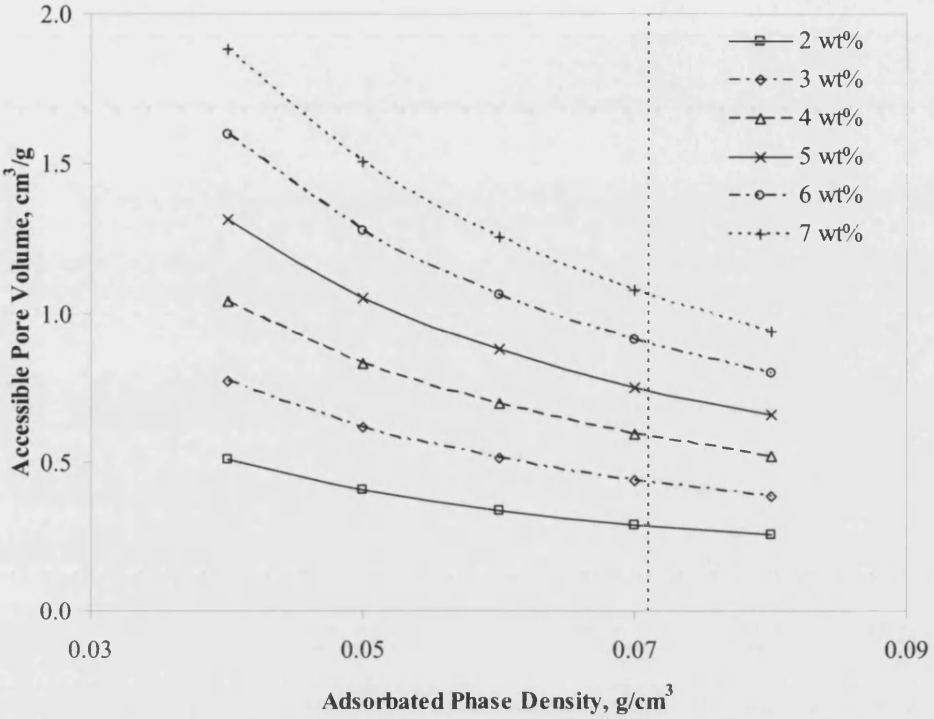

Fig. 4. Relationship between adsorbed-phase density and accessible pore volume. Dotted vertical line is for liquid hydrogen.

However, the pore volume for the AC-1 carbon in this work is 0.66 $cm^3\ g^{-1}$, estimated by N_2 adsorption at 77 K. It would therefore seem impossible for this carbon to have an uptake of about 7 wt%, since the adsorbed-phase density is equal or less than the density of liquid hydrogen (Fig. 6). Therefore, it is reasonable to suspect that there are some pores not accessible to N_2 at 77 K in the carbons. But these pores may still be accessible to pure H_2 since the smallest slit pore accessible to N_2 is 0.58 nm while H_2 can access a slit pore with a pore size of 0.52 nm. Accordingly, we propose a pore blocking mechanism as follows.

Simulations suggest that in low concentrations (< 50 ppm) nitrogen will be preferentially adsorbed in certain small pores compared to hydrogen due to higher interaction energies with pore walls. Nitrogen will not be important in larger pores, where affects due to differences in interaction energies are reduced (Fig. 2), nor in inaccessible smaller pores. These filled pores may restrict access to the rest of the pore network accessible to hydrogen, and hence reduce capacity, even though they do not contribute much to total uptake. Similar pore blocking arguments have been presented before [6]. The extent of pore blocking will be less for lower impurity concentrations (Fig. 2), and here it seems that reducing impurities from 50 to 5 ppm increases capacity by about a factor of about two. We are currently testing these ideas with further experimental measurements and simulations of hydrogen adsorption.

5. CONCLUDING REMARKS

We have observed that low cost, readily available commercial nanoporous activated carbons are capable of storing large amounts of hydrogen (up to 10 wt.%) at cryogenic temperatures (77 K), at pressures below 2000 kPa and in very pure gas. Molecular simulations of adsorption suggest that the reduced capacity of the carbons in lower purity gas is due to restriction of the pore network by the blocking of some small pores by impurities. While the simple materials, high capacities and low pressures are certainly attractive for hydrogen storage, the requirements of cryogenic temperatures and high purity gas would add to the cost.

REFERENCES

[1] D. Frenkel and B. Smit, Understanding Molecular Simulation, Academic Press, San Diego, 1996.
[2] R.F. Cracknell, Phys. Chem. Chem. Phys., 3 (2001) 2091.
[3] A.R. Turner and N. Quirke, Carbon, 36 (1998) 1439.
[4] W.A. Steele, Interaction of Gases with Solid Surfaces, Pergamon Press, Oxford, 1974.
[5] K.A.G. Amankwah and J.A. Schwarz, Int. J. Hydrogen Energy, 16 (1991) 339.
[6] M.W. Maddox, N. Quirke and K.E. Gubbins, Molecular Simulation, 19 (1997) 267.

ACKNOWLEDGEMENTS

We thank the EPSRC for funding and the members of the United Kingdom Sustainable Hydrogen Energy Consortium (UK-SHEC, see http://www.uk-shec.org/) for their support.

SET for Britain Final Award Poster, 2005

Hydrogen Storage on Nanoporous Carbons

Toni Odunsi, Yufeng He, Tim Mays

Advanced Materials and Porous Solids Group, Department of Chemical Engineering, University of Bath, BATH. BA2 7AY, U. K.

UK-SHEC United Kingdom Sustainable Hydrogen Energy Consortium

INTRODUCTION

The use of hydrogen as a tool in solving the world's energy issues is a promising one.

- Products of its combustion are environmentally benign;
- Can be produced from renewable and sustainable resources;
- Improved energy security;
- Better air quality.

Technological Setback

- Storing hydrogen is difficult, being the lightest gas it occupies a large space at ambient conditions;
- Hydrogen currently needs to be compressed to high pressures (> 300 bar) or liquefied to store a useful amount (energy intensive).

AIM: Potential Solution

To store hydrogen on nanoporous carbon materials.

WHY?

- Storage space greatly reduced for stationary and mobile applications;
- Nanoporous carbons have high surface areas;
- They are cheap and readily available from sustainable sources.

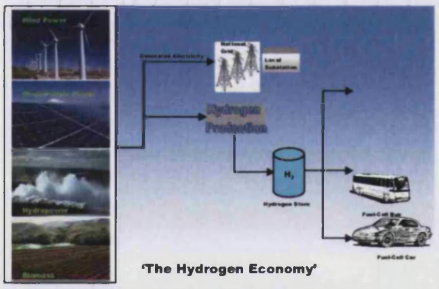

'The Hydrogen Economy'

EXPERIMENTAL

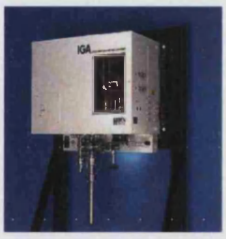

The IGA-001 Gas Adsorption System

- Pressure is changed and then held constant during sorption at the set-point P_n.
- Weight data is acquired and analysed in real-time to determine kinetic parameters and predict the point of equilibrium uptake.
- Equilibrium points are collected and plotted as an isotherm.

RESULTS AND DISCUSSION

Hydrogen Adsorption Measurements

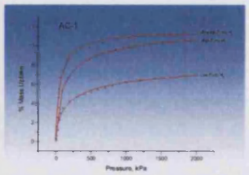

- Hydrogen purity affects the amount that can be stored.
- High storage results are obtained at cryogenic temperatures (77 K).
- Of the 3 materials studied, AC-1 has the highest storage capacity for hydrogen.

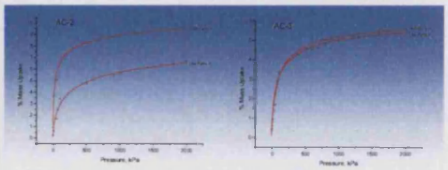

The experimental data shown above fitted to Toth models to help in understanding the adsorption process.

$$n = n_0 \frac{bp}{(1+(bp)^c)^{1/c}}$$

- n (wt-%) is the experimental amount stored on the adsorbent,
- n_0 (wt-%) is the maximum storage capacity of the adsorbent,
- b (kPa^{-1}) is a measure of how strong an adsorbate molecule is attracted to an adsorbent surface and
- c is a constant that characterises the system's heterogeneity.

Material Properties and Structure Characterisation Results

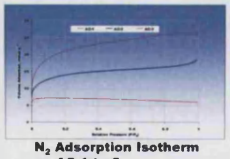

N_2 Adsorption Isotherm on AC-1 to 3.

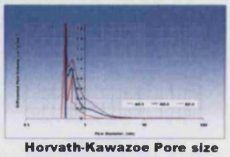

Horvath-Kawazoe Pore size distributions for AC-1 to 3.

Material	Precursor	Particle size range, mm	Ash content, mass % db	Moisture content, mass %	Bulk density, g cm^{-3}	BET Surface Area, $m^2 g^{-1}$	Pore Volume, $cm^3 g^{-1}$	Hydrogen Storage Capacity, mass %
AC-1	Coal	Pellets with average diameter 2 mm	10.0	8.0	1.8	1645	0.91	11.4
AC-2	Bituminous coal	2.8 by 1.0	8.0	5.0	1.7	1000	0.64	9.5
AC-3	Coconut shells	1.4 by 0.7	1.7	6.0	2.5	405	0.26	5.6

[1] Obtained using thermogravimetry and values quoted are on dry basis (db). [2] Obtained by drying samples under vacuum. [3] Obtained from Helium pycnometry at room temperature.

CONCLUSIONS

- Nanoporous carbons are capable of storing high amounts of hydrogen. Storage amounts of 11 wt-% on AC-1 and 9.5 wt-% on AC-2 have been obtained.
- This is dependent on the experimentally observed sensitivity to the purity of the hydrogen gas used. This effect can be attributed to a possible pore blocking effect.
- These results will have a significant impact on the application of nanoporous carbons as H_2 storage media for vehicular and stationary applications.

ACKNOWLEDGMENTS

We thank the EPSRC for funding and the members of the United Kingdom Sustainable Hydrogen Energy Consortium (UK-SHEC, see (http://www.uk-shec.org/) for their support.